Numerical simulations of shock and rarefaction waves interacting with interfaces in compressible multiphase flows

by

Marc T. Henry de Frahan

A dissertation submitted in partial fulfillment
of the requirements for the degree of
Doctor of Philosophy
(Mechanical Engineering)
in The University of Michigan
2016

Doctoral Committee:

Assistant Professor Eric Johnsen, Chair
Professor David R. Dowling
Professor R. Paul Drake
Associate Professor Krzysztof J. Fidkowski

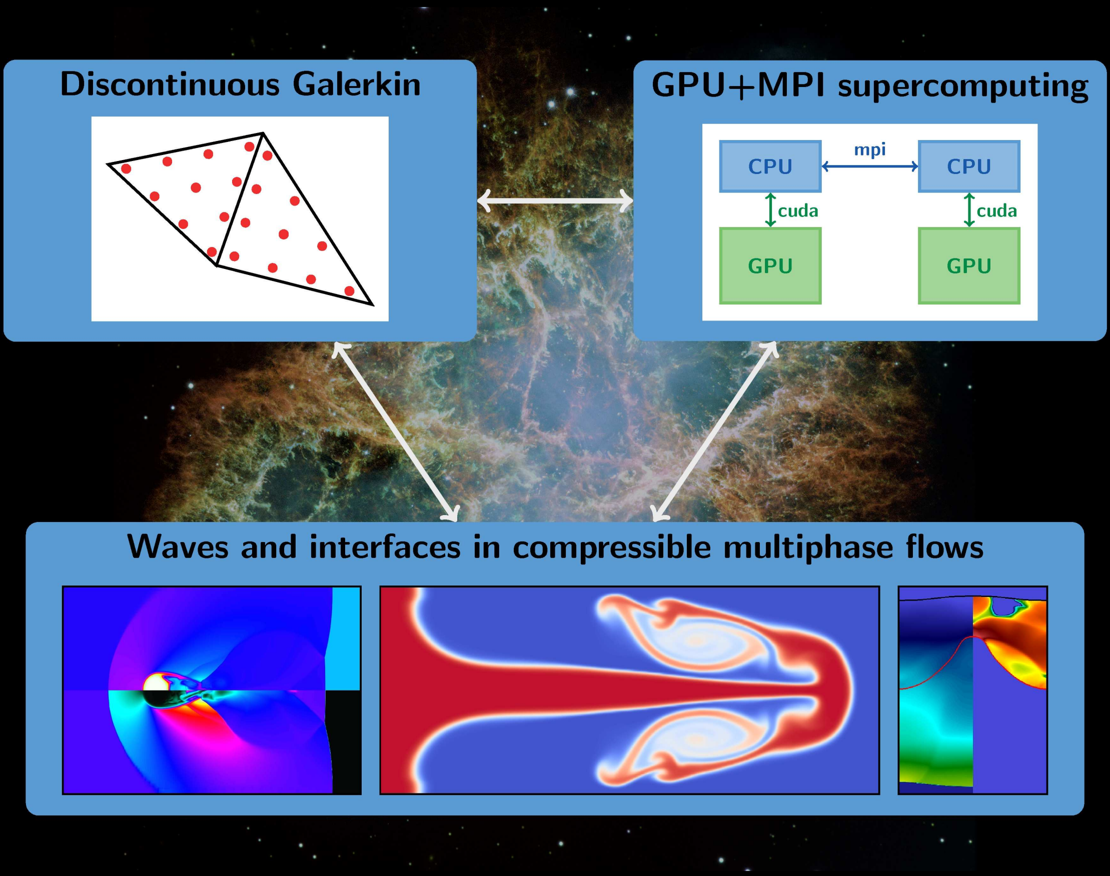

Background photo credit: NASA.

To Aku and Pati.

ACKNOWLEDGEMENTS

I would like to express my gratitude to Eric Johnsen, my adviser, for his support, advice, and encouragement during my Ph.D. His guidance and mentorship was invaluable for my research and professional development. I extend my thanks to my committee members, Prof. Drake, Prof Fidkowski, and Prof. Dowling, for their advice and thoughts on my work. Rob Cavallo at Lawrence Livermore National Laboratory introduced me to the exciting intersection of numerical simulations and experiments, as well as international collaborations.

This work would have been impossible without the friendships I made at the University of Michigan. I am grateful to everyone in that corner of the Autolab: Brandon for lending me a tape measure and being a partner in crime, Shahab for introducing me to honeycomb, Darian for his characteristic wit, Mauro for the in-depth conversations about our society, Sam for not speaking French and taking care of Freyja, Phil for his frowns, Kevin for the March madness bracket, Suyash for the website tips, Siddhesh for his Linux issues, Aditya for the dance lessons, Renaud for his landlord stories, Pooya for his knowledge of everything CFD related, Sreenivas for his understanding of DG error metrics, Jonathan for his Bernie enthusiasm, Adaleena for the dog pictures, Brian for his willingness to get to the bottom of everything (especially color theory), TJ for his whiteboard problems, Harish for his existential philosophy, Louise for the cooking discussions, Alex for the podcast recommendations, and Joel for organizing the IM games. I would also like to thank everyone at the Mechanical Engineering Graduate Council for helping me get involved in campus events and making life in the department that much more fun. Thanks in particular to the members of my dissertation writing group who provided valuable feedback on early chapters and the motivation to just sit and write every week. Thanks as well to Jonathon

Woods for giving me an outlet by organizing so many soccer teams. Thanks to my friends in Belgium, Quentin, Jonathan, F-X, Arnaud, Mathieu, Cedric, Ludovic, Cyrille, Erik, and Alex, for all the adventures, conversations, and book recommendations. My grandparents, Aku and Pati, my parents, Victoire and Bruno, and my siblings, Valentine, Jack, and Philip, have been particularly supportive during all these years. Finally, I thank Cassie for her encouragement during the many frustrations and jubilations, and for her willingness to explore the world with me through plays, traveling, hiking, cooking, and conversation.

This research was supported in part by the DOE NNSA/ASC under the predictive Science Academic Alliance Program by Grant No. DEFC52-08NA28616, by ONR grant N00014-12-1-0751 under Dr. Ki-Han Kim, by NSF grant CBET 1253157, by the Rackham Predoctoral Fellowship at the University of Michigan, and through computational resources and services provided by Advanced Research Computing at the University of Michigan, Ann Arbor. This work used the Extreme Science and Engineering Discovery Environment (XSEDE), which is supported by National Science Foundation grant number OCI-1053575.

TABLE OF CONTENTS

CHAPTER

LIST OF FIGURES

Figure

LIST OF TABLES

Table

LIST OF APPENDICES

Appendix

LIST OF ABBREVIATIONS

DG Discontinuous Galerkin

RKDG Runge-Kutta Discontinuous Galerkin

RDG Recovery Discontinuous Galerkin

ICB Interface-Centered Reconstruction with Binary Projection

HR Hierarchical Reconstruction

FV Finite Volume

CPU Computing Processing Units

GPU Graphics Processing Units

MPI Message Passing Interface

ICF Inertial Confinement Fusion

RM Richtmyer-Meshkov

RT Rayleigh-Taylor

KH Kelvin-Helmholtz

ABSTRACT

Numerical simulations of shock and rarefaction waves interacting with interfaces in compressible multiphase flows

by

Marc T. Henry de Frahan

Chair: Eric Johnsen

Developing a highly accurate numerical framework to study multiphase mixing in high speed flows containing shear layers, shocks, and strong accelerations is critical to many scientific and engineering endeavors. These flows occur across a wide range of scales: from tiny bubbles in human tissue to massive stars collapsing. The lack of understanding of these flows has impeded the success of many engineering applications, our comprehension of astrophysical and planetary formation processes, and the development of biomedical technologies. Controlling mixing between different fluids is central to achieving fusion energy, where mixing is undesirable, and supersonic combustion, where enhanced mixing is important. Iron, found throughout the universe and a necessary component for life, is dispersed through the mixing processes of a dying star. Non-invasive treatments using ultrasound to induce bubble collapse in tissue are being developed to destroy tumors or deliver genes to specific cells. Laboratory experiments of these flows are challenging because the initial conditions and material properties are difficult to control, modern diagnostics are unable to resolve the flow dynamics and conditions, and experiments of these flows are expensive. Numerical simulations can circumvent these difficulties and, therefore, have become a necessary component of any scientific challenge.

Advances in the three fields of numerical methods, high performance computing, and multiphase flow modeling are presented: (i) novel numerical methods to capture accurately the multiphase nature of the problem; (ii) modern high performance computing paradigms to resolve the disparate time and length scales of the physical processes; (iii) new insights and models of the dynamics of multiphase flows, including mixing through hydrodynamic instabilities.

The Discontinuous Galerkin (DG) method has been shown to be a highly scalable, geometrically flexible, high-order accurate numerical method to solve systems of partial differential equations. This powerful method has not yet been successfully adapted to multiphase flows. Conventional implementation of this method to multiphase flows resulted in numerical errors that led to incorrect solutions or simulation failures. A new procedure in the DG method is developed. This new method preserves high-order accuracy while avoiding these numerical errors and reducing them to unit roundoff ($\sim 10^{-14}$). This method is coupled to numerical sensors which detect flow discontinuities to apply limiting procedures only where necessary and retain broadband motions in smooth regions of the flow. This method has been validated with the usual numerical tests as well as through comparisons with theory and experiments of hydrodynamic instabilities as well as experiments of a shock in air hitting a drop of water. Solution enhancement techniques that increase the order of accuracy of the method from $2P+1$ to $3P+1$, where P is the polynomial order of the solution, are also presented.

To resolve the physics of interest, the method is implemented in a high performance computing framework. Graphics Processing Units (GPU), traditionally used to manipulate computer graphics, are used to perform fast, computationally intensive, and highly parallel vector operations. Since on-chip GPU memory is limited, the problem must be distributed across multiple GPUs and the data must be moved efficiently across the network to minimize communication costs. The new multi-GPU parallel code uses the Message Passing Interface to communicate between GPUs. Excellent weak and strong scaling up to at least 32 GPUs is also demonstrated. This work presents a viable path towards exascale computing.

Using this computational framework, key insights are provided into the dynamics of multiphase flows relevant to engineering, basic science, and biomedical applications. Simulations with shocks interacting with multiple layers of different materials illustrate how to control the level of mixing by varying the material composition, material ordering, material thickness, and perturbation phase alignment. This result is key to many engineering applications involving flows with shocks and multiple fluids where controlling mixing is important (*e.g* fusion energy and supersonic combustion). Vorticity generation mechanisms are shown to offer important insight into the growth of blast-driven hydrodynamic instabilities. Circulation generated at the interface scales linearly with the length of the blast wave and scales as a power law of the wave strength. When the wave has left the interface, the perturbation growth scales as the square root of the circulation and time. Finally, the Rayleigh-Taylor (RT) instability is used to characterize the strength of metals at extreme pressures and strain-rates. In this case, simulations and experiments are compared to validate theoretical models of material strength. These studies have direct applications to engineering and biomedical fields such as fuel injection problems, plasma deposition, cancer treatments, and turbomachinery.

CHAPTER I

Introduction

This chapter defines the scope of this dissertation and emphasizes the importance and relevance of this work to many scientific and engineering problems. This work is placed in the context of several applications, with a primary focus on Inertial Confinement Fusion (ICF) and supernova collapse. The key concepts in this work, particularly mixing in compressible multiphase flows and phenomena at interfaces, are defined. The main assumptions behind the modeling framework are presented and the validity of using the Euler equations for the problems of interest examined. The next section presents the motivation for using high-order numerical methods for high fidelity simulations. Finally, this chapter concludes with the thesis objective, the outline, and the main contributions of this work.

1.1 Physical context

Gases, liquids, and plasmas belong to the general family of fluids, *i.e.* they are substances that change shape and deform continuously under the effect of a shear stress; they are said to *flow*. Fluid flows are observed throughout nature and span many length scales, from the blood in our veins to the interstellar medium. Due to their prevalence, understanding fluid flows is critical to many applications. The study of *single fluid flows*, flows where there is only one type of fluid in a particular state, e.g. the flow of air over an airplane wing, has led to countless breakthroughs in scientific, engineering, and medical fields.

This thesis focuses on more complex flows, specifically flows which contain multiple types of fluid. *Multifluid flows* are flows which involve the interactions of fluids in the same phase. These flows occur, for example, when different types of liquids are in the same system. Pouring honey into hot tea, for example, involves two liquids with different temperatures, densities, and viscosities. Multifluid flows are generally more difficult to analyze than singlefluid flows because the differences in the fluid material properties have a strong effect on the flow dynamics.

Many of the flows discussed pertain to multifluid flows, particularly flows with different gases. However, the tools developed and several flows studied in this thesis pertain to *multiphase flows* as well, a broader class of flows in which fluids in different phases are present. The injection of fuel, a liquid spray, into a diesel engine's combustion chamber filled with hot gases, is an example of a multiphase flow. The scope of this work is restricted to multiphase flows where fluids are not actively changing phases, e.g. going from a liquid phase to a gaseous one. The numerical treatment of multiphase flows and the study of several specific multiphase flows are the primary focus of this work.

Compressible multiphase flows are of particular interest as they occur in many different applications. These flows contain local changes in density, high pressure regions, and velocities that are not necessarily small compared to the speed of sound.

In the context of this work, *mixing* refers to the process in which two or more fluids of different composition are entrained and dispersed within each other. A mixed region of the flow is a macroscopic region where the mass fractions of the respective fluids are less than one. As opposed to passive mixing between scalar fields, mixing in this work is coupled to the flow dynamics, defined by Dimotakis [2] as level-2 mixing. Examples of this type of mixing occur in flows containing varying density fluids in acceleration fields, such as the Rayleigh-Taylor (RT) and Richtmyer-Meshkov (RM) instabilities, Sections 1.3.1 and 1.3.2, and temperature and salinity-driven ocean currents and climate phenomena. Mixing phenomena in compressible multiphase flows most relevant to this work are detailed in Section 1.3. For hydrodynamic instabilities, perturbation amplitude usually quantifies the amount of mixing in the flow. Additional metrics for quantifying mixing between fluids at large and intermediate scales are presented and used in Section 4.6.

1.2 Scientific and engineering applications

Compressible multiphase flows are ubiquitous in science and engineering. Mitigating cavitation erosion, which involves small vapor bubbles created by tensile forces in the wake of a ship's propeller collapsing violently and damaging the propeller, is crucial to many naval engineers [3]. For high speed multiphase nozzle injection, such as variable phase turbines used in geothermal waste heat recovery systems [4, 5], understanding liquid droplet breakup in supersonic flow is important for developing liquid atomizations models [6]. In manufacturing, plasma deposition is a technique in which thin films of solid are deposited using a vaporized liquid. The gas and liquid droplets usually travel at high velocities, and understanding their impact on the substrate is important for controlling surface roughness and defects [7, 8]. In diesel engines, the liquid fuel is injected as a high speed spray into the combustion chamber. Efficient mixing of the fuel and oxygen is important to minimize particulates and maximize the combustion rate and, thus, fuel efficiency [9]. In supersonic combustion ramjets, or scram-jets, a type of jet engine for hypersonic flight, increasing the rate of mixing between the fuel and oxidizer is critical to the engine's success as the typical residence time in the combustion chamber is milliseconds [10]. Shock induced mixing has been proposed as an efficient mixing method for accomplishing this [10].

In the biomedical sciences, therapies have been developed where flows of complex tissues interacting with high pressure waves are prevalent. In shockwave lithotripsy [11], a common technique for treating kidney stones, ultrasound pulses are used to crush the kidney stones in the patient. Histotripsy also uses ultrasound to induce tissue necrosis and tissue fractionation to treat cancer tumors [12]. These non-invasive therapy tools focus energy into tissue and create pressure waves interacting with interfaces of different materials. Though the ultrasound phenomena do not have high velocities, the associated cavitation phenomena do.

At much larger scales, though usually at lower speeds, terrestrial flows, like atmospheric inversions [13], magma flow and solidification [14], and ocean mixing due to sudden temperature changes [15], can also be subject to mixing instabilities. Planetary formation processes and planetary object collisions are governed by flows in which shocks are interacting with fluids in different phases [16].

Of particular interest to this thesis and a specific focus and application of this work is ICF and supernovae.

1.2.1 Inertial confinement fusion

ICF is a technology for harnessing energy from fusion reactions to generate electricity using a nearly unlimited source of material, hydrogen, without producing carbon products [17]. In ICF, a deuterium and tritium gas is encased in a small spherical capsule, about 5 mm in diameter. The capsule's shell is formed by an outer shell, the ablator, primarily plastic doped with several other elements, Figure 1.1, and an inner shell, usually a cryogenic deuterium and tritium ice. It is heated to very high temperatures using various energy sources. For indirect drive ICF, as pursued at the National Ignition Facility at Lawrence Livermore National Laboratory, the capsule is suspended inside a gold canister, called a hohlraum. One hundred and ninety two laser beams are aimed at the inner hohlraum walls, Figure 1.1, and the laser light is converted to x-rays by the gold walls. The x-rays then uniformly bathe the capsule with intense radiation and ablate the outer portion of the capsule shell. The ablation of shell surface material drives the implosion of the fuel shell. The fuel's kinetic energy is then converted to internal energy as the fuel is decelerated to rest by the matter at the core of the spherical capsule. Temperatures can reach several tens of millions of degrees [18]. At these temperatures, the compressed fuel in the core is expected to undergo thermonuclear burn and produce helium and very energetic neutrons.

One of the key challenges in ICF is achieving the very high densities and temperatures necessary for initiating thermonuclear burn. This imposes very tight constraints on the sphericity of the compression, *i.e.* a non-spherical implosion will not compress the fuel to high enough temperatures in the center of the capsule, the hotspot. Hydrodynamic instabilities, such as the Kelvin-Helmholtz (KH), RT, and RM instabilities, significantly perturb the uniform compression and induce mixing between the hot fuel and the relatively cold outer shell of the capsule. The mixing reduces the temperature in the hotspot and inhibits ignition. Mixing through hydrodynamic instabilities is a main reason for the fact that ICF efforts have yet to achieve high gain [20].

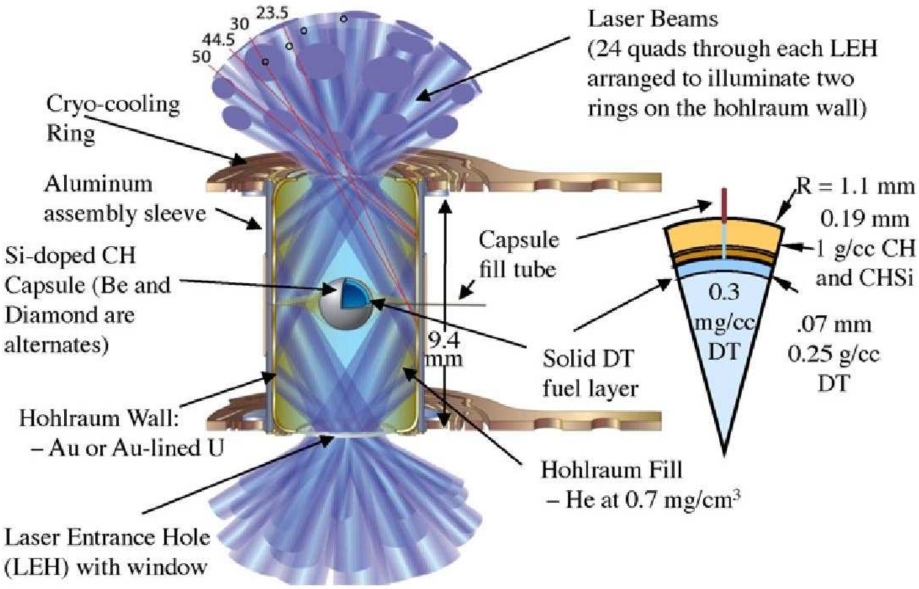

Figure 1.1: Indirect drive ICF schematic of the hohlraum (left) and fuel capsule (right). From Landen et al. [19], © IOP Publishing. Reproduced with permission. All rights reserved.

1.2.2 Core collapse supernovae

At the other end of the length scale spectrum, core collapse supernovae form the biggest explosions in the universe, Figure 1.2. Approximately 10^{46} J/s is released through neutrinos during a core-collapse supernova [21]. No other natural phenomenon comes close to this amount of power. Core collapse supernovae are immensely important in astrophysics as they are the most abundant manufacturers of elements in the universe. They lead to the creation of neutron stars and black holes, and they are thought to be a source of shocks instrumental in accelerating Galactic cosmic rays [22]. The focus in this work is on the more frequent type of supernovae, core collapse supernovae, hereafter referred to as supernovae, which are caused by the collapse of the iron core in a massive star. Before summarizing the key components of the collapse dynamics, the reader is referred to the following review articles [23, 24, 25, 21, 26, 22].

A supernova starts as a massive star, a star larger than eight solar masses, in hydrostatic equilibrium and burning hydrogen, that collapses due to gravitational forces [21]. A cycle of nuclear fusion reactions beginning with hydrogen produces helium. A helium core is formed, leaving hydrogen burning in the outer shell. The helium core eventually contracts, raising the density and temperature enough so that the helium begins to fuse, in a cycle that leads to carbon and oxygen. This cycle of fuel burning, core contraction, and ignition of the products of the previous fusion reactions continues, producing neon, silicon, and, finally, iron. Each successive stage is shorter than the previous one: for a fifteen solar mass star, the hydrogen and helium burning stages can last millions of years, whereas silicon burns for a couple of weeks [21]. As this process evolves, the star forms an "onion-like" structure, each inner layer denser than the outer ones, with the heaviest element, iron, at the core, Figure 1.3. Because iron has the maximum nuclear binding energy per nucleon, no net energy is released from iron fusion and the burning cycle stops. The mass of the iron core increases until it exceeds the Chandrasekhar limit ($M > 1.4M_{\odot}$). At this point, the electron degeneracy pressure is overwhelmed by gravitational forces and the core collapses in seconds. Material in the outer edge of the core reach velocities close to a quarter of the speed of light. During the collapse, the core density increases by a factor of 10^6, akin to Earth being compressed to a diameter of 50km in 1 second. Because this collapse occurs on time scales much faster than those for the speed of sound and gravity is much weaker away from the core, the outer layers (neon, carbon/oxygen, helium, and hydrogen) remain motionless, unaware of the collapse. Once the core has reached nuclear density ($\rho \sim 10^{14}\mathrm{g/cm^3}$), the short range nuclear force, attractive at long distances, becomes repulsive at the core center. The collapse suddenly stops and the core rebounds. Material from the outer edges of the core, still falling inwards, slams into the central rebounding core, forming an outward moving shock. Energy losses from the shock through photodisintegration and neutrino emission are such that, seconds after collapse, as the shock arrives at the outer edge of the core, it stalls. The mechanisms explaining how the shock is restarted are not well understood and much debated. The predominant theory is that neutrinos from the core deposit enough energy at the shock to restart the shock [22]. Once restarted, the shock continues its outward trajectory and interacts with each successive layer of the star. Since the explosion is short compared to the shock passage time through the star, a rarefaction wave overtakes the shock to form a blast wave [27]. This blast wave encounters density gradients at the different interfaces between the element layers. When the shock interacts with the different layers, it briefly increases the temperature and density of the gases, leading to several rounds of explosive nucleo-synthesis and the creation of many other elements such as nickel, cobalt, and titanium [22]. As the supernova explosion proceeds, much of the star material is dispersed in the interstellar medium where gravitational forces will slowly coalesce the dispersed elements to form new stars and planets.

Experimental observations of supernovae, such as one of the most studied supernovae, SN1987A, [23], have exhibited failures in spherically symmetric theoretical models to predict the light curves from the supernovae. In the case of SN1987A, heavy material from the inner regions of the star was observed five days after the explosion instead of the predicted six months [28]. To explain these discrepancies, scientists are predicting that hydrodynamic instabilities, arising from the interaction of the blast wave with the perturbations at the layer interfaces, are mixing heavy core elements into the outer portions of the star. Simulations such as those performed by Kifonidis et al. [29], Miles [28] indicate that the light curves observed from supernovae may be explained by hydrodynamic mixing. This active area of study forms the context and motivation for our fundamental research of the mixing dynamics of a blast wave interacting with a perturbed interface in an idealized system, Chapter V. While most studies to date have focused on buoyancy-drag descriptions of the mixing, this work provides circulation-based descriptions and models to highlight the physics of blast-driven instabilities.

1.3 Mixing in compressible multiphase flows

The phenomena important to the applications of interest, described in Section 1.2, occur at interfaces between fluids in compressible multiphase flows. *Hydrodynamic instabilities* are particularly interesting as they initiate mixing between different fluids, determine the evolution and amount of mixing, and thus directly influence the overall flow dynamics. Hydrodynamic instabilities occur when small perturbations on an interface between fluids grow because of the dynamics of the flow. The process behind the perturbation growth dictates the nature and type of instability. Over time, the flow may transition to turbulence, in which case the flow dynamics stretch the interface sufficiently that viscosity and mass diffusion may be important during the relevant time scales [2].

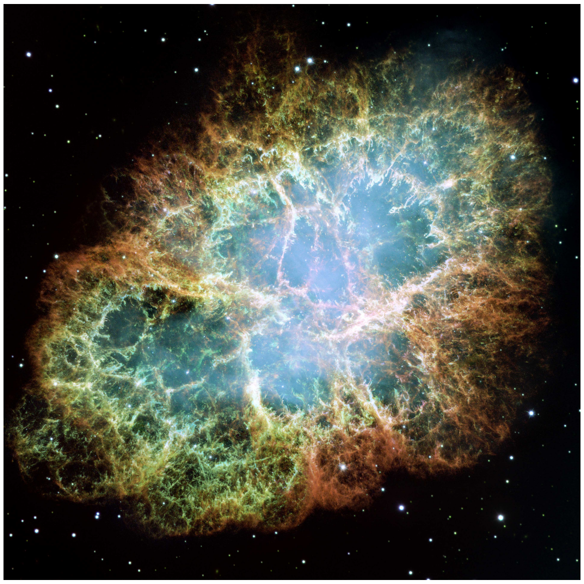

Figure 1.2: Image of the Crab Nebula, a supernova explosion remnant, by the Hubble Space Telescope. The explosion remnant is approximately six light years wide. Photo credit: National Aeronautics and Space Administration.

1.3.1 The Richtmyer-Meshkov instability

The RM instability occurs when a shock traverses a perturbed interface between fluids of different densities [30, 31]. The growth of the perturbation is due to the shock generating baroclinic vorticity at the interface [32]. Specifically, the vorticity is created by the misalignement of the pressure gradient across the shock and the density gradient across the interface, as illustrated by the last term in the vorticity evolution equation for a compressible inviscid flow,

$$\frac{\partial \boldsymbol{\omega}}{\partial t} + \mathbf{u} \cdot \nabla \boldsymbol{\omega} = (\boldsymbol{\omega} \cdot \nabla)\mathbf{u} - \boldsymbol{\omega} \nabla \cdot \mathbf{u} + \frac{1}{\rho^2}(\nabla \rho \times \nabla p) \tag{1.1}$$

where ρ is the density, p is the pressure, $\mathbf{u}$ is the velocity, and $\boldsymbol{\omega} = \nabla \times \mathbf{u}$ is the vorticity. Vortex stretching, the first term on the right-hand side, only appears in three-dimensional flows. Vortex compression, the second term, includes compressibility effects.

When the shock interacts with the interface, it first compresses the perturbations. If the shock is moving into a lighter fluid ($\nabla p \cdot \nabla \rho > 0$), it induces a phase inversion in the perturbation. After the shock has left the interface, the only mechanism left to drive the interface growth is the vortex sheet at the interface formed by baroclinic vorticity generation, Figure 1.4. As such, the RM instability is not a classical instability because it

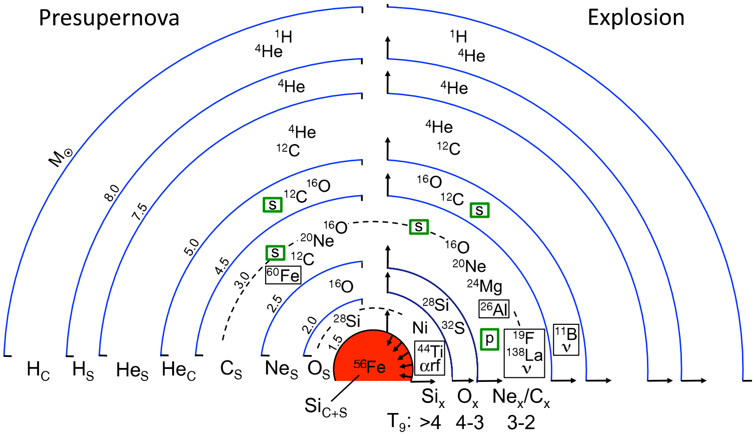

Figure 1.3: Illustration of the main element layers of an evolved star (not to scale). Left: before the supernova explosion. In thin shells at the interface between the layers, indicated in blue lines, nuclear burning of the elements noted at the bottom produce the main components of the layers (C and S denote core and shell burning). The approximate interior mass is indicated through the diagonal numbers. Right: shock induced nucleo-synthesis processes. From José and Iliadis [22].

does not exhibit exponential linear growth and does not contain any feedback mechanisms.[1] The vortex sheet induces different velocities at different points along the interface. These velocities deform the interface and create a bubble, defined as the light fluid moving into the heavier fluid, and a spike – a heavy fluid moving into lighter fluid.

The RM instability has been extensively studied in the past. Initial growth models were proposed by Richtmyer [30], Meyer [33]. These models use RT instability perturbation analysis with an impulsive acceleration. They are valid at early time and predict a constant growth rate. Other perturbation models have since been proposed for the entire growth of the perturbation. The most successful ones are those by Zhang and Sohn [34] and Sadot et al. [35]. This latter model is in very good agreement with experiments. Another modeling approach focuses on modeling the vorticity deposition and deforming the interface based on vortex sheet evolution equations. Samtaney and Zabusky [36], Jacobs and Sheeley [37] evaluated the strength of the vortex sheet and used it to predict the perturbation growth. Experimental and numerical studies of the RM instability have been performed extensively to explore many different configurations, effects, and regimes, [32].

---

[1] To stay consistent with the literature, we will keep calling it an instability. We should really be referring to the RM process.

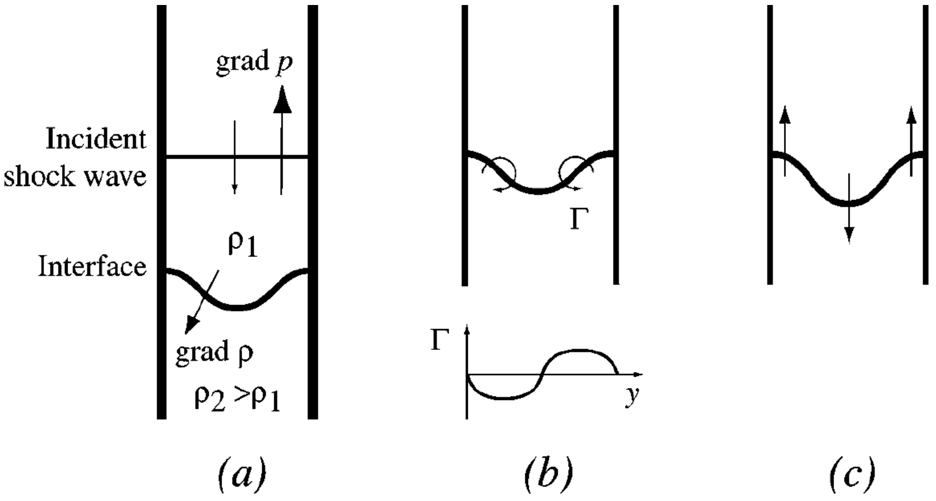

Figure 1.4: Illustration of a RM unstable flow for the vorticity generated at a light/heavy interface. a) Initial condition. b) Circulation at the interface and vortex sheet strength. c) Perturbation growth. From Brouillette [32]. Reproduced with permission.

1.3.2 The Rayleigh-Taylor instability

The RT instability occurs when a heavy fluid is accelerated into a lighter one. A classic example of this instability is when a heavy fluid is above a light fluid in a gravitational field. The gravitational acceleration amplifies the perturbations at the interface between the fluids, making spikes of heavy fluid fall and bubbles of light fluid rise, Figure 1.5. The perturbation growth in the RT instability is driven by buoyancy.

Taylor [38] predicted the exponential growth of the perturbations in the early phase of the instability, when the perturbation can still be described using normal mode analysis. The next phase of the perturbation growth is typically described using buoyancy-drag models [39]. These models look at the momentum balance of a bubble of light fluid rising in a heavier one and consider buoyancy and drag forces on the bubble (or spike). For a single-mode perturbation, the velocity of the bubble and spike can be described using the Layzer model with [39]

$$(\rho_1 + C_a\rho_2)\,\frac{\mathrm{d}u}{\mathrm{d}t} = (\rho_2 - \rho_1)\,g - \frac{C_d}{\lambda}\rho_2 u^2 \tag{1.2}$$

where u is the velocity, g is the acceleration, ρ_1 and ρ_2 are the fluid densities, λ is the perturbation wavelength, C_a is the added mass coefficient (2D: $C_a = 2$; 3D: $C_a = 1$), and C_d is the drag coefficient (2D: $C_d = 6\pi$; 3D: $C_d = 2\pi$). There is a clear competition between the buoyancy force, the first term on the right side of Eq. (1.2), and the drag force, the second term on the right side of Eq. (1.2). The terminal velocities of the bubble and spike are, therefore,

$$u_{b/s} = \sqrt{\frac{2A}{1 \pm A} \frac{\lambda_{b/s}}{C_d} g} \tag{1.3}$$

where $A = \frac{\rho_1 - \rho_2}{\rho_1 + \rho_2}$ is the Atwood number and $\lambda_{b/s}$ is the bubble/spike wavelength. As the height of the bubbles increase, the perturbation growth phase reaches the self-similar regime, where the underlying assumption is that $h_b \sim \lambda_b$ (h_b is the bubble height). In this phase, the growth is best described as bubbles rising and spikes falling quadratically in time, according to

$$h_{b/s} = \alpha_{b/s} A g t^2 \tag{1.4}$$

where h is the height of the bubble/spike and t is the time. Eq. (1.4) can be shown by setting $\lambda_{b/s} \sim h_{b/s}$ in Eq. (1.3) and integrating the velocity to get the height. In recent years, a lot of work in this field has been focused on measuring the model constants $\alpha_{b/s}$ [40, 41, 42, 43, 44, 45, 46]. In general, as the instability develops, the growth region transitions to a turbulent mixing region. This transition to turbulence is an active research area today [47].

1.3.3 The Kelvin-Helmholtz instability

Though relevant to many of the flows of interest, the KH instability is not discussed here in depth. The KH instability occurs at the interface between fluids where there is a velocity gradient across the interface. This typically happens in shear flows where fluids are moving parallel to each other at different speeds, Figure 1.6. For example, the interface of a fluid injected into a quiescent fluid is KH unstable. The KH instability can also be seen in the shear flows in the massive storm near Jupiter's Great Red Spot, Figure 1.7. The late-time roll-ups near the bubble and spike observed in the RM and RT instabilities are

Figure 1.5: Slightly denser dyed water spikes fall in water due to the RT instability. Experimental pictures by James Riordon, AIP.

also due to the KH instability.

1.4 Dimensional analysis

This section addresses the assumptions and validity of modeling the fluids in the systems of interest with the Euler equations, written here in conservative form ($i, j = 1, 2, 3$):

$$\frac{\partial \rho}{\partial t} + \frac{\partial}{\partial x_j}\left(\rho u_j\right) = 0, \tag{1.5a}$$

$$\frac{\partial (\rho u_i)}{\partial t} + \frac{\partial}{\partial x_j}\left(\rho u_i u_j + p\delta_{ij}\right) = 0, \tag{1.5b}$$

$$\frac{\partial E}{\partial t} + \frac{\partial}{\partial x_j}\left[u_j(E + p)\right] = 0, \tag{1.5c}$$

where ρ is the density, u_i the velocity, $E = \rho e + \frac{1}{2}\rho u_i u_i$ the total energy, e the internal energy, p the pressure and δ_{ij} the Kronecker delta. This system of hyperbolic partial differential equations models conservation of mass, momentum, and energy for an inviscid compressible fluid where heat transport can be neglected. In this work, to relate internal energy and pressure, the system is closed with an ideal equation of state or the stiffened equation of state, both belonging to the Mie-Grüneisen family of equations of state (see

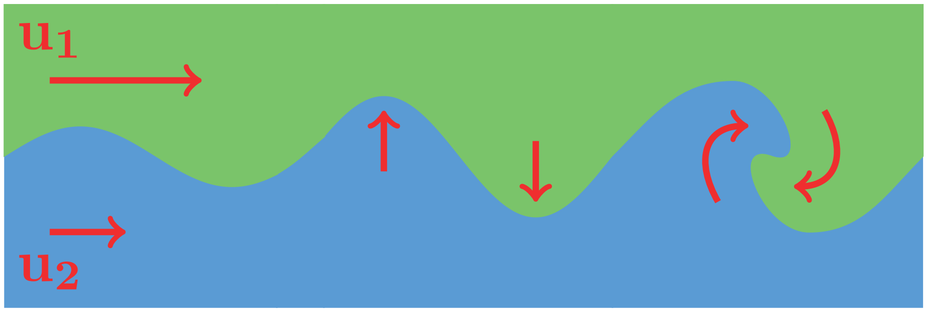

Figure 1.6: Illustration of a KH unstable flow. The fluid on the top is moving at a different velocity than the fluid on the bottom. In this shear flow configuration, the perturbations at the interface are KH unstable and will grow accordingly, thereby mixing the two fluids.

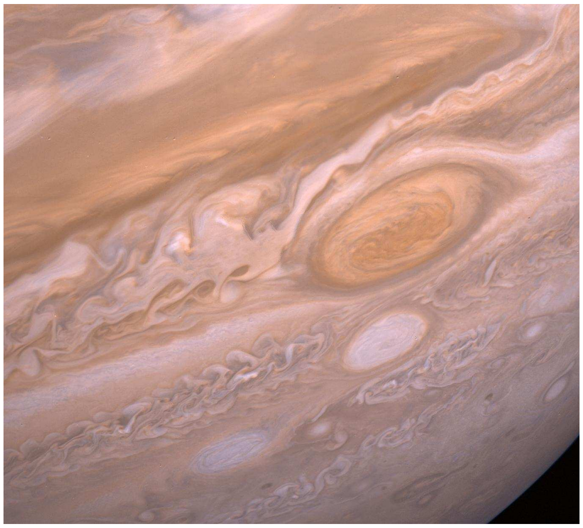

Figure 1.7: Shear flow in the storm near Jupiter's Great Red Spot have created a large scale example of the KH instability. Image of Jupiter from Voyager 2 flyby. Photo credit: National Aeronautics and Space Administration.

Section 2.3 for more details). Additional advection equations for the material parameters are used to capture flows of fluids with different material properties.

The invariance property and similarity conditions for the Euler equations are central to the notion of performing laboratory experiments and numerical simulations of physical phenomena that occur in, for example, supernova explosions and turbomachinery. While summarizing some of the key points here (and trying to retain the same notation), the reader is referred to the article by Ryutov et al. [48] for a detailed discussion of the invariance property and similarity condition of the Euler equations. The following transformation (denoted with a subscript 1) is an invariance of the Euler equations:

$$\mathbf{x} = a\mathbf{x_1},\ \rho = b\rho_1,\ \mathbf{p} = c\mathbf{p}_1, \tag{1.6a}$$

$$t = a\sqrt{\frac{b}{c}}t_1,\ \mathbf{u} = \sqrt{\frac{c}{b}}\mathbf{u}_1, \tag{1.6b}$$

where a, b, and c are arbitrary positive constants. Additionally, using this invariance transformation, it can be shown that two systems $(\mathbf{x}, \rho, p, t)$ and $(\mathbf{x_1}, \rho_1, p_1, t_1)$ are similar and will describe the same physics if they satisfy the similarity condition:

$$\widetilde{u}\sqrt{\frac{\widetilde{\rho}}{\widetilde{p}}} = \widetilde{u}_1\sqrt{\frac{\widetilde{\rho}_1}{\widetilde{p}_1}} \tag{1.7}$$

given the scaling factors $\widetilde{u}$, $\widetilde{p}$, $\widetilde{\rho}$, and h for the initial condition of the system $(\mathbf{x}, \rho, p, t)$:

$$\mathbf{u_0} = \widetilde{u}\mathbf{F}\left({}^{\mathbf{x}}\!/_{h}\right),\ p_0 = \widetilde{p}G\left({}^{\mathbf{x}}\!/_{h}\right),\ \text{and}\ \rho_0 = \widetilde{\rho}H\left({}^{\mathbf{x}}\!/_{h}\right) \tag{1.8}$$

where $\mathbf{F}$, G, and H are dimensionless functions, and given the scaling factors $\widetilde{u}_1$, $\widetilde{p}_1$, $\widetilde{\rho}_1$, and h_1 for the other system. The time scales of both systems are related through

$$t_1 = t\frac{h_1}{h}\sqrt{\frac{{}^{\widetilde{p}}\!/_{\widetilde{\rho}}}{{}^{p_1}\!/_{\rho_1}}}. \tag{1.9}$$

These relationships provide a mapping from one system to another, without any assumptions on compressibility or the subsequent physical evolution of the systems (shocks, non-linear growth regimes, etc). As long as these relationships hold and the Euler equations are a valid model, the same physics will be probed. The validity of the model assumptions for several applications discussed in Section 1.2 is now examined.

1.4.1 The Euler equations for supernova explosions

The following discussion is borrowed from Ryutov et al. [48] and the reader is referred to that article for a complete analysis of the problem. This discussion is limited to the early stages of the supernova explosion, when the blast wave, after originating from the center of the star, interacts with the different material layers, thereby instigating hydrodynamic instabilities. In this case, it can safely be assumed that the accelerations due to the supernova explosion are much larger than gravitational forces, which can therefore be neglected. Additionally, the features of interest (e.g. the perturbation growth) are much smaller than the radius of the star. Therefore, sphericity is neglected and a planar geometry is assumed.

For the Euler equations to model appropriately the astrophysical phenomena of interest, the following must hold:

- Collisionality: To be able to use a fluid description of the system, the particles must be localized. In a star, magnetic fields and collisions are responsible for localizing the particles on scales much smaller than the characteristic length scale of the system, h. Therefore, the ion Larmor radius and the collisional mean free path must be much smaller than h. This is indeed the case during the supernova explosion [48].

- Negligible heat conduction: To use the Euler equations, diffusive heat transport must be negligible. This assumption can be characterized through the Peclet number, the ratio of heat convection to heat conduction. The main source of heat conduction in an exploding star is the thermal diffusivity of electrons ($1.2 \times 10^{6}\,{}^{\mathrm{cm}^2}\!/\!{}_{\mathrm{s}}$). However, the resulting Peclet number is quite large ($\approx 1.5 \times 10^{12}$) and heat conduction can be safely neglected [48].

- Negligible viscous effects: Viscous forces, which can be compared to the inertial forces through the Reynolds number, must be negligible for the Euler equations to be valid. The dominant viscosities, namely the photon viscosity and ion particle viscosity, are small ($7.0\times10^{7}\,{}^{\mathrm{cm}^2}\!/\!{}_{\mathrm{s}}$)compared to the typical length scale ($h \approx 9\times10^{10}$cm) and velocity scale ($\widetilde{v} \approx 200\,{}^{\mathrm{km}}\!/\!{}_{\mathrm{s}}$), resulting in a Reynolds number $\approx 2.6 \times 10^{10}$.

- Small radiation energy fluxes: The energy transported through radiation effects must be small compared to the hydrodynamic energy fluxes. When the photon mean free path (bremsstrahlung: 37000cm ; Compton: 680cm)is smaller than h, as is the case in the exploding star, the photon thermal diffusivity ($6.8 \times 10^{12}\,{}^{\mathrm{cm}^2}\!/\!{}_{\mathrm{s}}$) can be used to define a Peclet number, which is close to 2.6×10^{5}. The hydrodynamic description of the system is therefore valid.

1.4.2 The Euler equations for multiphase flows

The multiphase phenomena discussed in this thesis, such as the supersonic water droplet in a turbomachine or the shock induced collapse of an air bubble in naval environments, are characterized by highly compressible phenomena and high velocities. For these liquid-gas interfacial flows, the Euler equations are a valid approximation when the following forces are negligible:

- Viscous forces: As previously stated, the Reynolds number, the ratio of inertial forces to viscous forces, must be large. For the supersonic water droplet interacting with a Mach 1.18 shock (drop diameter, $d = 4.8\text{mm}$, shocked gas density, $\rho_g = 1.53\,{}^{\text{kg}}/{}_{\text{m}^3}$, and shocked gas velocity, $u_g = 96\,{}^{\text{m}}/{}_{\text{s}}$, and the dynamic viscosity of air, $\mu = 1.8 \times 10^{-5}\,\text{Pa s}$) the Reynolds number is close to 10^5.
- Surface tension forces: The Weber number, the ratio of inertial forces to surface tension forces, must also be large. For the supersonic water droplet (surface tension, $\sigma = 0.07286\,{}^{\text{N}}/{}_{\text{m}}$), the Weber number is close to 10^4 [49].
- Gravitational forces: The Froude number, the ratio of inertial forces to external field forces, usually gravity, is large for our applications since the length scales of the bubbles and droplets are very small and flow velocities large.

Additionally, compressibility effects, characterized by the Mach number, the ratio of flow velocity to the sound speed, are usually important for our flows of interest ($M > 0.2$).

The flows discussed in this work are therefore appropriately modeled as inviscid compressible flows and the Euler equations will accurately describe the hydrodynamics. Throughout this thesis, the equations are solved in an Eulerian framework. Simulations of the Euler equations can not be said to converge in a point-wise fashion because they lack a physical diffusion mechanism to diffuse small scale features [50]. As the resolution increases in these simulations, additional small scale features will be resolved. However, the simulation results presented in this work, *e.g.* the perturbation amplitude, are converged in an integral sense. It should be noted that viscous and surface tension effects will become important during the late-time dynamics of some of the problems of interest, particularly when the lengths scales of interest become small, as in the breakup of the supersonic droplet into many smaller ones. Analyzing these particular flow features are beyond the scope of this work.

1.5 High-order numerical methods for multiphase flows

Experiments of compressible multiphase flows are costly to design, manufacture, and implement. Additionally, because of the complex nature of the problems, the short time scales, and the multiphysics aspects of the flows, diagnostic tools can only offer limited information about the flow dynamics. The sensitivity of these flows to the initial conditions and material properties make it difficult to attain good experimental repeatability.

Numerical simulations can circumvent these challenges and are a cost effective way of understanding the flow dynamics by exploring the relevant parameter space, isolating the physical effects of interest, and providing a complete description of the system's evolution. High-order numerical methods for discretizing systems of partial differential equations that model the system, Section 1.4, are increasingly important in computational fluid dynamics.

These methods are usually defined as having an order of accuracy greater or equal to two, which implies that the error from numerical discretization, E, decreases as $E \sim \mathcal{O}(h^n)$, where h is the grid spacing and $n \geq 2$. By increasing the rate of convergence, high-order methods make it possible to achieve errors within engineering tolerances in a reasonable amount of computational time. Borrowing from Fidkowski [51, 52], an estimate of the time to a solution with the desired error is

$$\log(T) = d\left(-\frac{1}{P+1}\log(E) + a\log(P+1)\right) - \log(F) + \text{constant} \tag{1.10}$$

where T is the simulation time, P is the solution interpolation order, d is the problem's spatial dimension, a is the complexity of the solution algorithm (e.g. $a = 2$ for matrix-vector operations), and F is the time to complete a single operation. This equation is valid for smooth flows, *i.e.* the solution is not discontinuous. The term in $\log(E)$ dominates when the algorithm complexity is not too large and the desired error is very small ($E << 1$). In this case, any increase in the interpolation order will lead to large gains in solution time because this time depends exponentially on the inverse of the order of accuracy. Another

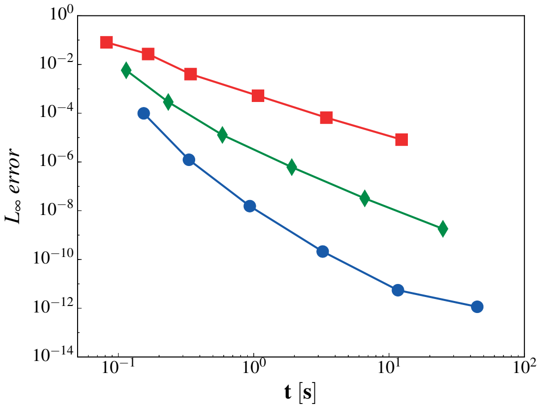

Figure 1.8: Error as a function of computational time for simulations of the advection of a sinusoidal density variation. Red squares: $P = 1$; green diamonds: $P = 2$; blue circles: $P = 3$.

way of interpreting this result is that more complex problems (larger a) can be solved in the same amount of time with a high-order method. Figure 1.8 illustrates this concept by showing the error as a function of computational time. For a fixed computational time, increasing the order of accuracy decreases the error. Similarly, a higher order numerical method reaches a desired error level with less computational time.

Despite the advantages of high-order methods, the current methods most commonly used in laboratory and industrial codes are based on Finite Volume (FV) methods and are, at most, second order. Higher order implementations of these methods lead to an increased numerical stencil, in effect increasing the interpolation by using data from beyond the nearest neighbors. This introduces several complications. In parallel computation, the increased stencil leads to more data movement and increased communication time. Boundary conditions can be difficult to implement and require the addition of ghost cells. An increased stencil also decreases the wave resolution of the scheme. For implicit time solvers, these high-order FV methods with larger stencils require more memory and adversely impact the stability of iterative algorithms [51, 53].

The Discontinuous Galerkin (DG) method, detailed in Chapter IV, combines the finite element method and the FV method to preserve a compact stencil. Degrees of freedom are added to each cell to represent the solution as a high-order polynomial. The solution is allowed to be discontinuous across the cells.[2] Borrowing from FV method, fluxes between immediately neighboring cells are used to exchange information between the cells. While the DG method is a high-order numerical method which presents many advantages, it has yet to be consistently adapted to flows containing multiple fluids in different phases. This and other issues related to advection-diffusion problems are addressed in Chapters IV and VI.

1.6 Thesis overview

As explained in this introduction, understanding mixing in compressible multiphase flows is important to many scientific and engineering problems. However, compressible multiphase flows are challenging to simulate as they require a robust and accurate treatment of flow discontinuities, which separate regions of different density, pressure, and velocity, high numerical resolution to resolve the disparate length and time scales, and methods adapted to unsteady flows. Numerical simulations of these flows are currently limited by (i) the numerical methods used to solve the partial differential equations describing the system, and (ii) the computational expense. These two points are addressed in the first part of this thesis. In the second part, the computational framework is used to analyze several flow configurations of interest. This thesis has two main objectives:

1. to develop an accurate and consistent numerical framework to simulate compressible multiphase flows: The guiding hypothesis is that the high-order DG method, a powerful numerical method for discretizing flow evolution equations, must be adapted and combined with a suitable high performance computing paradigm to provide accurate physical insights into multiphase flow dynamics. Applying traditional numerical methods to the evolution equations describing compressible multiphase flows with interfaces can lead to spurious numerical errors that change the dynamics of the flow, Chapter II. These errors can result in an incomplete or erroneous understanding of the flow. The high computational resolution required to simulate the system accurately and the wide parameter space motivates the use of graphics processing units, a

---

[2] Though this does not necessarily make discontinuities in the flow easier to model.

novel parallel paradigm for high performance computing, Chapter II. Finally, improvements to the DG method for the discretization of the advection term are provided in Chapter III.

2. to explore the fundamental dynamics of compressible multiphase flows through the study of multilayered RM instabilities, Chapter IV, blast wave-driven instabilities, Chapter V, and experiments of high-explosive-driven RT instabilities to understand beryllium strength, Chapter VI: The guiding hypothesis is that the mixing dynamics in these flows can be controlled by appropriately changing the waves driving the instabilities and the material properties and configurations. Time-varying acceleration fields at interfaces and vorticity deposition dynamics can be used equivalently to describe perturbation growth evolution.

This work's main contributions to the field of numerical simulations of mixing in compressible multiphase flows are

- A new numerical method to simulate multiphase flows with different types of equations of state while avoiding spurious numerical errors that could contaminate the flow physics;
- A demonstration of a new framework for high performance computing that combines graphics processing units with distributed memory parallelism;
- A novel way of increasing the order of accuracy of the DG method for the discretization of the advection term in evolution equations;
- A study of the multilayered RM instability, of particular applicability to ICF, illustrating control of the instability growth by tuning the material layers;
- A novel description of different growth phases and the vorticity dynamics of the blast-driven hydrodynamic instability, specifically circulation production is shown to be a function of the important blast parameters, and the perturbation growth is shown to scale with circulation;

- A numerical analysis of experimental RT instabilities in beryllium to validate material strength models.

Part I

Numerical methods for multiphase flows and validation

CHAPTER II

A new limiting procedure for Discontinuous Galerkin methods applied to compressible multiphase flows with shocks and interfaces

Sections 2.1 through 2.6 of this chapter are adapted from Henry de Frahan, M. T., Varadan, S. & Johnsen, E. 2015 A new limiting procedure for Discontinuous Galerkin methods applied to compressible multiphase flows with shocks and interfaces. *J. Comput. Phys.*, **280 (0)**, 489–509. Section 2.7 is a validation study published in Henry de Frahan, M. T., Khieu, L. & Johnsen, E. 2015 High-order Discontinuous Galerkin Methods Applied to Multiphase Flows. 22^d *AIAA Computational Fluid Dynamics Conference*, doi: 10.2514/6.2015-3045.

2.1 Abstract

Although the Discontinuous Galerkin (DG) method has seen widespread use for compressible flow problems in a single fluid with constant material properties, it has yet to be implemented in a consistent fashion for compressible multiphase flows with shocks and interfaces. Specifically, it is challenging to design a scheme that meets the following requirements: conservation, high-order accuracy in smooth regions and non-oscillatory behavior at discontinuities (in particular, material interfaces). Following the interface-capturing approach of Abgrall [54], we model flows of multiple fluid components or phases using a single equation of state with variable material properties; discontinuities in these properties correspond to interfaces. To represent compressible phenomena in solids, liquids, and gases, we present our analysis for equations of state belonging to the Mie-Grüneisen family. Within the DG framework, we propose a conservative, high-order accurate, and non-oscillatory limiting procedure, verified with simple multifluid and multiphase problems. We show analytically that two key elements are required to prevent spurious pressure oscillations at interfaces and maintain conservation: (i) the transport equation(s) describing the material properties must be solved in a non-conservative weak form, and (ii) the suitable variables must be limited (density, momentum, pressure, and appropriate properties entering the equation of state), coupled with a consistent reconstruction of the energy. Further, we introduce a physics-based discontinuity sensor to apply limiting in a solution-adaptive fashion. We verify this approach with one- and two-dimensional problems with shocks and interfaces, including high pressure and density ratios, for fluids obeying different equations of state to illustrate the robustness and versatility of the method. The algorithm is implemented on parallel Graphics Processing Units (GPU) to achieve high speedup.

2.2 Introduction

The DG method is a numerical approach for partial differential equations that combines advantages of the finite element and Finite Volume (FV) formulations. The solution is discretized locally in each computational cell through an expansion in terms of polynomial basis functions. As such, the DG method is high-order accurate, has a compact stencil that makes it highly scalable on parallel architectures, and is readily implementable on unstructured grids. The DG approach exhibits superconvergent properties [55, 56], at a rate of $2P+1$ based on cell averages, where $P+1$ is the number of basis functions in each cell. In a series of articles, Cockburn and Shu popularized the Runge-Kutta Discontinuous Galerkin (RKDG) for time-dependent convection-dominated problems [57, 58, 59, 60, 61]. As with FV methods, Riemann solvers are used to calculate the numerical fluxes between neighboring cells. These solvers provide means to introduce dissipation, so that discontinuities can be treated in a stable fashion. Limiters are further required to damp the oscillations caused by high-order interpolation across a discontinuity. For example, Cockburn and Shu [58] proposed a total variation bounded projection limiter that truncates higher-order Legendre polynomials at detected discontinuities. To prevent excessive dissipation, Biswas et al. [62] developed a hierarchical procedure that limits the Legendre coefficients from the highest to lowest moments. Recently, different high-order limiters have been proposed by Krivodonova [63] and Kuzmin [64]. In particular, Hierarchical Reconstruction (HR) [65, 66] is high-order accurate and conservative; additionally, this compact limiting procedure does not require a characteristic decomposition and is adaptable to unstructured grids.

While the DG method has been used extensively for single-fluid problems [61], the treatment of compressible multicomponent and multiphase flows with interfaces has received little attention. Our present interest lies in interface capturing for the Euler equations, in which interfaces are regularized over a few grid points in analogy to shock capturing. We seek to use methods that conserve the relevant physical quantities (mass, momentum, energy) and are high-order accurate in smooth regions, non-oscillatory at discontinuities, and physically consistent. In the FV formulation, Abgrall [54] showed that spurious pressure oscillations are generated at interfaces between gases of different ratios of specific heats γ if the transport equation describing the fluid composition is solved in conservative form. Such errors may lead to negative pressures or trigger unphysical interfacial instabilities. In FV methods, these oscillations can be prevented by solving a non-conservative evolution equation for a specific function of γ [54]. Multicomponent flows are thus modeled as a medium described by a single equation of state with variable material properties that must be transported in an appropriate form; discontinuities in these properties correspond to interfaces. Saurel and Abgrall [67] and Abgrall and Karni [68] detailed various approaches to solve this problem in the FV context, which can be extended to high-order accuracy [69, 70] and finite differences [71, 72]. Such methods also conserve the total mass, momentum, and energy in the system.

For compressible multiphase problems, the approach of Abgrall [54] can be generalized to more complicated equations of state in the FV context. Transport equations for appropriate material-dependent parameters have been detailed for various equations of state, *e.g*, stiffened equation [73], Van der Waals [74], Mie-Grüneisen [75]. Such approaches have been used to simulate problems involving shock waves interacting with interfaces separating different fluids [76, 77]. Variations of the physical model, *e.g*, five- to seven-equations models, have also been explored [78, 79, 80, 81]. These approaches have yet to be extended to the DG framework. Furthermore, based on experience with high-order accurate FV methods [69], we anticipate that limiting may have to be modified to prevent pressure errors.

At this time, a high-order accurate, conservative, non-oscillatory, and consistent treatment of the Euler equations for capturing interfaces between fluids of different composition and/or phase in the DG framework is lacking. Tokareva and Toro [82] and Franquet and Perrier [83] used the DG approach for the Baer-Nunziato system of equations for multiphase flows while Michoski et al. [84] solved the compressible Navier-Stokes equations. In these papers, limiting is based on first-order accurate slope limiters proposed by Cockburn and Shu [85]. Franquet and Perrier [86] introduced a maximum-preserving limiter for the color function used to distinguish the different fluids; their limiting procedure truncates the higher-order terms (second order and above) and they do not discuss potential spurious pressure oscillations and conservation issues introduced by the limiting procedure. Wang and Shu [87] used an interface tracking method with a level-set advection equation solved with the DG method for Hamilton-Jacobi equations. Gryngarten and Menon [88] extend the Local DG method to the five-equations model [89], in which auxiliary variables are introduced for consistency when solving the Hamilton-Jacobi equations, and a moment limiter [63] is applied to the conserved and primitive variables. Although the amplitude of the pressure oscillations appears to be reduced in this latter article, the authors do not discuss possible conservation issues related to limiting the primitive variables. Several of the above references used solution-adaptive strategies to apply limiting only where needed, *i.e.*, near discontinuities. As stated earlier, these recent DG multiphase flows lack either one or more of the three following properties: conservation of mass, momentum, and energy, non-oscillatory pressure fields at material interfaces, and high-order accuracy. The goal of this work is to fill this gap.

We propose a new approach to limiting in compressible multiphase flows that is conservative, high-order accurate, and that prevents oscillations at interfaces (and shocks). Using a capturing approach for DG, we show that two key elements are necessary to satisfy the three properties listed above: (i) solving transport equations in a non-conservative weak form, and (ii) limiting the suitable variables (density, momentum, pressure and appropriate properties from the equation of state) coupled with a consistent reconstruction of the energy. This procedure is general, and we show how it can be applied to other multiphase models such as the five-equations model and Mie-Grüneisen family of equation of state. This chapter is organized as follows. In Section 2.3, we present the physical model, followed by the DG framework and limiting in Section 2.4. In Section 2.5, we discuss how spurious pressure oscillations occur in multiphase flows in the DG framework; based on this knowledge, we propose a strategy to avoid these errors through a new limiting procedure in the central part of this study (Section 2.5.2.2). Finally, we provide numerical verification with various one- and two-dimensional problems in Section 2.6.

2.3 Physical model

Neglecting physical diffusion, we consider the Euler equations for compressible flow, written in three dimensions ($i, j = 1, 2, 3$):

$$\frac{\partial \rho}{\partial t} + \frac{\partial}{\partial x_j} (\rho u_j) = 0, \tag{2.1a}$$

$$\frac{\partial (\rho u_i)}{\partial t} + \frac{\partial}{\partial x_j} (\rho u_i u_j + p\delta_{ij}) = 0, \tag{2.1b}$$

$$\frac{\partial E}{\partial t} + \frac{\partial}{\partial x_j} [u_j(E + p)] = 0, \tag{2.1c}$$

where summation is implied on repeated indices, ρ is the density, u_i the velocity, $E = \rho e + \frac{1}{2}\rho u_i u_i$ the total energy, e the internal energy, p the pressure and δ_{ij} the Kronecker delta.

The system is closed by an equation of state relating the internal energy to the pressure. We focus on analytical expressions for general compressible phenomena in fluids and solids. For this purpose, we consider the Mie-Grüneisen equation of state [90],

$$p = \left(E - \frac{\rho u_i u_i}{2} + \frac{p_{\text{ref}}}{\Gamma} - \rho e_{\text{ref}}\right) \Big/ \left(\frac{1}{\Gamma}\right), \tag{2.2}$$

where $\Gamma = \frac{1}{\rho} \left.\frac{\partial p}{\partial e}\right|_{\rho}$ is the Grüneisen coefficient, e_{ref} the reference internal energy, and p_{ref} the reference pressure. A wide range of equations of state belong to the Mie-Grüneisen family, *e.g*, the Jones-Wilkins-Lee equation for gaseous explosives [91], or the Cochran-Chan equation for solid explosives [92]. For the problems of interest, we assume that the material properties (Γ_{ref}, p_{ref}, e_{ref}) do not vary with density. Setting $e_{\text{ref}} = 0$ reduces this equation to the stiffened equation of state for liquids and solids, and setting $p_{\text{ref}} = 0$ and $\Gamma = \gamma - 1$ further reduces it to the ideal gas law, where γ is the specific heats ratio.

To represent multiple components or phases, we follow an approach in which a single equation of state describes all media, but with variable material properties; discontinuities in these properties correspond to interfaces. These properties thus depend on the mass fraction $Y^{(i)}$. Since the mass fraction obeys a mass conservation equation, any function $f(Y^{(i)})$ does as well, *e.g*,

$$\frac{\partial}{\partial t}\left(\rho f(Y^{(i)})\right) + \frac{\partial}{\partial x_j}\left(\rho u_j f(Y^{(i)})\right) = 0, \qquad i = 1, \ldots, m-1, \tag{2.3}$$

where m is the number of different fluids. In this work, we focus on binary systems ($m = 2$). Using conservation of mass, Eq. (2.3) can be written in advection (non-conservative) form,

$$\frac{\partial}{\partial t}\left(f(Y^{(i)})\right) + u_j \frac{\partial}{\partial x_j}\left(f(Y^{(i)})\right) = 0, \qquad i = 1, \ldots, m-1. \tag{2.4}$$

Although physical diffusion is ignored, mixture regions may occur due to numerical diffusion, thus requiring mixture rules. For instance, the physical relationship between γ

and $Y^{(i)}$ for a binary gas mixture is

$$\frac{1}{\gamma-1}\frac{1}{M}=\frac{Y^{(1)}}{\gamma_1-1}\frac{1}{M_1}+\frac{1-Y^{(1)}}{\gamma_2-1}\frac{1}{M_2}, \qquad \frac{1}{M}=\frac{Y^{(1)}}{M_1}+\frac{1-Y^{(1)}}{M_2}, \tag{2.5}$$

where γ_i is the ratio of specific heats and M is the mixture molecular mass and the indices denote fluids one and two. Similar relationships can be obtained for the other material properties in the Mie-Grüneisen equation of state [77].

2.4 Numerical framework

2.4.1 Discontinuous Galerkin discretization

For simplicity, consider the one-dimensional hyperbolic equation

$$\frac{\partial W}{\partial t}+\frac{\partial F}{\partial x}=0, \tag{2.6}$$

for the conserved variable $W(x,t)$, where $F(W)$ is the flux, discretized in computational cell $\Omega_k=\{x|x\in[x_{k-1/2},x_{k+1/2}]\}$ with uniform grid spacing Δx. In the DG approach, the solution is expanded in terms of $P+1$ basis functions $\varphi_n(x)$ (*e.g*, Legendre or Lagrange polynomials) in each cell, $W(x,t)\simeq W_h(x,t)=\sum_{n=0}^{P} w_n(t)\varphi_n(x)$, where W_h is a projection of W onto a finite-dimensional space. Taking the inner product of the conservation law with a basis function over cell Ω_k, the weak form of Eq. (2.6) is obtained

$$\int_{\Omega_k}\varphi_i\frac{\partial W}{\partial t}\,\mathrm{d}x=\int_{\Omega_k}\frac{\mathrm{d}\varphi_i}{\mathrm{d}x}F\,\mathrm{d}x-\left[\varphi_i\hat{F}\right]_{x_{k-1/2}}^{x_{k+1/2}}. \tag{2.7}$$

Substituting $W(x)$ by its polynomial representation, and using the orthogonality of the polynomials and the fact that $\phi_i(x=1)=1$ and $\phi_i(x=-1)=(-1)^i$, the evolution equation for the coefficients $w_n(t)$ is

$$\frac{\Delta x}{2n+1}\frac{\mathrm{d}w_n}{\mathrm{d}t}=\int_{\Omega_k}\frac{\mathrm{d}\varphi_n}{\mathrm{d}x}F\,\mathrm{d}x-\left[\left.\hat{F}\right|_{x_{k+1/2}}-(-1)^n\left.\hat{F}\right|_{x_{k-1/2}}\right], \tag{2.8}$$

where $\hat{F}$ is an appropriate numerical flux.

The DG discretization is not straightforward for non-conservative equations, such as advection equations. A theoretical framework for determining weak solutions to non-conservative products was proposed by LeFloch [93] and Dal Maso et al. [94]. Parés [95], Castro et al. [96], and Canestrelli et al. [97] developed and implemented these ideas in a FV framework, which was extended to DG by Rhebergen et al. [98] (followed here) and Sollie et al. [99]. The non-conservative equation

$$\frac{\partial V}{\partial t} + \frac{\partial G}{\partial x} + H\frac{\partial V}{\partial x} = 0, \qquad G = G(V), \quad H = H(V), \tag{2.9}$$

for $V(x,t)$ can be written in weak form

$$\int_\Omega \varphi_i \frac{\partial V}{\partial t}\,\mathrm{d}x = \int_\Omega \frac{\mathrm{d}\varphi_i}{\mathrm{d}x} G\,\mathrm{d}x - \int_\Omega \varphi_i H\frac{\partial V}{\partial x}\,\mathrm{d}x \quad - \left[\varphi_i \hat{G} - \{\!\{\varphi_i\}\!\}\, H\frac{\partial V}{\partial x}\right]_{x_{k-1/2}}^{x_{k+1/2}}, \tag{2.10}$$

where $\{\!\{\alpha\}\!\} = \frac{1}{2}(\alpha_L + \alpha_R)$ and L and R denote the left and right states at the cell edges. The last term in Eq. (2.10) contains the interface flux due to the non-conservative product. This formulation attempts to reconcile the DG approach with the absence of a weak solution for non-conservative products at the interface. Conservative fluxes are implemented with the usual Riemann solvers. We use the Dal Maso-LeFloch-Murat theory [94] to evaluate

$$\left[H\frac{\partial V}{\partial x}\right]_{x_{k+1/2}} = \int_0^1 H(\psi(\tau; V^L, V^R))\frac{\partial \psi}{\partial \tau}(\tau; V^L, V^R)\,\mathrm{d}\tau, \tag{2.11}$$

where ψ is a path connecting the left and right states. In this work, a simple linear path connecting the left and right states is used. Several approximate Riemann solvers have been developed for non-conservative products to solve for the non-conservative flux at the interface in Eq. (2.10). Rhebergen et al. [98] proposed an HLL-like approach [100], which can be extended to Lax-Friedrichs [101], Rusanov [102], and HLLC [103] solvers. Dumbser and Toro [104] extended the Osher solver to non-conservative hyperbolic systems. Finally, Toumi [105] proposed a weak definition of the approximate Riemann solver of Roe [106].

2.4.2 Limiting procedure: hierarchical reconstruction

We use HR, developed by Liu et al. [65] and Xu et al. [66] to limit the solution at discontinuities, which preserves high-order accuracy in smooth regions. The idea underlying

HR is to recompute the coefficients of the polynomials inside a cell, from the highest degree coefficient to the lowest, *e.g*, using a MUSCL [107] or WENO [108] approach. The advantage of this hierarchical procedure is that the order of accuracy remains high (although not superconvergent, as demonstrated later). Let the polynomial in cell k be

$$U_k(x) = \sum_{n=0}^{P} c_k^{(n)} \frac{x^n}{n!}. \tag{2.12}$$

The limited coefficient $c_k^{(n)}$ is computed by applying a limiter function to candidates of $c_k^{(n)}$. To find these candidates, we calculate the $n-1$ derivative of $U_k(x)$ in terms of a linear polynomial L_k and a higher-order polynomial R_k: $\partial^{n-1} U_k = L_k(x) + R_k(x)$. Since the cell averages of L_k in the element and the adjacent ones are known, we can form the candidate coefficients for L_k and, therefore, candidates for $c_k^{(n)}$. In HR, the cell averages in an element k and its neighbors are approximated in the following way:

$$\overline{L}_{k-1} = \overline{\partial^{n-1} U}_{k-1} - \widetilde{R}_k, \qquad \overline{L}_k = \overline{\partial^{n-1} U}_k - \widetilde{R}_k, \qquad \overline{L}_{k+1} = \overline{\partial^{n-1} U}_{k+1} - \widetilde{R}_k, \tag{2.13}$$

where $\widetilde{R}_k(x)$ is the cell average of the remainder polynomial with the limited coefficients and extends into the adjacent elements. The cell averages are then combined, here using a standard MUSCL procedure [107], to reconstruct the limited first-order coefficient of L_k and, equivalently, $c_k^{(n)}$. This procedure preserves the cell average of the limited variable. While, in theory, limiting applied to the characteristic variables prevents small oscillations in shock-tube problems [57], this approach is computationally expensive and leads to other problems related to multi-dimensional inconsistencies and unstructured grids [65, 88].

2.5 Preventing spurious pressure oscillations at interfaces

The DG procedure works well for single-fluid compressible problems (*e.g*, constant material properties in the equation of state). However, a naive implementation to flows of non-constant material properties generally produces numerical errors. Starting with ideal gases, we show that spurious pressure oscillations may be produced by two mechanisms: (i) an unsuitable form of the transport equation, and (ii) a limiting procedure that does not preserve pressure equilibrium. We then propose an approach that prevents these errors, and extend it to multiphase flows obeying a Mie-Grüneisen equation of state. By considering the advection of an isolated interface between two ideal gases with different values of γ moving at a constant velocity $u > 0$, we verify our analysis.

2.5.1 The cause for the oscillations

2.5.1.1 Oscillations due to the form of the transport equation

We first show that an unsuitable weak form of the transport equation causes spurious pressure oscillations. Let the initial data in two neighboring cells $k-1$ and k be $(\rho, \rho u, E)^{k-1}$ and $(\rho, \rho u, E)^{k}$, respectively, with the interface located between the two cells. For the advection of a material interface, $\rho^{k-1} \neq \rho^{k}$ and $\gamma^{k-1} \neq \gamma^{k}$, but $u^{k-1} = u^{k}$ and $p^{k-1} = p^{k}$. The density, momentum, and energy are $\rho^k = \sum_{n=0}^{P} \rho_n^k \varphi_n$, $(\rho u)^k = \sum_{n=0}^{P} (\rho u)_n^k \varphi_n$, $E^k = \sum_{n=0}^{P} E_n^k \varphi_n$. Thus, the semi-discrete continuity equation for cell k becomes:

$$\frac{\Delta x}{2n+1}\frac{\mathrm{d}\rho_n^k}{\mathrm{d}t} + \rho u|_{x_{I+1/2}} - (-1)^n\, \rho u|_{x_{I-1/2}} - \int_{\Omega_k} \rho u \frac{\mathrm{d}\varphi_n}{\mathrm{d}x}\,\mathrm{d}x = 0. \tag{2.14}$$

We use an upwind flux to approximate the mass flux value at $x_{I-1/2}$ (and $x_{I+1/2}$),

$$\rho u|_{x_{I-1/2}} = (\rho u)^{k-1}\Big|_{x_{I-1/2}} = \sum_{m=0}^{P} (\rho u)_m^{k-1}\varphi_m\Big|_{x_{I-1/2}} = \sum_{m=0}^{P} (-1)^m (\rho u)_m^{k-1}. \tag{2.15}$$

Since the velocity is positive and constant across the interface between the left and right cells,

$$\frac{\Delta x}{2n+1}\frac{\mathrm{d}\rho_n^k}{\mathrm{d}t} + u\sum_{m=0}^{P}\left[\rho_m^k - (-1)^{n+m}\rho_m^{k-1}\right] - u\sum_{m=0}^{P}\rho_m^k \int_{\Omega_k}\varphi_m\frac{\mathrm{d}\varphi_n}{\mathrm{d}x}\,\mathrm{d}x = 0. \tag{2.16}$$

Similarly, for conservation of momentum:

$$\begin{aligned}\frac{\Delta x}{2n+1}\frac{\mathrm{d}(\rho u)_n^k}{\mathrm{d}t} &+ u^2\sum_{m=0}^{P}\left[\rho_m^k - (-1)^{n+m}\rho_m^{k-1}\right] \\ &- u^2\sum_{m=0}^{P}\rho_m^k\int_{\Omega_k}\varphi_m\frac{\mathrm{d}\varphi_n}{\mathrm{d}x}\,\mathrm{d}x + p\left[1-(-1)^n\right] - p\int_{\Omega_k}\frac{\mathrm{d}\varphi_n}{\mathrm{d}x}\,\mathrm{d}x = 0,\end{aligned} \tag{2.17}$$

where the last two terms cancel out. Therefore, the evolution of the n^{th} transport coefficient is

$$\frac{\Delta x}{2n+1}\frac{\mathrm{d}(\rho u)_n^k}{\mathrm{d}t} + u^2 \sum_{m=0}^{P}\left[\rho_m^k - (-1)^{n+m}\rho_m^{k-1}\right] - u^2 \sum_{m=0}^{P}\rho_m^k \int_{\Omega_k} \varphi_m \frac{\mathrm{d}\varphi_n}{\mathrm{d}x}\,\mathrm{d}x = 0, \tag{2.18}$$

such that

$$\frac{d}{dt}(\rho u)_n^k = u\frac{d\rho_n^k}{dt}. \tag{2.19}$$

Thus, the kinematic interfacial condition (constant velocity) is preserved.

For conservation of energy,

$$\frac{\Delta x}{2n+1}\frac{\mathrm{d}E_n^k}{\mathrm{d}t} + u(E+p)|_{x_{I+1/2}} - (-1)^n\, u(E+p)|_{x_{I-1/2}} - \int_{\Omega_k} u(E+p)\frac{\mathrm{d}\varphi_n}{\mathrm{d}x}\,\mathrm{d}x = 0. \tag{2.20}$$

Noting that the velocity and pressure are uniform initially, we write $E^k = p\left(\frac{1}{\gamma-1}\right)^k + \frac{1}{2}\rho^k u^2$. Collecting the kinetic energy terms, which cancel out similar to the momentum equation, and using Eq. (2.16),

$$\begin{aligned}\frac{\Delta x}{2n+1}\frac{\mathrm{d}}{\mathrm{d}t}\left\{p\left(\frac{1}{\gamma-1}\right)_n^k\right\} + up\left\{\left.\frac{1}{\gamma-1}\right|_{x_{I+1/2}} - (-1)^n \left.\frac{1}{\gamma-1}\right|_{x_{I-1/2}}\right\}&\\ - up\sum_{m=0}^{P}\int_{\Omega_k}\left(\frac{1}{\gamma-1}\right)^k \frac{\mathrm{d}\varphi_n}{\mathrm{d}x}\,\mathrm{d}x = 0.&\end{aligned} \tag{2.21}$$

Noting that, in general, we can express the ratio of specific heats as a function of the mass fraction, $f(Y) = \frac{1}{\gamma-1}$, we expand the temporal derivative to obtain:

$$\begin{aligned}\frac{\Delta x}{2n+1}\frac{\mathrm{d}p}{\mathrm{d}t}f(Y)_n^k + p\Bigg\{\frac{\Delta x}{2n+1}\frac{\mathrm{d}}{\mathrm{d}t}f(Y)_n^k + u\left[f(Y)|_{x_{I+1/2}} - (-1)^n\, f(Y)|_{x_{I-1/2}}\right]&\\ -u\sum_{m=0}^{P}\int_{\Omega_k} f(Y)^k\frac{\mathrm{d}\varphi_n}{\mathrm{d}x}\,\mathrm{d}x\Bigg\} = 0.&\end{aligned} \tag{2.22}$$

The term in braces is a discrete form of a non-conservative evolution equation for $f(Y)$.

Recalling Eq. (2.5),

$$\frac{1}{\gamma-1} = f(Y) = \frac{1}{\frac{Y}{M_1} + \frac{1-Y}{M_2}} \left(\frac{Y}{\gamma_1 - 1} \frac{1}{M_1} + \frac{1-Y}{\gamma_2 - 1} \frac{1}{M_2} \right). \tag{2.23}$$

Thus, because of the nonlinearity of f in Y, solving the transport equation for Y in conservative or non-conservative form cannot ensure that the term in the braces in Eq. (2.22) is identically zero. As a result, the dynamic interfacial condition (pressure equilibrium) is violated: the pressure is no longer uniform at the next time step, or any subsequent, thus leading to spurious pressure oscillations.

2.5.1.2 Oscillations due to the limiting procedure

Even if the correct form of the transport equation is used, pressure equilibrium may be violated by the limiting procedure, *i.e.*, given a constant pressure at the beginning of a time step, fully conservative limiting may produce pressures that no longer are constant. To show this, let us denote three adjacent computational cells $L : x \in [-3, -1]$, $C : x \in [-1, 1]$, and $R : x \in [1, 3]$, with

$$\begin{aligned} &\rho^L \neq \rho^C \neq \rho^R, \qquad \gamma^L \neq \gamma^C \neq \gamma^R, \\ &u^L = u^C = u^R = u > 0, \qquad p^L = p^C = p^R = p. \end{aligned}$$

Before limiting, the pressures at the nodal values are equal, *e.g*, $p(1) = p(-1)$ for $P = 1$. To prevent pressure errors, the nodal values after limiting must be the same, *i.e.*, $\widetilde{p}(1) = \widetilde{p}(-1)$, where $\widetilde{p}(x) = \widetilde{\frac{1}{\gamma-1}}(\widetilde{E} - \frac{1}{2}\frac{(\widetilde{\rho u})^2}{\widetilde{\rho}})$. The following development shows that this condition cannot be met by limiting the conserved variables, specifically the total energy, as traditionally done.

Without loss of generality, consider $P = 1$ and HR limiting [65, 66]. In each cell, let the solution be

$$\begin{aligned} &\rho(x) = \rho_0 + \rho_1 x, \quad \rho u(x) = (\rho u)_0 + (\rho u)_1 x, \\ &E(x) = E_0 + E_1 x, \quad \frac{1}{\gamma-1}(x) = \left(\frac{1}{\gamma-1}\right)_0 + \left(\frac{1}{\gamma-1}\right)_1 x, \end{aligned} \tag{2.24}$$

and the limited solution be

$$
\begin{aligned}
&\widetilde{\rho}(x) = \widetilde{\rho}_0 + \widetilde{\rho}_1 x, \quad \widetilde{\rho u}(x) = \widetilde{(\rho u)}_0 + \widetilde{(\rho u)}_1 x, \\
&\widetilde{E}(x) = \widetilde{E}_0 + \widetilde{E}_1 x, \quad \widetilde{\frac{1}{\gamma - 1}}(x) = \widetilde{\left(\frac{1}{\gamma - 1}\right)}_0 + \widetilde{\left(\frac{1}{\gamma - 1}\right)}_1 x.
\end{aligned}
\tag{2.25}
$$

For density, the limiting procedure leads to $\widetilde{\rho}_0 = \rho_0$ and $\widetilde{\rho}_1 = \operatorname{minmod}\left(\rho_0^C - \rho_0^L, \rho_0^R - \rho_0^C\right)/2$. The minmod () function of two numbers a and b is defined as

$$
\operatorname{minmod}(a, b) = \begin{cases} \min(a, b), & \text{if } a, b > 0, \\ \max(a, b), & \text{if } a, b < 0, \\ 0, & \text{otherwise.} \end{cases}
\tag{2.26}
$$

For momentum, $\widetilde{\rho u} = u \widetilde{\rho}$, such that velocity equilibrium is preserved. Limiting of the conserved variables produces the following slope in energy:

$$
\begin{aligned}
\widetilde{E}_1 = \frac{1}{2} \operatorname{minmod} \Bigg(& p \left\{ \left(\frac{1}{\gamma - 1}\right)_0^C - \left(\frac{1}{\gamma - 1}\right)_0^L \right\} + \frac{u^2}{2}(\rho_0^C - \rho_0^L), \\
& p \left\{ \left(\frac{1}{\gamma - 1}\right)_0^R - \left(\frac{1}{\gamma - 1}\right)_0^C \right\} + \frac{u^2}{2}(\rho_0^R - \rho_0^C) \Bigg).
\end{aligned}
\tag{2.27}
$$

Since, in general, $\operatorname{minmod}(x_1 + y_1, x_2 + y_2) \neq \operatorname{minmod}(x_1, x_2) + \operatorname{minmod}(y_1, y_2)$ for variable x_i and y_i, pressure cannot be factored out of the minmod function.

As a preview of Section 2.5.2.2, the condition $\widetilde{p}(1) = \widetilde{p}(-1) = p(1) = p(-1) = p$ can be enforced to produce a slope in total energy as follows:

$$
\begin{aligned}
\widetilde{E}_1 &= \frac{1}{\left(\frac{1}{\gamma - 1}\right)_0} \left(E_0 - \frac{u^2}{2}\rho_0\right) \widetilde{\left(\frac{1}{\gamma - 1}\right)}_1 + \frac{u^2}{2}\widetilde{\rho}_1 \\
&= p \frac{1}{2} \operatorname{minmod} \left(\left(\frac{1}{\gamma - 1}\right)_0^C - \left(\frac{1}{\gamma - 1}\right)_0^L, \left(\frac{1}{\gamma - 1}\right)_0^R - \left(\frac{1}{\gamma - 1}\right)_0^C \right) \\
&\quad - \frac{u^2}{2} \frac{1}{2} \operatorname{minmod}\left(\rho_0^C - \rho_0^L, \rho_0^R - \rho_0^C\right).
\end{aligned}
\tag{2.28}
$$

By construction, such a definition preserves a uniform pressure. Clearly, Eq. (2.27) does not reduce to Eq. (2.28) and therefore does not preserve pressure equilibrium, *i.e.*, $\widetilde{p} =$

$\widetilde{\frac{1}{\gamma-1}}(\widetilde{E}-\frac{1}{2}\frac{(\widetilde{\rho u})^2}{\widetilde{\rho}}) = p$. Thus, fully conservative limiting introduces pressure errors in flows with variable γ. We generalize this approach to arbitrary P and multiphase flows in Section 2.5.2.2.

2.5.2 Strategy to prevent oscillations

Now that the cause for spurious pressure oscillations has been established, we propose a strategy to avoid these errors. Our approach relies on (i) the transport equation(s) describing the material properties must be solved in a non-conservative weak form, and (ii) the suitable variables must be limited (density, momentum, pressure and appropriate properties entering the equation of state), coupled with a consistent reconstruction of the energy.

2.5.2.1 Transport equations for the material properties

To prevent spurious pressure oscillations, the form of the transport equations for the material properties is crucial. From Eq. (2.21) in Section 2.5.1.1, to ensure that the pressure remains constant in time and space (*i.e.*, $dp/dt|_k = 0$), the following equation must hold

$$\begin{aligned}\frac{\Delta x}{2n+1}\frac{\mathrm{d}}{\mathrm{d}t}\left(\frac{1}{\gamma-1}\right)_n^k + u\left\{\left.\frac{1}{\gamma-1}\right|_{x_{I+1/2}} - (-1)^n \left.\frac{1}{\gamma-1}\right|_{x_{I-1/2}}\right\} \\ - u\sum_{m=0}^{P}\left(\frac{1}{\gamma-1}\right)_m^k \int_{\Omega_k}\varphi_m \frac{\mathrm{d}\varphi_n}{\mathrm{d}x}\,\mathrm{d}x = 0,\end{aligned} \tag{2.29}$$

which is the weak form of

$$\frac{\partial}{\partial t}\left(\frac{1}{\gamma-1}\right) + u\frac{\partial}{\partial x}\left(\frac{1}{\gamma-1}\right) = 0. \tag{2.30}$$

This result is consistent with the findings of Abgrall [54] for FV methods.

For multiphase flows with the Mie-Grüneisen equation of state (2.2), a similar analysis shows that the weak form of the following equations must be solved:

$$\frac{\partial}{\partial t}\left(\frac{1}{\Gamma}\right) + u\frac{\partial}{\partial x}\left(\frac{1}{\Gamma}\right) = 0, \tag{2.31a}$$

$$\frac{\partial}{\partial t}\left(\frac{p_{\text{ref}}}{\Gamma}\right) + u\frac{\partial}{\partial x}\left(\frac{p_{\text{ref}}}{\Gamma}\right) = 0, \tag{2.31b}$$

$$\frac{\partial}{\partial t}\left(\rho e_{\text{ref}}\right) + \frac{\partial}{\partial x}\left(\rho u e_{\text{ref}}\right) = 0. \tag{2.31c}$$

These equations are consistent with those obtained by Shyue [75] for FV methods and could include density-dependent material properties. The difference lies in the fact that the equations must be written in the appropriate weak form for DG, as described in Section 2.4.1.

2.5.2.2 Conservative, high-order accurate, and non-oscillatory limiting for DG

For discontinuous problems, it is necessary to limit the solution to avoid numerical oscillations with high-order methods. Our goal is to ensure that this limiting procedure does not lead to oscillations at interfaces for non-constant γ (and other material properties). Let $A(x)$, $B(x)$, $C(x)$, and $U(x)$ be Taylor polynomials inside a cell $\Omega = \{x | x \in [-1, 1]\}$,

$$A(x) = \sum_{n=0}^{P} A_n \frac{x^n}{n!}, \quad B(x) = \sum_{n=0}^{P} B_n \frac{x^n}{n!}, \quad C(x) = \sum_{n=0}^{P} C_n \frac{x^n}{n!}, \quad U(x) = \sum_{n=0}^{P} U_n \frac{x^n}{n!}. \tag{2.32}$$

Let a be a constant inside a cell and the limiting operation be denoted by a tilde. Let us assume $A(x)$, $B(x)$, and $U(x)$ are coupled through an algebraic relation $U = f(A, B, C)$, or, equivalently, $C = f^{-1}(A, B, U)$. We seek a limiting procedure for U that is non-oscillatory, *i.e.*, if $C(x) = a$, then $\widetilde{C}(x) = f^{-1}(\widetilde{A}, \widetilde{B}, \widetilde{U}) = a$, high-order accurate, and conservative, *i.e.*, $\int \widetilde{U}\, \mathrm{d}\Omega = \int U\, \mathrm{d}\Omega$. The second and third properties can generally be achieved using high-order limiting such as HR [65, 66] for single fluids. However, such limiting procedures are nonlinear, which lead to the following difficulties (see proofs thereof in C): (i) the limited value of a sum is not equal to the sum of limited values, and (ii) limiting a product of functions violates conservation. In other words, $\widetilde{A + B} \neq \widetilde{A} + \widetilde{B}$ and $\int \widetilde{A}\widetilde{B}\, \mathrm{d}\Omega \neq \int AB\, \mathrm{d}\Omega$. Satisfying these latter two properties is essential to prevent pressure errors due to limiting.

We show how these two difficulties can be overcome to produce a non-oscillatory limiting procedure.

(i) *Sum of limited functions.* First, let $U(x) = f(A, B, a) = aA + B$. If we limit U as $\widetilde{U} = \widetilde{aA + B}$ and use the limited values of A and B to recover a, we obtain:

$$\widetilde{a} = f^{-1}(\widetilde{A}, \widetilde{B}, \widetilde{U}) = \frac{1}{\widetilde{A}}(\widetilde{U} - \widetilde{B}) = \frac{1}{\widetilde{A}}(\widetilde{aA + B} - \widetilde{B}). \tag{2.33}$$

This expression is generally not equal to a because of the nonlinearity of the limiting procedure. On the other hand, if we compute the limited value of U based on $\widetilde{A}$ and $\widetilde{B}$, *i.e.*, $\widetilde{U} = \widetilde{aA} + \widetilde{B}$, then the constant is recovered:

$$\widetilde{a} = f^{-1}(\widetilde{A}, \widetilde{B}, \widetilde{U}) = \frac{1}{\widetilde{A}}(\widetilde{U} - \widetilde{B}) = \frac{1}{\widetilde{A}}(\widetilde{aA} + \widetilde{B} - \widetilde{B}) = a. \tag{2.34}$$

Hence, limiting the terms in the addition separately ensures that a constant function remains constant after limiting and therefore that this procedure is non-oscillatory. Furthermore, limiting a sum of functions (possibly multiplied by a constant) is conservative:

$$\int \widetilde{U}\,\mathrm{d}\Omega = \int \widetilde{aA}\,\mathrm{d}\Omega + \int \widetilde{B}\,\mathrm{d}\Omega = a \int A\,\mathrm{d}\Omega + \int B\,\mathrm{d}\Omega = \int U\,\mathrm{d}\Omega. \tag{2.35}$$

High-order accuracy is guaranteed as long as the limiting procedure is high-order accurate.

(ii) *Product of limited functions.* Limiting a product of functions separately violates the conservation property: if $U = f(A, B, C) = AC$ and $\widetilde{U} = \widetilde{A}\widetilde{C}$, then $\int \widetilde{U}\,\mathrm{d}\Omega \neq \int U\,\mathrm{d}\Omega$. We propose a remedy to this problem. Using the chain rule for the product of A and

C, the coefficients of U can be expressed in terms of the coefficients of A and C

$$U_0 = \left.\frac{\partial^0 U}{\partial x^0}\right|_0 = \left.\frac{\partial^0 (AC)}{\partial x^0}\right|_0 = A_0 C_0, \tag{2.36a}$$

$$U_1 = \left.\frac{\partial^1 U}{\partial x^1}\right|_0 = \left.\frac{\partial^1 (AC)}{\partial x^1}\right|_0 = A_1 C_0 + A_0 C_1, \tag{2.36b}$$

$$U_2 = \left.\frac{\partial^2 U}{\partial x^2}\right|_0 = \left.\frac{\partial^2 (AC)}{\partial x^2}\right|_0 = A_2 C_0 + 2A_1 C_1 + A_0 C_2, \tag{2.36c}$$

$$\dots$$

$$U_n = \sum_{k=0}^{n} \binom{n}{k} A_{n-k} C_k, \tag{2.36d}$$

where $\binom{n}{k}$ is the binomial coefficient. We reconstruct the limited coefficients of U by

$$\widetilde{U}_n = \sum_{k=0}^{n} \binom{n}{k} \widetilde{A}_{n-k} \widetilde{C}_k, \quad \text{for } n = 0, \dots, P. \tag{2.37}$$

We then impose conservation,

$$\int \widetilde{U} \, \mathrm{d}\Omega = \int U \, \mathrm{d}\Omega \quad \Leftrightarrow \quad \sum_{k=0,2,4,\dots} \frac{2}{(k+1)!} \left(\widetilde{U}_k - U_k \right) = 0. \tag{2.38}$$

These $P + 2$ conditions constrain $P + 1$ coefficients. We relax these conditions and use

$$\widetilde{U}_n = \sum_{k=0}^{n} \binom{n}{k} \widetilde{A}_{n-k} \widetilde{C}_k, \quad \text{for } n = 1, \dots, P, \tag{2.39a}$$

$$\widetilde{U}_0 = U_0 - \sum_{k=2,4,\dots} \frac{1}{(k+1)!} \left(\widetilde{U}_k - U_k \right). \tag{2.39b}$$

If $C = a$, then $C_0 = a$ and $C_k = 0$ for $k > 0$, so that this procedure reduces to $\widetilde{U} = a\widetilde{A}$, thus verifying the non-oscillatory condition. This procedure naturally preserves high-order accuracy.

In conclusion, the present limiting procedure is conservative and non-oscillatory, and preserves the high-order moments of the solution. Additionally, this procedure requires approximately the same number of operations as fully conservative limiting. This discussion is general and applies to different limiting approaches beyond HR.

2.5.2.3 Application to multiphase flows

The derivations above can be directly applied to multiphase flows. It is immediately clear that limiting the total energy in the multiphase Euler equations results in oscillatory pressure fields. It is therefore necessary to apply our modified limiting procedure by reconstructing coefficients of the total energy through

$$\widetilde{E}_n = \widetilde{\rho e}_n + \widetilde{K}_n, \quad \text{for } n = 1, \ldots, P \tag{2.40a}$$

$$\widetilde{E}_0 = E_0 - \sum_{k=2,4,\ldots} \frac{1}{(k+1)!} \left(\widetilde{E}_k - E_k \right), \tag{2.40b}$$

where the limited kinetic energy $\widetilde{K}$ is reconstructed from the limited density and momentum polynomials. Limiting the density and momentum, instead of ρ and u, ensures that the method is conservative with respect to those variables. The limited internal energy polynomial, $\widetilde{\rho e}$, is reconstructed to ensure that the pressure remains non-oscillatory. For the different equations of state, this implies:

- Ideal gases: we limit p and $\frac{1}{\gamma-1}$, and reconstruct the internal energy as

$$\widetilde{\rho e}_n = \sum_{k=0}^{n} \binom{n}{k} \widetilde{p}_{n-k} \widetilde{\left(\frac{1}{\gamma-1}\right)}_k, \quad \text{for } n = 1, \ldots, P. \tag{2.41}$$

- Stiffened equation of state with $\rho e = \frac{p+\gamma B}{\gamma-1}$, where γ and B are constant: we limit p, $\frac{1}{\gamma-1}$ and $\frac{\gamma B}{\gamma-1}$, and reconstruct the internal energy as

$$\widetilde{\rho e}_n = \sum_{k=0}^{n} \binom{n}{k} \widetilde{p}_{n-k} \widetilde{\left(\frac{1}{\gamma-1}\right)}_k + \widetilde{\left(\frac{\gamma B}{\gamma-1}\right)}_n, \quad \text{for } n = 1, \ldots, P. \tag{2.42}$$

- Mie-Grüneisen equation: we limit p, $\frac{1}{\Gamma}$, $\frac{p_{\text{ref}}}{\Gamma}$ and ρe_{ref}, and reconstruct the internal energy as

$$\widetilde{\rho e}_n = \sum_{k=0}^{n} \binom{n}{k} \widetilde{p}_{n-k} \widetilde{\left(\frac{1}{\Gamma}\right)}_k - \widetilde{\left(\frac{p_{\mathrm{ref}}}{\Gamma}\right)}_n + \widetilde{(\rho e_{\mathrm{ref}})}_n, \quad \text{for } n = 1, \ldots, P. \tag{2.43}$$

By contrast to other limiting approaches, *e.g*, [88], our proposed reconstruction, while relying on limiting pressure, is not a straightforward application of limiting the primitive variables, as this would lead to conservation errors (see Section 2.6.2). Our limiting approach is readily extended to other multiphase models such as the five-equations model (see C).

2.5.3 Verification

We now verify that the proposed approach is oscillation-free, high-order accurate, and conservative. For simplicity, we consider gases; similar tests can readily be performed for the other equations of state under consideration. We define the L_∞ error in the cell average of a quantity U as

$$L_\infty = \max_{i=1\ldots N_E} \left| \frac{1}{\Delta x} \int_{\Omega_i} U_{\mathrm{exact}} \, \mathrm{d}x - \frac{1}{\Delta x} \int_{\Omega_i} U_{\mathrm{numerical}} \, \mathrm{d}x \right|, \tag{2.44}$$

where N_E is the number of cells in the mesh and the integrals are evaluated with a Gaussian quadrature of order $2P+1$. In our comparisons, we consider three approaches:

A. Conservative transport equation for ρY with the physical relationship between Y and γ (2.23) assuming $M = M_1 = M_2$ as in [73], and limiting of the conserved variables $(\rho, \rho u, E, \rho Y)$, which we call the "fully conservative approach,"

B. Non-conservative transport equation for $1/(\gamma - 1)$ and limiting of the conserved variables $(\rho, \rho u, E)$ and $1/(\gamma - 1)$,

C. Non-conservative transport equation for $1/(\gamma-1)$ and limiting of the variables $(\rho, \rho u, p, 1/(\gamma-1))$, which we call "our approach."

2.5.3.1 Verification of the non-oscillatory property: sharp interface advection

We consider the advection of sharp isolated material interfaces to show that both an appropriate form of the transport equation and our modified limiting are necessary to prevent pressure oscillations. Two interfaces, characterized by discontinuities in ρ and γ, are advected at a constant velocity $u = 1$ and under constant pressure in the periodic domain $x \in [-1, 1]$. The initial conditions are

$$(\rho, u, p, \gamma) = \begin{cases} (1, 1, 1, 1.4), & \text{for } x \in [-0.5, 0.5], \\ (0.125, 1, 1, 1.6), & \text{otherwise.} \end{cases} \tag{2.45}$$

Because of the sharp interfaces, limiting is required. The exact solution for this problem is a translation of the initial profiles, with velocity and pressure remaining constant throughout.

Fig. 2.1 shows the pressure field at $t = 2$ (after one period) for the three approaches A, B, and C. Quantitatively, examining the flow solution, the L_∞ error in the cell averages for pressure is $\mathcal{O}(10^{-2})$ with the fully conservative approach (A); it is smaller for approach B ($\mathcal{O}(10^{-3})$). For the proposed approach (C), it is essentially negligible ($\mathcal{O}(10^{-11})$). The pointwise errors are approximately two orders of magnitude larger. The errors for the first two approaches are observed to propagate away from the interface and affect the solution in the entire domain. The amplitude of these oscillations may grow physically upon interaction with other flow features. While these oscillations are small in this test case, we show in later validation tests that they propagate in the flow field, interact with other flow features, and cause the simulations to fail (Sections 2.6.3 and 2.6.4). It is clear that the errors arise for two reasons: the form of the transport equation for the material properties and the limiting procedure. The non-conservative formulation coupled with our modified limiting (our approach C) presents an oscillation-free pressure.

2.5.3.2 High-order property: smooth variation in γ

We consider the advection of a smooth variation in γ and density to ensure that the proposed approach does not affect the convergence rate. This distribution moves at a constant velocity $u = 1$ and under constant pressure in the periodic domain $x \in [-1, 1]$.

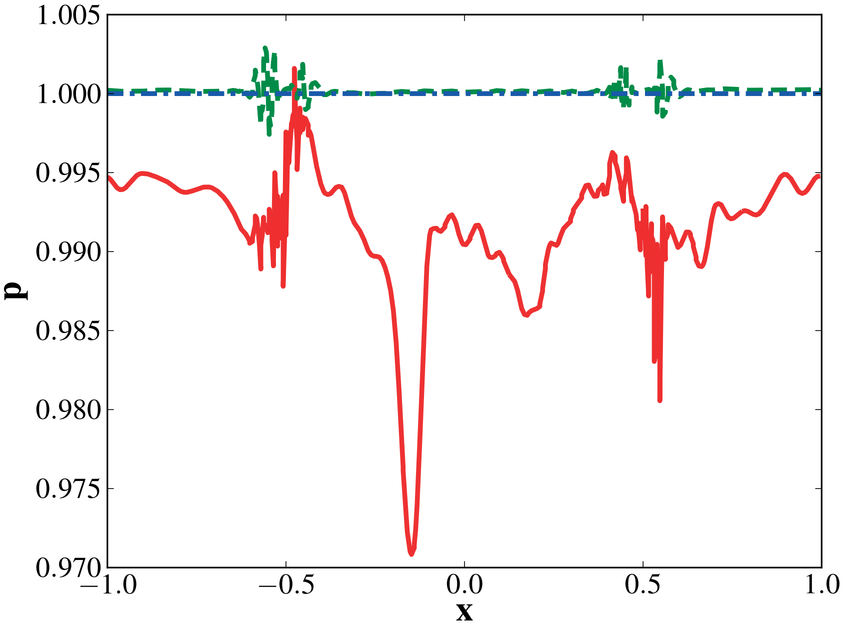

Figure 2.1: Pressure profile at $t = 2$ for the advection of a sharp material interface ($P = 2$, $\Delta x = 1/128$). Solid red: conservative transport equation and limiting of the conserved variables (fully conservative approach). Dashed green: non-conservative equation and limiting of the conserved variables. Dash-dotted blue: non-conservative equation and modified limiting (our approach).

The initial conditions are

$$(\rho, u, p, \gamma) = (1 + 0.2\sin(4\pi x), 1, 1, 1.4 + 0.2\sin(\pi x)). \tag{2.46}$$

Since this problem is smooth, a stable solution can be achieved without limiting. The exact solution for this problem is a translation of the initial profiles, with velocity and pressure remaining constant throughout.

We first consider the solution to this problem with no limiting, to ensure that the non-conservative form of the transport equation produces the expected convergence rate, independently of limiting. Fig. 2.2 shows the L_∞ error in cell averages of $1/(\gamma - 1)$ and pressure after one period for the conservative and non-conservative transport equations (*e.g*, comparing approaches A and B/C with no limiting). For pressure, errors are produced with the conservative approach, and decrease at the expected rate of convergence for DG $(2P + 1)$; a sufficiently fine resolution is required to achieve this convergence rate. With the non-conservative approach, errors lie at the round-off level for all grids. For $1/(\gamma-1)$, the convergence rate is $2P+1$ in both cases. The error is slightly larger for the conservative approach due to the pressure oscillations that affect all fields.

We now consider the solution to this problem with limiting, to evaluate its effect on the convergence rate. In Fig. 2.3, we compare the three approaches A, B and C. Overall, limiting reduces the convergence rate to $P+1$ at best, as expected. Again, approach A (conservative equation and limiting) produces the largest pressure errors. In this case, the pressure oscillations affect all fields and reduce the convergence rate in $1/(\gamma-1)$; the errors decrease at a rate lower than $P+1$. The non-conservative form of the equations with limiting of the conserved variables (approach B) exhibits minor errors in γ; the pressure errors do not decrease at rate $P+1$ until a sufficiently fine grid is used. Our approach C produces round-off errors in pressure, as expected.

These problems illustrate two points. First, pressure oscillations are prevented only by both solving a suitable form of the transport equation and limiting the appropriate variables; the fully conservative approach A produces the largest errors. Second, even if no pressure oscillations are produced, limiting significantly reduces the convergence rate in smooth regions ($P+1$ instead of $2P+1$). To prevent this reduction in accuracy in flows with smooth and discontinuous features, a solution-adaptive approach is presented in Section 2.5.4, in which a sensor discriminates between discontinuities in γ, where our limiting approach should applied, and smooth regions, in which no limiting should be used, *e.g*, as in [72] for finite differences.

2.5.3.3 Conservation property

Our proposed limiting procedure is conservative by construction, in that it preserves the cell averages of the relevant conserved variables and the telescoping property of the fluxes. Although we do not display results for conciseness, we verified that energy is conserved using the two above verification problems. In both verification cases, the error in energy lies at the round-off level for all approaches.

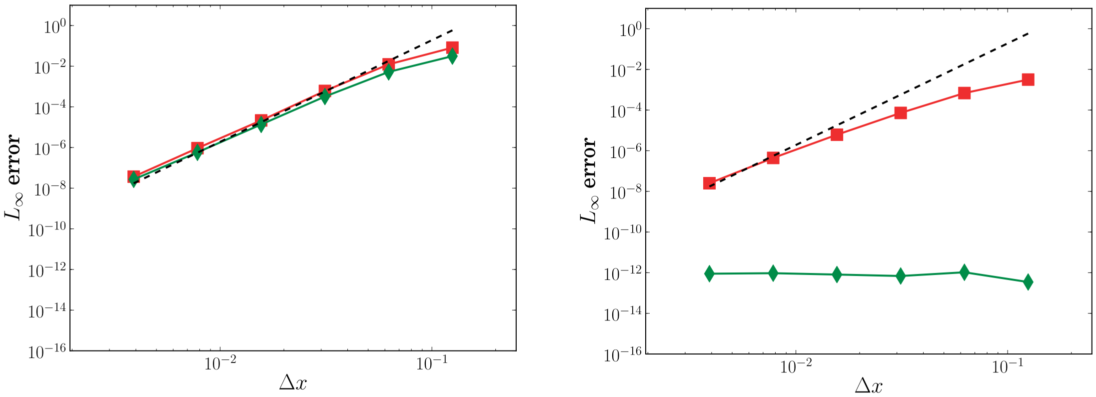

(a) $\frac{1}{\gamma-1}$. (b) Pressure.

Figure 2.2: L_∞ cell-average error vs. Δx for the advection of a smooth distribution in γ with no limiting ($P = 2$). Red squares: conservative transport equation. Green diamonds: non-conservative equation. Dashed line: $2P + 1$ slope.

2.5.4 Solution-adaptive approach: discontinuity sensors

The numerical treatment of discontinuities (introducing numerical dissipation), even with high-order accurate methods, lies in direct contradiction with that of smooth broadband motions (preventing numerical dissipation). For such problems, applying limiting only where needed and using non-dissipative methods elsewhere constitutes a more accurate and efficient approach [109]. To discriminate between smooth and discontinuous regions, a discontinuity sensor is required. The overall accuracy and efficiency strongly depends on the discontinuity sensor. However, designing such sensors that are independent of the numerical scheme is challenging. Thus, there is a need for physics-based discontinuity sensors. Another difficulty with hybrid finite difference/volume methods is that the stencil size increases with order of accuracy. As a result, transition regions between the capturing and central schemes exist [110]. Because of its compactness, the DG approach allows for the use of high order immediately next to cells that contain discontinuities.

A characteristics-based sensor inspired by the physics is developed for the Euler equations. In a first sweep, the sensor first identifies cells affected by material/contact discontinuities. Then, shock waves are detected. A different approach is used for each feature. First, we consider interfaces/contacts. At each element interface, let L and R denote the cell-average value of the corresponding variable on the left and right cell, respectively. The

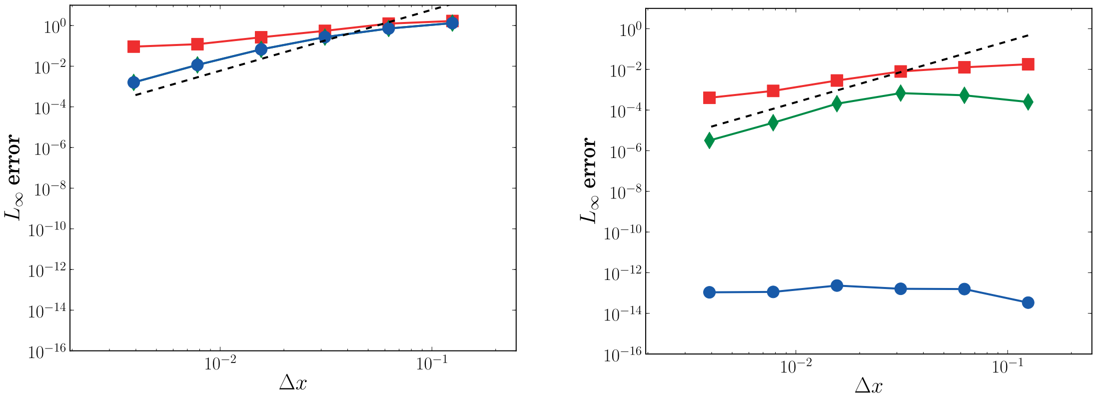

(a) $\frac{1}{\gamma-1}$.

(b) Pressure.

Figure 2.3: L_∞ cell-average error vs. Δx for the advection of a smooth distribution in γ with limiting ($P = 2$). Red squares: conservative transport equation and limiting of the conserved variables (fully conservative approach A). Green diamonds: non-conservative equation and limiting of the conserved variables (approach B). Blue circles: non-conservative equation and modified limiting (our approach C). Dashed line: $P + 1$ slope.

discrete characteristic variables for the Euler equations are

$$\Delta\alpha = \mathcal{R}^{-1}\Delta W, \qquad \Delta W = W_R - W_L = \sum_{i=1}^{3} \widehat{\Delta\alpha_i}\widehat{\mathcal{R}}^{(i)}, \tag{2.47}$$

where $\mathcal{R}$ is the matrix of right eigenvectors, W the vector of conserved variables, α the vector of characteristic variables, and the hat values denote average values, *e.g*, Roe's [106]. Specifically, the strength of a contact discontinuity propagating the density jump $\Delta\rho$ is

$$\Delta\widehat{\alpha_2} = \frac{\Delta\rho\hat{c}^2 - \Delta p}{\hat{c}^2} \tag{2.48}$$

where c is the speed of sound. This quantity is used as a sensor for contact discontinuities, with the following normalization:

$$\xi = \frac{|\Delta\alpha_2|}{\rho_L + \rho_R}, \qquad \Xi = \frac{2\xi}{(1+\xi)^2}. \tag{2.49}$$

Similarly, we construct a sensor for the multifluid Euler equations based γ,

$$\zeta = \frac{|\gamma_R - \gamma_L|}{\gamma_L + \gamma_R}, \qquad Z = \frac{2\zeta}{(1+\zeta)^2}. \tag{2.50}$$

If Ξ or Z is greater than 0.01, limiting is used in the cells that share that interface.

To detect shocks, we use the sensor developed by Lombardini [111]. At each cell edge, we test the Lax entropy condition, which is satisfied by a physical shock wave:

$$u_L - c_L > \hat{u} - \hat{c} > u_R - c_R. \tag{2.51}$$

If this condition is satisfied at the interface, the following pressure sensor is used:

$$\phi = \frac{|p_R - p_L|}{p_L + p_R}, \quad \Phi = \frac{2\phi}{(1+\phi)^2}. \tag{2.52}$$

with a threshold of 0.001.

These sensors lead to robust detection of shocks and discontinuities and are straightforward to implement in multiple dimensions. Though the thresholds are heuristically chosen to be widely applicable (to all problems under consideration), it is likely that an optimal value is problem-dependent. The sensors' detection of discontinuities is not sensitive to the threshold values used in this work (within an order of magnitude).

2.5.5 Algorithm

Our proposed algorithm for interface capturing of compressible multiphase flows using DG can be summarized as follows:

1. Given the coefficients $w_n(t)$ at time t,
2. Identify the cells that require limiting with our proposed solution-adaptive approach,
3. In the detected cells, limit the flow variables (ρ, ρu, p) and the appropriate material properties, *e.g*, $1/(\gamma-1)$ for ideal gases, $1/(\gamma-1)$ and $\gamma B/(\gamma-1)$ for the stiffened equation of state, or $1/\Gamma$, p_{ref}/Γ and ρe_{ref} for the Mie-Grüneisen equation,

4. Reconstruct the internal energy coefficients according to our non-oscillatory procedure following Eq. (2.41), (2.42) or (2.43),
5. Use the DG discretization to march the Euler equations (2.1) forward in time, and the non-conservative transport equations for the material properties, *i.e.*, Eqs. (2.31).

2.6 Numerical tests

We use one- and two-dimensional test problems involving shock waves and interfaces for different equations of state to illustrate the robustness and versatility of our method. For all problems, the standard explicit fourth-order Runge-Kutta method is used, with a Courant number of 0.5. All the numerical tests were performed with the Roe solver and a Lagrange basis. Due to discontinuities, HR with discontinuity sensors is used in all problems. We implemented a highly parallel version of the code on a GPU, which allows for simulations approximately two orders of magnitude faster than on a single Computing Processing Units (CPU). Multi-GPU parallelism using the Message Passing Interface (MPI) is implemented to achieve high speedup for large problems. CUDA is used to communicate data from the GPU to the CPU and MPI transfers data between the host CPU, Figure 2.4. The code exhibits good weak and strong scaling with increasing number of GPU, Figure 2.5. Though the increase in communication across the network negatively impacts strong scaling from one to two GPUs, strong scaling follows the ideal trend beyond two GPUs. The supercomputing cluster used for the scaling analysis, Stampede operated by the Texas Advanced Computing Center, has one GPU per computing node. This means that GPU to GPU communication is particularly expensive as data needs to be moved between nodes.

The two-dimensional simulations were performed using GPUs on the Flux cluster at the Center for Advanced Computing at the University of Michigan. Gmsh is used for the mesh generation and post-processing visualization [112]. The code's workflow and main features are presented in Figure 2.6. Git is used as the main version control system. The code has been used previously to simulate the multilayered Richtmyer-Meshkov (RM) and Rayleigh-Taylor (RT) instabilities [113] and experiments of blast-wave-driven shear flow in high-energy-density regimes [114].

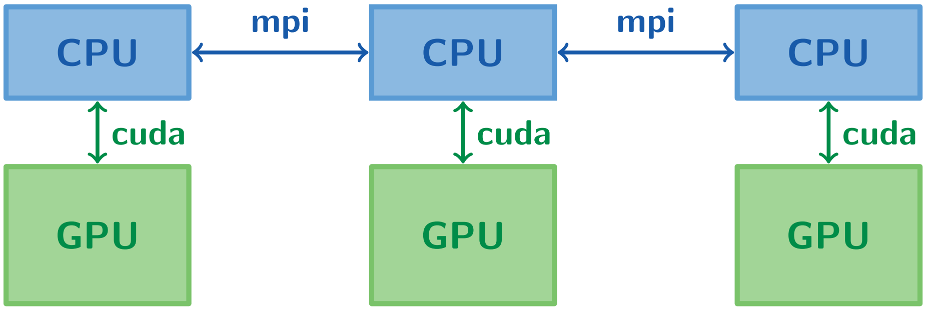

Figure 2.4: High performance computing paradigm combining GPUs and CPUs with CUDA and MPI.

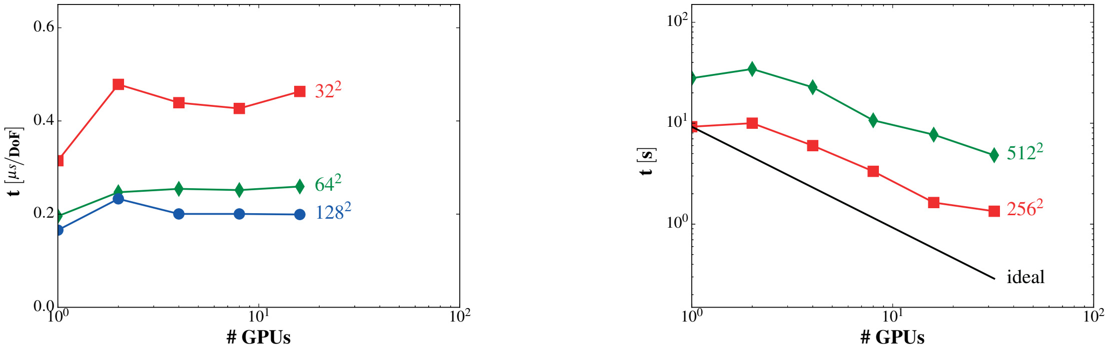

(a) Weak scaling. Time to compute one degree of freedom (DoF)as a function of the number of GPUs. Red squares: 32^2DoF per processor; green diamonds: 64^2 DoF per processor;blue circles: 128^2 DoF per processor.

(b) Strong scaling. Simulation runtime as a function of thenumber of GPUs. Red squares: mesh with 256^2 elements;green diamonds: mesh with 512^2 elements; black line:theoretical power law with slope 2.

Figure 2.5: Code scaling as a function of the number of GPUs.

2.6.1 Multifluid Shu-Osher problem

We consider the Shu-Osher problem [115], extended to include two ideal gases of different γ [72]. A Mach $M_s = 3$ shock interacts with a sharp material interface preceding a smooth variation in density and γ. The initial conditions are

$$\left(\rho, u, p, \frac{1}{\gamma - 1}\right) = \begin{cases} (3.857143, 2.629369, 10.3333, 2.5), & \text{for } x \leq 1, \\ (1 + 0.2\sin(5(x-5)), 0, 1, 1.33 + 0.2\sin(5(x-5))), & \text{otherwise.} \end{cases} \tag{2.53}$$

In Fig. 2.7, we compare the pressure profile for approaches A, B, and C at early time. The fully conservative approach A leads to large pressure oscillations and the simulation

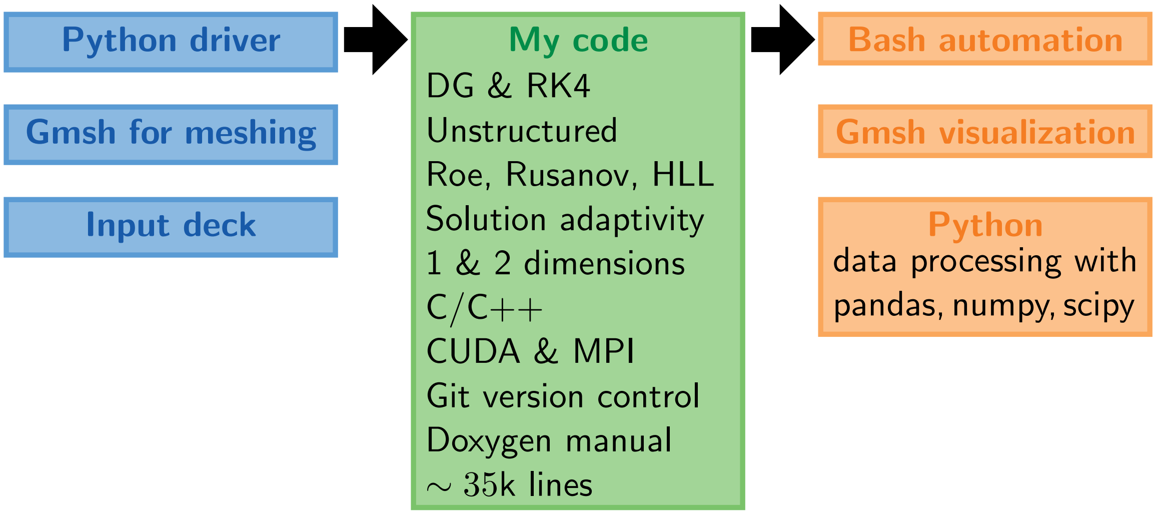

Figure 2.6: Simulation workflow. Blue: pre-processing scripts; green: main simulation code; orange: post-processing scripts.

fails at the illustrated time. The pressure oscillations with approach B are small enough to not significantly impact the solution in this problem. Our approach C does not exhibit any pressure oscillations and adequately represents the solution at time 1.8 (Fig. 2.8). As with finite difference methods for similar resolutions, the entropy waves are damped as they propagate away from the shock [109].

2.6.2 Strong shock impacting on an interface

We consider a strong shock (Mach 8.96) interacting with a moving gas-gas interface [116]. We denote the post-shock region with index 4 ($-1 < x < -0.8$), the pre-shock region with the first gas by 02 ($-0.8 < x < -0.2$), and the pre-shock region with the second gas

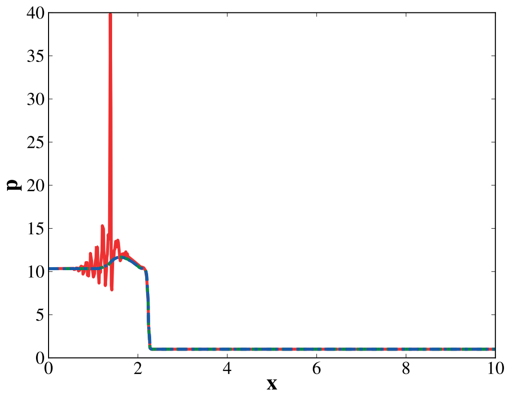

Figure 2.7: Pressure profile at $t = 0.31$ for the multifluid Shu-Osher problem ($P = 2$, $\Delta x = 1/30$). Solid red: conservative transport equation and limiting of the conserved variables (fully conservative approach A). Dashed green: conservative equation and limiting of the conserved variables (approach B). Dash-dotted blue: non-conservative equation and modified limiting (our approach C).

by 01 ($-0.2 < x < 1$). The initial conditions for this problem are:

$$\rho = \begin{cases} \rho_4 = \rho_{02} \frac{(\gamma_{02}+1)M_s^2}{(\gamma_{02}-1)M_s^2+2}, \\ \rho_{02} = 0.1, \\ \rho_{01} = 1.0, \end{cases} \qquad u = \begin{cases} u_4 = \frac{c_{02}}{M_s} \frac{2(M_s^2-1)}{\gamma_{02}+1} + u_c, \\ u_{02} = u_c, \\ u_{01} = u_c, \end{cases}$$
$$p = \begin{cases} p_4 = r p_0, \\ p_{02} = p_0, \\ p_{01} = p_0, \end{cases} \qquad \gamma = \begin{cases} \gamma_4 = \gamma_{02}, \\ \gamma_{02} = \frac{5}{3}, \\ \gamma_{01} = 1.4, \end{cases} \tag{2.54}$$

with $r = \frac{p_4}{p_0} = 100$ and $p_0 = 1$ such that $M_s = \sqrt{\frac{\gamma_{02}+1}{2\gamma_{02}} r + \frac{\gamma_{02}-1}{2\gamma_{02}}} = 8.96$. We add a background velocity, $u_c = -2$, so that the interesting flow features remain near the middle of the domain. As a result, the interface dissipates slightly as it moves to the left before interacting with the shock. Fig. 2.9 shows the density, velocity, pressure, and γ profiles at $t = 0.04$ for $P = 2$. Limiting the total energy (approach B) leads to significant oscillations in pressure (5% overshoot near the contact) and velocity. Approach A produce 11% overshoots in pressure (data not shown). These errors are avoided with our proposed approach (C). The small bumps in u and p around $x = -0.6$ are due to shock startup errors [117, 118].

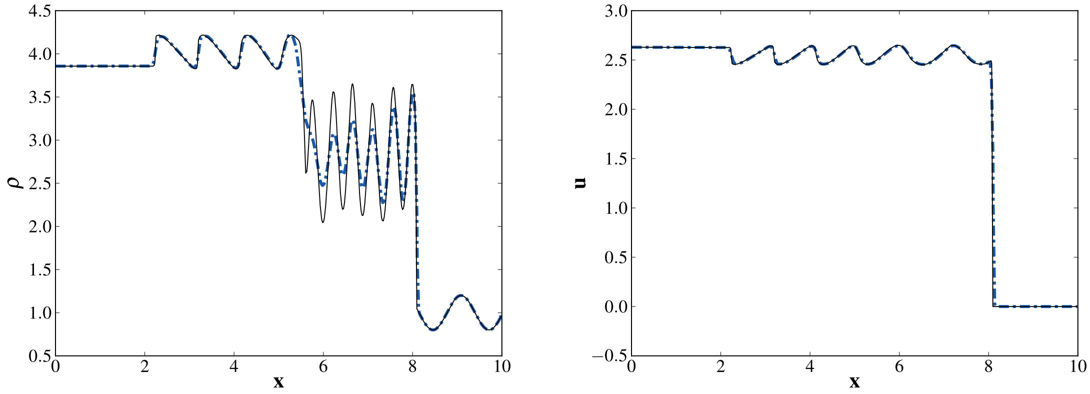

(a) Density.

(b) Velocity.

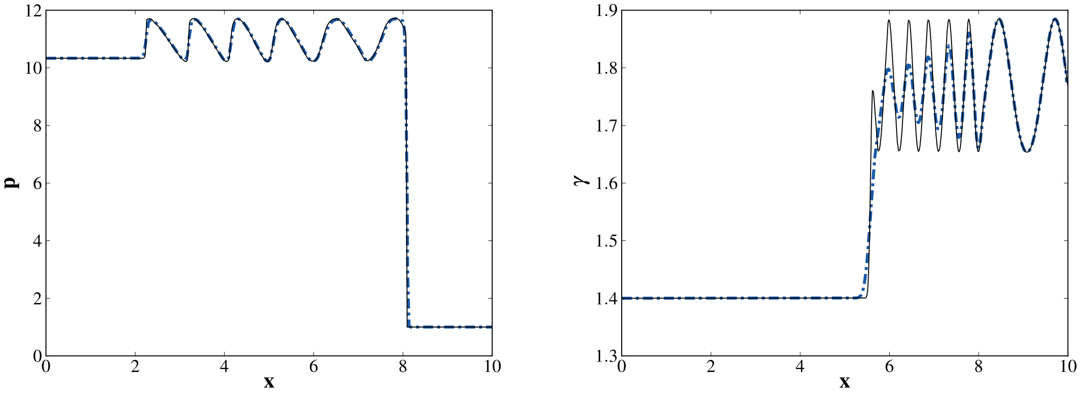

(c) Pressure.

(d) Ratio of specific heats.

Figure 2.8: Profiles at $t = 1.8$ for the multifluid Shu-Osher problem using our approach C ($P = 2$). Solid black: reference solution (1280 cells). Dash-dotted blue: (300 cells).

This particular case illustrates the importance of the conservative nature of our approach. If one directly limits the primitive variables (ρ,u,p) as suggested in [88], energy conservation errors are $\mathcal{O}(10^{-1})$, compared to $\mathcal{O}(10^{-14})$ for our proposed approach. Such errors lead to incorrect shock speeds and interface positions.

2.6.3 Richtmyer-Meshkov instability

We use the single-mode RM instability experiments from [119] for validation. A shock ($M_s = 1.21$) initialized in air ($\rho_{air} = 1.351\,\mathrm{kg/m}^3$, $\gamma_{air} = 1.276$, $M_{air} = 34.76\,\mathrm{kg/kmol}$) and moving downwards impinges a perturbed interface between the air and the denser SF_6 ($\rho_{SF_6} = 5.494\,\mathrm{kg/m}^3$, $\gamma_{SF_6} = 1.093$, $M_{SF_6} = 146.05\,\mathrm{kg/kmol}$), thereby initiating the RM

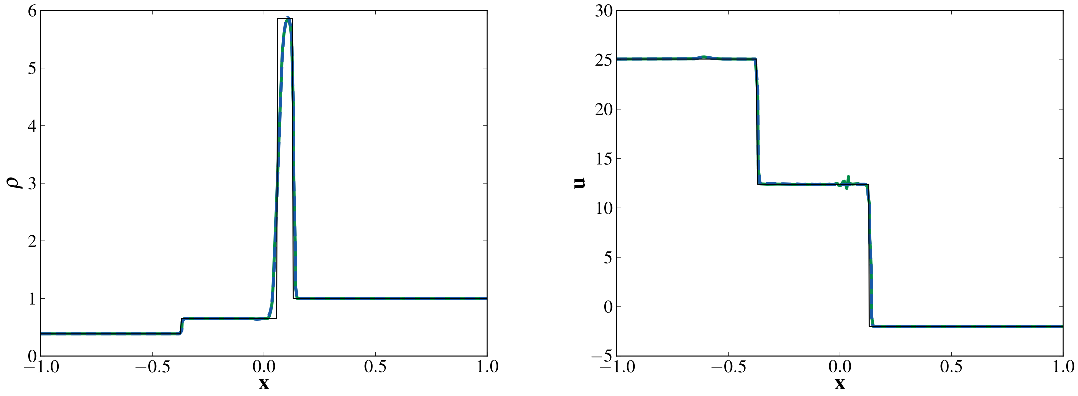

(a) Density.

(b) Velocity.

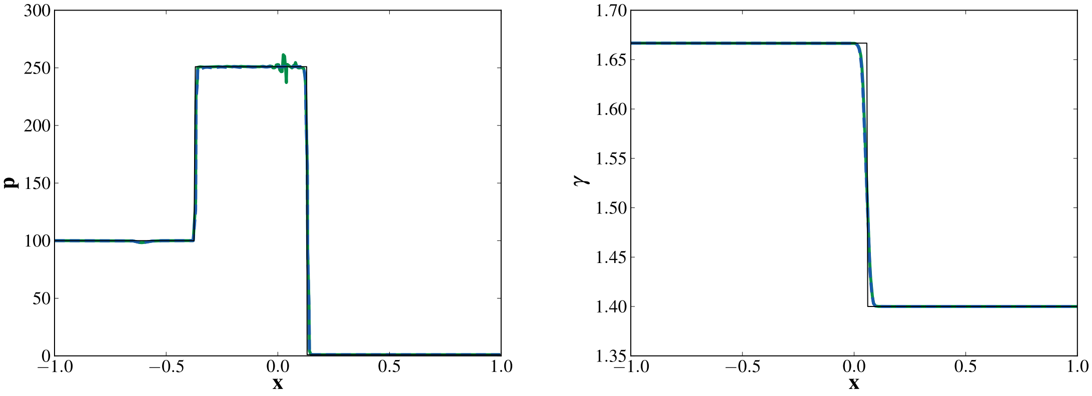

(c) Pressure.

(d) Ratio of specific heats.

Figure 2.9: Profiles at $t = 0.04$ for the strong shock-interface interaction ($P = 2$, $\Delta x = 1/128$) using the non-conservative equation for $1/(\gamma - 1)$. Solid green: limiting of the conserved variables (approach B). Dashed blue: modified limiting (our approach C). Solid black: exact solution.

growth through baroclinic vorticity deposition. The initial perturbation amplitude and wavelength are $A_0 = 0.183$ cm and $\lambda_0 = 5.933$ cm. The diffuse interface is initialized in a thermodynamically consistent fashion using an exponential diffusion function [120], with a diffusion length of 0.5 cm. We impose periodic boundaries on the sides and zero-gradient conditions at the entrance and exit of the shock tube. The gases have an initial upward velocity such that the interface remains in the domain after the shock interaction.

With the fully conservative approach A, pressure oscillations are produced and lead to negative densities early in time, causing the simulations to fail just after the shock interaction (Fig. 2.10). Even with approach B, pressure errors at the interface are significant.

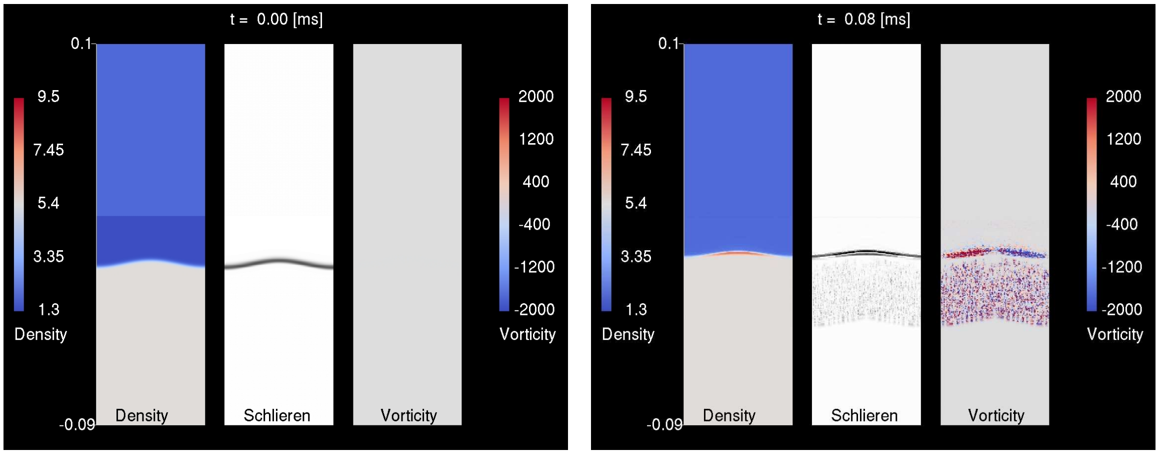

(a) $t = 0$ms. (b) $t = 0.08$ms.

Figure 2.10: Density, simulated Schlieren, and vorticity ($|\nabla \times \mathbf{u}|$) for the single-mode RM instability ($P = 2$, 128 cells per wavelength). Conservative transport equation and limiting of the conserved variables (fully conservative approach A).

These errors in pressure modify the velocity field, and therefore the vorticity, to eventually distort the interface morphology (Fig. 2.11). Furthermore, these initially small errors lead to a loss in symmetry at late times, as explained in [72].

These oscillations are avoided when using our approach C as evidenced by comparing the vorticity contours of Fig. 2.12 to those of Fig. 2.11. The early-time growth of the instability (before reshock) from the simulation agrees well with the experimental data, as shown through convergence of the perturbation amplitude in the integral sense on a sequence of grids (Fig. 2.13). With our approach, we can accurately simulate the physics of such problems, unlike certain prior studies that had to assume gases of constant γ [120].

2.6.4 Interaction of a shock in water with a gas bubble

We consider a shock initiated in water impinging upon a cylindrical (two-dimensional) air bubble to assess our approach for more complicated equations of state, and for high pressures and large density ratios. An air bubble of radius $r_0 = 1$ initially lies at rest in water at atmospheric pressure; surface tension is neglected. A Mach 1.82 shock, corresponding to a pressure ratio of 1.9×10^4, is initialized in the water upstream of the bubble at $x = -2$ [121, 81, 122, 123]. The density, velocity, and pressure, non-dimensionalized by the

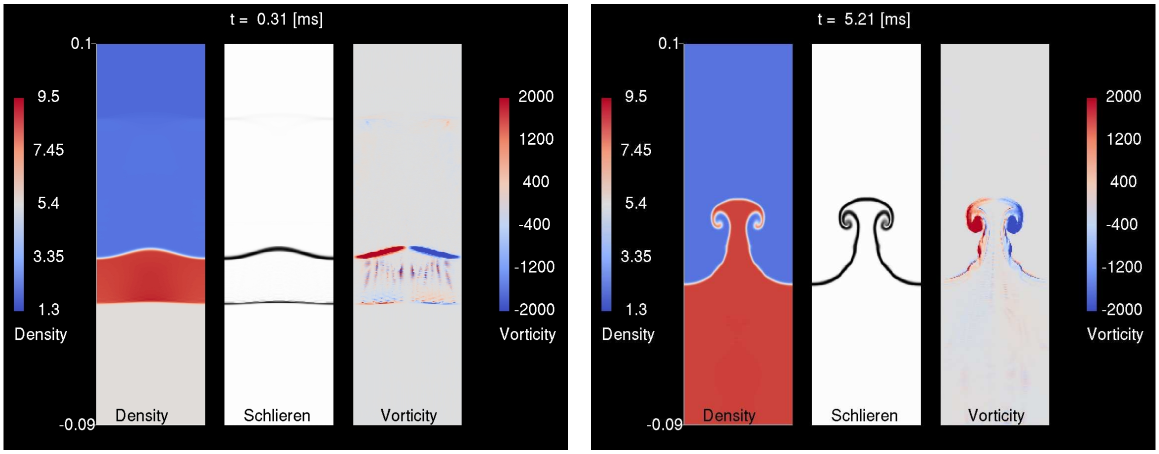

(a) $t = 0.31$ms.

(b) $t = 5.21$ms.

Figure 2.11: Density, simulated Schlieren, and vorticity for the single-mode RM instability ($P = 2$, 128 cells per wavelength) using non-conservative transport equation and limiting of the conserved variables (approach B).

properties of air at atmospheric pressure, in the different parts of the domain are

$$(\rho, u, p) = \begin{cases} (1, 0, 0.71), & \text{in the bubble,} \\ (846.58, 0, 0.71), & \text{in the water upstream of the shock,} \\ (1078.12, 644.28, 1.36 \times 10^5), & \text{in the water downstream of the shock.} \end{cases} \tag{2.55}$$

For air, $\gamma = 1.4$ and $B = 0$ bars. The values of these properties for water for the stiffened equation of state are determined through empirical fits [124, 125]: $\gamma = 5.5$ and $B = 4921.15$ bars [126].

Fig. 2.14 shows a sequence of simulated Schlieren contours for this problem using our approach C. Simulated Schlieren contours are a function of the density gradient norm and were generated by post-processing the density field with the following formula:

$$\Phi(x, y) = \exp\left(-k \frac{|\nabla \rho|}{\max_{x,y} |\nabla \rho|}\right)$$

where k is an positive constant chosen to visualize the density gradients. As in past simulations a re-entrant jet forms and impacts the opposite side of the bubble, thereby generating a strong shock moving radially outward. When limiting the conserved variables (approaches

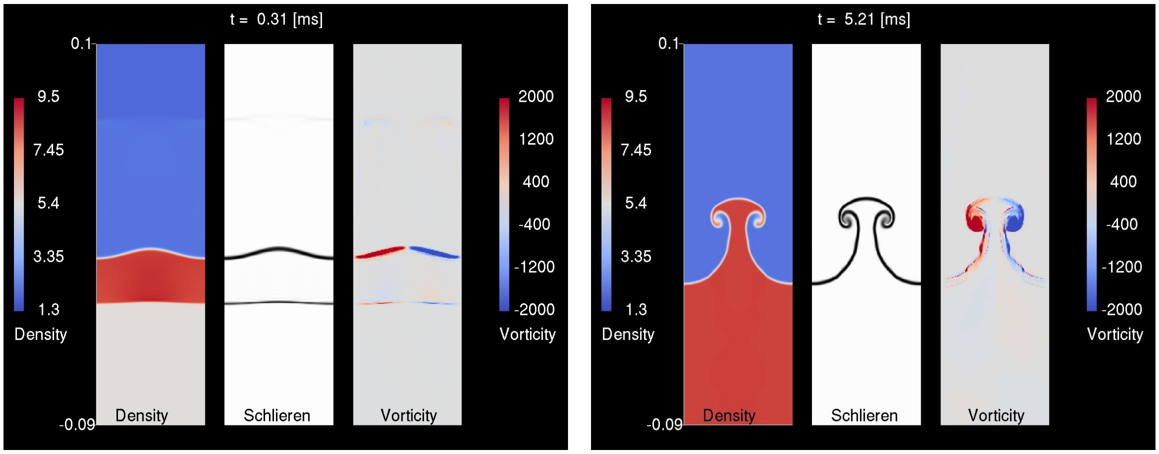

(a) $t = 0.31$ms.

(b) $t = 5.21$ms.

Figure 2.12: Density, simulated Schlieren, and vorticity for the single-mode RM instability using our approach ($P = 2$, 128 cells per wavelength).

A and B), large spurious pressure oscillations are generated, which lead to negative densities as the shock starts to interact with the bubble; thus, the simulations fail. For such large pressure and density ratios, higher resolution (*e.g*, order of accuracy, grid refinement or Riemann solver) may lead to large negative pressures in the numerically diffuse interface regions and thus cause simulations to fail for reasons beyond the scope of this chapter [127, 128, 67, 74]. For this reason, we use the Rusanov flux solver with all three approaches for this problem only.

2.7 Validation study: the supersonic drop

As a validation study, we present numerical simulations of a multiphase problem applicable to many engineering fields, including fuel injection, plasma deposition, raindrops impacting high speed vehicles, and turbomachinery[7, 8]. Simulations of a shock interacting with a drop of water in air are compared to experimental data. We present the flow dynamics and discuss the interactions between a supersonic air flow and a compliant water cylinder.

In this problem, an initial 2D water drop of radius r_0 is stationary in air. A Mach 2.5 shock coming from the left impinges on the drop, Figure 2.15. This setup is similar to past experiments and simulations of a shock interacting with a water column [49, 129]. The

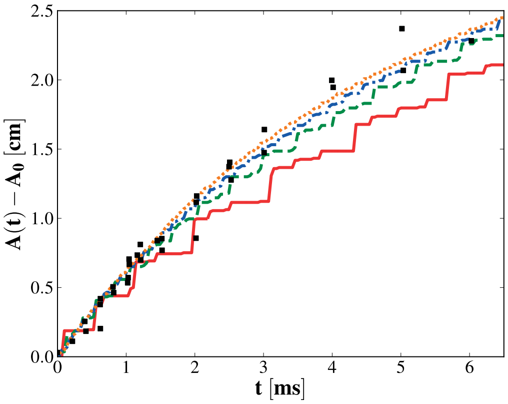

Figure 2.13: Amplitude growth vs. t for the single-mode RM instability using our approach C ($P = 2$). Black square: experimental data [119]. Solid red: 16 cells per wavelength; dashed green: 32; dash-dot blue: 64; dotted orange: 128.

simulation domain size is $23r_0$ in the x-direction and $16r_0$ in the y-direction. The drop is initially located at $(x, y) = (0, 0)$. The mesh is refined around the drop and the grid is stretched from $2r_0$ above and below the centerline to the edge of the domain to allow for high resolution of the drop dynamics while maintaining a reasonable computational runtime. The entire domain contains approximately 5 million degrees of freedom. Each simulation was performed in parallel on eight GPU for approximately 24 hours. The properties of the air are $\rho_{\text{air}} = 1.1765\text{kg}/\text{m}^3$, $\gamma_{\text{air}} = 1.4$, and $p_{\infty,\text{air}} = 0\text{Pa}$. Those for water are $\rho_{\text{water}} = 996\text{kg}/\text{m}^3$, $\gamma_{\text{water}} = 5.5$, and $p_{\infty,\text{water}} = 492115000\text{Pa}$ [126]. All materials are initially at atmospheric pressure. The non-dimensional time is defined as $t = T\frac{u_s}{2r_0}$, where T is the physical time and u_s is the post-shock air velocity. Density is non-dimensionalized by ρ_{air}, velocity by c_{air}, and pressure by $\rho_{\text{air}} c_{\text{air}}^2$, where c_{air} is the speed of sound in air.

As the shock impinges on the drop, it creates a supersonic flow around the drop. The initial shock is deflected by the drop and the reflected shock evolves into a bow shock, Figure 2.16a. Baroclinic vorticity generated at the drop surface by the passage of the shock creates a wake downstream of the drop which forms into a reentrant flow at later times, Figure 2.16b. This flow causes a decrease in the drop width and an increase in the height, Figure 2.16c. The strong coupling between the wave dynamics and the deforming geometry causes a series of compressions which steepen into shocks in the wake of the drop, Figures 2.16c and 2.16d.

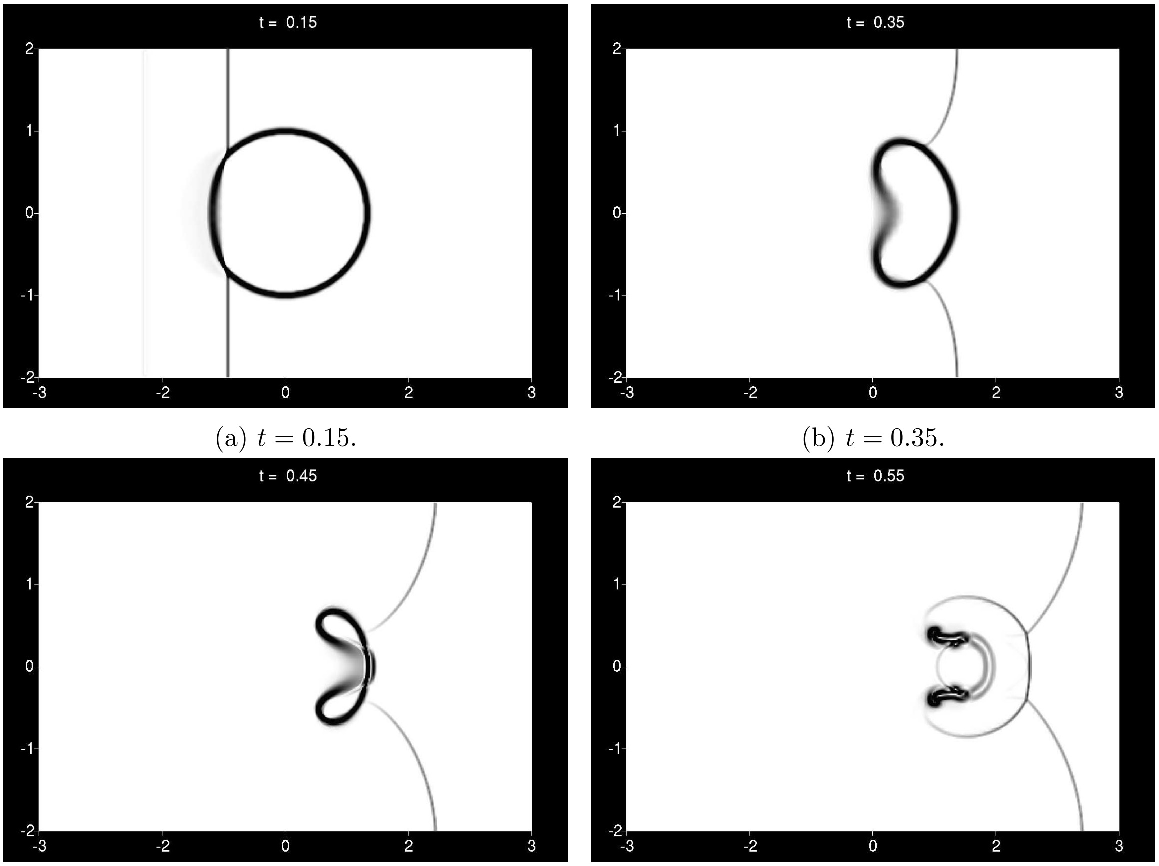

(a) $t = 0.15$.

(b) $t = 0.35$.

(c) $t = 0.45$.

(d) $t = 0.55$.

Figure 2.14: Simulated Schlieren of density for a strong shock impacting a two-dimensional air bubble in water using our approach C ($P = 2$, 128 cells per diameter).

In Figure 2.17, we compare our simulation results to the experiments of the same setup as the experiments of Igra and Takayama [49]. There is good qualitative agreement with the experiments as the shape and wake of the drop in both the simulation and experiment look similar. The dark region upstream of the drop in the experimental pictures is most likely due to the experimental visualization technique which might be capturing evaporation effects or might be distorted by edge effects from the walls holding the water column. Experimental measurements of the drop width are accurately described by the simulation, Figure 2.18. There is very good agreement early in time and this agreement improves as the mesh is refined. Late time discrepancies can be explained by 3D effects and transport phenomena such as evaporation which are not modeled in the simulations.

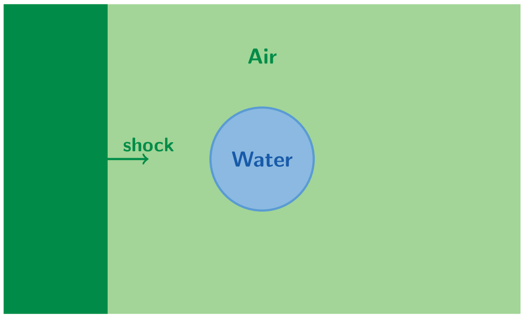

Figure 2.15: Problem setup for a shock impinging on a drop of water in air.

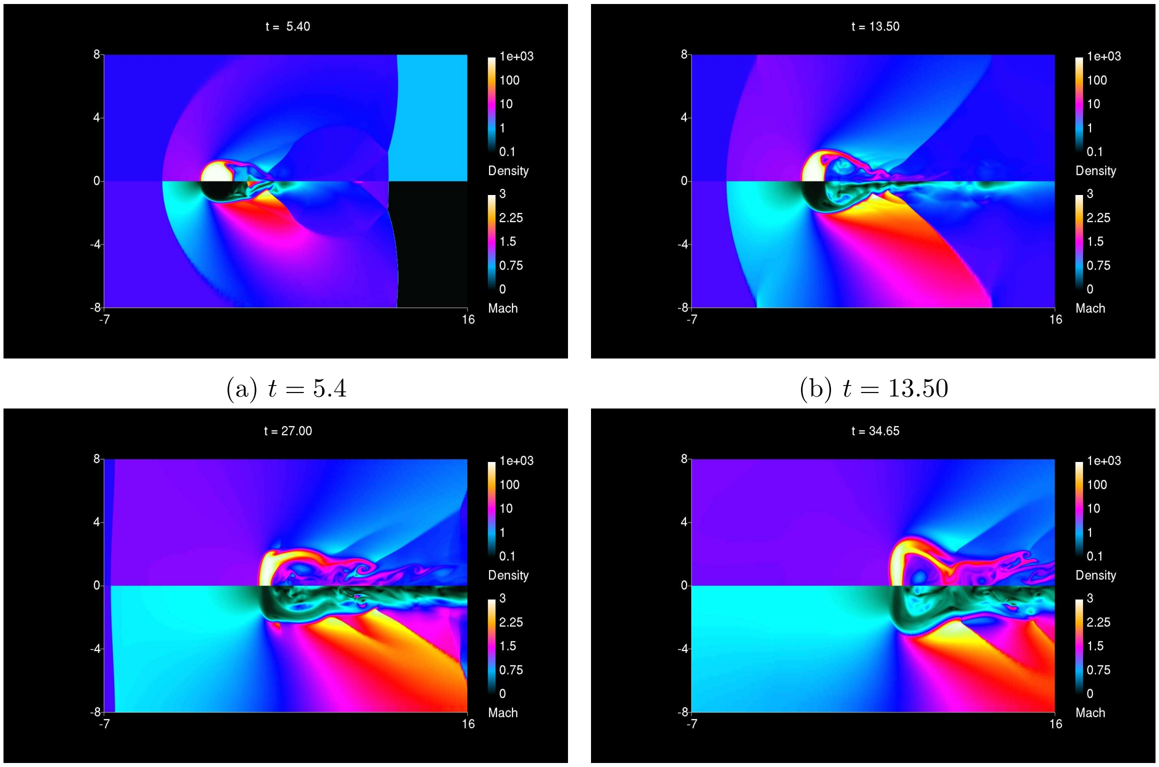

(a) $t = 5.4$

(b) $t = 13.50$

(c) $t = 27.00$

(d) $t = 34.65$

Figure 2.16: Density (top half) and Mach number (bottom half) contours for a 2.5 shock Mach number.

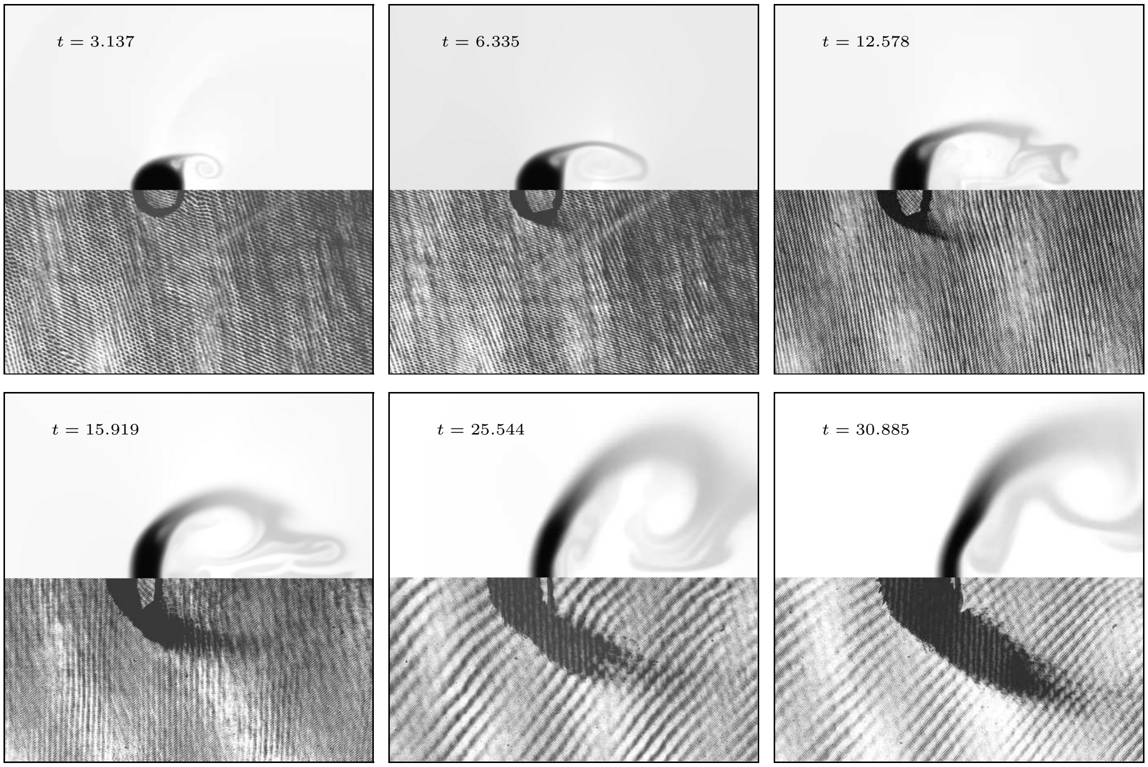

Figure 2.17: Comparison of experimental visualization of the droplet using a holographic interferogram [130, 49] (bottom) and simulated density (top) at a 1.18 Mach number.

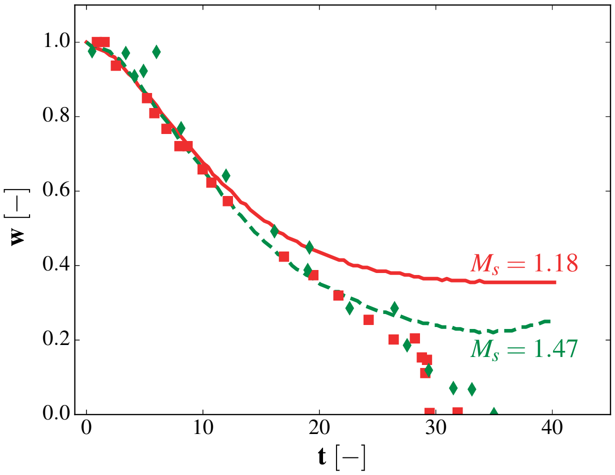

Figure 2.18: Centerline drop width as a function of time. Solid red line: simulation results at $M_s = 1.18$; dashed green line: simulation results at $M_s = 1.47$. Red squares: experimental data at $M_s = 1.18$ [49]; green pentagons: experimental data at $M_s = 1.47$.

2.8 Conclusions

In this chapter, we introduce a solution-adaptive[1] DG method to simulate compressible multiphase flows with shocks and interfaces in a stable and accurate fashion. Following the interface-capturing approach of Abgrall [54], we model flows of multiple fluid components or phases using a single equation of state with varying material properties. To represent compressible phenomena in solids, liquids and gases, we consider the Mie-Grüneisen family of equations of state, which describes a wide range of media, including stiffened and ideal gas equations of state. We show why spurious pressure oscillations occur in the DG framework when material properties vary, and how to remedy this problem. Using stringent test problems in one and two dimensions, we verify our approach. We can make the following conclusions:

- We develop a DG method that is conservative, non-oscillatory at interfaces (and shocks) and high-order accurate in smooth regions.
- Two key steps must be followed to avoid spurious pressure oscillations at interfaces between fluids of different material properties:
    1. Transport equations for appropriate material properties must be solved in a suitable weak form. *E.g*, for ideal gases, a non-conservative equation for $1/(\gamma-1)$ must be solved, as suggested by Abgrall [54] for FV methods.
    2. Solution limiting must be applied to the appropriate variables (density, momentum, pressure, and the appropriate properties in the equation of state) to result in a non-oscillatory, conservative, and high-order accurate procedure. Limiting of the primitive variables does not ensure conservation. Our proposed approach does not require more operations than fully conservative limiting.
- We develop a new characteristic-based discontinuity sensor inspired by the physics for shocks, interfaces, and contacts.

---

[1] In this work, solution adaptivity implies that the limiting procedure is only applied at solution discontinuities. In other work, it might refer to mesh adaptivity to the solution.

- We can handle strong shocks in multi-dimensional settings involving possibly large density ratios for gas/gas, gas/liquid and fluid/solid interfaces in which the media obey an equation of state in the Mie-Grüneisen family.

- Results indicate that the largest errors are produced when solving the transport equation in conservative form and limiting the conserved variables (approach A). This approach fails for relatively simple problems involving gas/gas interfaces. Using a non-conservative transport equation and limiting the conserved variables (approach B) produces non-negligible errors shown to affect interface morphology in gas/gas problems and produce negative pressures in gas/liquid problems.

CHAPTER III

Improvement of the accuracy of Discontinuous Galerkin methods for advection-dominated problems

This chapter presents work on improving the accuracy of the discretization of the advection terms by the Discontinuous Galerkin method. Some of the results in this section have been published in Henry de Frahan, M. T., Khieu, L. & Johnsen, E. 2015 High-order Discontinuous Galerkin Methods Applied to Multiphase Flows. 22^d *AIAA Computational Fluid Dynamics Conference*, doi: 10.2514/6.2015-3045.

3.1 Introduction

The Discontinuous Galerkin (DG) method is a numerical method for partial differential equations, in which the solution is discretized in a computational cell through an expansion in terms of polynomial basis functions. This approach combines advantages of the finite element and the Finite Volume (FV) methods. In addition to being high-order accurate, the DG method is a compact-stencil scheme, so it is highly scalable on parallel architectures, and implementable on unstructured grids. The discontinuity of the solution at the cell interfaces naturally provides a means to introduce dissipation as needed. As with FV methods, physical fluxes between neighboring cells are calculated using Riemann solvers. The DG approach exhibits superconvergence properties for the advection terms, at a rate of $2P+1$, where P is the polynomial order [55, 56]. Cockburn and Shu popularized the Runge-Kutta Discontinuous Galerkin (RKDG) for time-dependent convection-dominated problems [57, 58, 59, 60, 61]. Shocks and discontinuities can accurately be captured using limiters to dampen the oscillations that are caused by high-order interpolation across a discontinuity [58, 62, 63, 64, 65, 66, 131].

Because of the discontinuous representation of the solution at the cell interfaces, the DG method is not naturally amenable to discretizing second order derivatives, which appear, for example, in the diffusion terms of the Navier-Stokes equations. Past approaches to resolve this issue have involved interior penalty methods for elliptic and parabolic equations [132, 133, 134] and rewriting the second order terms as a system of first-order derivatives [135, 136]. However, these approaches are not consistent and require tunable parameters. The Recovery Discontinuous Galerkin (RDG) method was developed to provide a unified and consistent framework for discretizing second order derivatives [137, 138, 139]. This method removes the discontinuity at the interface by recovering the underlying high-order polynomial spanning neighboring cells. This is achieved by matching polynomial moments in cells that share interfaces. The RDG method for a structured quadrilateral mesh is stable, works in multiple dimensions, and can be applied to non-linear diffusion operators. It also exhibits superconvergent properties at a rate greater than $3P$. However, using the RDG method leads to a mismatch in the convergence properties of the advection terms $(2P + 1)$ and the diffusion terms $(> 3P)$. In a system containing both advective and diffusive processes, the numerical discretization of the diffusive terms is more accurate than the discretization commonly used for the advective terms of the partial differential equations. This mismatch in the order of accuracy implies that the convergence of a simulation with advective and diffusive processes will be dominated by the slower advective convergence rate. Improving the order of accuracy of the advection terms' discretization would allow us to converge equally rapidly for both the diffusive and advective processes. This is important when simulating large systems requiring high numerical resolution, such as direct numerical simulations of turbulent processes.

This chapter builds on previous research [140] to fix the order of accuracy mismatch between the advection and diffusion discretizations by increasing the discretization order of accuracy of the advection terms. We propose several new ideas and frameworks to enhance the advection discretization of the DG method.

3.2 Advection equation discretization with the Discontinuous Galerkin method

We consider, without loss of generality, the one-dimensional hyperbolic equation

$$\frac{\partial u}{\partial t}+\frac{\partial F}{\partial x}=0 \tag{3.1}$$

for the conserved variable u, where $F(t,x,u)$ is the flux. In the DG scheme, the solution u is expanded in each cell of the domain Ω_j in terms of $P+1$ basis functions $\phi_n(x)$, $u_j(t,x)\approx u_h(t,x)=\sum_{n=0}^{P}u_j^{(n)}(t)\phi_n(x)$. In the rest of this chapter, we choose $\phi_n(x)$ to be the Legendre polynomial of order P, without loss of generality. The flux at an arbitrary interface $j+1/2$ is evaluated using a Riemann solver, which involves the left and right values of u at that interface, u_L and u_R, which are provided by the polynomial representation of u_j and u_{j+1}. The cells $j-1$, j, and $j+1$ represent the computational stencil of the DG method used to evolve the solution in time. This compact stencil is one of the method's defining properties and we wish to keep the stencil compact when improving the DG method.

To study the stability of our DG enhancement schemes, we analyze the scalar linear advection equation 3.1, where $F(t,x,u)=au$ and $a>0$. The DG update equations are:

$$\frac{\mathrm{d}}{\mathrm{d}t}\int_{\Omega_j}v_ju_j\,\mathrm{d}x=-a\int_{\Omega_j}v_j\frac{\partial u_j}{\partial x}\,\mathrm{d}x,$$

and, using integration by parts,

$$\frac{\mathrm{d}}{\mathrm{d}t}\int_{\Omega_j}v_ju_j\,\mathrm{d}x=-a[v_ju_j]_{x_{j-1/2}}^{x_{j+1/2}}+a\int_{\Omega_j}\frac{\partial v_j}{\partial x}u_j\,\mathrm{d}x, \tag{3.2}$$

where v_j is a test function in Ω_j. By using the solution basis functions as the test functions, expanding $u(t,x)$ on the solution basis, and using an upwind flux (without loss of generality), we rewrite the update equations as a linear system for the solution coefficients:

$$\frac{\Delta x}{a}\frac{\mathrm{d}}{\mathrm{d}t}\mathbf{u}_j=\mathbf{M}(T)\mathbf{u}_j \tag{3.3}$$

where T represents the translation of the solution by one cell: $T\mathbf{u}_j=\mathbf{u}_{j+1}$ and $T^{-1}\mathbf{u}_j=$

$\mathbf{u}_{j-1}$. The Fourier transform of $\mathbf{M}(T)$, $\widehat{\mathbf{M}}(\beta)$, is obtained by substituting T for its transform $e^{i\beta}$. Calculations of the eigenvalues of $\widehat{\mathbf{M}}(\beta)$ and their respective Taylor-series expansions are used to compare with the exact differential operator, $\lambda_e = -i\beta$, and to establish the numerical scheme's stability and order of accuracy.

3.3 Interface-Centered Reconstruction schemes

Systematic approaches to exploring improvements to the DG scheme have previously been presented [140]. This previous work has shown that an improved DG scheme for advection called Interface-Centered Reconstruction with Binary Projection (ICB) exhibits a $3P+1$ order of accuracy and has reasonable stability properties. We recall the scheme here and study its stability properties. This approach relies on increasing the polynomial order of the numerical representations u_j and u_{j+1} to calculate interface approximations $\hat{u}_{j+1/2,L}(x)$ and $\hat{u}_{j+1/2,R}(x)$, from which u_L and u_R are evaluated.

The central idea of the ICB scheme is as follows. The reconstruction of $\hat{u}_{j+1/2,L}(x)$ is biased towards the left, cell j, meaning that the enhanced representation can contain more moments of u_j than u_{j+1},

$$\int_{x_{j-1/2}}^{x_{j+1/2}} \phi_n^j \hat{u}_{j+1/2,L}\,\mathrm{d}x = \int_{x_{j-1/2}}^{x_{j+1/2}} \phi_n^j u_j\,\mathrm{d}x \qquad n = 0,\dots,P \tag{3.4a}$$

$$\int_{x_{j+1/2}}^{x_{j+3/2}} \phi_n^{j+1} \hat{u}_{j+1/2,L}\,\mathrm{d}x = \int_{x_{j+1/2}}^{x_{j+3/2}} \phi_n^{j+1} u_{j+1}\,\mathrm{d}x \qquad n \in \mathcal{N} \tag{3.4b}$$

where $\mathcal{N}$ is a subset of $\{0,\dots,P\}$, the set of indexes of the moments of the original polynomial. A similar set of equations can be derived for $\hat{u}_{j+1/2,R}(x)$, which is then biased towards cell $j+1$. This binary reconstruction scheme achieves a $3P+1$ order of accuracy if $\mathcal{N}$ contains P original moments. This implies that there are $P+1$ subsets $\mathcal{N}$ formed with combinations of the set $\{0,1,\dots,P\}$, leading to $P+1$ reconstructions schemes that exhibit $3P+1$ accuracy. We denote the schemes of this type by ICB#1[#2] where #1 is the original polynomial order P and #2 is the subset $\mathcal{N}$.

For $P=1$, we can construct two enhancement schemes, ICB1[0] and ICB1[0], to enhance the cell interface values. Von Neumann analysis of the resulting schemes show that both

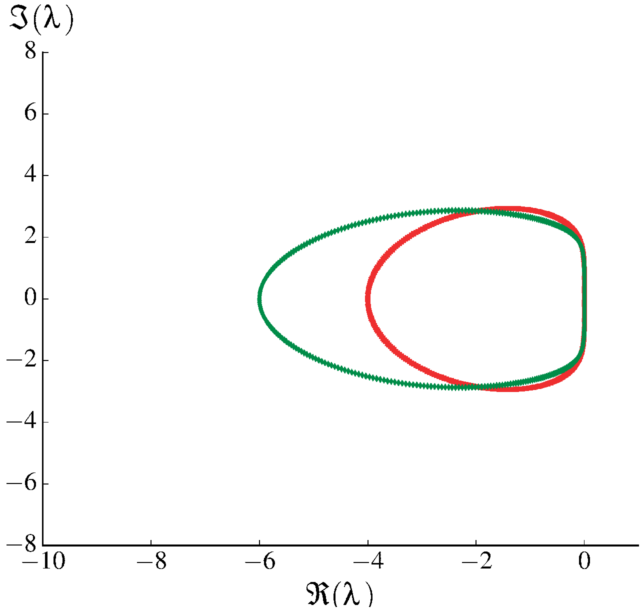

Figure 3.1: Loci of eigenvalues of the enhanced schemes for $P = 1$ in the complex plane. Red squares: ICB1[0]; green diamonds: ICB1[0].

schemes exhibit fourth order accuracy and are stable ($\Re(\lambda_i) \leq 0 \; \forall \; i = 0, \ldots, P$), Figure 3.3.

For $P = 2$, there are three optimal enhancement schemes, ICB2[0, 1], ICB2[1, 2], and ICB2[0, 2]. These schemes lead to seventh order accuracy (as opposed to fifth order accuracy for standard DG). However, as illustrated in Figure 3.2b, the real part of the eigenvalues are positive for some values of β. This incursion into the real positive half of the complex plane can lead to numerical instabilities if the time-marching scheme is inadequate. These incursions are small enough (their maximum value is 0.00073) to be covered by a standard fourth order Runge-Kutta time integration scheme. However, this implies the existence of a lower bound on the CFL number to ensure that the scheme remains stable. For very small CFL numbers, these incursions will eventually lie outside the region of stability of the time-integration scheme.

For $P = 2$, instead of using two moments from neighboring cells to enhance the interface, we can use suboptimal sets using only one moment of the neighboring cell: ICB2[0], ICB2[1], and ICB2[2]. These suboptimal schemes are stable and exhibit sixth order accuracy.

In conclusion, Von Neumann analysis of the ICB enhancement method shows that, for the one-dimensional scalar advection equation and for various suboptimal choices of the set

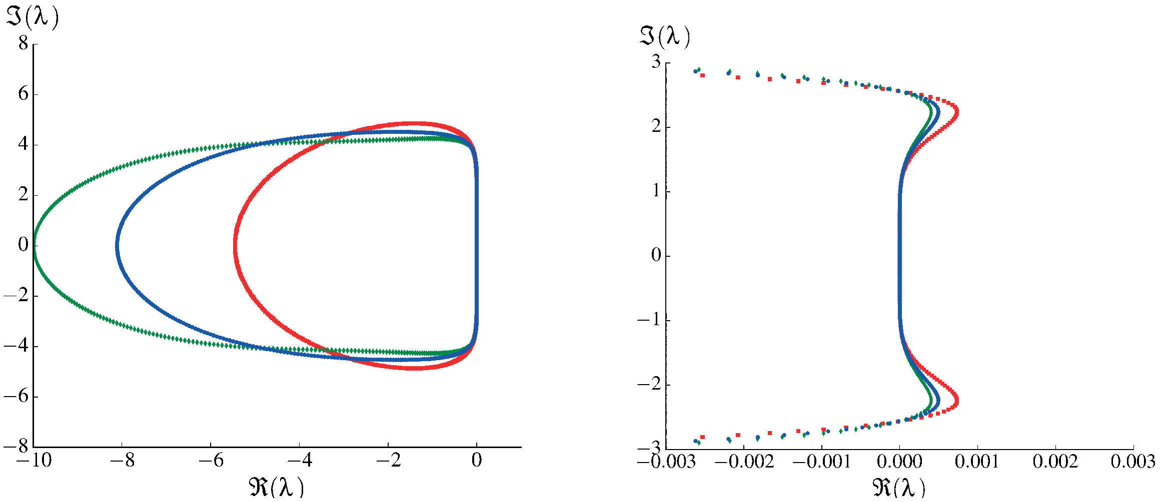

(a) Eigenvalue loci.

(b) Zoom of Figure 3.2a.

Figure 3.2: Loci of eigenvalues of the enhanced schemes for $P = 2$ in the complex plane. Red squares: ICB2[0, 1]; green diamonds: ICB2[1, 2]; blue circles: ICB2[1, 2].

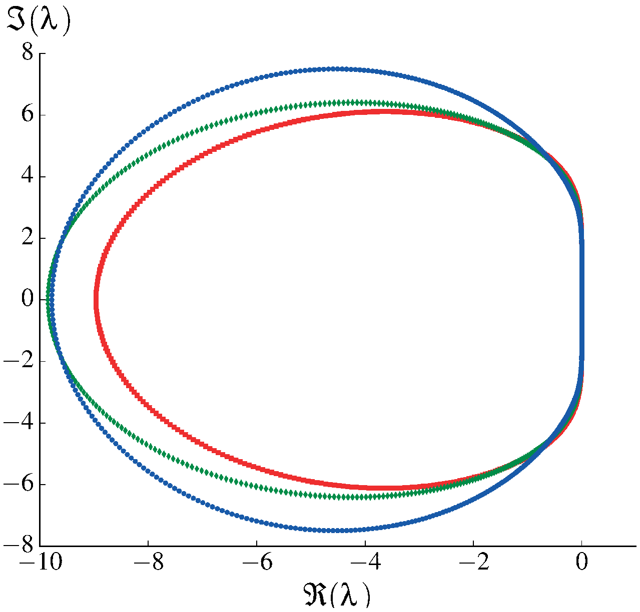

Figure 3.3: Loci of eigenvalues of the enhanced schemes for $P = 2$ in the complex plane. Red squares: ICB2[0]; green diamonds: ICB2[1]; blue circles: ICB2[2].

$\mathcal{N}$, the scheme exhibits improved convergence and is stable. Using one moment from the neighboring cell for the enhancement scheme leads to a stable and $2P + 2$ order of accuracy scheme. Including additional moments in the enhancement scheme leads to a numerical method with increased accuracy but unstable properties. This is most likely due to the fact that, as more neighboring modes are included, the scheme tends to a central scheme, i.e. unstable for advection equations due to the lack of upwinding.

3.4 Interior enhancement schemes

While the ICB schemes focus on enhancing the order of accuracy of the interface fluxes, another approach is to enhance the interior solution accuracy. Replacing u_j by an enhanced solution $\hat{u}_j$ in the interior integral $a \int_{\Omega_j} \frac{\partial v_j}{\partial x} u_j \, \mathrm{d}x$ in Eq. (3.2) may lead to an increase in the method order.

3.4.1 Increasing the number of modes

The simplest way of increasing the order of accuracy of the interior solution is by increasing the polynomial representation while preserving the original solution coefficients:

$$\hat{u}_j = u_j + \sum_{n=P+1}^{N} \hat{u}_j^{(n)} \phi_n(x) \tag{3.5}$$

The new coefficients, $\hat{u}_j^{(n)}$ can be obtained through a variety of ways, including using the ICB schemes or downprojecting the RDG solution.

However, a close analysis of the DG discretization shows that any additional higher order coefficients will not affect the evolution equations for the original coefficients. Orthogonality of the Legendre polynomials and their derivatives implies that

$$\begin{aligned} \int_{\Omega_j} \frac{\partial \phi_i}{\partial x} \hat{u}_j \, \mathrm{d}x &= \int_{\Omega_j} \frac{\partial \phi_i}{\partial x} \left(\sum_{n=0}^{P} u_j^{(n)} \phi_n(x) + \sum_{n=P+1}^{N} \hat{u}_j^{(n)} \phi_n(x) \right) \mathrm{d}x \\ &= 0 \qquad \forall i < n \end{aligned}$$

Therefore, all the additional entries for the original coefficients ($i = 0, \ldots, P$) are zero when integrated against higher order coefficients ($n \geq P+1$). Hence, any increase in the interior solution accuracy by increasing the solution basis space and preserving the original coefficients will not result in a different DG discretization scheme. The only way to do so is to change the original coefficients.

3.4.2 Enhancing the original coefficients of the interior solution basis

As discussed previously, we can envision replacing the original coefficients of the solution by more accurate coefficients,

$$\hat{u}_j = \sum_{n=0}^{P} \hat{u}_j^{(n)} \phi_n(x),$$

where $\hat{u}_j^{(n)}$ are different than the original solution coefficients $u_j^{(n)}$. We propose two ways for determining these new coefficients.

The first involves constraining the new coefficients by (i) preserving the cell average to maintain a conservative scheme and (ii) fitting the new polynomial to the enhanced cell interface values, leading to the following system of equations:

$$\begin{aligned} &\hat{u}_j^{(0)} = u_j^{(0)} \\ &\sum_{n=0}^{P} \hat{u}_j^{(n)} \phi_n(x_{j+1/2}) = \hat{u}_{j+1/2,L} \\ &\sum_{n=0}^{P} \hat{u}_j^{(n)} \phi_n(x_{j-1/2}) = \hat{u}_{j-1/2,R} \end{aligned}$$

where $\hat{u}_{j+1/2,L}$ and $\hat{u}_{j-1/2,R}$ could be obtained through the ICB schemes. Unfortunately, this method, tested for $P=2$ and various edge enhancement schemes, is unstable. This is most likely because the resulting approximation relies on using information from the left and right neighbors in a central fashion, thereby losing the upwinding property.

A second way of determining the new coefficients is through least-squares matching of the solution in neighboring cells,

$$
\begin{aligned}
\int_{x_{j-1/2}}^{x_{j+1/2}} \phi_i \hat{u}_j \,\mathrm{d}x &= \int_{x_{j-1/2}}^{x_{j+1/2}} \phi_i(x) u_j \,\mathrm{d}x \\
\int_{x_{j+1/2}}^{x_{j+3/2}} \phi_i^{j+1} \hat{u}_j \,\mathrm{d}x &= \int_{x_{j+1/2}}^{x_{j+3/2}} \phi_i^{j+1} u_{j+1} \,\mathrm{d}x \\
\int_{x_{j-3/2}}^{x_{j-1/2}} \phi_i^{j-1} \hat{u}_j \,\mathrm{d}x &= \int_{x_{j-3/2}}^{x_{j-1/2}} \phi_i^{j-1} u_{j-1} \,\mathrm{d}x.
\end{aligned}
$$

Though this provides new coefficients for the interior solution, this technique, tested for $P = 1, 2$, leads to a reduced order of accuracy method which is unstable even if paired with ICB at the interfaces. Solely increasing the interior solution accuracy does not seem to be a promising avenue for enhancing the DG advection discretization accuracy.

3.4.3 Simultaneous enhancement of the interior and interface solution

In this section, we explore a cell-centered enhancement approach of both the interior and interface solution. A variation of this scheme was first proposed in [140]. We generalize this scheme here and explore some of the resulting properties. The key idea of the scheme is to enhance the interior solution by matching modes on either side of the cell of interest. For cell j, we therefore solve the following system of equations:

$$
\begin{aligned}
\int_{x_{j-1/2}}^{x_{j+1/2}} \phi_i \hat{u}_j \,\mathrm{d}x &= \int_{x_{j-1/2}}^{x_{j+1/2}} \phi_i(x) u_j \,\mathrm{d}x \qquad && i = 0, \dots, P \\
\int_{x_{j-3/2}}^{x_{j-1/2}} \phi_m^{j-1} \hat{u}_j \,\mathrm{d}x &= \int_{x_{j-3/2}}^{x_{j-1/2}} \phi_m^{j-1} u_{j-1} \,\mathrm{d}x \qquad && m \in \mathcal{M} \\
\int_{x_{j+1/2}}^{x_{j+3/2}} \phi_n^{j+1} \hat{u}_j \,\mathrm{d}x &= \int_{x_{j+1/2}}^{x_{j+3/2}} \phi_n^{j+1} u_{j+1} \,\mathrm{d}x \qquad && n \in \mathcal{N}
\end{aligned}
$$

where $\mathcal{M}$ and $\mathcal{N}$ are subsets of $\{0 \dots P\}$. An important difference with previous schemes is that $\mathcal{M}$ and $\mathcal{N}$ can be completely different. Though similar to `ccp` schemes of Khieu and Johnsen [140] and $P_n P_M$ methods, this framework generates a large family of enhanced polynomials. The enhanced solution therefore belongs to $\mathcal{P}(P + |\mathcal{M}| + |\mathcal{N}|)$, were $|.|$ is the number of elements in a set.

Von Neumann analysis shows that the order of accuracy of the method is stable if

$|\mathcal{M}| = |\mathcal{N}| \leq P+1$. Though this method shows increased accuracy while preserving stability, it exhibits an increased stencil because it is based on a cell-centered reconstruction, i.e. $\hat{u}_{j+1/2,L} = f(u_{j-1}, u_j, u_{j+1})$.

3.5 Interface enhancement schemes

For the rest of this chapter, we return to discussing cell interface enhancement schemes.

3.5.1 Upwinding ICB schemes

One reason we believe ICB schemes become unstable when using too much information from neighboring cells is that the scheme becomes too close to a central scheme and loses the upwinding property. One way of restoring the upwinding property is by evaluating the flux at the right edge of the cell using the ICB polynomial enhanced by the neighboring left cell. Instead of enhancing the cell interface value using downwind information, the solution is enhanced using upwinding. Instead of the ICB reconstruction procedure Eq. (3.4), we propose

$$\int_{x_{j-1/2}}^{x_{j+1/2}} \phi_n^j \hat{u}_{j+1/2,L}\,\mathrm{d}x = \int_{x_{j-1/2}}^{x_{j+1/2}} \phi_n^j u_j\,\mathrm{d}x \qquad n = 0,\ldots,P \tag{3.6a}$$

$$\int_{x_{j-1/2}}^{x_{j-3/2}} \phi_n^{j-1} \hat{u}_{j+1/2,L}\,\mathrm{d}x = \int_{x_{j-1/2}}^{x_{j-3/2}} \phi_n^{j-1} u_{j-1}\,\mathrm{d}x \qquad n \in \mathcal{N} \tag{3.6b}$$

This idea can be expanded to more complex situations where linear combinations of left and right cell enhancement can be chosen according to wave propagation directions. Unfortunately, this method does not lead to a stable and high-order accurate method.

3.5.2 Linear combination of different ICB schemes

While the previous section explored the idea of linear combinations of differing neighbor ICB enhanced polynomials in order to restore the upwinding property, another strategy involves combining ICB schemes with different neighboring modes. Enhancing the cell interface value becomes

$$\hat{u}_{j+1/2,L} = \sum_{k=0}^{P} \omega_k \hat{u}^k_{j+1/2,L}$$

where $\hat{u}^k_{j+1/2,L}$ is given by ICB$P[k]$ and the weights ω_k satisfy $\sum_{n=0}^{P} = 1$. For $P = 1$, this implies a linear combination of ICB1[0] and ICB1[1]. An equal weighting of the ICB schemes, *i.e.* $\omega_k = \frac{1}{P+1}\ \forall k$, leads to a stable, $2P+2$ scheme. Though this scheme is an improvement on the traditional DG method, it is comparable to the previous ICB schemes. An optimal set of weights leading to a $3P+1$ scheme may exist and may be calculated using optimization tools though it is not clear that this problem is well-posed.

3.5.3 Hierarchical ICB schemes

We previously discussed how the ICB schemes are stable with an order of accuracy of $2P+2$ when using one mode from the neighboring cell. Building on this observation, we propose hierarchically enhancing the cell interface value through stable ICB schemes through the following algorithm:

```
For $i = 0, \ldots, P$
    - Set $n = P + 1 + i$
    - Determine $\hat{u}_j^{(n)}$ using ICB$P + i[k_i]$
```

where the values k_i are chosen from the set $\{0, \ldots, P\}$. For $P = 2$, the algorithm for evaluating $\hat{u}^k_{j+1/2,L}$ can be illustrated by the following:

- Step 1: Starting with the original solution coefficients $\{u_j^{(0)}, u_j^{(1)}, u_j^{(2)}\}$ and using ICB2$[k]$, we can determine three values for the new coefficient $\hat{u}_j^{(3)}$:
    - for $k = 0$, $\hat{u}_j^{(3)} = -\frac{u_j^{(0)}}{22} - \frac{u_j^{(1)}}{11} - \frac{3u_j^{(2)}}{11} + \frac{u_{j+1}^{(0)}}{22}$
    - for $k = 1$, $\hat{u}_j^{(3)} = -\frac{u_j^{(1)}}{30} - \frac{u_j^{(2)}}{5} + \frac{u_{j+1}^{(1)}}{30}$
    - for $k = 2$, $\hat{u}_j^{(3)} = -\frac{u_j^{(2)}}{10} + \frac{u_{j+1}^{(2)}}{10}$
- Step 2: Perform ICB3$[k]$ on $\{u_j^{(0)}, u_j^{(1)}, u_j^{(2)}, \hat{u}_j^{(3)}\}$, where $\hat{u}_j^{(3)}$ is defined by one of the expressions in step 1 or by the equivalent ICB expression using the left cell $(j-1)$:

- for $k = 0$, $\hat{u}_j^{(4)} = -\frac{u_j^{(0)}}{90} - \frac{u_j^{(1)}}{45} - \frac{u_j^{(2)}}{15} - \frac{11\hat{u}_j^{(3)}}{45} + \frac{u_{j+1}^{(0)}}{90}$
- for $k = 1$, $\hat{u}_j^{(4)} = -\frac{u_j^{(1)}}{146} - \frac{3u_j^{(2)}}{73} - \frac{15\hat{u}_j^{(3)}}{73} + \frac{u_{j+1}^{(1)}}{146}$
- for $k = 2$, $\hat{u}_j^{(4)} = -\frac{u_j^{(2)}}{70} - \frac{\hat{u}_j^{(3)}}{7} + \frac{u_{j+1}^{(2)}}{70}$
- for $k = 3$, $\hat{u}_j^{(4)} = -\frac{\hat{u}_j^{(3)}}{14} + \frac{\hat{u}_{j+1}^{(3)}}{14}$

It should be noted that none of these approximations, except the last one, requires information from non-nearest neighbor cells. The stencil remains compact.

We performed Von Neumann analysis for various polynomial orders and different combinations of enhancement schemes. For example, for $P = 2$, we can construct an enhanced $P = 4$ polynomial by hierarchically using ICB3$[k_1]$ for $\hat{u}_j^{(4)}$ and an average of ICB2$[k_0]$ from the left cell and ICB2$[k_0]$ from the right cell for $\hat{u}_j^{(3)}$. This family of schemes, for all $k_1 \in \{0, 1, 2\}$ and $k_1 \in \{0, 1, 2\}$ are stable and seventh order $(3P + 1)$. We have therefore identified a family of enhancement schemes which are $3P + 1$ order accurate for the linear advection equation and stable. This is not a strictly compact scheme as the enhancement procedure for an interface requires information from both the left and right cell. However, each step in the algorithm has a compact stencil. This family of schemes when $k_1 = k_0$ is equivalent to the family of schemes proposed in Section 3.4.3 with $\mathcal{M} = \mathcal{N} = \{k_1 = k_0\}$.

3.6 General problem formulation and properties

Though not of immediate practical use, a general formulation of the enhancement problem can be stated and the properties of the problem can be explored. In this section, we formulate the enhancement problem using linear algebra.

The DG evolution matrix $\mathbf{M}(T)$ in Eq. (3.3) can be written for the conventional DG method as, using Legendre basis functions:

$$\mathbf{M} = \mathbf{D}^{-1} \left(- \left(\mathbf{G_1} - \mathbf{G_0} \right) + \mathbf{F} \right)$$

where $\mathbf{D}^{-1} = \left[(2i + 1)\delta_{i,j}\right]_{\substack{i=0,\dots,P \\ j=0,\dots,P}}$ is the inverse mass matrix, $\mathbf{G_1} = [1]_{\substack{i=0,\dots,P \\ j=0,\dots,P}}$ is the interface flux matrix at the right cell edge, $\mathbf{G_0} = T^{-1} \left[(-1)^i \delta_{i,j}\right]_{\substack{i=0,\dots,P \\ j=0,\dots,P}} \mathbf{G_1}$ is the interface flux matrix at the left cell edge, and $\mathbf{F} = \left[2\sum_{k=0}^{P} \delta_{i-k-1,j+1}\right]_{\substack{i=0,\ldots,P\\ j=0,\ldots,P}}$ is the interior flux matrix. Here, $\delta_{i,j}$ is the Kronecker delta and we use i for the row index and j for the column index.

Interface-centered enhancing strategies can be incorporated in this framework by defining $\mathbf{G_e}$, an unknown flux enhancement matrix. This enhancement interface flux matrix can be written as $\mathbf{G_e} = \mathbf{A} + T\mathbf{C}$, where $\mathbf{A}$ determines which modes are used from the cell and $\mathbf{B}$ determines the modes used from the neighboring cell. The rows of $\mathbf{G}$ should be identical because the interface value is the same regardless of the coefficient being updated, *i.e.* $u_{j+1/2}$ does not depend on the coefficient $u_j^{(i)}$ being considered. We can therefore write

$$\begin{aligned}
\mathbf{G} &= \mathbf{G_1} + \mathbf{G_e}\\
&= [1]_{\substack{i=0,\ldots,P\\ j=0,\ldots,P}} + \begin{bmatrix}1\\ \vdots\\ 1\end{bmatrix}\begin{bmatrix}\alpha_0 & \ldots & \alpha_P\end{bmatrix} + T\begin{bmatrix}1\\ \vdots\\ 1\end{bmatrix}\begin{bmatrix}\gamma_0 & \ldots & \gamma_P\end{bmatrix}
\end{aligned}$$

where α_i and γ_i are the unknowns that determine the enhancement scheme. Substituting $\mathbf{G_1}$ by $\mathbf{G} = \mathbf{G_1} + \mathbf{G_e}$ in Eq. (3.7) leads to the following enhanced DG evolution matrix:

$$\mathbf{M_e} = \mathbf{D}^{-1}\left(\mathbf{u}\mathbf{v}^{\mathbf{T}} + \mathbf{F}\right) \tag{3.7}$$

where $\mathbf{u} = \left[(-1)^i T - (P+1)\right]_{i=0,\ldots,P}$ and $\mathbf{v} = \left[1 + \alpha_i + T\gamma_i\right]_{i=0,\ldots,P}$ are column vectors. The objective for enhancement is to determine α_i and γ_i ($i = 0, \ldots, P$) such that

1. the eigenvalues of $\widehat{\mathbf{M}}_{\mathbf{e}}(\beta)$, λ_i, have negative real parts, *i.e.* $\mathcal{R}(\lambda_i) < 0$;
2. one these eigenvalues has a Taylor series expansion around $\beta = 0$ equal to $-i\beta + K(i\beta)^{3P+1}$;

where $\widehat{\mathbf{M}}_{\mathbf{e}}(\beta) = \mathbf{M_e}(e^{i\beta})$ and K is an arbitrary constant.

Several interesting eigenvalue properties can be explored using this framework. The rank of a matrix which can be written as $\mathbf{u}\mathbf{v}^{\mathbf{T}}$, where $\mathbf{u}$ and $\mathbf{v}$ are non-zero column vectors with n entries, is equal to one. The rank nullity theorem then implies that the nullity of the matrix is equal to $n-1$, i.e. $\text{rank}(\mathbf{A}) + \text{nullity}(\mathbf{A}) = n$, where $\text{nullity}(\mathbf{A}) = \dim(\ker(\mathbf{A}))$. The $\ker(\mathbf{A})$ is the eigenspace of the matrix for the zero eigenvalue. Therefore, zero is an eigenvalue of the matrix with multiplicity $n-1$. We also know that the trace of the matrix is equal to the sum of the eigenvalues and equal to the product of $\mathbf{u}$ and $\mathbf{v}$:

$$\mathrm{tr}(\mathbf{A}) = \sum_{i=0}^{n} \lambda_i = \mathbf{v}^{\mathbf{T}}\mathbf{u}. \tag{3.8}$$

Hence, the only non zero eigenvalue of the interface flux matrix is

$$\lambda = \mathbf{v}^{\mathbf{T}}\mathbf{u} = \sum_{i=0}^{P} \big((-1)^i T - (P+1)\big)\left(1 + \alpha_i + T\gamma_i\right) \tag{3.9}$$

It can also be shown that the only eigenvalue of $\mathbf{F}$ is zero with multiplicity $P+1$.[1] Unfortunately, while these properties are interesting, it is difficult to infer much about the properties of the eigenvalues of the sum of these matrices $(\mathbf{u}\mathbf{v}^{\mathbf{T}} + \mathbf{F})$. However, this general formulation of the enhancement problem may be of use in future work.

3.7 Conclusions

In this chapter, we explored several new ways of enhancing the DG method's discretization of the advection equation. While the original DG method is $2P+1$ order accurate, Recovery DG, recently proposed to discretize the diffusion equation, is greater than $3P$ accurate. Our objective is to fix the order of accuracy mismatch for advection-diffusion simulations by increasing the advection discretization order of accuracy while maintaining a compact stencil. Building on previous work, we proposed several new families of enhancement schemes, the most promising of which is the hierarchical ICB family which is $3P+1$ and stable. However, this leads to numerical schemes that are not strictly compact, though each step in the hierarchical enhancement process has a compact stencil.

Future work along this direction to explore enhancement schemes for discretizing the advection equation with the DG method should be performed. In Section 3.5.2, we proposed a linear combination of ICB schemes with weights ω_k. An optimization problem can be

---

[1] The proof is sketched as follows:

1. $\mathbf{F}$ is a strictly lower triangular matrix.
2. Strictly lower triangular matrices are nilpotent, i.e. $\mathbf{N}$ is nilpotent if $\mathbf{N}^k = 0$ for $k > 0$ integer.
3. The eigenvalues of nilpotent matrices are zero.

formulated and, possibly, solved to determine the appropriate weights, under the constraint that the scheme is stable (eigenvalues in the negative real part of the complex plain), while maximizing the order of accuracy. Another potential solution strategy could be to explore different polynomial bases for enhancing the solution. Finally, exploring enhancement in combination with limiting procedures, such as hierarchical limiting presenting in Chapter II, could lead to a new limiter that does not reduce the order of accuracy to $P+1$.

Part II

Shocks, waves, and blasts at interfaces

CHAPTER IV

Numerical simulations of a shock interacting with successive interfaces using the Discontinuous Galerkin method

This chapter is adapted from Henry de Frahan, M. T., Movahed, P. & Johnsen, E. 2015 Numerical simulations of a shock interacting with successive interfaces using the Discontinuous Galerkin method: the multilayered Richtmyer–Meshkov and Rayleigh–Taylor instabilities. *Shock Waves*, **25 (4)**, 329–345.

4.1 Abstract

In this work, we investigate the growth of interface perturbations following the interaction of a shock wave with successive layers of fluids. Using the Discontinuous Galerkin (DG) method, we solve the two-dimensional multifluid Euler equations. In our setup, a shock impacts up to four adjacent fluids with perturbed interfaces, Figure 6.2. At each interface, the incoming shock generates reflected and transmitted shocks and rarefactions, which further interact with the interfaces. By monitoring perturbation growth, we characterize the influence these instabilities have on each other and the fluid mixing as a function of time in different configurations. If the third gas is lighter than the second, the reflected rarefaction at the second interface amplifies the growth at the first interface. If the third gas is heavier, the reflected shock decreases the growth and tends to reverse the Richtmyer-Meshkov (RM) instability as the thickness of the second gas is increased. We further investigate the effect of the reflected waves on the dynamics of the small scales and show how a phase difference between the perturbations or an additional fluid layer can enhance growth. This study supports the idea that shocks and rarefactions can be used to control the instability growth.

4.2 Introduction

Hydrodynamic instabilities play important roles in high-energy-density physics (HEDP) problems [20], such as in Inertial Confinement Fusion (ICF) [17] and supernova collapse [29]. The RM instability (RM instability) occurs in flows where a shock interacts with a perturbed interface between two fluids of different densities. At interfaces, the incoming shock deposits baroclinic vorticity that drives the perturbation growth [32]. ICF capsules and supernovae both consist of concentric layers of different materials in a spherical geometry. As a result of high-energy lasers or star collapse, shocks are generated and interact with these multiple layers. The interfaces, already unstable to the shock interaction, further experience accelerations due to the converging geometry [141]. As a result, situations in which a heavy material is accelerated into a light material are also Rayleigh-Taylor (RT) [38] unstable. These hydrodynamic instabilities govern the subsequent hydrodynamics of the ICF capsule and the supernovae. In ICF capsules, mixing between the outer ablator

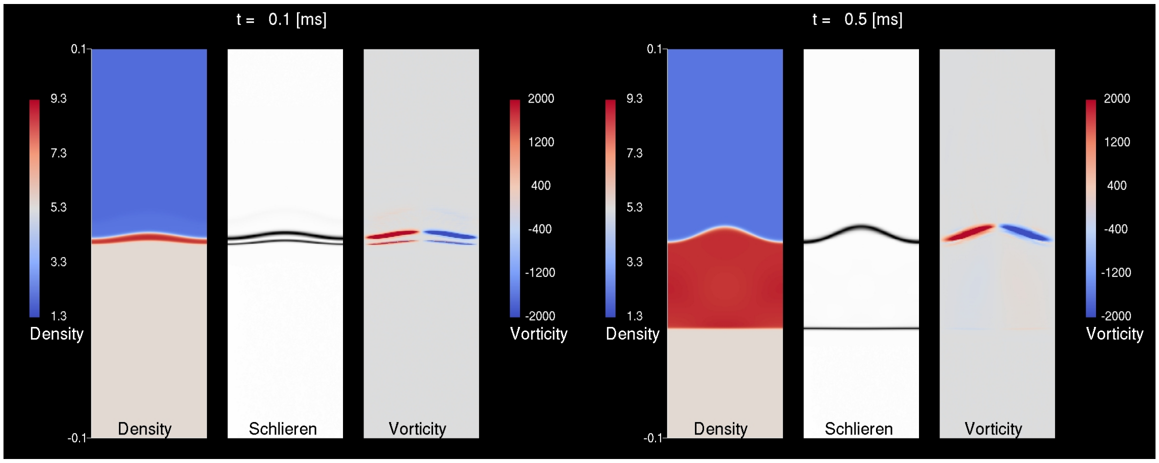

(a) $t = 0.1$ms. (b) $t = 0.5$ms.

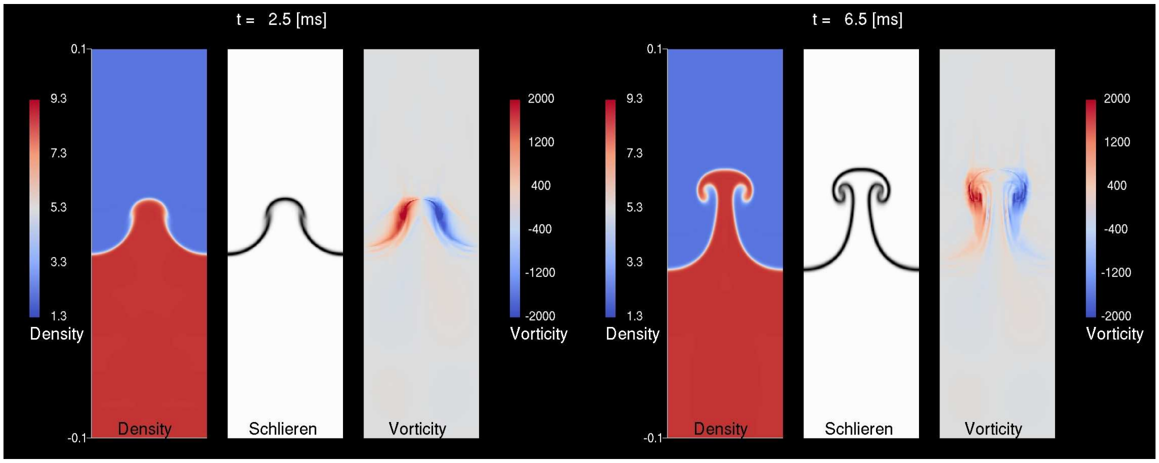

(c) $t = 2.5$ms. (d) $t = 6.5$ms.

Figure 4.1: Density (left), density gradient (numerical Schlieren, middle), and vorticity fields (right) for the single-interface RM instability. Shock wave moving downwards. Air (top) – SF_6 (bottom).

shell and the inner fuel is one of the dominant limitations preventing fusion burn [19].

The canonical RM instability, consisting of a single planar shock wave interacting with a single planar interface separating two fluids, has been studied extensively in the past, both experimentally [142, 143, 119, 144] and numerically [145, 120, 146, 147, 72]. While some of these studies have considered late-time mixing, most have focused on the early time dynamics. Furthermore, little attention has been given to shocks interacting with multiple interfaces, a set-up relevant to ICF and supernova explosion. Most of the research involving multiple layers focused on gas curtains, as in [148, 149, 150], which consider a thin layer of fluid within another fluid.

Systematic studies involving shocks interacting with three or more different fluids have yet to be performed. Following the interaction of a wave with an interface, a reflected and a transmitted wave are produced. Depending on the acoustic impedance of each fluid and the incoming wave, the waves resulting from this interaction may be compressions or rarefactions. For systems with many layers, many such interactions occur, and whether the growth of a given perturbed interface is enhanced or inhibited depends on the direction of the baroclinic vorticity deposited by all the waves. Thus, although perturbations are expected to grow due to the RM instability of the incoming shock, this growth may be inhibited or enhanced by rarefactions (*i.e.*, transient acceleration fields due to a varying pressure) depending on whether the system is RT-stable. Furthermore, the growth may be enhanced by additional RM instability due to subsequent shock interactions. Eventually, these instabilities contribute to mixing between the layers.

Our objective is to use numerical simulations to investigate the interaction of a shock wave with successive perturbed interfaces, and specifically RM (due to shocks) and RT (due to rarefactions) growth. We are interested in determining whether perturbation growth is enhanced or inhibited due to the fluid properties (acoustic properties of the gases and separation). We consider multiple adjacent ideal gases separated by single-mode perturbed interfaces. We use the high-order accurate DG method to solve the multifluid Euler equations [151, 113]. Using two-dimensional simulations, we analyze the effects of the shocks, rarefactions, and the separation distance on the mixing between the three fluids. The chapter is organized as follows. First, the physical model and numerical model are presented, followed by a validation study. We then investigate the perturbations growth for our baseline problem (a shock interacting with three adjacent gases), and quantify the mixing and small-scales dynamics. We close with a discussion of phase differences between the perturbations and the addition of a fourth fluid layer.

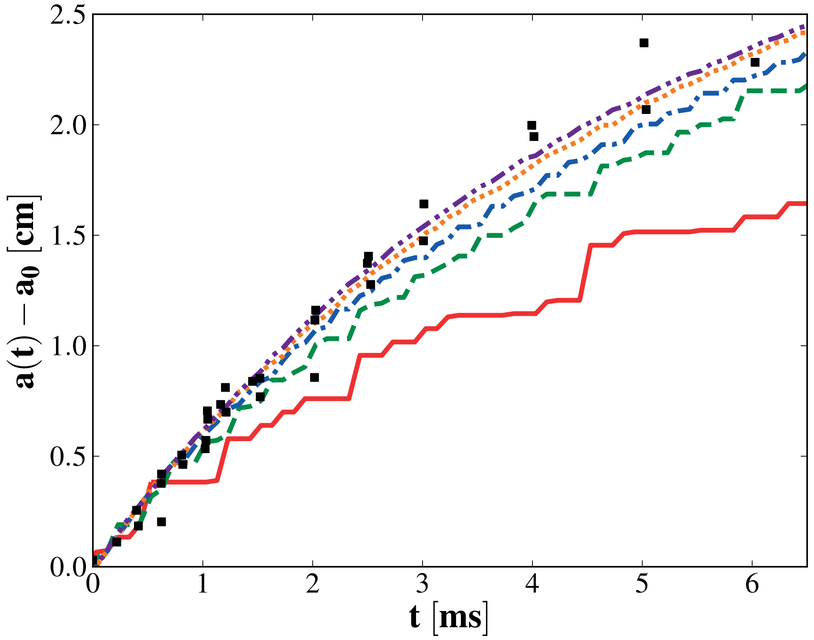

Figure 4.2: Instability growth versus time for the single-interface RM instability. Black squares: experimental data from [119]. Lines: simulation results at 16 (solid red), 32 (dash green), 64 (dash-dot blue), 128 (dot orange), and 256 (dash-dot-dot purple) cells per wavelength.

4.3 Physical model and numerical method

We consider the two-dimensional Euler equations,

$$\frac{\partial \rho}{\partial t} + \frac{\partial}{\partial x_j}\left(\rho u_j\right) = 0, \tag{4.1a}$$

$$\frac{\partial (\rho u_i)}{\partial t} + \frac{\partial}{\partial x_j}\left(\rho u_i u_j + p\delta_{ij}\right) = 0, \tag{4.1b}$$

$$\frac{\partial E}{\partial t} + \frac{\partial}{\partial x_j}\left[u_j(E+p)\right] = 0, \tag{4.1c}$$

where ρ is the density, u_i is the velocity, $E = \rho e + \frac{1}{2}\rho u_i u_i$ is the total energy, e is the internal energy, p is the pressure and δ_{ij} is the Kronecker delta. The system is closed by the ideal gas equation of state relating the internal energy to the pressure, $\rho e = \frac{p}{\gamma-1}$, where γ is the ratio of specific heats. Here, physical diffusion processes are neglected since we consider high Reynolds number flows.

To avoid spurious pressure oscillations in flows with variable γ, it is necessary to solve an additional non-conservative transport equation for γ to capture interfaces [54],

$$\frac{\partial}{\partial t}\left(\frac{1}{\gamma-1}\right) + u_j \frac{\partial}{\partial x_j}\left(\frac{1}{\gamma-1}\right) = 0. \tag{4.2}$$

We extended this approach to the DG method [151, 113]. The DG method [57, 58, 59, 60, 61] is a numerical method for solving partial differential equations which combines the advantages of the finite element and Finite Volume (FV) methods. In contrast with previous RM instability studies using finite difference and FV methods [148, 145, 120, 146, 147], the numerical solution is represented in each computational cell of the domain with high-order polynomial basis functions. The method is therefore high-order accurate and is superconvergent in the cell averages at a rate of $2P+1$ [55, 56], where $P+1$ is the number of basis function in each cell. The method's compact stencil, *i.e.*, cells communicate only with their direct neighbors, enables a highly scalable implementation for parallel architectures. Additionally, the DG method is naturally amenable to unstructured grids. At cell interfaces, a Riemann solver is implemented to calculate the fluxes between the cells. In this chapter, the cell fluxes are calculated by the approximate Riemann solver of Roe [106]. Additionally, a limiting procedure is required to avoid solution oscillations at flow discontinuities. We use a non-oscillatory, conservative, and high-order accurate limiting procedure based on hierarchical reconstruction, which has been suitably modified to prevent spurious pressure oscillations [113]. Solution limiting is performed gradually and hierarchically from the highest polynomial degree to the lowest to retain as much of the high-order accuracy of the method as possible. In contrast with other limiters, *e.g*, [57], the present limiter does not reduce the solution to first order in the flow domain but is $(P+1)$st order accurate. At discontinuities, the scheme reduces to first order, as do all FV, finite difference, and DG method shock-capturing schemes. The system is evolved in time using the standard explicit fourth-order Runge-Kutta method [152] with a Courant number of 0.5.

Taking advantage of the method's compact stencil [57], a highly parallel version of the method on Graphics Processing Units (GPU) is implemented. This allows for simulations completing approximately two orders of magnitude faster than on a single Computing Processing Units (CPU). The high-resolution simulations in this chapter completed in approximately one hour. The simulations were performed on GPUs at the Flux cluster at the Center for Advanced Computing at the University of Michigan. Mesh generation and post-processing visualization were carried out with Gmsh, a three-dimensional finite element mesh generator with built-in pre- and post-processing facilities [112]. Our code has been used previously to simulate HEDP experiments of blast-wave-driven shear flow [114].

4.4 Single-interface RM instability validation

We use the single-mode RM instability experiments of [119] to validate our numerical method. Two gases, air and SF_6, lie in a shocktube at atmospheric pressure, and the interface between the two is sinusoidally perturbed. The properties of air are $\rho_{air} = 1.351\,\mathrm{kg/m^3}$, $\gamma_{air} = 1.276$, and those of SF_6 are $\rho_{SF_6} = 5.494\,\mathrm{kg/m^3}$, $\gamma_{SF_6} = 1.093$ [120]. The initial amplitude and wavelength of the interfacial perturbations are $a_0 = 0.183$ cm and $\lambda = 5.933$ cm, respectively. The mean air-SF_6 interface is initially at $y = 0$. A Mach 1.21 shock initialized in air impinges upon the perturbed interface, thereby initiating the RM instability growth.

For these simulations, the domain is one perturbation wavelength wide in the x-direction and 20 cm long in the y-direction. The boundaries are periodic on the sides, and we impose non-reflecting boundary conditions, modeled as zero gradient boundary conditions, at the entrance and exit of the shock tube. The domain is discretized uniformly in x and y. The number of cells per wavelength is 128. We use a linear polynomial basis ($P = 1$) for the DG method, resulting in third-order accuracy in smooth regions. An exponential diffusion function is used to initialize a thermodynamically consistent diffuse interface between the gases [120], with a thickness set to 0.5 cm. To avoid a large spatial domain, we add a constant upward velocity calculated from an exact Riemann solver so that the post-shock upward mean velocity is zero and the interfaces remain in the domain. As we are interested in the mixing layer width, the perturbation amplitudes in this chapter are measured as half the difference between the maximum and the minimum y-position of the perturbation. The perturbation location is found by taking the 0.5 contour level of the mass fraction field. This measure of the amplitude does not take into account the phase of the perturbation.

Upon interaction with the interface, the shock generates baroclinic vorticity due to the misalignment of the density and pressure gradients (Fig. 4.1a and 4.1b). As a result, the perturbed interface grows in time, leading to bubbles of light fluid penetrating the heavier one, and spikes of heavy fluid penetrating the lighter one (Fig. 4.1c and 4.1d). Figure 4.2 compares the early-time experimental growth (before reshock, at 6.6 ms in the experiment) of the instability with the simulation growth at different resolutions. As the grid is refined, the results (amplitude) converge in an integral sense, with good agreement with the experimental data. The numerical results in this chapter were performed using the grid with 128 cells per wavelength.

4.5 Shock interaction with two successive interfaces

Our baseline problem consists of a shock interacting successively with two interfaces separated by a distance h. Our set-up can be described as three adjacent gases (A, B, and C) with interfaces initially perturbed with the same single mode, and a shock initialized in the first gas (Fig. 6.2). For comparison with single-interface RM instability studies [119], we choose air for gas A, SF_6 for gas B, and a shock Mach number of 1.21. The goal is to

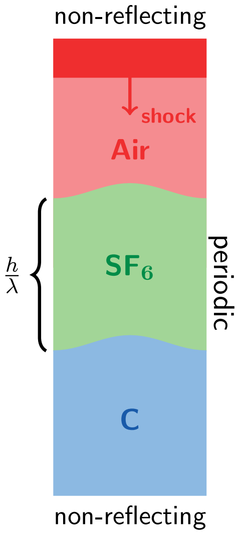

Figure 4.3: Baseline multi-layered problem setup.

Table 4.1: Relevant properties for the different gases.

Case	ρ_A [kg/m^3]	γ_A	ρ_B [kg/m^3]	γ_B	ρ_C [kg/m^3]	γ_C
nominal [119]	1.351	1.276	5.494	1.093	–	–
1	1.351	1.276	5.494	1.093	0.178	5/3
2	1.351	1.276	5.494	1.093	10	5/3

understand how the physics depend on the nature of the third gas (heavy or light — see Table 4.1). In particular, we study the effect of increasing the thickness of gas B (*i.e.*, the distance separating gas A from gas C) measured by the non-dimensional distance $\frac{h}{\lambda}$, where λ is the perturbation wavelength. We also change the density of gas C, Table 4.1, to create either a reflected rarefaction or shock at the second interface. The nominal case (no gas C) corresponds to the experiment in [119] with no reshock, as in Section 4.4.

4.5.1 Light third gas

We first consider a third gas (C), whose properties correspond to helium and is lighter than SF$_6$ (B). Figure 4.4 shows the waves produced during the process in an $x-t$ diagram, and Fig. 4.5 provides a qualitative illustration of the effect these waves have on the dynamics of the interfaces through contours of density, density gradient (displayed as a numerical Schlieren image) and vorticity. When the shock interacts with the first interface and de-

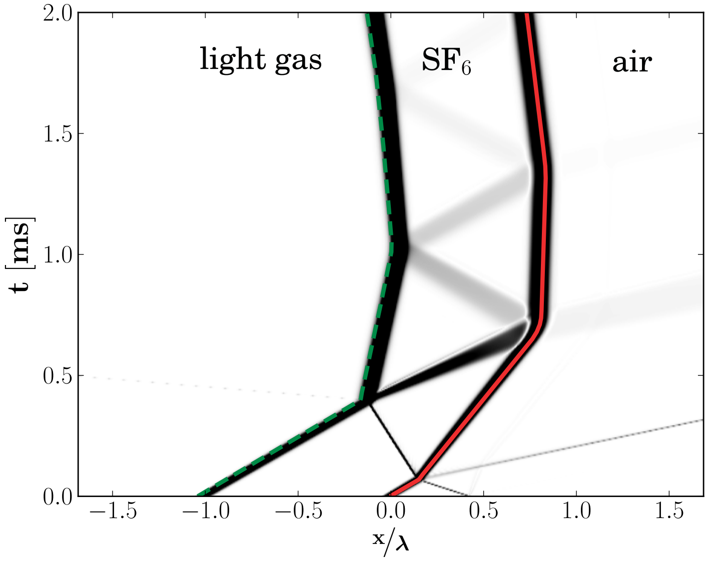

Figure 4.4: Wave diagram from a one-dimensional simulation for the baseline problem with a light third gas (initial shock coming from the right, $\frac{h}{\lambda} = 1$). Solid red: air-SF_6 interface; dashed green: SF_6-light third gas interface.

posits baroclinic vorticity (Fig. 4.5a), a transmitted and a reflected shock are created; the reflected shock eventually leaves the domain. The transmitted shock then impinges upon the second interface, and deposits vorticity (Fig. 4.5b). From this latter interaction, a reflected rarefaction and another transmitted shock, which eventually leaves the domain, are produced (Fig. 4.5c). The reflected rarefaction propagates back towards the first interface and interacts with the evolving instability (Fig. 4.5c). Given the sign of the vorticity already present along the interface due to the first shock interaction, this rarefaction further increases the vorticity (Fig. 4.5d). Alternately, this process can be understood as an accelerated interface in an RT-unstable configuration due to the transient passage of the rarefaction. This overall process thus initiates two spikes moving in opposite directions: one into gas A (produced by the incoming shock and reflected rarefaction) and the other into gas C (due to the transmitted shock). The nonlinear evolution of the perturbations is visible in Fig. 4.5e and 4.5f. Eventually the reflected waves diminish in strength and do not affect the dynamics of the interfaces anymore.

The perturbation growth at both interfaces is shown in Fig. 4.6 for different non-dimensional spacings $\frac{h}{\lambda}$ between the interfaces. We start by considering the first interface (Fig. 4.6a).

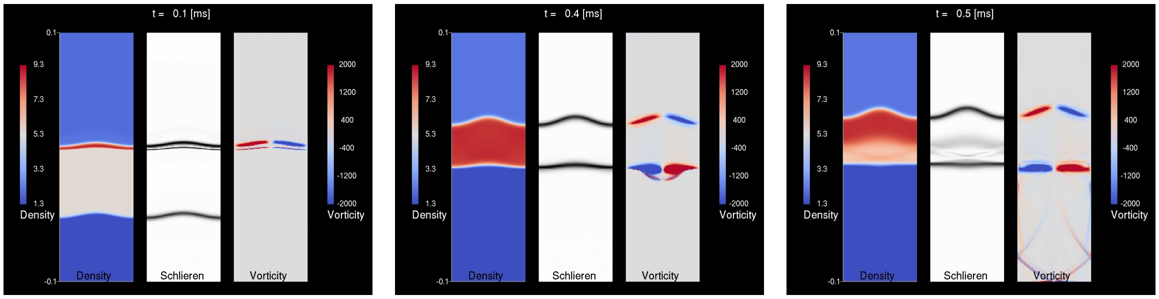

(a) $t = 0.1$ms. (b) $t = 0.4$ms. (c) $t = 0.5$ms.

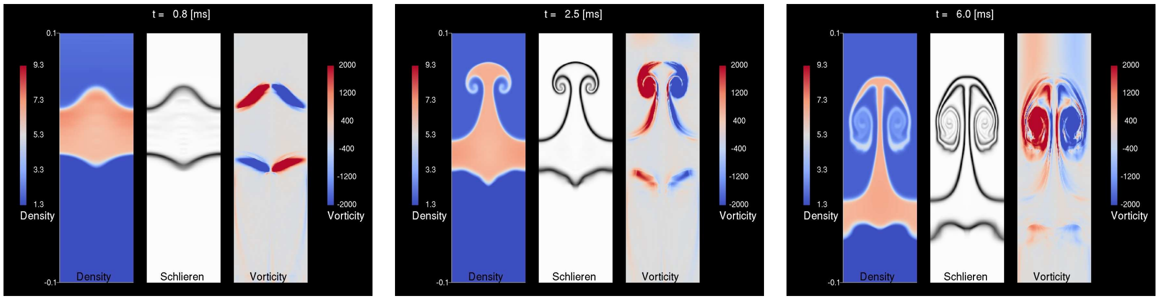

(d) $t = 0.8$ms. (e) $t = 2.5$ms. (f) $t = 6.5$ms.

Figure 4.5: Density (left), density gradient (numerical Schlieren, middle), and vorticity (right) fields for the baseline problem with a light third gas and $\frac{h}{\lambda} = 1$. Shock wave moving downwards. Air (top) – SF_6 (middle) – light gas (bottom).

Until the reflected rarefaction reaches it, the growth of the first interface is that of the nominal case. A transition immediately follows where the growth is nonlinear and increases dramatically. This behavior is caused by rarefactions reflected from the second interface and interacting with the first. These rarefactions deposit vorticity at the first interface in the same direction as the initial shock, thus amplifying the initial growth. These waves have the effect of accelerating the heavy fluid into the light fluid, an unstable configuration that leads to transient RT growth. As $\frac{h}{\lambda}$ is increased, these waves reach the first interface at later times. As a result, the perturbation amplitude is larger when the rarefaction reaches the interface, thus enhancing the baroclinic vorticity generation. Additionally, the rarefactions have spread more, increasing the interaction time with the interface. In this RT unstable set-up, the acceleration is applied for a longer time. For these two reasons, the growth rate of the first interface increases with increasing $\frac{h}{\lambda}$. After $t > 3$ms, the growth rate is constant; it is higher for larger values of $\frac{h}{\lambda}$ due to the larger amplitude at the time of interaction. By then, the reflected and transmitted waves have left the domain or decreased in amplitude such that their effect on the growth is negligible.

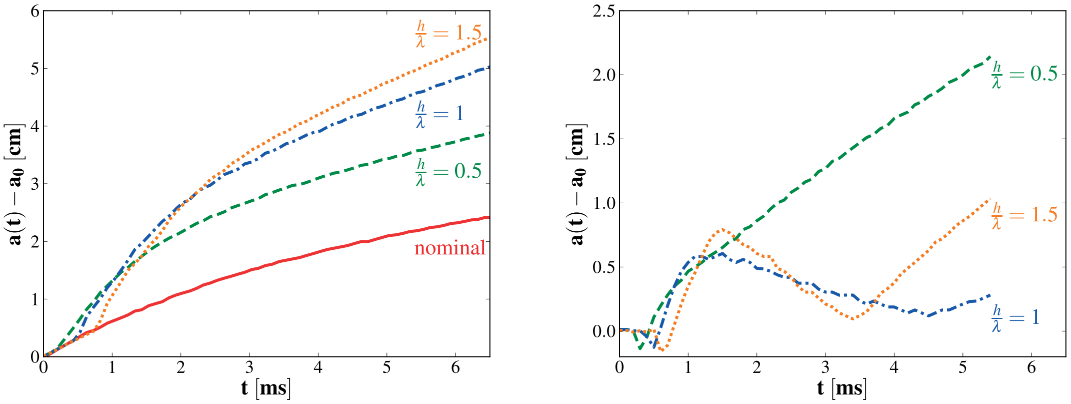

(a) Air-SF_6 interface.

(b) SF_6-light third gas interface.

Figure 4.6: Interface growth versus time for the baseline problem with a light third gas for different thicknesses of gas B.

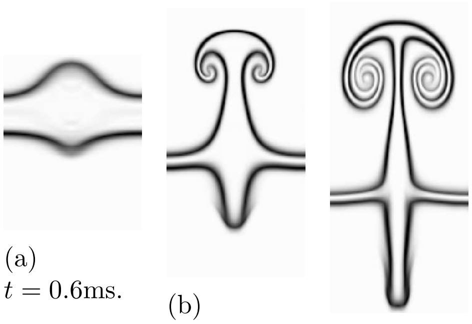

(a) $t = 0.6$ms.

(b) $t = 2.5$ms.

(c) $t = 5$ms.

Figure 4.7: Density gradient (numerical Schlieren) for the baseline problem with a light third gas for $\frac{h}{\lambda} = 0.5$

The morphology and evolution of the second interface is different and strongly depends on $\frac{h}{\lambda}$ (Fig. 4.6b). In the case of $\frac{h}{\lambda} = 0.5$, a single SF_6 spike moves downward while the air and helium interfaces start interacting on the sides of the spike, (Fig. 4.6b, 4.7). The evolution of this interface for $\frac{h}{\lambda} = 1.5$ is very different. An initial central SF_6 spike moves downward. The interface then experiences a phase reversal following interaction with the compression generated by the reflection of the rarefaction at the first interface (Fig. 4.6b, 4.8). This effect is less important for the $\frac{h}{\lambda} = 1$ case, Fig. 4.6b. At later times, interface proximity effects affect the flow dynamics by enabling or preventing the phase reversal. In addition, reflecting waves in the SF_6 interact with higher amplitude perturbations as the separation distance increases, thereby increasing the baroclinic vorticity generation.

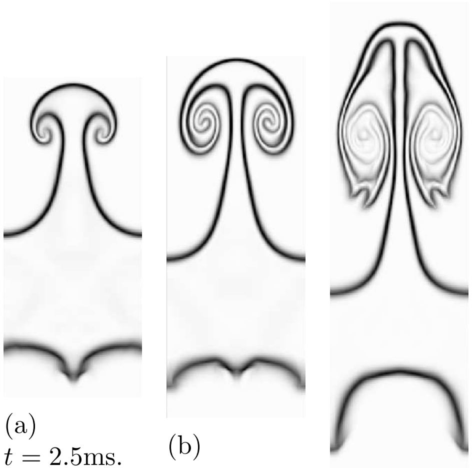

(a)
$t = 2.5$ms.

(b)
$t = 3.8$ms.

(c)
$t = 6.5$ms.

Figure 4.8: Density gradient (numerical Schlieren) for the baseline problem with a light third gas for $\frac{h}{\lambda} = 1.5$.

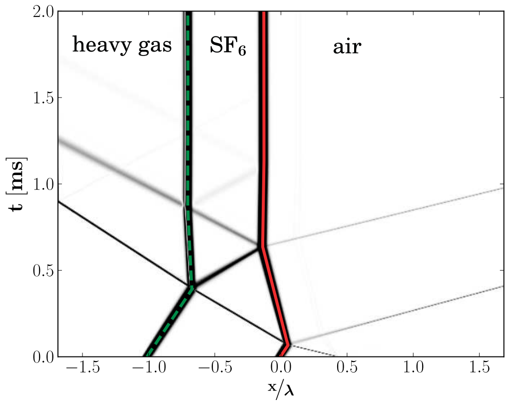

Figure 4.9: Wave diagram from a one-dimensional simulation for the baseline problem with a heavy third gas (initial shock coming from the right, $\frac{h}{\lambda} = 1$). Solid red: air-SF_6 interface; dashed green: SF_6-heavy third gas interface.

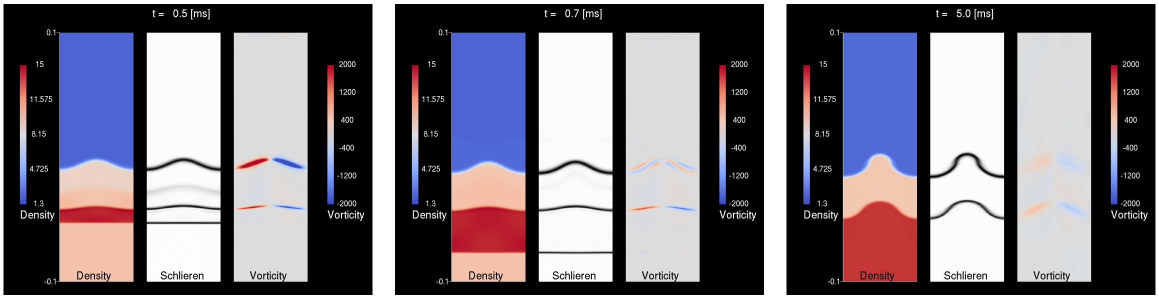

(a) $t = 0.5$ms.
(b) $t = 0.7$ms.
(c) $t = 5$ms.

Figure 4.10: Density (left), density gradient (numerical Schlieren, middle), and vorticity (right) fields for the baseline problem with a heavy third gas and $\frac{h}{\lambda} = 1$.

Table 4.2: Density, velocity, and pressure from solving the shock interactions with an exact Riemann solver for the baseline problem with a heavy third gas (SI units).

Interaction		air	SF_6	heavy third gas
Shock at 1^{st} interface	ρ	1.87	5.5	10
	u	103.6	0	0
	p	$1.52\ 10^5$	10^5	10^5
Transmitted shock at 2^{nd} interface	ρ	2.07	9.02	10
	u	71.75	71.75	0
	p	$1.72\ 10^5$	$1.72\ 10^5$	10^5
Reflected shock from 2^{nd} interface at 1^{st} interface	ρ	2.07	10.1	14.79
	u	71.75	55.43	55.43
	p	$1.72\ 10^5$	$1.95\ 10^5$	$1.95\ 10^5$
Post-shock refraction	ρ	2.21	9.74	14.79
	u	50.21	50.21	55.43
	p	$1.87\ 10^5$	$1.87\ 10^5$	$1.95\ 10^5$

4.5.2 Heavy third gas

We now consider a third gas (C), which is heavier than SF_6 (B). Figure 4.9 shows the different transmitted and reflected waves in an $x - t$ diagram, and Fig. 4.10 provides a qualitative illustration of the effect these waves have on the dynamics of the interfaces. In this set-up, the transmitted shock from the first interface leads to a reflected and transmitted shock at the second interface (Fig. 4.10a). Upon interaction with the evolving RM instability at the first interface, the reflected shock decreases the amount of vorticity at the first interface by depositing vorticity in the opposite direction (Fig. 4.10b). Both perturbations grow in the same direction, with the first spike moving slowly into gas A (Fig. 4.10c).

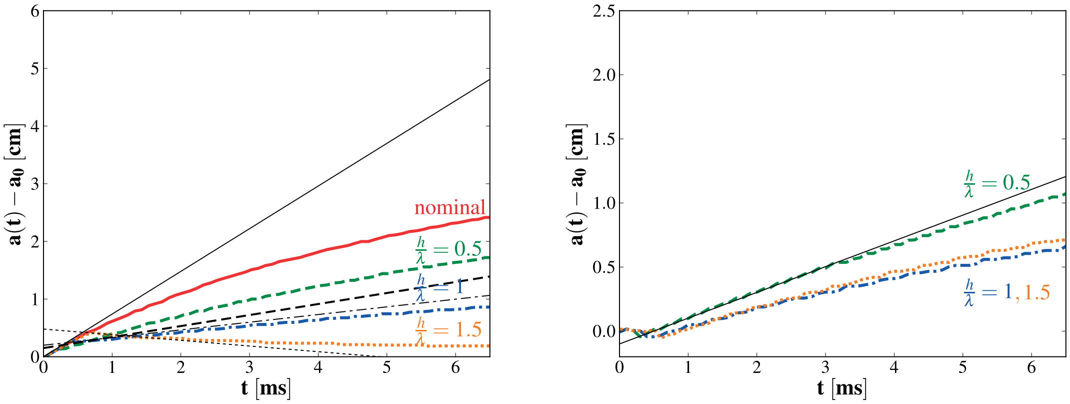

(a) Air-SF_6 interface.

(b) SF_6-heavy third gas interface.

Figure 4.11: Interface growth versus time for the baseline problem with a heavy third gas for different thicknesses of gas B. Black lines: impulsive model [30] for the growth after the interaction with the first shock and the reflected shock.

Figure 4.11b illustrates the growth of the RM instability at the first interface for different $\frac{h}{\lambda}$. The growth follows that of the nominal case until the reflected shock from the second interface reaches it. The growth and growth rate decrease thereafter, more so as $\frac{h}{\lambda}$ increases. Because the reflected shock moves from a dense to a less dense gas, the reflected shock deposits vorticity in the opposite direction as the initial shock. Further amplifying this effect, the greater distance implies that the perturbation has grown more before interacting with the reflected shock. As $\frac{h}{\lambda}$ increases, the growth rate becomes negative, indicating a phase reversal of the RM instability. Although the set-up is analogous, the growth of the perturbation amplitude does not increase as significantly as in experiments with reshock [119] because of the weaker transmitted shock and smaller interface perturbations at the time of interaction, as in the previous section. The monotonic attenuation in the amplitude with increasing $\frac{h}{\lambda}$ is most likely limited to cases when the second shock interacts with the interface before the perturbation becomes nonlinear. It is to be expected that a reflected shock interacting with a nonlinear interface leads to a large increase in the perturbation amplitude and increased mix. For $\frac{h}{\lambda} = 1.5$, we observe “freeze-out” of the growth due to the multiple wave interactions [148]. This supports the idea that shell thickness and shock timing could be used advantageously to minimize the amount of mix and spike penetration in ICF capsules [20]. The second interface (between the SF_6 and the heavy gas) exhibits continuous growth and no phase reversal (Fig. 4.11a). The growth rates are similar since the subsequent waves interact weakly with this interface after the transmitted shock interaction.

In Fig. 4.11b, we compare the impulsive model [30] to the initial growth rate of the instability and the growth rate after the interaction with the reflected shock. The impulsive model growth rate is given by

$$\frac{\mathrm{d}a}{\mathrm{d}t} = k\Delta u A^+ a_0^+, \tag{4.3}$$

where $a(t)$ is the perturbation amplitude, a_0^+ is the post-shock amplitude, k is the perturbation wave number, $A^+ = (\rho_1^+ - \rho_2^+)/(\rho_1^+ + \rho_2^+)$ is the post-shock Atwood number, and Δu is the velocity jump at the interface following shock refraction. For the nominal case, the growth rate is 7.4 m/s [120]. We solve three Riemann problems using an exact Riemann solver to calculate the numerical values of A^+ and Δu to determine the growth due to the reflected shock from the second interface: (i) the initial shock interacting with the first interface; (ii) the transmitted shock interacting with the second interface; and (iii) the reflected shock from the second interface interacting with the first interface. The various states of the gases are reported in Table 4.2. The a_0^+ is measured from two-dimensional simulations right after shock refraction: $a_0^+ = 0.38$ cm for $\frac{h}{\lambda} = 0.5$, $a_0^+ = 0.42$ cm for $\frac{h}{\lambda} = 1$, and $a_0^+ = 0.58$ cm for $\frac{h}{\lambda} = 1.5$. We subtract the growth rate due to the reflected shock from the initial nominal growth rate to obtain the growth after reflected shock interaction: $\frac{\mathrm{d}a}{\mathrm{d}t} = 5.49$ m/s for $\frac{h}{\lambda} = 0.5$, $\frac{\mathrm{d}a}{\mathrm{d}t} = 6.07$ m/s for $\frac{h}{\lambda} = 1$, and $\frac{\mathrm{d}a}{\mathrm{d}t} = 8.38$ m/s for $\frac{h}{\lambda} = 1.5$. From Fig. 4.11b, the impulsive model accurately predicts the initial growth rates after both shock interactions and deviates from the simulation results at later times, as expected. In Fig. 4.11a, the impulsive model agrees well with the initial growth rate of the second interface for the three separation distances.

4.6 Fluid mixing

Although physical diffusion is neglected, we are interested in mixing between the different fluids through fluid entrainment and dispersion, *i.e.*, at large and intermediate scales. For analysis purposes, we use metrics analogous to those used to measure chemical mixing. We quantify the amount of mixing between the fluids using two different approaches.

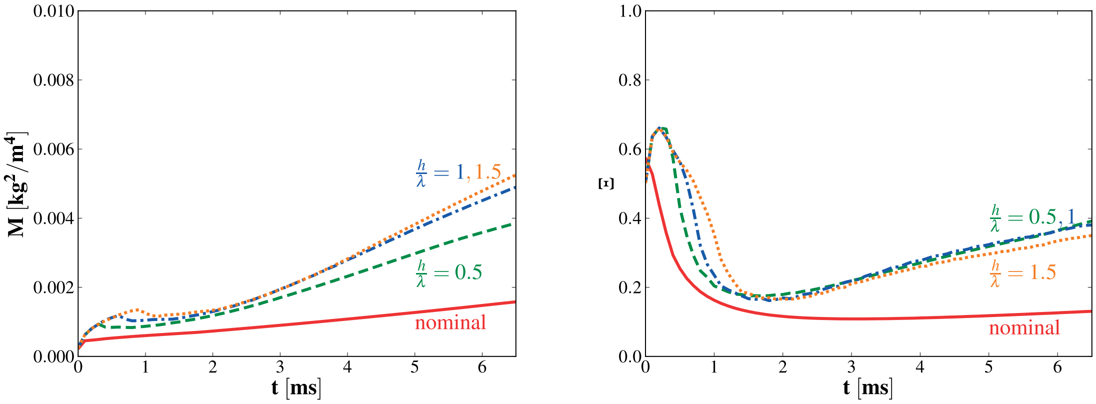

(a) M.

(b) Ξ.

Figure 4.12: Mixing metrics versus time for the baseline problem with a light third gas for different thicknesses of gas B.

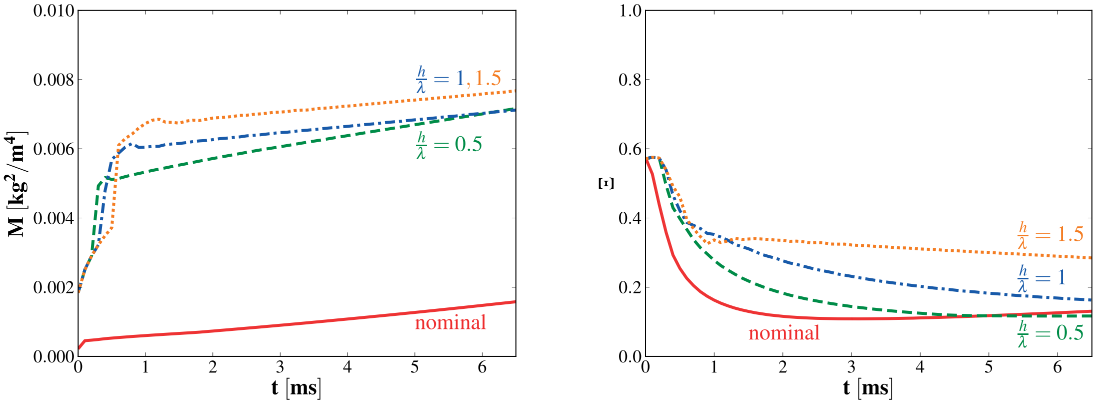

(a) M.

(b) Ξ.

Figure 4.13: Mixing metrics versus time for the baseline problem with a heavy third gas for different thicknesses of gas B.

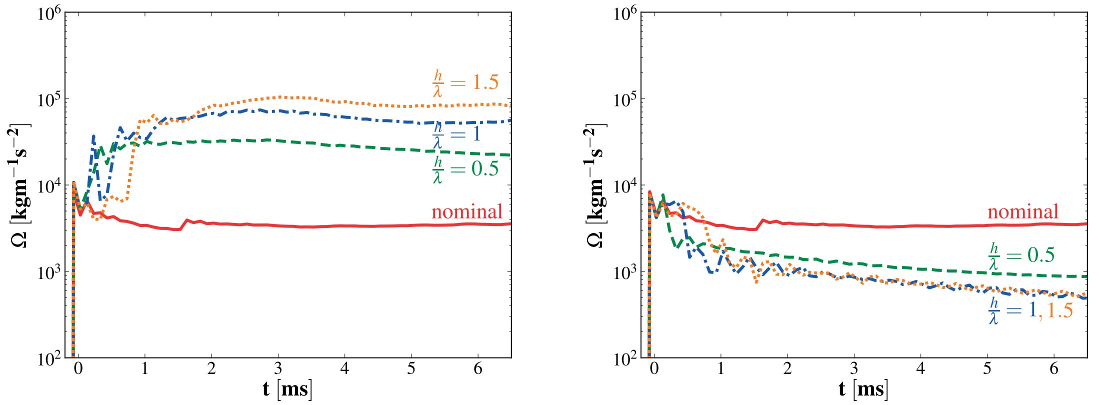

(a) Light third gas.

(b) Heavy third gas.

Figure 4.14: Enstrophy versus time for the baseline problem for different thicknesses of gas B.

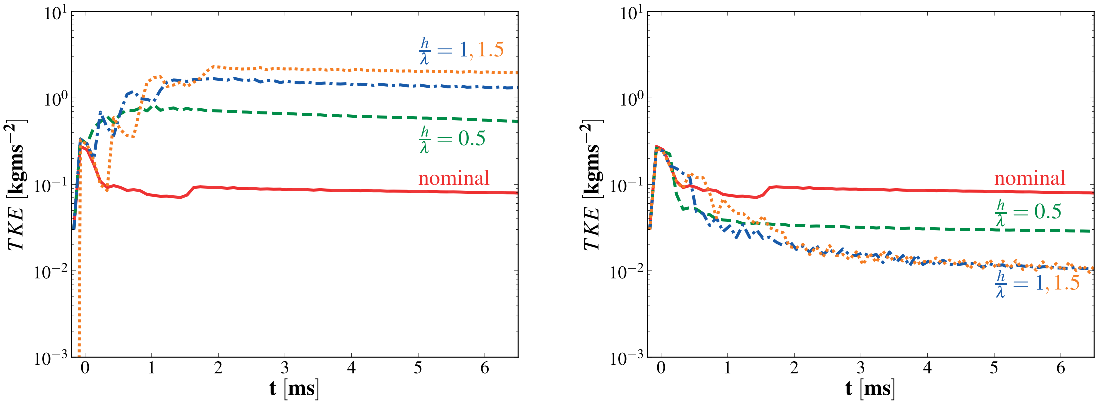

(a) Light third gas.

(b) Heavy third gas.

Figure 4.15: Turbulent kinetic energy versus time for the baseline problem for different thicknesses of gas B.

We first define the mix between fluid A and B as

$$M_{AB} = \int_S \rho^2 Y_A Y_B \, \mathrm{d}S, \tag{4.4}$$

where $Y_{(i)}$ is the mass fraction of fluid i. This equation represents the total reaction rate in a chemical reaction between fluid A and B with a temperature invariant reaction rate [153, 154, 155]. The total mix, M, in the system is defined as

$$M = M_{AB} + M_{BC} + M_{AC}, \tag{4.5}$$

where fluid A is the air, fluid B is the SF_6, and fluid C is the third gas.

To study mix without the effect of the density difference between the first and second interface and to distinguish between mixed gas and unmixed entrained gas, we use the ratio of the total chemical product formed by the mixing fluids and the entrainment length [47]. The chemical product formed by a chemical reaction between fluid A and B limited by the lean reactant and, with a stoechiometric coefficient of 0.5, is

$$Y_{AB} = \begin{cases} 2Y_A, & \text{if } Y_A \leq 0.5, \\ 2Y_B, & \text{if } Y_B < 0.5. \end{cases} \tag{4.6}$$

The total chemical product in the system from this reaction is equal to

$$P_{AB} = \int_{-\infty}^{\infty} \langle Y_{AB} \rangle \, \mathrm{d}y, \tag{4.7}$$

where $\langle \cdot \rangle$ denotes the average in the (transverse) x-direction. The maximum chemical product possible resulting from complete mixing (homogenization) of the two fluids in each y-plane is

$$h_{AB} = \int_{-\infty}^{\infty} Y_{AB}(\langle Y_A \rangle, \langle Y_B \rangle) \, \mathrm{d}y. \tag{4.8}$$

This quantity is the entrainment length [47], which is also a measure of mixing layer thickness. Another measure of mixing can be defined as

$$\Xi_{AB} = \frac{P_{AB}}{h_{AB}}. \tag{4.9}$$

This quantity is close to unity when the fluids are completely mixed, *i.e.*, $P_{AB} \approx h_{AB}$, and close to zero when the fluids are segregated, *i.e.*, $P_{AB} \ll h_{AB}$. It, therefore, distinguishes between mixed fluids and unmixed entrained fluids. We quantify the total mixing in the system as

$$\Xi = \frac{P_m}{h_m} = \frac{P_{AB} + P_{BC} + P_{AC}}{h_{AB} + h_{BC} + h_{AC}}. \tag{4.10}$$

For the light third gas case, M is shown in Fig. 4.12a. M is larger for the light third gas case than the nominal case. This is due to the large perturbation growth from the

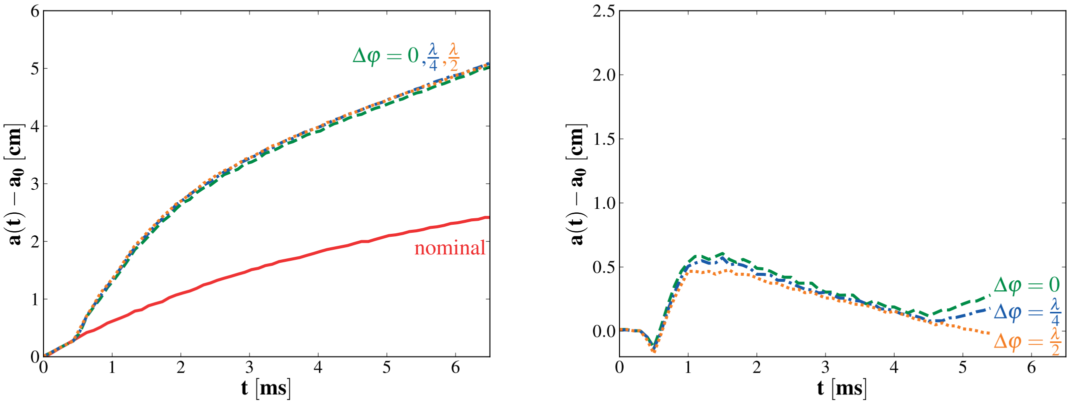

(a) Air-SF_6 interface.

(b) SF_6-light third gas interface.

Figure 4.16: Interface growth versus time for the baseline problem with a light third gas and $\frac{h}{\lambda} = 1$ for different phase misalignments.

RT-unstable phase driven by the rarefactions and the presence of two interfaces mixing. M increases as $\frac{h}{\lambda}$ increases because of the high growth of the first interface for larger $\frac{h}{\lambda}$. Because of the high density at the air-SF_6 interface relative to that at the SF_6-light gas interface, M mostly measures the mixing of the air with the SF_6. Figure 4.12b shows the temporal evolution of Ξ. This quantity starts at a high value because the perturbed interfaces are initially diffuse and no small-scale features are present. The decrease in Ξ, after the shock and rarefaction interactions, is due to the entrainment of the fluids that do not mix on these time scales as the mixing region width increases. As time increases, the mixing between the fluids increases, as does Ξ. As $\frac{h}{\lambda}$ is varied, Ξ does not change significantly, indicating that an increase in entrainment length is balanced with a corresponding increase in unmixed interpenetrating fluids. The mix between the first and third gases, M_{AC} and Ξ_{AC}, is essentially zero for all cases.

For the heavy third gas case, because of the density weighing, M is dominated by the mixing at the second interface (Fig. 4.13a). As $\frac{h}{\lambda}$ increases, the transmitted shock reaches the second interface later in time. By then, the second interface has stretched more before being shocked. The increased length of this diffusion layer results in increased M with $\frac{h}{\lambda}$ after the transmitted shock interaction. M is almost constant after the shock interaction because there is little entrainment of the fluids. For the heavy third gas, Ξ is generally much lower than that for the light third gas (Fig. 4.13b). There is little mixing of the fluids

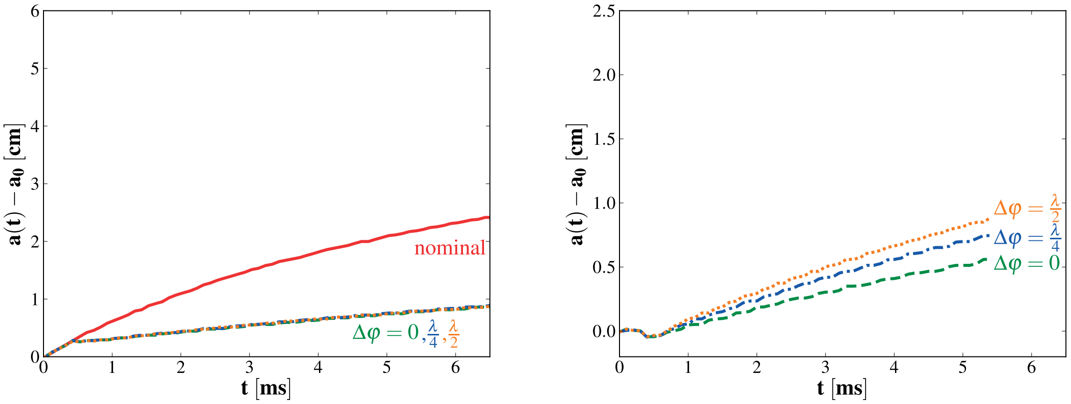

(a) Air-SF$_6$ interface.

(b) SF$_6$-light third gas interface.

Figure 4.17: Interface growth vs time for the baseline problem with a heavy third gas and $\frac{h}{\lambda} = 1$ for different phase misalignments.

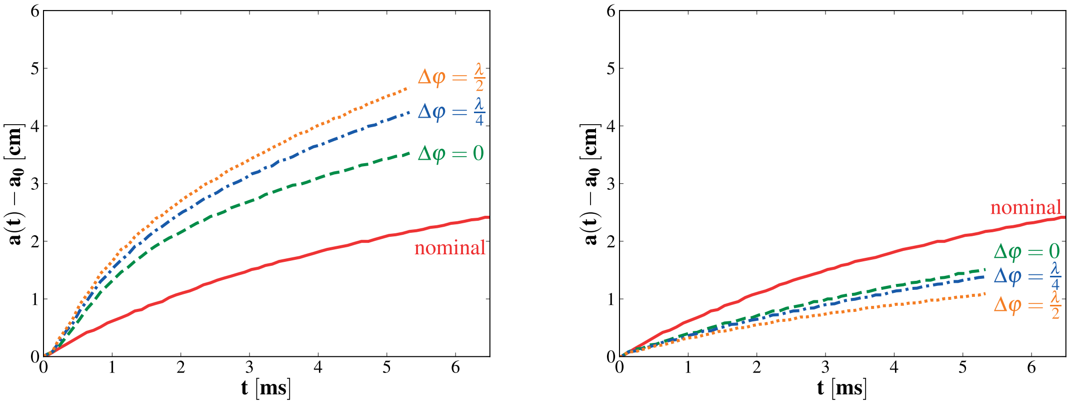

(a) Light third gas.

(b) Heavy third gas.

Figure 4.18: Air-SF$_6$ interface growth versus time for the baseline problem, $\frac{h}{\lambda} = 0.5$ for different phase misalignments.

relative to the entrainment of the fluids. When freeze-out occurs ($\frac{h}{\lambda} = 1.5$), there is a sharp reversal of the downward trend in Ξ because the interface is diffusing numerically and no longer growing. For all cases, there is no mix between the first and third gases.

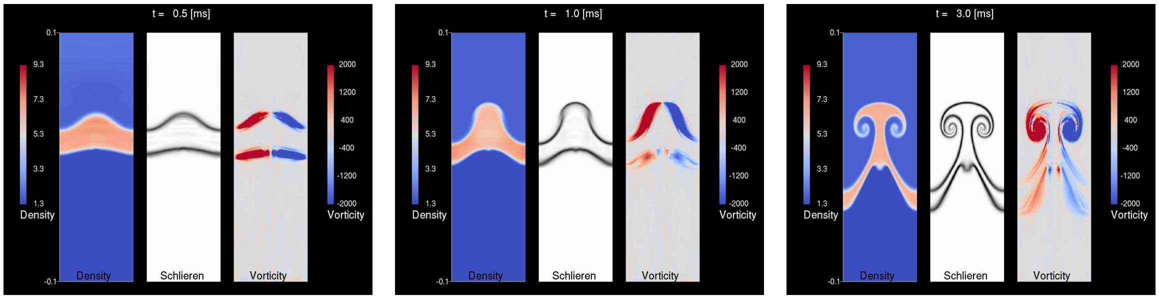

(a) $t = 0.5$ms. (b) $t = 1$ms. (c) $t = 3$ms.

Figure 4.19: Density (left), density gradient (numerical Schlieren, middle) and vorticity (right) fields for the baseline problem and a light third gas $\left(\frac{h}{\lambda} = 0.5 \text{ and } \Delta\varphi = \frac{\lambda}{2}\right)$.

4.7 Characterization of the dynamics at the small scales

To characterize the small-scale dynamics, we present the time evolution of the mass-weighted enstrophy in the whole domain,

$$\Omega = \int_S \rho\omega^2 \, \mathrm{d}S, \tag{4.11}$$

where $\omega = \nabla \times \mathbf{u}$ is the vorticity (Fig. 4.14). The curl is computed using the Gmsh Curl plugin which evaluates the derivatives of the Lagrange shape functions in each cell. The derivative operator for the present simulations is, therefore, second-order accurate. Ω varies with resolution for inviscid calculations but the overall trend, main features, and conclusions remain unchanged when comparing to higher resolution simulations.

For both the heavy and the light third gas, the shock passage creates a jump in enstrophy due to baroclinic vorticity deposition at the interfaces and the generation of small scales. These small-scale features are more prevalent in the light third gas case, as indicated by the higher enstrophy (Fig. 4.14a). The increase in enstrophy by the reflected rarefaction waves as explained in Section 4.5.1 is clearly noticeable. For this case, increasing $\frac{h}{\lambda}$ further amplifies the small scales in the domain because the rarefaction interacts with a larger perturbed interface for a longer time.

For the heavy third gas case, the small-scale features are not as prevalent (Fig. 4.14b). The reflected shock interacts with a heavy-light interface, as opposed to the initial shock,

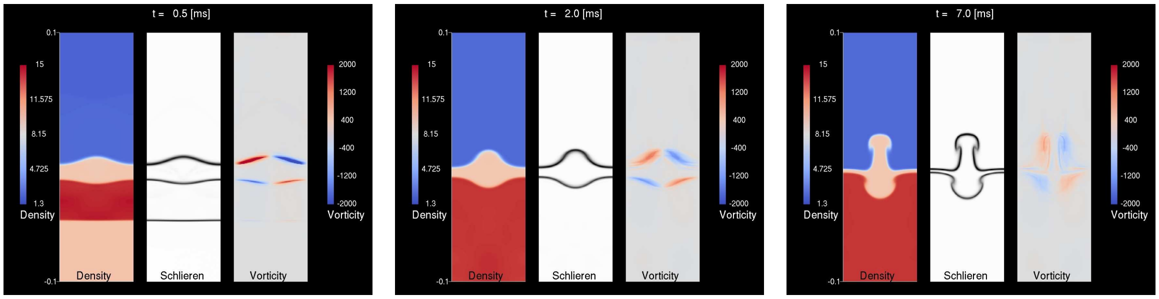

(a) $t = 0.5$ms.

(b) $t = 2$ms.

(c) $t = 7$ms.

Figure 4.20: Density (left), density gradient (numerical Schlieren, middle) and vorticity (right) fields for the baseline problem with a heavy third gas ($\frac{h}{\lambda} = 0.5$ and $\Delta\varphi = \frac{\lambda}{2}$).

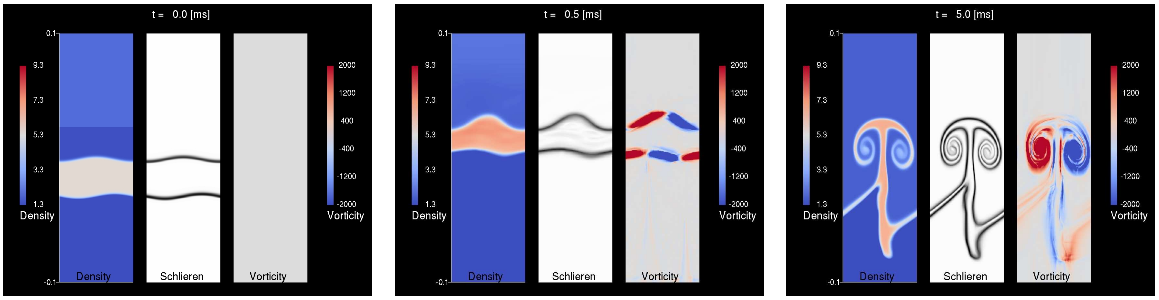

(a) $t = 0$ms.

(b) $t = 0.5$ms.

(c) $t = 5$ms.

Figure 4.21: Density (left), density gradient (numerical Schlieren, middle) and vorticity (right) fields for the baseline problem with a light third gas ($\frac{h}{\lambda} = 0.5$ and $\Delta\varphi = \frac{\lambda}{4}$).

and, therefore, the density gradient direction is opposite to that of the initial shock. As a result, this reflected shock generates baroclinic vorticity in the direction opposite to that of the initial shock, thereby reducing the amount of enstrophy in the domain (Fig. 4.14b). For this case, the enstrophy decreases as $\frac{h}{\lambda}$ increases because the perturbation is larger, amplifying the baroclinic vorticity generation of the reflected shock.

At the time of interaction with the second interface, the curvature of the shock wave depends on the distance it has traveled since the first interaction. For $\frac{h}{\lambda} = 0.5$, it retains some curvature upon interaction due to the first interface interaction. For large values of $\frac{h}{\lambda}$, the shock wave adopts a planar configuration by the time it reaches the second interface. This effect may account for the observed differences in the growths of the second interface (Fig. 4.11a) as a curved shock deposits more baroclinic vorticity at the interface. Higher enstrophy is in fact observed for $\frac{h}{\lambda} = 0.5$ while the other two distances have similar enstrophy

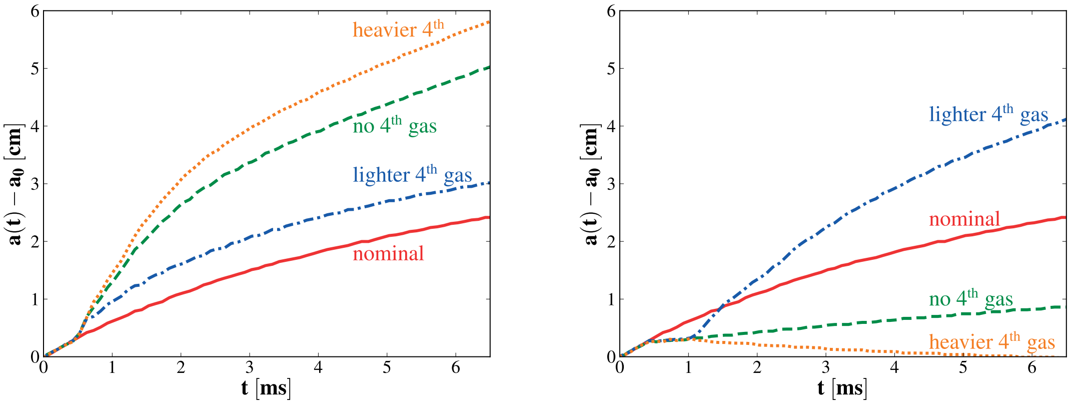

(a) Light third gas.

(b) Heavy third gas.

Figure 4.22: Air-SF$_6$ interface growth vs time at $\frac{h}{\lambda} = 1$ with a fourth gas.

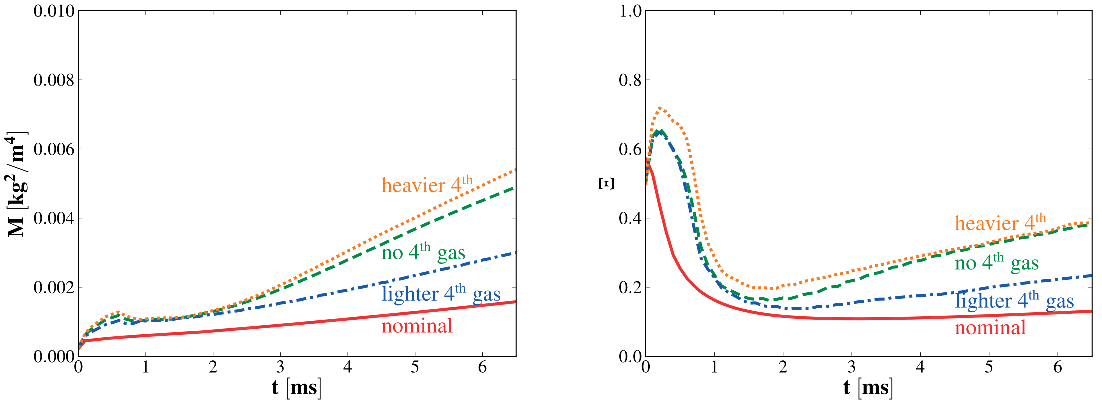

(a) M.

(b) Ξ.

Figure 4.23: Mixing metrics vs time for the light third gas case at $\frac{h}{\lambda} = 1$ with a fourth gas.

profiles (Fig. 4.14b).

Calculating the energy of the small-scale motions can further expand our understanding of the energy at the small scales. We denote the average velocities in each horizontal cross section (spanwise direction) $\bar{u}$ and $\bar{v}$ and calculate the "turbulent kinetic energy" (TKE),[1]

$$TKE = \int_S \frac{1}{2}\rho \left[(u - \bar{u})^2 + (v - \bar{v})^2\right] \, \mathrm{d}S, \tag{4.12}$$

shown in Fig. 4.15. In the case of a light third gas, the initial shock and subsequent re-

---

[1] Since the present simulations are two-dimensional, they cannot represent vortex stretching, and thus turbulence. By TKE, our intent is to describe the energy contained in the small scales.

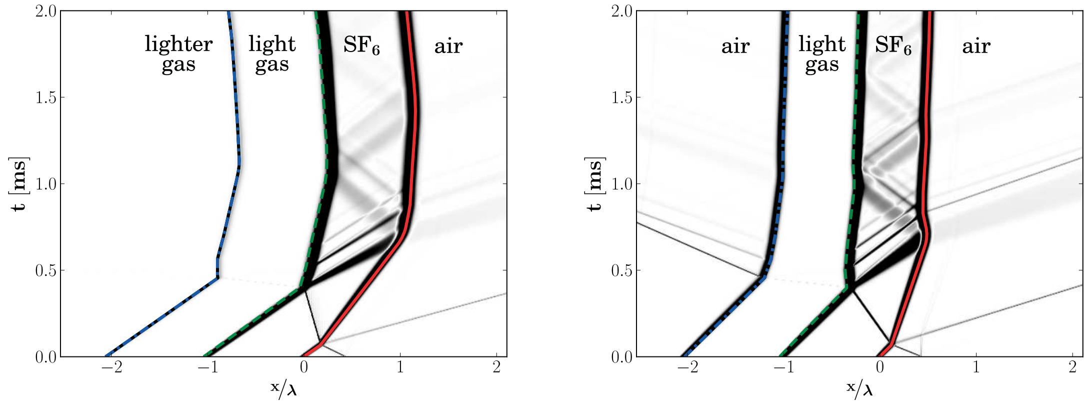

(a) Lighter fourth gas.

(b) Heavier fourth gas.

Figure 4.24: Wave diagram from a one-dimensional simulation for the light third gas case with a fourth gas (initial shock coming from the right, $\frac{h}{\lambda} = 1$). Solid red: air-SF_6 interface; dashed green: SF_6-light third gas interface; dashed-dot blue: third-fourth gas interface.

flected rarefaction greatly increase the TKE in the domain with respect to the nominal case (Fig. 4.15a). This is due to the effect of the reflected rarefaction as detailed previously. However, for the heavy third gas case, the reflected shock causes a significant drop in TKE when it deposits vorticity in the opposite direction as the initial shock (Fig. 4.15b). For all cases, the slight decrease in enstrophy and TKE as a function of time is most likely due to numerical diffusion.

4.8 Effect of a phase difference between successive interfacial perturbations

In the problems to this point, we aligned the interfaces so that the initial perturbations are in phase. In this section, we investigate the effect of a "misalignment" on the perturbation growth. Because of the periodic nature of the problem, we restrict our study to a phase difference between the first and second interfaces $\Delta\varphi \in [0, \frac{\lambda}{2}]$. Specifically, we choose $\Delta\varphi = \frac{\lambda}{4}$ and $\frac{\lambda}{2}$ to compare to our baseline problem, where $\Delta\varphi = 0$.

The effect of the phase difference depends on the separation distance between the interfaces. When the interfaces are separated by a distance larger than $\frac{h}{\lambda} = 1$, the effect of $\Delta\varphi$ on the growth of either interface is negligible for both the light and heavy third gas cases

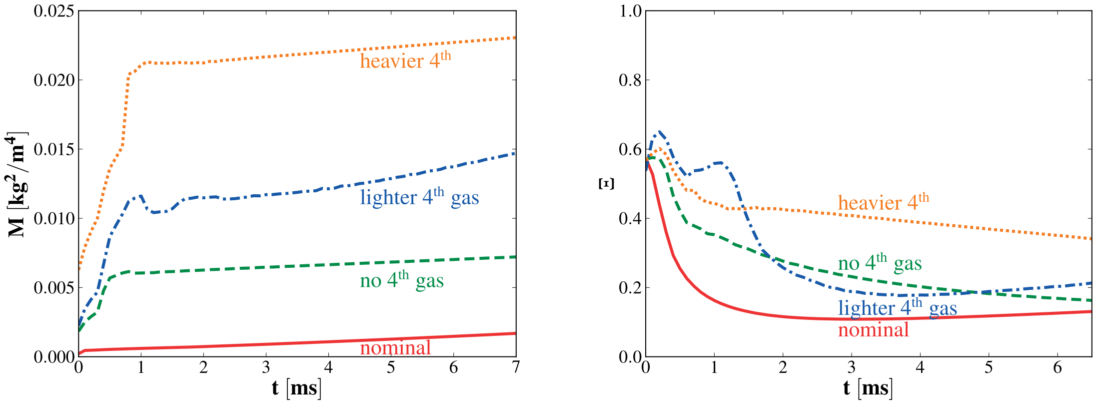

(a) M.

(b) Ξ.

Figure 4.25: Mixing metrics vs time for the heavy third gas case at $\frac{h}{\lambda} = 1$ with a fourth gas.

(Fig. 4.16, 4.17). A slight asymmetry in the interface perturbation appears at late times but it is not very noticeable.

When the interfaces are closer to each other, *e.g*, $\frac{h}{\lambda} = 0.5$, the effect of $\Delta\varphi$ is more noticeable. For the light third gas case, the growth of the perturbations is enhanced (Fig. 4.18a). When $\Delta\varphi = \frac{\lambda}{2}$, the vorticity is deposited in the same direction at both interfaces in each half of the domain (Fig. 4.19), thereby increasing the growth. This happens to a lesser extent for $\Delta\varphi = \frac{\lambda}{4}$. The case $\Delta\varphi = \frac{\lambda}{2}$ with a light third gas is analogous to the SF_6 gas curtain presented in [148] when the amplitudes of both interfaces are equal and opposite. Although our setup differs in the shock Mach number, initial perturbation amplitudes, and density ratios, Mikaelian [148] observes the same qualitative perturbation growth at both interfaces.

For the heavy third gas case, the growth diminishes as $\Delta\varphi$ increases (Fig. 4.18b). For $\Delta\varphi = \frac{\lambda}{2}$, the vorticity is deposited in the opposite direction at both interfaces in each half of the domain (Fig. 4.20), thereby decreasing the growth. This happens to a lesser extent for $\Delta\varphi = \frac{\lambda}{4}$. When $\Delta\varphi = \frac{\lambda}{4}$, there is a clear asymmetry in the evolution of the interfaces (Fig. 4.21). This behavior is due to asymmetric wave reflections and interface proximity effects.

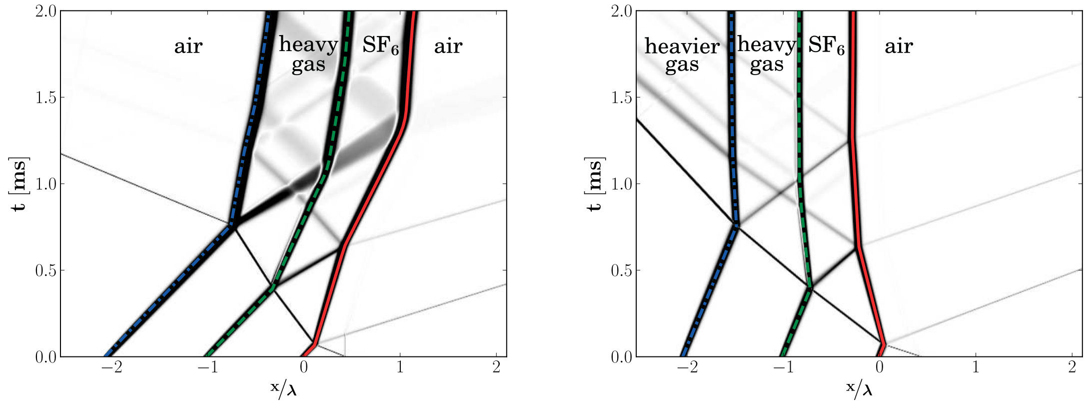

(a) Lighter fourth gas.

(b) Heavier fourth gas.

Figure 4.26: Wave diagram from a one-dimensional simulation for the heavy third gas case with a fourth gas (initial shock coming from the right, $\frac{h}{\lambda} = 1$). Solid red: air-SF$_6$ interface; dashed green: SF$_6$-heavy third gas interface; dashed-dot blue: third-fourth gas interface.

4.9 Effect of a fourth gas

In this section, we study the effect of a fourth gas on the growth of the instability at the first interface. For the light third gas case, we use air as a heavier fourth gas and a gas with $\rho = 0.05\,\mathrm{kg/m^3}$ and $\gamma = \frac{5}{3}$ as a lighter gas. For the heavy third gas case, we use air as a lighter fourth gas and a gas with $\rho = 15\,\mathrm{kg/m^3}$ and $\gamma = \frac{5}{3}$ as a heavier gas.

The presence of a fourth gas can significantly change the growth. For a heavier fourth gas (Fig. 4.22a), growth of the first interface is enhanced. However, the amount of mix does not change significantly (Fig. 4.23). The heavier fourth gas has little effect on the mix. The wave dynamics are such that the reflected rarefactions are stronger and affect the interface for a longer period of time (Fig. 4.24). A lighter third gas suppresses the growth and the mixing as the reflected waves are weaker and their interactions decrease the baroclinic vorticity.

For the heavy third gas case, the growth is enhanced when using a lighter fourth gas (Fig. 4.22b). At the third interface, a rarefaction is reflected back towards the first interface (Fig. 4.26a), initiating a RT growth phase at the first interface. When using a heavier fourth gas, a shock is reflected at the third interface, further amplifying the effect of the first reflected shock by depositing vorticity in the opposite direction as the initial shock and thereby decreasing the growth. Since the growth is small, Ξ increases because there is a small amount of entrained fluid relative to the mixed fluid (Fig. 4.25). For both the heavier and lighter fourth gas cases, M is larger because of the density weighing of the mass fractions. Though the perturbation growth for the heavier fourth gas case is smaller, there is increased mix in the domain.

4.10 Conclusions

In this work, we used a high-order accurate DG method to simulate the interaction of a shock wave with successive interfaces separating different gases. In particular, we investigated the effect of the acoustic impedance (and density) of the third gas on the growth of the RM instability at the different interfaces. Through this study, we make the following conclusions:

- If the third gas is lighter than the second gas, the reflected rarefaction at the second interface amplifies the growth at the first interface for two main reasons: the reflected rarefaction deposits vorticity in the same direction as the incoming shock and the perturbation amplitude at the time of interaction with the rarefaction has grown. If the third gas is heavier, the reflected shock decreases the growth and tend to reverse the perturbation growth as the thickness of the second gas increases. This behavior is governed by RM (instantaneous acceleration of the interface) and RT (acceleration of a heavy fluid into a light one) instabilities, which are both transient in this problem.
- The results strongly depend on the separation distance between the interfaces. We observed freeze-out in the case of a heavy third gas. This study supports the idea that perturbation growth may be controlled using rarefactions and shocks [17].
- We characterized fluid mixing through two different metrics. The light third gas resulted in higher fluid mixing relative to entrained unmixed fluid than the heavy third gas case.
- To represent the behavior at the small scales, we characterized the temporal evolution of enstrophy and energy of the small scales by relating this to the effect of the reflected

waves.

- The phase difference between the perturbations does not affect the growth if the interfaces are far from each other. Because of baroclinic vorticity and interface proximity, the phase difference has a significant effect on the growth if the interfaces are initially close to each other.
- By adding a fourth gas, we can significantly increase the growth in a light-heavy-light-heavy or a light-heavy-heavier-light configuration. This effect is due to the RT-unstable phase of the growth induced by reflected rarefactions.

The present work presents an exploration of a small range of the parameter space; future exploration of the number of layers, gas properties and thicknesses, and amplitude properties are desirable to better understand this problem. This study forms the basis for further three-dimensional studies of randomly perturbed interfaces, transition to turbulence, and late-time mixing evolution. A more in-depth investigation of such a set-up may be beneficial to control perturbation growth in ICF.

CHAPTER V

Interaction of a blast wave with a perturbed interface

5.1 Introduction

Blast wave-driven hydrodynamic instabilities are prevalent in many different scientific and engineering applications [156, 17, 157, and references therein]. Blast waves are formed by a sudden localized deposition of energy which increases the density and pressure of the material at that point [158, 159]. This deposition of energy leads to a shock moving outwards from the energy source point and a rarefaction wave which follows behind the shock. The rarefaction eventually overtakes the shock. The resulting interaction decreases the shock strength [160].

In astrophysics, the explosion from a supernova initiates a blast wave which interacts with many different layers of materials as it radiates outwards from the center of the core collapse [161, 29]. Collisions of comets with planets and their atmospheres may lead to blast waves interacting with different materials [162]. A solar flare can also form a blast wave which then interacts with the solar wind [20].

As a blast wave interacts with a perturbed interface between two fluids, two important hydrodynamic phenomena may take place at interfaces [27]. The shock at the front of a blast wave initiates a Richtmyer-Meshkov (RM) instability[1] [30] by instantaneously depositing baroclinic vorticity at the interface because of the misalignment of the pressure gradient across the shock and the density gradient across the interface. The rarefaction which imme-

---

[1] We emphasize again that this is not a classical instability because it does not exhibit exponential linear growth and does not contain any feedback mechanisms. To stay consistent with the literature, we will keep calling it an instability. We should really be referring to the RM process.

diately follows the shock front imposes a time varying acceleration of the interface, leading to a form of the Rayleigh-Taylor (RT) instability [163, 38].

While shock accelerated or RM instabilities and constant acceleration RT instabilities have been extensively studied in the past [32, 164, 165, 166], blast wave-driven hydrodynamic instabilities and hydrodynamic instabilities with time varying accelerations have recently generated some interest in the community. In traditional fluid mechanics, Vetter and Sturtevant [142], Leinov et al. [167], Morgan et al. [168], Morgan [169] have looked interfaces driven by complex accelerations including RM with reshock and rarefaction driven instabilities.

In high energy density physics, Drake et al. [170] performed initial blast wave-driven experiments of a three-dimensional "egg-crate" patterned perturbation. The experiments suggested that the RT spikes (dense material penetrating into a less dense one) overtook the shock. Kuranz et al. [27] studied the perturbation growth by considering both the compressibility effects of the blast wave as well as the RT instability process due to the blast wave acceleration of the interface. Kuranz et al. [171] performed blast wave-driven instability experiments to study spike penetration. Experimental results showed narrow spikes penetrating deep behind the blast wave shock front. Discrepancies in spike penetration and morphology with simulations were discussed and several hypotheses were proposed.

Computational studies of blast-driven perturbations have explored the effect of the initial conditions on late-time mixing dynamics and transition to turbulence. Miles et al. [172] performed simulations of two-dimensional multimode blast-driven instabilities at drive conditions similar to those achievable at the National Ignition Facility. The authors did not find a self-similar behavior for the development of the mixing layer and showed sensitivity of the mixing layer width to the initial conditions. In a similar study, Miles et al. [173] simulated strong blast waves interacting with perturbed interfaces and discussed the effects of the spike-spike and bubble-bubble interaction on the mix layer growth. In [174], the flow's transition to turbulence was shown to be sensitive to the initial conditions and spectra of the perturbations. Miles [175] combines a buoyancy-drag and bubble-merger model with divergence and compressibility effects and compares the predictions to simulations of cylindrical blast wave-driven instabilities. Finally, Mori [176] used simulations to study the effects of a blast wave interacting with a bubble on suppressing the vorticity production by the rarefaction.

Models for hydrodynamic instabilities generally follow two different directions: the first uses vorticity models to infer the perturbation growth, the second relies on potential flow models. The present discussion will focus on growth and vorticity models that pertain to hydrodynamic instabilities driven by blast waves or subject to time varying accelerations.

Vortex models for the RM instability were first proposed by Samtaney and Zabusky [36], Zabusky et al. [177], Zabusky [178]. Jacobs and Sheeley [37] modeled the growth of single-mode RM instability experiments by assuming a row of line vortices at the interface. Similarly, Rikanati et al. [179] expanded this model and used multi-mode RM instabilities to validate a model of the mixing zone growth using vortex dynamics. Vortex deposition models have had much success modeling RM instabilities [143, 180, 181, 182, 168].

Using potential flow arguments, Oron et al. [39] proposed a buoyancy drag model for the late-time growth of bubbles subject to a RT instability with time varying acceleration. Srebro et al. [183] expanded this model to span the early-mid-late time growth evolution by incorporating exponential decay terms based on the perturbation growth. Miles [184, 28] develop a buoyancy drag model for blast-driven instabilities which incorporate the effects of the shock (RM instability), compressibility, and time dependent acceleration (RT instability). This model was compared successfully to experiments by Kuranz et al. [27]. Miles [184] presents a bubble merger model for multimode perturbations interacting with blast waves. Building on [185], Mikaelian [186] proposed a generalized Layzer model for non-constant complex accelerations of perturbed interfaces with time-varying Atwood numbers. This modeled resulted in a coupled set of ordinary differential equations to solve numerically. Drake [187] modeled the spike and drag induced by the broadening of the spike tip to find that that the resulting drag had a strong effect on the spike penetration.

The objective of this work is to use numerical simulations to investigate two-dimensional planar blast waves interacting with perturbed gas interfaces. The resulting interaction gives rise to RM and RT growth, depending on the shock strength and blast profile. Specifically, we want to identify regimes in which one or the other instability dominates. In contrast with previous studies, we seek to provide models of both the perturbation growth and vorticity production mechanisms for two configurations.

We focus here on a blast wave going from a heavy fluid to a lighter one (RT unstable configuration) as this is the fluid configuration most relevant to supernova physics. However, most of the models we propose do not rely on this assumption. Our analysis is based on simulations of a two-dimensional planar blast wave, modeled by a shock (instantaneous acceleration) followed by a rarefaction (time-dependent deceleration), interacting with a sinusoidal perturbation at an interface between two fluids. Our blast wave model is such that we can control the shock front Mach number, the rarefaction strength and the rarefaction length. Varying these three parameters, as well as the configuration, enables a rigorous exploration of the instability dynamics. We use a high-order accurate Discontinuous Galerkin (DG) method to solve the multifluid Euler equations that model the system.

The chapter is organized as follows. First, we present the physical model and numerical methods. The problem setup, including the fluid properties and blast wave model, is then detailed. After a qualitative description of the problem, we provide models of the position, velocity, and acceleration of a one-dimensional interface driven by a blast wave, as well as models for the volumetric expansion or compression of the interface. These models are validated with one-dimensional simulations. Finally, using simulations of two-dimensional blast wave-driven hydrodynamic instabilities, we develop and validate models of the perturbation growth and vorticity production mechanisms.

5.2 Problem setup

5.2.1 Domain and fluid properties

For the two-dimensional simulations, the domain is half a perturbation wavelength-wide, λ, in the x-direction and 70λ long in the y-direction. Since we are interested in the time evolution of the interface growth, the large domain is necessary to ensure that the interface stays inside the domain as it is being driven by the blast wave. The $x = 0$ and $x = \lambda/2$ boundaries are reflective boundaries, *i.e.* walls, to enable the simulation of just half the domain. Non-reflecting boundary conditions, modeled as zero gradient boundary conditions, are used at the ends of the shock tube. Grid stretching at the top and bottom

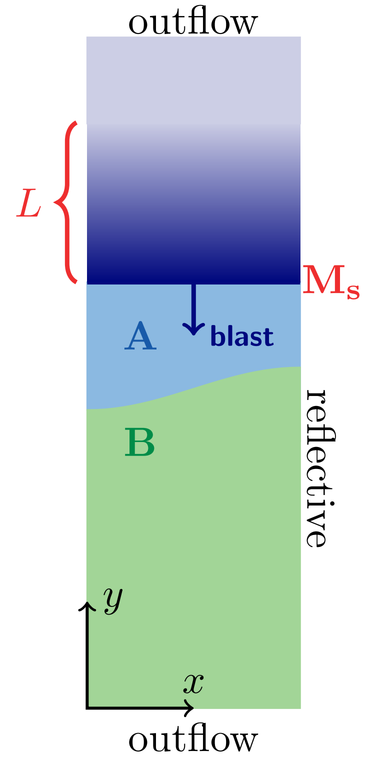

Figure 5.1: Problem setup.

of the shock tube is used to minimize reflections from the boundaries. Otherwise, the mesh is uniform in x and y from $y = -30\lambda$ to $y = 20\lambda$ and there are 200 cells per wavelength. At this resolution, integral quantities are converged. For the DG method, a quadratic polynomial basis ($P = 2$) is used to achieve fifth-order accuracy in smooth regions of the flow. A thermodynamically consistent diffuse interface between the gases [120] is initialized using an exponential diffusion function with an initial thickness of 0.08λ. To measure the mixing layer width, the reported perturbation amplitude is the half difference between the $x = 0$ and $x = 0.5\lambda$ interface locations. The location of the perturbation is defined as the 0.5 contour level of the mass fraction field. The initial perturbation amplitude, a_0, is 0.03λ. The setup is similar for the one-dimensional simulations.

Our problem consists of a model blast wave propagating downwards to interact with with an initially perturbed interface separating two gases A and B of different densities and a constant ratio of specific heats, $\gamma = 1.4$, Figure 5.1. The density of the top fluid ρ_A, is the reference density and the density of the bottom fluid, $\rho_B = \frac{1}{3}\rho_A$. This corresponds to the configuration of a a heavy fluid on top of a light one where the Atwood number

$A = \frac{\rho_A - \rho_B}{\rho_A + \rho_B} = 0.5$. All quantities in this chapter are appropriately normalized by λ, ρ_A, and the speed of sound $c_A = \sqrt{\frac{\gamma \rho_A}{p_0}}$, where $p_0 = 10^5$Pa.

5.2.2 Modeling the blast wave

A sudden and large deposition of energy in a highly localized region in space often results in the formation of a blast wave. The blast wave propagates in the radial direction outwards from the energy source. The blast configuration is that of a shock followed by a rarefaction and analytical solutions of the blast propagation, often referred to as the Taylor-Sedov blast wave solutions, have been extensively studied [158, 159].

In the present study, the blast wave is modeled explicitly as a shock followed by a rarefaction, Figure 5.2. This flexible initialization was chosen to provide precise control over the blast front Mach number, M_s, blast wave strength, K, and blast wave length when it reaches the interface, L. We denote the region ahead of the shock with a subscript 0, the post-shock/pre-rarefaction region with 1, the region inside the rarefaction with r, and the region behind the rarefaction with 2. In contrast with previous studies of blast-drive instabilities where there is an adiabatic rarefaction expanding into a vacuum, the post-rarefaction region is maintained at a constant pressure and velocity. Experimentally, these conditions can be achieved in a shock tube by initiating a shock and designing the reservoir such that the rarefaction reflects off the end of the shock tube and catches up with the shock just as it reaches the interface.

In one-dimensional simulations, the shock is located at y_s, the head of the rarefaction is at y_h and the tail is at y_t. The shock and the rarefaction are both moving towards the left (or downwards in two-dimensional simulations). The distance between the initial positions of the shock and the following rarefaction is such that the rarefaction reaches the interfaces at the same time as the shock, i.e. $y_s = y_h = y_{i0}$ at t_i, where y_{i0} is the initial interface location and t_i is the time of when the blast wave reaches the interface.

In the post-shock region, given a Mach number, the shock relations determine ρ, u, and

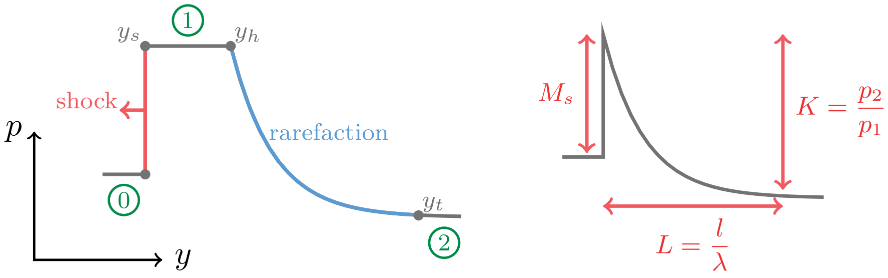

(a) Initial profile and definition of the different flow regions.

(b) Profile at interface interaction time, t_i, with the problem parameters.

Figure 5.2: Schematics of modeled blast wave pressure profile.

p:

$$\frac{\rho_1}{\rho_0} = \frac{(\gamma+1)M_s^2}{(\gamma-1)M_s^2+2}, \tag{5.1a}$$

$$u_1 = 1 - \frac{\rho_0}{\rho_1}u_s, \tag{5.1b}$$

$$\frac{p_1}{p_0} = \frac{2\gamma M_s^2 - (\gamma-1)}{\gamma+1}, \tag{5.1c}$$

where the shock velocity $u_s = -M_s c_0$. The shock position is $y_s(t) = u_s t + y_{s0}$ where y_{s0} is the shock origin.

The strength of the rarefaction, K, is defined as $K = \frac{p_2}{p_1}$ and determines the flow conditions in region 2:

$$\frac{\rho_2}{\rho_1} = K^{\frac{1}{\gamma}}, \tag{5.2a}$$

$$u_2 = \frac{2c_1}{\gamma-1}\left(1 - K^{\frac{\gamma-1}{2\gamma}}\right) + u_1, \tag{5.2b}$$

The rarefaction is moving into a flow moving at the post-shock velocity u_1. Inside the rarefaction, we have

$$\frac{\rho_r}{\rho_1} = \left(1 - \frac{\gamma - 1}{2}\frac{|u_r - u_1|}{c_1}\right)^{\frac{2}{\gamma-1}}, \tag{5.3a}$$

$$u_r = \frac{2}{\gamma + 1}\left(c_1 - u_1 + \frac{y - y_{r0}}{t}\right) + u_1, \tag{5.3b}$$

$$\frac{p_r}{p_1} = \left(1 - \frac{\gamma - 1}{2}\frac{|u_r - u_1|}{c_1}\right)^{\frac{2\gamma}{\gamma-1}}, \tag{5.3c}$$

where y_{r0} is the rarefaction origin. The rarefaction head location is $y_h = -(c_1 - u_1)t + y_{r0}$ and the tail location is $y_t = -\left(c_1 - u_1 - \frac{\gamma+1}{2}(u_2 - u_1)\right)t + y_{r0}$. The non-dimensional length of the rarefaction is therefore $L = \frac{l}{\lambda} = |y_h - y_t| = \frac{\gamma+1}{2}(u_2 - u_1)t$. Given M_s, K, and L, we can determine y_{s0} and y_{r0} such that the shock and rarefaction coalesce to form a blast wave as they reach the interface. The time at which a rarefaction of length L reaches the interface is $t_i = \frac{2}{\gamma+1}\frac{L}{u_2-u_1}$. Using t_i, we can solve for the shock and rarefaction origins:

$$y_{i0} = y_s(t_i) \quad \Rightarrow \quad y_{s0} = y_{i0} - u_s t_i, \tag{5.4a}$$

$$y_{i0} = y_h(t_i) \quad \Rightarrow \quad y_{r0} = y_{i0} + (c_1 - u_1)t_i. \tag{5.4b}$$

The simulations are initialized at $t_0 = 0.5t_i$. This setup provides similar Mach number decay rates and blast profiles as the point blast initialization, Figure 5.3, and allows us to explicitly control the shock Mach number, the rarefaction length, and the rarefaction strength.

5.3 Perturbation growth of a blast-driven interface

Before exploring our analysis of the blast-driven hydrodynamic instability, we first present some qualitative results of the perturbation dynamics through visualizations of density, simulated Schlieren, and vorticity from a blast wave with $M_s = 3$, $K = 0.1$, and $L = 1$ interacting with a heavy-light interface, Figure 5.4. We also show plots of the amplitude and circulation corresponding to each of the snapshots, Figures 5.4e and 5.4f. Figure 5.4a illustrates the initial condition. The blast wave moves downward and can be clearly identified in the density and Schlieren figures. When the shock hits the interface, Figure 5.4b,

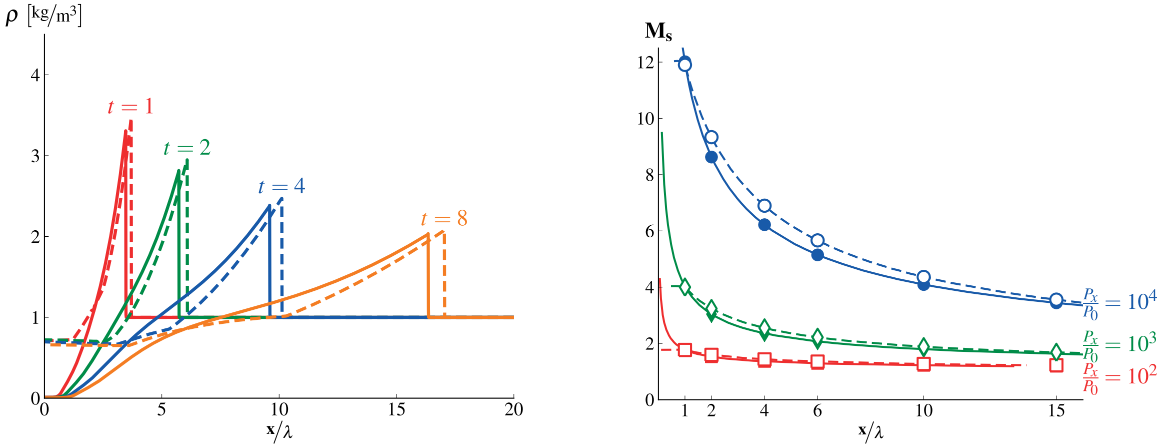

(a) Density profile of the blast wave as a function of time.

(b) Decay of the shock front Mach number as a function of distance traveled by the blast wave for different initial blast pressure ratios.

Figure 5.3: Comparison of the density profile and shock Mach number for a blast wave initialized by a localized deposition of energy and our model of the blast wave using a shock and a rarefaction. Solid lines and symbols: point-source blast wave; dashed lines and empty symbols: model blast wave.

it induces a phase reversal of the interface and generates vorticity at the interface because of the misalignment of the density gradient across the interface and the pressure gradient across the shock. We refer to this early and short-lived phase as the RM phase. As the rarefaction behind the shock interacts with the interface it continues to generate baroclinic vorticity because of the misalignment of the density and pressure gradients, Figure 5.4c. The perturbation amplitude and circulation in the domain increase accordingly. During this interaction phase, the interface is being both accelerated and decompressed. Finally, after the wave has left the interface, the circulation remains constant and the perturbation keeps growing because of the vorticity at the interface, Figure 5.4d. We refer to this as the coasting phase. In the following sections, we explore each phase and provide modeling insight into the growth and vorticity dynamics.

5.4 One-dimensional perturbation growth

In this section, we develop models of volumetric expansion, interface acceleration, and blast wave interaction time with the interface. Volume changes of the material due to the passage of the blast wave will contribute to the growth of the interface perturbation. Un-

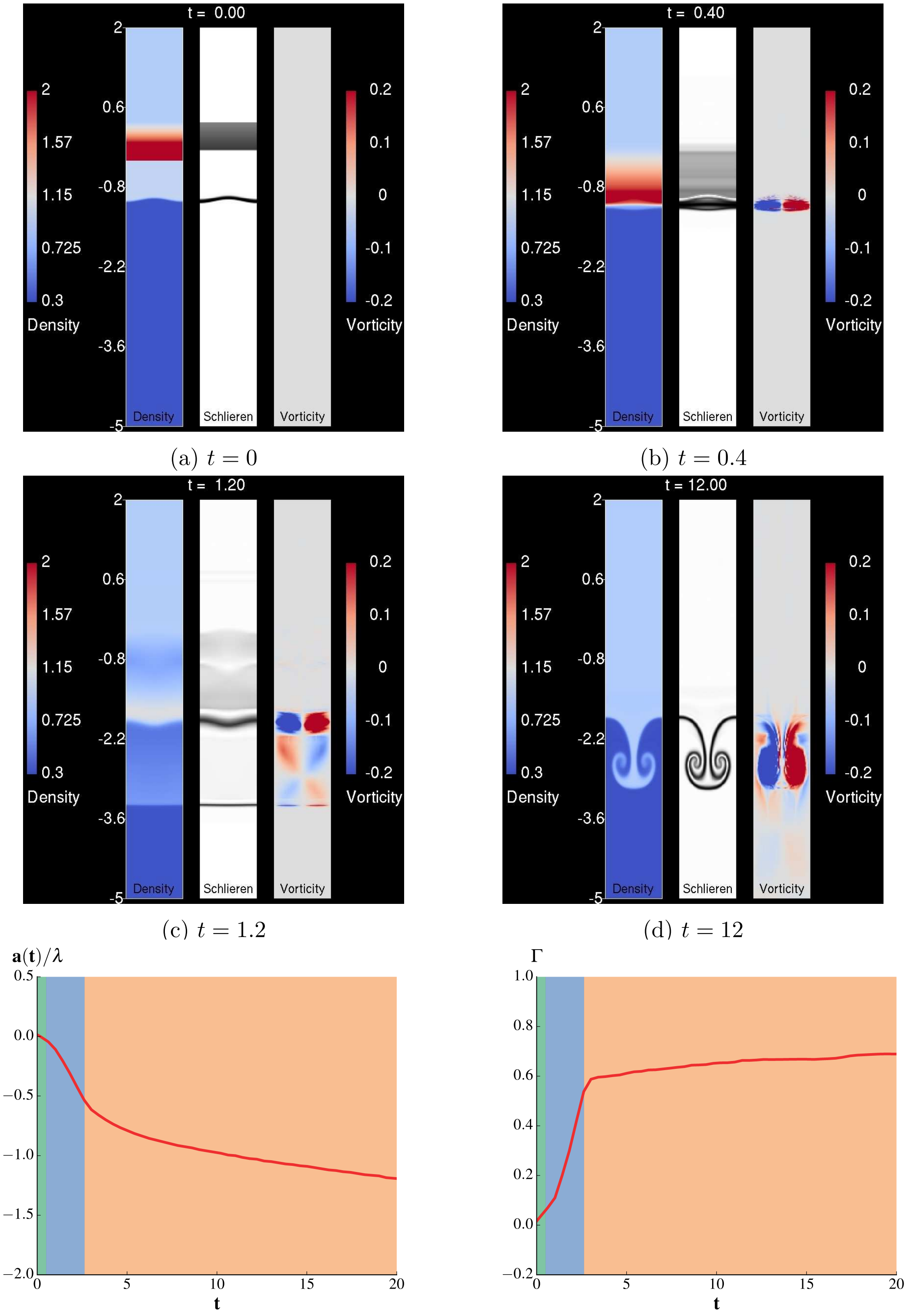

(a) $t = 0$

(b) $t = 0.4$

(c) $t = 1.2$

(d) $t = 12$

(e) Amplitude as a function of time.

(f) Circulation as a function of time.

Figure 5.4: A blast with $M_s = 3$, $K = 0.1$, and $L = 1$ interacts with an interface. Visualizations of density, simulated Schlieren, and vorticity, as well as plots of perturbation growth and circulation. Shaded green background: early phase (RM); shaded blue background: interaction phase; shaded orange background: coasting phase.

derstanding the interface acceleration is important for modeling the growth of the interface due to the RT instability. Finally, the interaction time between the blast wave and the interface will determine the duration during which the interface will undergo volumetric expansion and unstable growth. We explore these three quantities through one-dimensional models and simulations.

5.4.1 Volumetric expansions of blast waves at interfaces

As the blast wave traverses the material, it changes the material volume by compressing it first (the shock front) and then decompressing it (the following rarefaction). Volumetric changes will have an effect on the growth of the perturbation. Models for volumetric changes will be useful in determining the decompression effects on the two-dimensional perturbation growth.

We start by analyzing the volumetric expansion associated with a pure rarefaction interacting with an interface. Using the simple wave theory of gas dynamics and the method of characteristics, we can explicitly solve for the states of the gases after the rarefaction has interacted with the interface, Figure 5.5a. Assuming a pure rarefaction interacting with a gas-gas interface, with the rarefaction initialized in the A medium and moving into the B medium, the isentropic relations state that the ratio of sound speeds pre- and post-rarefaction interaction is

$$\frac{c_{Ar}}{c_A} = 1 - T\frac{\gamma - 1}{2}\frac{u_2}{c_A} \tag{5.5a}$$

$$\frac{c_{Br}}{c_B} = 1 - T\frac{\gamma - 1}{2}\frac{u_2}{c_A} \tag{5.5b}$$

where c_A is the initial sound speed in the A medium, c_{Ar} the sound speed in medium A after rarefaction interaction, c_B the initial sound speed in the B medium, c_{Br} the sound speed in medium B after rarefaction interaction, $T = \frac{2\alpha}{\alpha+1}$ the transmission coefficient ($\alpha = \frac{c_A}{c_B}$). By combining the isentropic relations and the expression relating the sound speed to pressure,

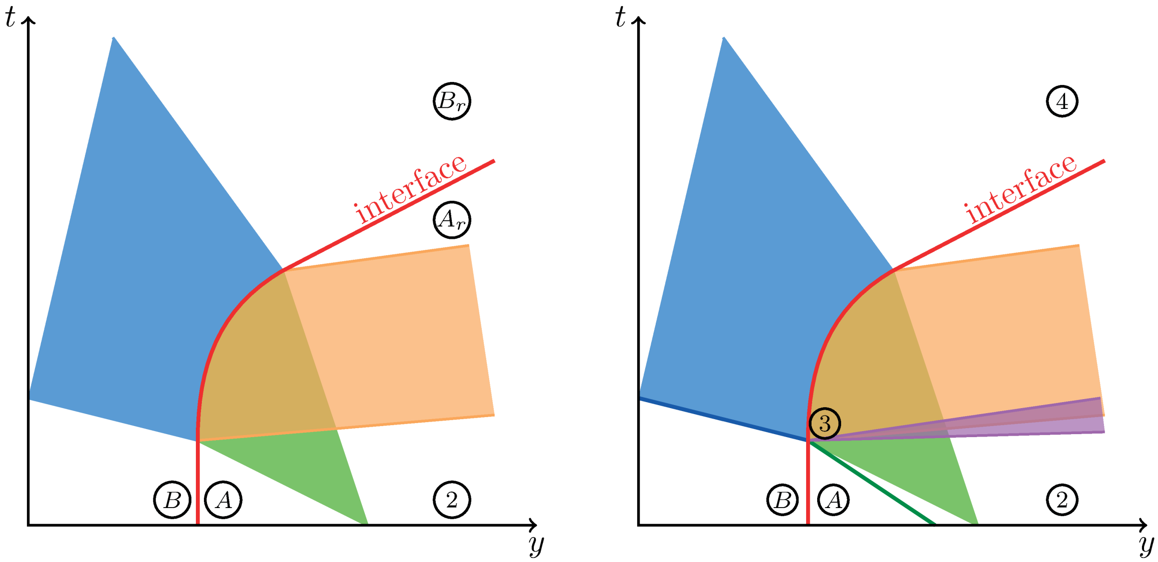

(a) Rarefaction interaction. Green: incoming rarefaction; blue: transmitted rarefaction; orange: reflected rarefaction.

(b) Blast wave interaction. Green: incoming rarefaction and shock; blue: transmitted wave; orange: reflected wave; purple: reflected wave from the shock.

Figure 5.5: Schematic representing the interaction of a waves with an interface.

we have

$$\frac{p_{Br}}{p_0} = \left(\frac{c_{Br}}{c_B}\right)^{\frac{2\gamma}{\gamma-1}} \tag{5.6a}$$

$$\frac{\rho_{Br}}{\rho_B} = \left(\frac{c_{Br}}{c_B}\right)^{\frac{2}{\gamma-1}} \tag{5.6b}$$

and similarly for material A. Therefore, the associated volume change due to the passage of the rarefaction is

$$a_{Ar} = a_A \left(\frac{p_{Ar}}{p_0}\right)^{\frac{-1}{\gamma}} \tag{5.7a}$$

$$a_{Br} = a_B \left(\frac{p_{Br}}{p_0}\right)^{\frac{-1}{\gamma}} . \tag{5.7b}$$

For a blast wave, we must take into account the effect of the shock. When the blast is going from a heavy gas into a lighter one, there is a reflected rarefaction and a transmitted shock, Figure 5.5b. The reflected rarefaction is going to interact with the incoming rarefaction wave (the main part of the blast wave) and change its properties.

Though the shock and incoming rarefaction reach the interface at the same time, for the purpose of determining the effect of the reflected waves on the the incoming rarefaction, we break down the problem into two parts:

1. the shock hits the interface and a reflected rarefaction is created;
2. this reflected rarefaction interacts with the incoming rarefaction wave.

For the first part, we assume that the characteristics of this reflected rarefaction are solely determined by solving the Riemann problem of the shock interacting with the interface. An exact Riemann solver provides the density, velocity, and pressure of the reflected rarefaction. We denote the state between the transmitted shock and the reflected rarefaction with subscript 3. We note that this region is used for derivation purposes only, in reality it is vanishingly small since the shock and rarefaction are timed to reach the interface at the same time.

Following the derivation of Courant and Friedrichs [188], we solve the interaction of this reflected wave with the incoming rarefaction to determine its effect on the main rarefaction. The state behind the incoming rarefaction, after the reflected wave has interacted with it, is denoted with subscript 4. The pressure and volume in this state can be determined as

$$\frac{p_4}{p_3} = \left(\frac{c_4}{c_3}\right)^{\frac{2\gamma}{\gamma-1}} \quad \text{and} \quad \frac{V_4}{V_3} = \left(\frac{p_4}{p_3}\right)^{\frac{-1}{\gamma}},$$

where $c_4 = \frac{\gamma-1}{4}\left(u_3 - u_2 + \frac{2}{\gamma-1}(c_3 + c_2)\right)$. The strength of the modified rarefaction, $\frac{p_4}{p_1}$ is increased with respect of the original rarefaction strength, K, because the reflected rarefaction decompresses the incoming one. The length of the rarefaction does not influence the volume change felt by the interface because the length does not influence the pressure in the post-wave region. This model for the volume change was implemented and shows good agreement with one-dimensional simulations across a wide range of shock mach numbers and rarefactions strengths, Figure 5.6. The volume change in the simulations was measured by tracking Lagrangian particles initially located at $\pm a_0$ with respect to the interface.

This model enables us to map the decompression ratio, $\nu = \frac{a_4}{a_0}$, as a function of M_s and K. The length of the rarefaction does not influence the decompression near the inter-

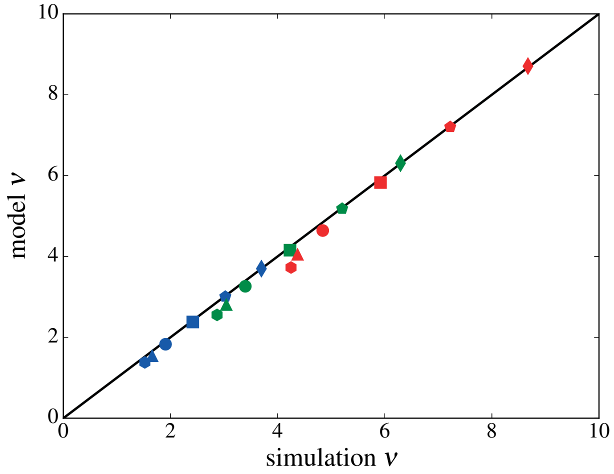

Figure 5.6: Volumetric change, ν, from simulation compared to the volumetric change, predicted by our model. Solid black line: exact. Symbol fill color denotes K: red: $K = 0.05$; green: $K = 0.1$; blue: $K = 0.3$. Symbol type denotes M_s: square: $M_s = 1$, diamond: $M_s = 1.2$, circle: $M_s = 2$, pentagon: $M_s = 2.5$; hexagon: $M_s = 3$.

face. Figure 5.7 shows how this ratio varies in the M_s-K phase space. As the blast wave strength increases ($K \to 0$), the decompression ratio increases. Similarly, as the Mach number increases, the decompression ratio increases as well. However, beyond $M_s = 5$, the compression from the shock reaches the strong shock limit, *i.e.* the maximum compression from a single shock is reached, and increasing M_s no longer has an effect on the volumetric change. The red line in Figure 5.7 delineates the $\nu = 1$ contour. To the right of this line, ν is less than one, indicating that volumetric change does not play a significant role in the perturbation growth. The region corresponding to $\nu < 1$ indicates a region in the phase space where volume changes significantly affect the perturbation growth.

5.4.2 Interface acceleration and interaction time

The duration over which the interface will experience an acceleration as well as the acceleration itself are important as they determine the RT unstable growth phase of the perturbation. Exact expressions for the interaction time, t_e, and accelerations, g, for the model blast wave do not exist. We propose here models to approximate these quantities.

To estimate the interaction time and interface acceleration, an example of which is shown in Figure 5.10, we combine two different approximations of the interface trajectory by the model blast wave. The first approximation relies on using the incoming rarefaction (main part of the blast wave), suitably modified to account for the reflected wave due to the shock and reflections at the interface, Figure 5.8a. The interface position driven by this rarefaction can be found by solving the following ordinary differential equation:

$$\frac{\mathrm{d}\widetilde{y}_i}{\mathrm{d}t} = (1-R)\frac{2}{\gamma+1}\left(c_{A1} - u_1 + \frac{\widetilde{y}_i - y_{r0}}{t}\right) + u_3$$

where R is the (post-shock) reflection coefficient accounting for the incoming rarefaction reflections at the interface, $c_{A1} - u_1$ is the velocity of the rarefaction wave head, and u_3 is the velocity of the interface right after the shock hits it. Solving this equation and then differentiating $\widetilde{y}_i(t)$ provides the interface velocity, $\widetilde{u}_i(t)$, and the interface acceleration, $\widetilde{g}(t)$. An approximation of the interaction time can be determined by solving for the intersection of the rarefaction tail and the interface position. The rarefaction tail does not follow a simple path in the y-t plane because it traverses a fluid with variable sound speed (due to the reflections from the interface). However, we assume that it travels at a constant velocity, given by the post-interaction state, $\frac{\gamma+1}{2}u_4 - c_{A4}$, where $u_4 = (1-R)u_2$, an approximation of the interface velocity after the blast wave interaction. This is similar to assuming that the interface is being driven by a rarefaction with a different post-rarefaction state. Though not immediately obvious, it can be shown, by comparing the velocities and trajectories of this assumed tail and the original tail, that this will provide an overestimate of the interaction time for the case of a heavy-light interface (and an underestimate for a light/heavy interface).

Similarly, a second approximation of the interface dynamics and the interaction time can be obtained by looking at the transmitted rarefaction wave, Figure 5.8b. We assume an interface driven now by a centered rarefaction originating at

$$\hat{y}_{r0} = y_{i0} + (c_{B3} - u_3)t_i.$$

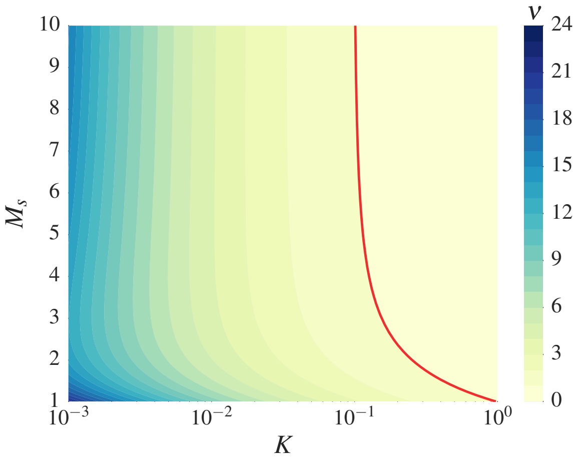

Figure 5.7: Decompression ratio, $\nu = \frac{V_4}{V_0}$, as a function of rarefaction strength, K, and shock Mach number, M_s. Solid red line: $\nu = 1$ contour.

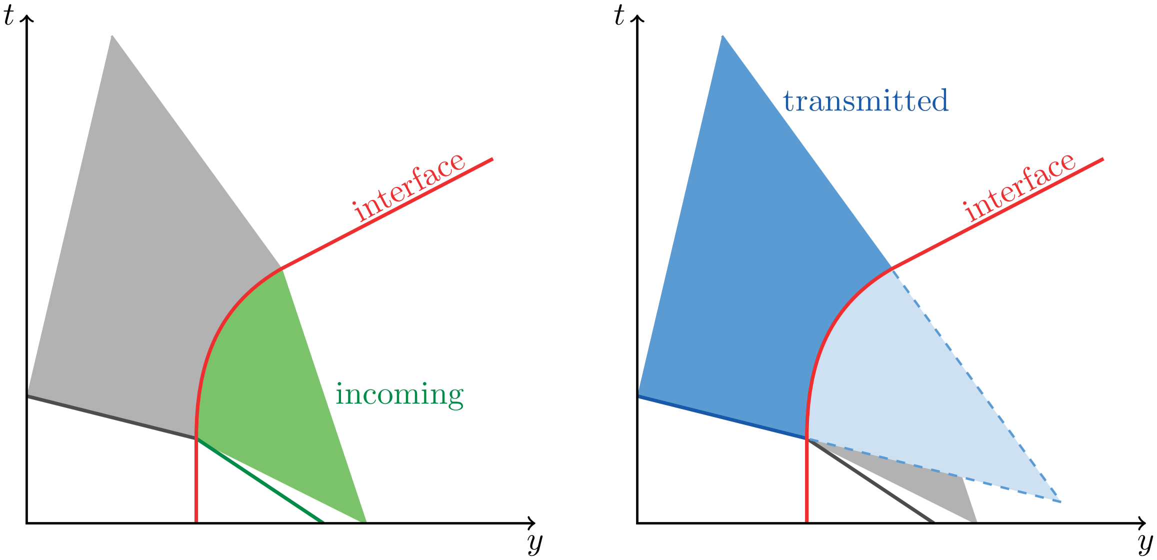

(a) Interface driven by the incoming wave.

(b) Interface driven by the transmitted wave.

Figure 5.8: Schematic representing the incoming and transmitted waves driving the interface.

The interface position is then given by

$$\frac{\mathrm{d}\hat{y}_i}{\mathrm{d}t} = (1-R)\frac{2}{\gamma+1}\left(c_{B3} - u_3 + \frac{\hat{y}_i - \hat{y}_{r0}}{t}\right) + u_3$$

where we recall that $c_{B3} - u_3$ is the velocity of the transmitted rarefaction wave head in the B fluid right behind the transmitted shock. Differentiating the solution to this equation provides the interface velocity and accelerations. Again, we assume that the tail of this rarefaction travels at a constant velocity, $\frac{\gamma+1}{2}u_4 - cB4$. Solving for the intersection of the interface with this tail determines a second approximation of the interaction time. In contrast with our previous estimate, a similar analysis of the tail velocities shows that this provides an underestimate of the interaction time for a heavy-light interface (and an overestimate for a light-heavy interface).

Since our two approximations of the interface dynamics, one based on the incoming rarefaction, the other on the transmitted rarefaction, provide an overestimate and an underestimate, we average the interface dynamics and interaction times from both predictions. We verified these predictions by comparing to one-dimensional simulations and obtained good agreement in the parameter range of interest, Figure 5.9.

Using this model of the interface dynamics enables the systematic analysis of the interface acceleration. According to Shvarts et al. [189], if the interface is experiencing an acceleration which decays as $g(t) \sim t^{\beta}$ and $\beta < -2$, then the interface is undergoing a RM instability. If $\beta > -2$, *i.e.* the acceleration decays slowly, then the interface is undergoing a RT instability. For $\beta = 0$, the acceleration is constant, corresponding to the classical RT instability. Our model of the interface acceleration can be used to provide an estimate of the decay parameter, β, as a function of M_s, K, for $L = 1$, Figure 5.11. Across the range of interest, β is close to one, indicating that the interface is in the RT regime. The decay parameters decreases with increasing L but increases with increasing Mach number and rarefaction strength. Since the wave has a finite length and the velocity is constant in the post-wave region, the interface acceleration goes to zero after the wave leaves the interface, Figure 5.10.

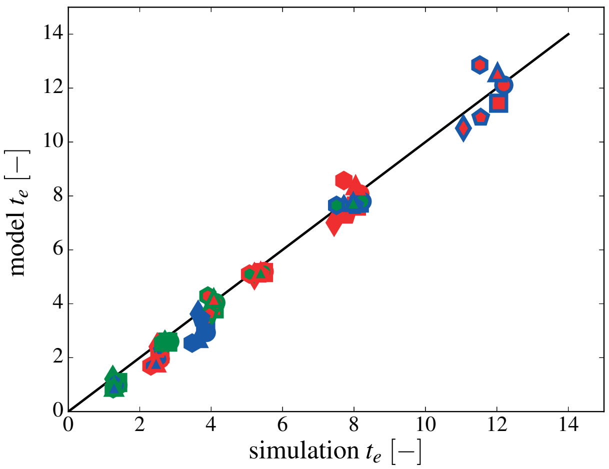

Figure 5.9: Interaction time from simulation compared to the interaction time predicted by our model. Solid black line: exact. Symbol fill color denotes K: red: $K = 0.05$; green: $K = 0.1$; blue: $K = 0.3$. Symbol edge color denotes L: red: $L = 1$; green: $L = 2$; blue: $L = 3$. Symbol type denotes M_s: square: $M_s = 1$, diamond: $M_s = 1.2$, circle: $M_s = 2$, pentagon: $M_s = 2.5$; hexagon: $M_s = 3$.

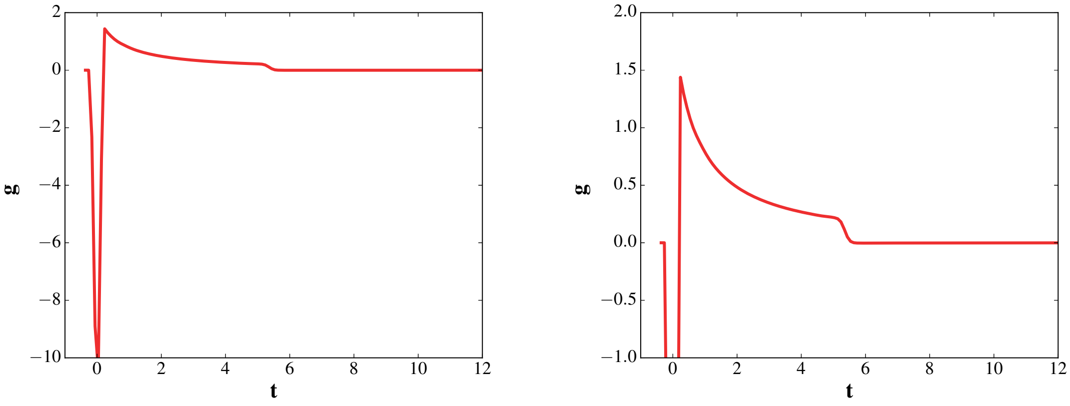

(a) Interface acceleration

(b) Zoom of left figure.

Figure 5.10: Acceleration as a function of time for $M_s = 3$, $L = 2$, $K = 0.1$.

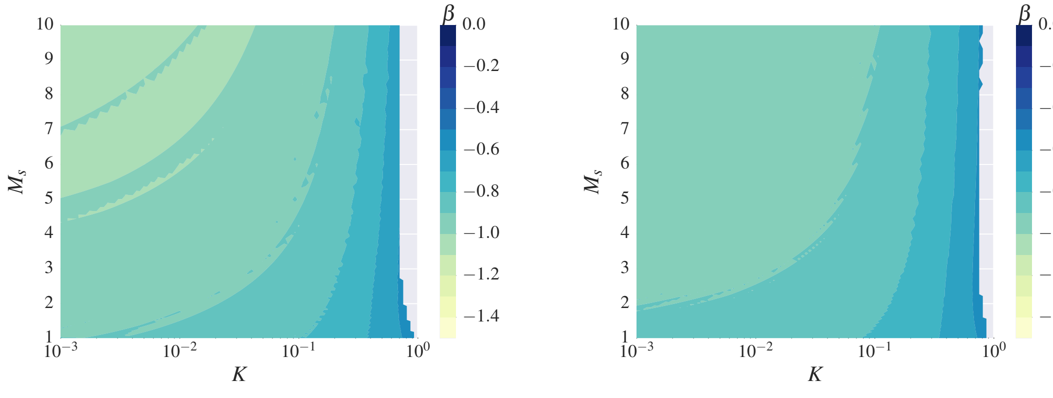

(a) $L = 1$.

(b) $L = 3$.

Figure 5.11: Acceleration decay parameter, β, as a function of rarefaction strength, K, and shock Mach number, M_s.

5.5 Growth and vorticity dynamics of a blast-driven instability

In this section, we explore the perturbation growth and the vorticity dynamics for a single-mode perturbation driven by the model blast wave.

5.5.1 The early phase

The early growth phase is dominated by shock dynamics. As previously discussed, the shock deposits baroclinic vorticity at the interface through the last term in the vorticity evolution equation for a two-dimensional inviscid flow:

$$\frac{\partial \omega}{\partial t} + (\mathbf{u} \cdot \nabla)\omega = \omega(\nabla \cdot \mathbf{u}) + \frac{1}{\rho^2}(\nabla \rho \times \nabla p). \tag{5.8}$$

The evolution equation for the circulation in the half-domain, $\Gamma = \int_S \omega \, \mathrm{d}S$, is

$$\frac{\partial \Gamma}{\partial t} = \int_S \frac{1}{\rho^2}(\nabla \rho \times \nabla p) \, \mathrm{d}S \tag{5.9}$$

It can be shown that the other two terms in Eq. (5.8), though they are different fields locally, balance each other when integrated in the half domain, see Appendix D. The following initial

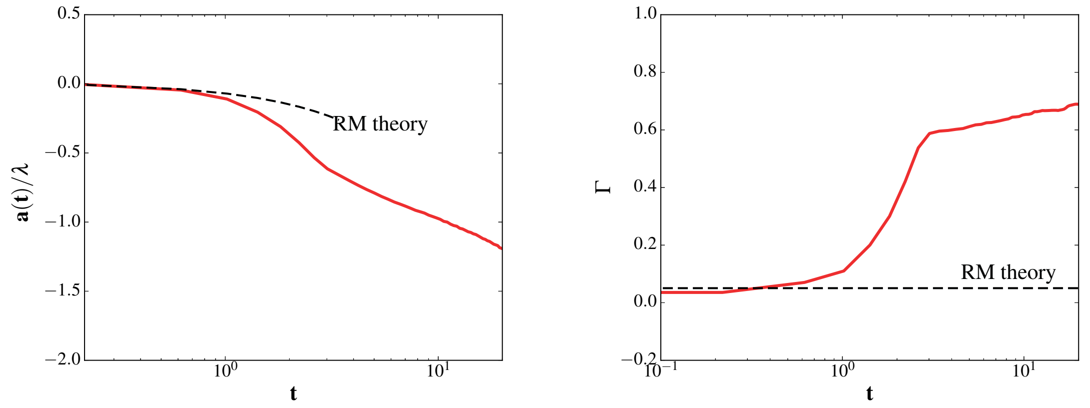

(a) Perturbation amplitude as a function of time.

(b) Circulation as a function of time.

Figure 5.12: Early phase amplitude and circulation for $M_s = 3$, $L = 1$, and $K = 0.1$.

perturbation growth rate has previously been proposed [30]:

$$\dot{a}(t) = k \Delta u A a_0$$

where $k = \frac{2\pi}{\lambda}$, Δu is the velocity change due to the shock, A is the Atwood number, and a_0 is the initial perturbation amplitude. Other work [190] has indicated that some restrictions to this model may apply. However, this model is a good first approximation for the growth in this phase.The vorticity distribution and the circulation have been shown to be [37]

$$\omega(x) = -2\dot{a}_0 \sin(kx) \quad \text{and} \quad \Gamma = \frac{-4}{k}\dot{a}_0.$$

There is good agreement between these predictions for the perturbation growth and circulation and the simulation results at early time, Figure 5.12. These quantities will form the initial conditions for modeling the interaction phase, the subsequent growth phase.

5.5.2 The interaction phase

During the interaction phase, the growth of the perturbation is driven by two simultaneous effects: volumetric change due to the change in pressure from the rarefaction; and the RT instability from the time-varying and transient acceleration of a heavy fluid into a light one. Similarly to previous studies [27], we assume that these effects are additive

$$a(t) = a_{\text{vol}}(t) + a_{\text{inst}}(t)$$

where $a_{\text{vol}}(t)$ is the perturbation growth due to volumetric change and $a_{\text{inst}}(t)$ is the growth due to the acceleration. We have already discussed and provided models for the growth of the perturbation due to volumetric change in Section 5.4.1. As indicated by our study of the interface acceleration, we focus on RT models of the perturbation growth. The most common model for the non-linear stage of the RT instability with a time varying acceleration field is a buoyancy-drag model detailed in [39],

$$(\rho_b + C_a\rho_s)\frac{\mathrm{d}u_b}{\mathrm{d}t} = (\rho_s - \rho_b)g(t) - \frac{C_d}{\lambda}\rho_s u_b^2 \tag{5.10a}$$

where ρ_b is the bubble density, ρ_s the spike density, u_b the bubble velocity with respect to the one-dimensional interface, C_a the added mass coefficient ($C_a = 2$ in two dimensions), and C_d the drag coefficient ($C_d = 6\pi$ in two dimensions). The model has some success describing the bubble evolution in the non-linear stages of the perturbation growth. Srebro et al. [183] proposed the addition of a dependence on the amplitude growth to model the early-mid-late stages of the growth through a term, $E(t) = \exp(-C_e k h_b)$, where h_b is the bubble height, $k = \frac{2\pi}{\lambda}$, and $C_e = 3$ in two dimensions. The bubble growth model then becomes

$$\begin{aligned}\left((C_aE(t)+1)\rho_b + (C_a + E(t))\rho_s\right)\frac{\mathrm{d}u_b}{\mathrm{d}t} &= \\ (1-E(t))(\rho_s-\rho_b)g(t) &- \frac{C_d}{\lambda}\rho_s u_b^2.\end{aligned} \tag{5.11a}$$

In the linear growth stage, a first order expansion about h_b reduces this model to

$$\frac{\mathrm{d}u_b}{\mathrm{d}t} = Akh_bg(t). \tag{5.12a}$$

Figure 5.13 illustrates the growth of the bubble and spike with respect to the interface (from one dimensional simulations) and compares it to the predictions from the buoyancy-drag

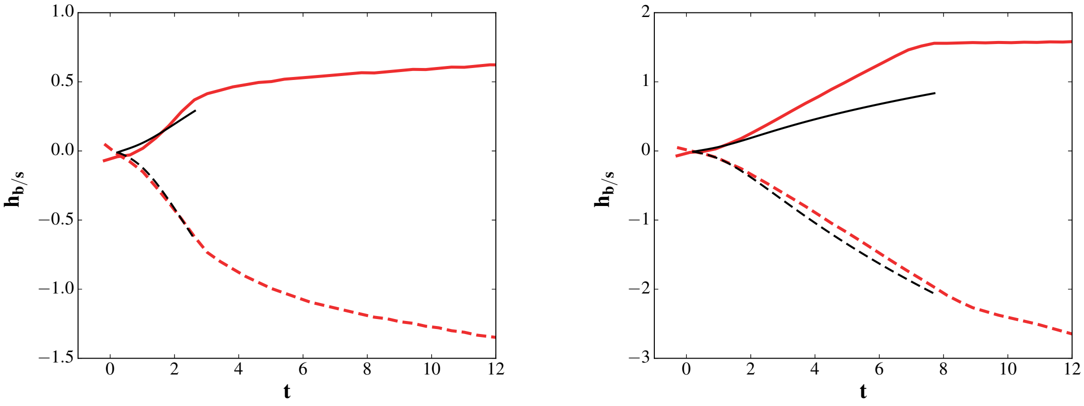

(a) $M_s = 3$, $L = 1$, $K = 0.1$ (b) $M_s = 3$, $L = 2$, $K = 0.05$

Figure 5.13: Bubble and spike growth as a function of time in the interaction phase (blue shading). Solid red: bubble growth, h_b; dashed red: spike growth, h_s; solid black: buoyancy drag model of bubble growth; dashed black: buoyancy drag model of spike growth.

model. The growth model seems to accurately describe the growth of the perturbation during the interaction phase.

5.5.3 The coasting phase

After the wave leaves the interface, the vorticity present at the interface continuously induces perturbation growth. The circulation is constant in this phase as there is no source or sink of circulation (excepting of course numerical diffusion). In this phase, buoyancy-drag models fail to capture the growth dynamics as the acceleration field is zero.

Dimensional analysis of the growth suggests that

$$a(t) \sim \sqrt{\Gamma_c t} \tag{5.13}$$

where Γ_c is the constant circulation in this growth phase and can be expressed as:

$$\begin{aligned}
\Gamma_c &= \int_{t_e} \int_S \frac{\nabla\rho \times \nabla p}{\rho^2} \, \mathrm{d}S \, \mathrm{d}t && (5.14) \\
&= \int_{t_e} \int_S \frac{|\nabla\rho||\nabla p| \sin\theta}{\rho^2} \, \mathrm{d}S \, \mathrm{d}t && (5.15) \\
&= f(|\nabla\rho|, |\nabla p|, \rho, \theta, a, \lambda, t) && (5.16)
\end{aligned}$$

where we integrate baroclinic vorticity generation over the wave interaction time and the area containing the interface, S. The quantities in the integral can be related to the input parameters. The $\sin\theta$ term depends on t and S but is mostly $\mathcal{O}(1)$, *i.e.* $\sin\theta \in [0,1]$. Since the interaction time between the interface and the blast wave also scales linearly with the blast wave length, the wave interacts for a longer time and, therefore, generates correspondingly more vorticity at the interface. Ignoring the effect of reflections on pressure, the pressure inside the rarefaction can be related to L and K as such:

$$p_r = p_0 \left(1 - \frac{\gamma-1}{\gamma+1} - \frac{\gamma-1}{\gamma+1}\frac{y_i}{L}\left(1 - K^{\frac{\gamma-1}{2\gamma}}\right)\right)^{\frac{2\gamma}{\gamma-1}} \tag{5.17}$$

Finally, assuming an isentropic flow, the density is related to the pressure:

$$\rho_r = \rho_0 \left(\frac{p_r}{p_0}\right) \tag{5.18}$$

and a corresponding equation for the density gradient can be obtained. Plugging the resulting expressions into Eq. (5.15), it can be shown after some manipulation, that

$$\Gamma_c = F(M_s, A) L \left(1 - K^{\frac{\gamma-1}{2\gamma}}\right)^2 . \tag{5.19}$$

This hypothesis can be verified by observing that Γ_c does indeed scale linearly with the blast wave length, Figure 5.14. However, the slope of this linear relationship depends strongly on the rarefaction strength and the shock Mach number. Additionally, Γ_c also follows a quadratic power law with the rarefaction strength, Figure 5.15. For $M_s = 1.2$, there seems to be a strong interaction between a weak shock and the rarefaction that negatively affects the power law scaling.

In Figures 5.16 and 5.17, we show for various parameter sets, the perturbation growth as a function of time. For a fixed M_s and K, increasing L increases the perturbation growth because the RT unstable phase lasts longer, Figure 5.16a. For a fixed K and different M_s, the growth increases with increasing M_s and K, Figure 5.17a. However, dividing the perturbation growth by $\sqrt{\Gamma_c t}$ leads to a collapse of the data around -0.4, Figure 5.16b and 5.17b. This indicates that vorticity is indeed the main driver of perturbation growth in this

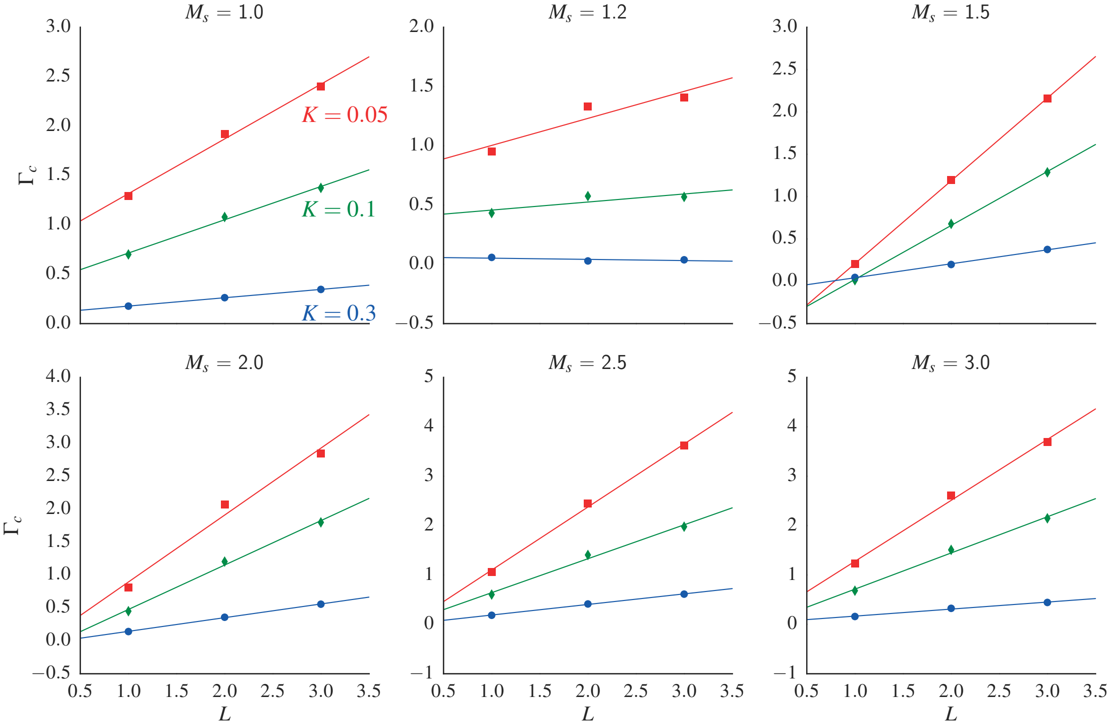

Figure 5.14: Circulation in the coasting phase, Γ_c, as a function of rarefaction length, L, for different shock Mach numbers, M_s, and rarefaction strengths, K. Red squares: $K = 0.05$; green diamonds: $K = 0.1$; blue circles: $K = 0.3$. Corresponding lines are a linear fit to the data.

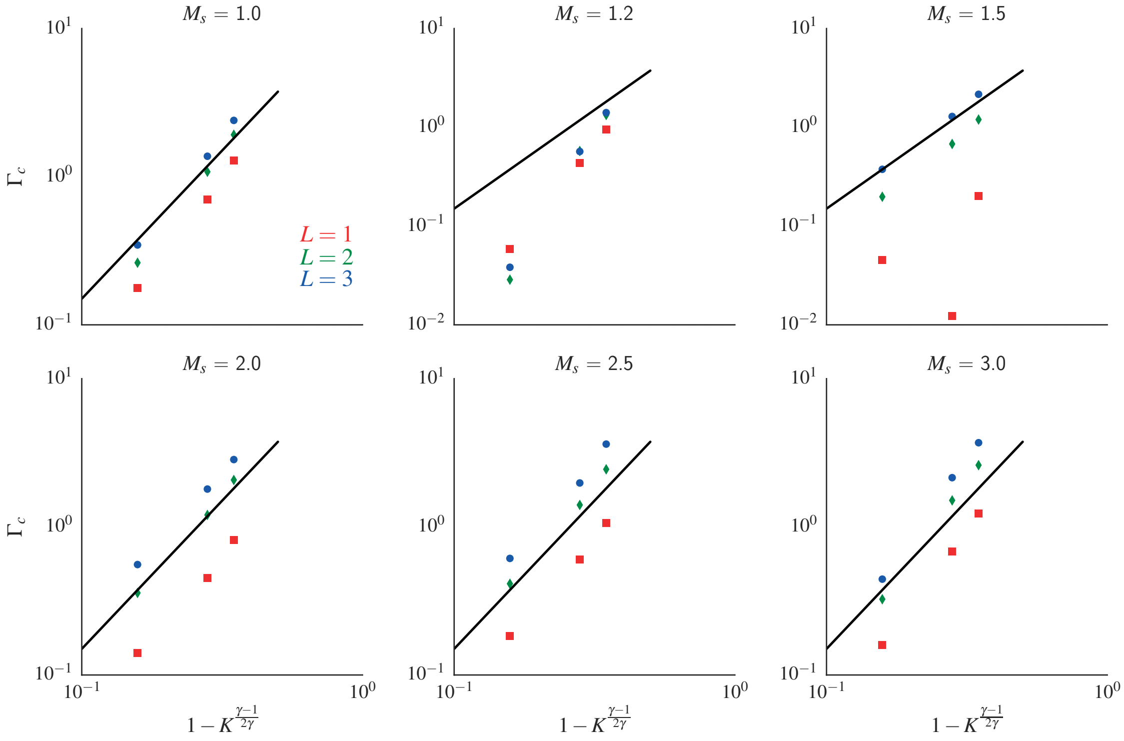

Figure 5.15: Circulation in the coasting phase, Γ_c, as a function of $\left(1 - K^{\frac{\gamma-1}{2\gamma}}\right)$, for different shock Mach numbers, M_s, and rarefaction lengths, L. Red squares: $L = 1$; green diamonds: $L = 2$; blue circles: $L = 3$. Black lines correspond to quadratic power law.

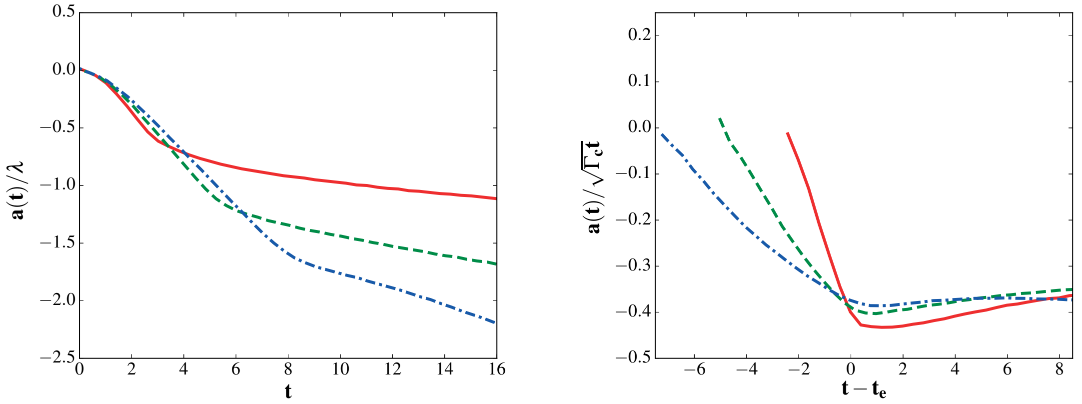

(a) Growth as a function of time.

(b) Growth normalized by $\sqrt{\Gamma_c t}$ and shifted by the interaction time t_e.

Figure 5.16: Perturbation growth as a function of time for a fixed $M_s = 3$ and $K = 0.1$. Solid red: $L = 1$; dashed green: $L = 2$; dot-dashed blue: $L = 3$.

phase and the circulation can be used to capture the perturbation growth.

5.6 Conclusion

In this chapter, we investigated the interaction of a blast wave with an interface in an RT-unstable configuration (based on the blast wave acceleration profile). We modeled the blast wave by a shock followed by a rarefaction, both initiated to reach the interface at the same time and form a blast wave profile. This blast wave model was validated through comparisons of point source blast wave simulations. Using fundamental gas dynamics theory, we elucidated the dynamics and, based on this knowledge, developed one-dimensional models of the interface dynamics, focusing on the volumetric change and interface acceleration due to the passage of the blast wave. These models agreed well with simulations and allowed for the subsequent modeling of two dimensional hydrodynamic instability growth.

The perturbation growth and vorticity dynamics were studied by looking at three phases of the growth:

1. The early phase: It is dominated by shock-driven instability growth similar to the RM instability and initiates the perturbation growth and vorticity at the interface.

2. The interaction phase: The main part of the blast wave interacts with the interface and increases the vorticity at the interface. The time-varying and transient acceleration

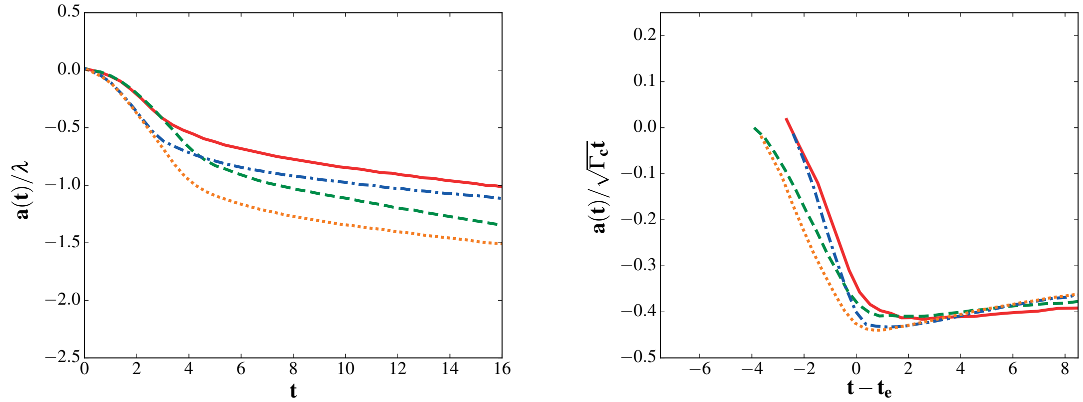

(a) Growth as a function of time.

(b) Growth normalized by $\sqrt{\Gamma_c t}$ and shifted by the interaction time t_e.

Figure 5.17: Perturbation growth as a function of time for a fixed $L = 1$. Solid red: $M_s = 2$, $K = 0.1$; dashed green: $M_s = 2$, $K = 0.05$; dot-dashed blue: $M_s = 3$, $K = 0.1$; dotted orange: $M_s = 3$, $K = 0.05$.

of the interface drives a RT instability which can be captured through buoyancy-drag models of the bubble and spike growth.

3. The coasting phase: After the wave has left the interface, circulation in the mixing region continue mixing the two fluids and increase the perturbation growth. The circulation is constant in this phase. This constant circulation scales linearly with the blast wave length and scales according to a power law in the rarefaction strength. Furthermore, this constant circulation can be used to non-dimensionalize the perturbation growth in this phase to show that the amplitude scales as the square root of this constant circulation multiplied by time. Across shock Mach numbers, rarefaction lengths, and rarefaction strengths, the normalized perturbation growth is constant.

This work sets the basis for continuing to investigate hydrodynamic instabilities driven by complex waves, including the impact of vortex stretching on perturbation growth in three dimensions and late time growth dynamics.

CHAPTER VI

Experimental and numerical investigations of beryllium strength models using the Rayleigh-Taylor instability

This chapter is adapted from Henry de Frahan, M. T., Belof, J. L., Cavallo, R. M., Raevsky, V. A., Ignatova, O. N., Lebedev, A., Ancheta, D. S., El-dasher, B. S., Florando, J. N., Gallegos, G. F., Johnsen, E. & LeBlanc, M. M.. 2015 Experimental and numerical investigations of beryllium strength models using the Rayleigh-Taylor instability *J. Appl. Phys.*, **117 (22)**, 225901.

This work was featured on the cover of volume 117 (issue 22) of the Journal of Applied Physics and was the subject of a Lawrence Livermore National Laboratory news article [191].

6.1 Abstract

We present a set of high explosive driven Rayleigh-Taylor (RT) strength experiments for beryllium to produce data to distinguish predictions by various strength models. Design simulations using existing strength model parameterizations from Steinberg-Lund and Preston-Tonks-Wallace (PTW) suggested an optimal design that would delineate between not just different strength models, but different parameters sets of the PTW model. Application of the models to the post-shot results, however, suggests growth consistent with little material strength. We focus mostly on efforts to simulate the data using published strength models as well as the more recent RING relaxation model developed at VNIIEF. The results of the strength experiments indicate weak influence of strength in mitigating the

growth with the RING model coming closest to predicting the material behavior. Finally, we present shock and ramp-loading recovery experiments.

6.2 Introduction

Beryllium (Be) is a metal with excellent structural properties and unique radiation characteristics [192]. It has a high elastic modulus, a low Poisson ratio, a low density, and a high melting point. Be has an elastic stiffness comparable to steel, at a quarter the density of steel [193]. Its high strength-to-weight ratio and high melting point make it ideal for many defense and aerospace applications [194, 195, 196, 197, 198]. However, Be's low ductility at room temperature presents challenges for both manufacturing and conditions where it might experience extreme deformations, thus limiting its use to low strain applications. It would, therefore, be helpful to understand the dynamic behavior of Be under more extreme conditions of high pressure, strain, and strain-rate.

Early investigations of Be focused primarily on dynamic material properties of polycrystalline Be under tensile stress conditions [199]. Initial Be equation of state descriptions and shock wave profiles up to 5 GPa provided material constants for early analytic models [200]. Christman and Feistmann [201] investigated the dynamic properties of Be, such as elastic constants and elastic precursor decay, which produced a yield plateau, strain hardening, and strain-rate behavior. Chhabildas et al. [202] studied the hcp-bcc phase transition in Be over the stress region 6–35 GPa using shock-release experiments. Using biaxial tensile tests, Lindholm et al. [203] and Lindholm and Yeakley [199] observed yield, plastic flow, and failure of Be under plane stress conditions. Pope and Johnson [204] performed the first attempt at studying yielding on primary slip planes of Be using shock loading planar impact of single crystal Be. They also studied the effects of material anisotropy on plane wave propagation. Jönsson and Beuers [205] studied the dislocation microstructure of single crystal Be at 2% strain. Christian and Mahajan [206] provided an extensive review of twinning in various crystal structures, including Be. Using Split-Hopkinson pressure bar (SHPB) experiments with strain-rates from 10^{-3} to 10^{-4} s^{-1}, Blumenthal et al. [192], Blumenthal [207] studied the evolution of dynamic mechanical behavior and crystallographic texture to understand deformation mechanisms and the role of texture in polycrystalline Be. Brown et al. [208] showed how active deformation mechanisms can be controlled via manipulation of straining direction [209], deformation temperature Brown et al. [210], deformation rate [193], and crystallographic texture [211]. Brown et al. [211] extensively investigated the importance and relative contribution of twinning and slip in Be over a range of strain-rates (10^{-4}–10^{4} s^{-1}). Other experimental data [193] showed the dominance of twinning at strain-rates around 10^{4} s^{-1}. Brown et al. [212] recently performed Be ramp-release experiments to investigate Be shear stress in high strain rate (10^{6} s^{-1}) and pressures (110 GPa).

Be failure modes and spall have been the focus of recent experimental work. Experiments of explosively loaded Be samples up to strain-rates of 10^{4}–10^{5} s^{-1} were used to investigate Be spall fracture and showed a weak dependence between the spall strength and strain-rate [213]. Adams et al. [214, 215] observed elastic precursor decay as a function of target thickness in plate impactor experiments. In earlier experiments, their data indicated brittle spall behavior and a long rise-time in the elastic and plastic waves, which they attribute to twinning being the predominant initial deformation mechanism [214]. In another set of plate-impactor experiments, Mescheryakov et al. [216, 217] instigated spallation in the Be sample and studied material tensile strength in the microsecond region of dynamic loading. Recent experiments [218, 219] used post-mortem analysis of explosively driven Be to evaluate failure behaviors. Peak shock pressures of 15 GPa were observed but no definite source of failure in Be was identified [218].

Few dynamic studies of Be have been performed in recent years and little is known about its strength properties at high strain ($\gtrsim 0.2$), strain-rate ($\gtrsim 10^{4}$ s^{-1}), and pressure ($\gtrsim 10$ GPa), yet there are many competing material strength models that try to characterize its behavior by extrapolating to these more extreme conditions with often diverging results. Most strength models are informed by physics (e.g., strain hardening laws, rate dependencies on thermal activation and phonon drag, pressure and temperature dependence of shear moduli, etc.), but are ultimately predicated on certain ansatz to facilitate practical applications to phenomena in regimes beyond those easily accessible with current experimental techniques. As a result, the governing equations contain multiple parameters that are calibrated using data from experiments in low pressure, strain, and strain-rate regimes, e.g., data from Split-Hopkinson pressure bar experiments (at zero pressure, strains of 10–20%, and rates below 10^4 s^{-1}) or Taylor anvil experiments ($\sim$ 10 GPa, strains of 0.1 (Ref. [220]), and rates near 10^5 s^{-1}). Because the models are typically tied to phenomenology, they tend to diverge when confronted with data far from their calibration points, whether that is in pressure, temperature, strain or strain-rate space, see Figure 6.1. In this paper, we discuss a set of dynamic experiments to characterize Be strength behavior under extreme conditions and use the results to discriminate among different strength models. A RT instability occurs at the interface between two materials accelerated such that the pressure and density gradients are anti-parallel [163, 38]. Under conditions where the accelerated material has no strength (and low viscosity), a surface perturbation grows non-linearly as t^2, where t is time. However, in the instances where the material remains solid, the perturbation growth is mitigated and even halted depending on the mode of the interface perturbation [221]. In 1974, [222] took advantage of this observation and developed a technique using high explosives (HE) to accelerate aluminum and stainless steel plates with perturbations machined on the HE facing surface. By setting off an HE charge at a stand-off distance of $\sim$ 1.3–2.5 cm, they accelerated the plates without shocking the material and reached peak pressures of 10 GPa. By modeling the growth of imposed sinusoidal perturbations on the side of the material facing the expanding HE products, they inferred the influence of strength during the dynamic loading process. Others have since expanded the technique to other materials using modern diagnostic techniques in addition to traditional flash radiography [223, 224], while others still have adopted the technique using lasers to drive targets with plasma to achieve yet higher strain rates and pressures [225, 226]. We designed HE-driven RT experiments for ramp loading of Be to reach pressures of 50 GPa and strain-rates of 10^6 s^{-1}. These are pressure and strain-rate regimes where data are sparse and strength models diverge in their predicted behavior.

This article is organized as follows. We describe the setup of the HE-driven RT experiments and present the experimental results in Section 6.3. After discussing the existing strength models, we compare the experimental results to simulations of the experiments in Section 6.4. We end with a discussion of Be recovery experiments. Though there are other effects besides plasticity, our analysis is predicated on the assumption that plasticity is the

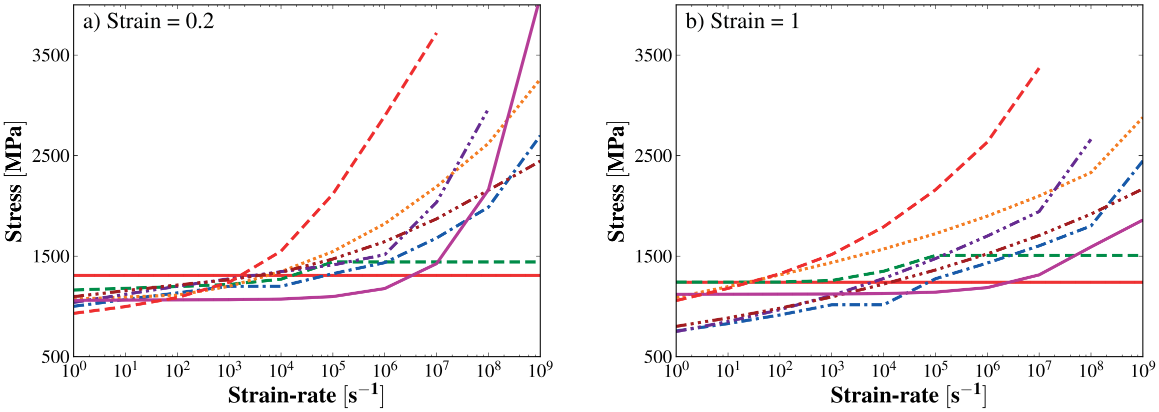

Figure 6.1: Total stress as a function of strain-rate in Be for different strength models (curves determined by setting the model parameters in MIDAS (Ref. [227]) for adiabatic uniaxial compression at 300 K and 0 initial pressure). Left (a): strain = 0.2; right (b): strain = 1. Solid red: SCG; dashed green: SL; dotted-dashed blue: PTW; dotted orange: PTW (Preston); dotted-dotted-dashed purple: PTW (Chen); dotted-dotted-dotted-dashed burgundy: PTW (Blumenthal); solid ma- genta: RING; dashed red: MTS. The models and different flavors of models are detailed in Section 6.3.1.

dominant effect governing the flow. We address and qualify this assumption in Section 6.4.

6.3 Experiments

6.3.1 Rayleigh-Taylor experimental design

The experimental setup is shown in Figure 6.2. A two-stage planar HE drive launches an iron impactor at a second charge of HE, overdriving it beyond the Chapman–Jouguet pressure. The detonated HE products expand across the vacuum gap and shocklessly load against the Be target, which has a machined sinusoidal perturbation on the loaded surface, Figure 6.3, with a quasi-isentropic compression wave, hereby initiating an RT instability at the HE-Be interface. A Plexiglas bracket initially holds the Be target in place before the target is accelerated by the HE. The Be targets are made of S200F Be composed of 98.5 wt.% pure Be with a maximum of 1.5%BeO. The targets were manufactured by Materion Electrofusion using a hot isostatic press. The rippled patterns were formed via wire electrical discharge machining. The Be microstructure was imaged using electron backscatter diffraction (EBSD), see Figure 6.4. The grain size distribution was calculated from the EBSD image, see Figure 6.5. The average grain size in the tested Be was 9.5μm.

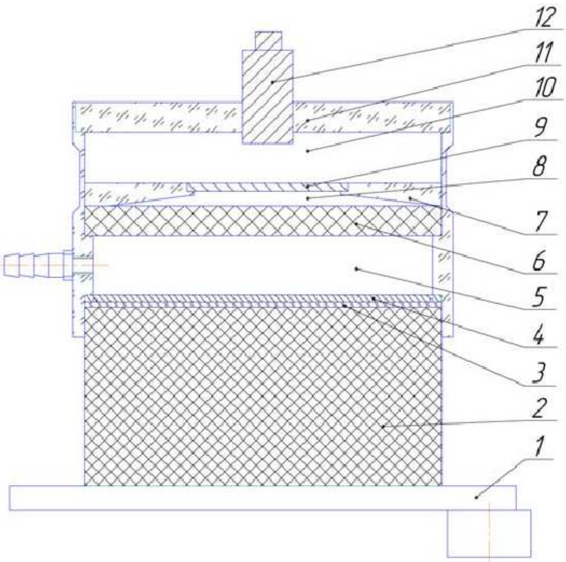

Figure 6.2: Two stage loading device for the quasi-isentropic loading of a rippled Be target. Planar shock wave generator (1); first stage HE (2, ∅90 mm ×80 mm); Plexiglas damper (3, ∅90 mm ×2 mm); iron impactor (4, ∅90 mm ×2.2 mm); vacuum gap (5, 10 mm); second stage HE (6, ∅90 mm ×10 mm); Plexiglas bracket (7); vacuum gap (8, 2 mm); Be target (9, ∅50 mm); vacuum volume (10); Plexiglas disk (11, ∅90 mm ×10 mm); optical gauge (12).

EBSD scans indicate a weak (0001) basal plane texture aligned with the drive direction, see Figure 6.6. Nine Vickers hardness tests determined the average Be hardness to be 1830±200 MPa (from a hardness of 186.9 kgf mm^{-2} from a load of 1 kg over a ~ 0.031 mm long diagonal spot). The perturbation is sinusoidal and the wavelength for all the RT experiments was $\lambda = 4$mm. The perturbation peak-to-valley amplitude for four experiments with 2 mm substrates (as measured to the middle of the perturbations) was 0.48 mm. For two other experiments, the perturbation amplitude was 0.38 mm on 1.78 mm thick substrates. An example of a machined Be target used in these experiments is shown in Figure 6.3. The experiments were designed by conducting a series of simulations over an ensemble of strength models and Be equations of state. To optimize the dispersion of the Be strength models (thereby maximizing model differentiation), the design simulations varied the perturbation wavelength, amplitude, target thickness, and HE stand-off distance. Bevels were machined into the outer edge of the targets to enable side-on imaging of the ripple growth as the target accelerates and deforms. Without these bevels, the outer edge of the target would hide the perturbation growth from the imaging diagnostic.

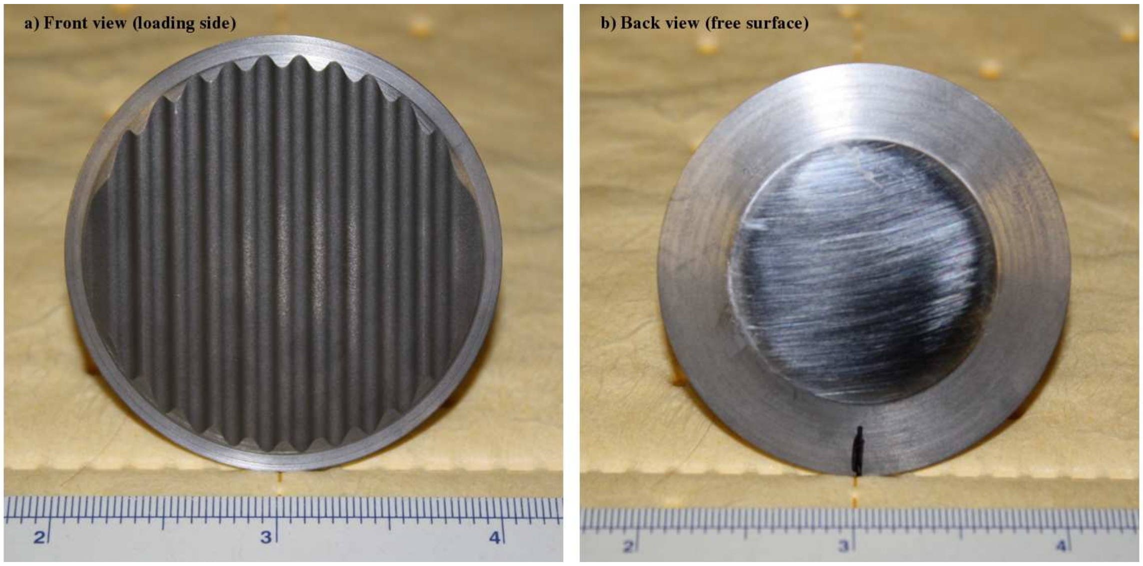

Figure 6.3: Pictures of a machined Be target. The graduated ruler is in inches. Left (a): front view; right (b): back view.

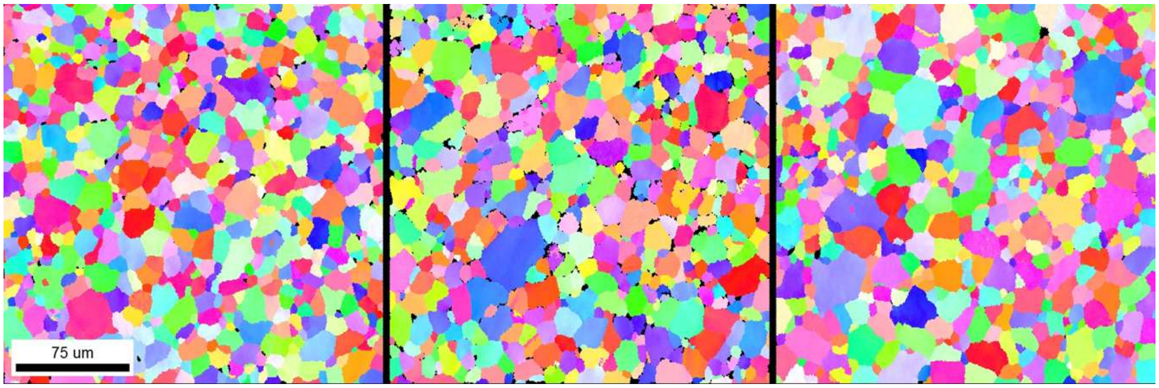

Figure 6.4: Be microstructure from three EBSD scans of 250 × 250 μm. The colors are a function of the lattice orientation and help distinguish the grains. The dark dots are assumed to be BeO.

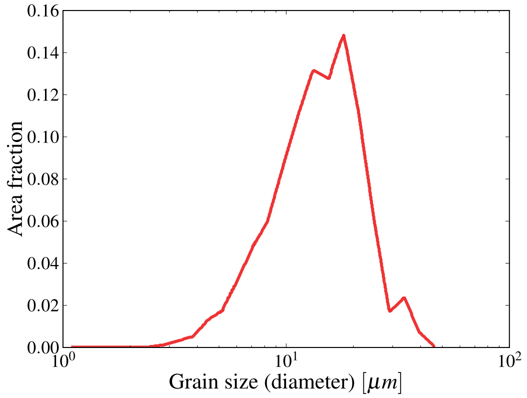

Figure 6.5: Grain size distribution from EBSD scans. 2038 grains were measured and the average grain size is 9.5 mm.

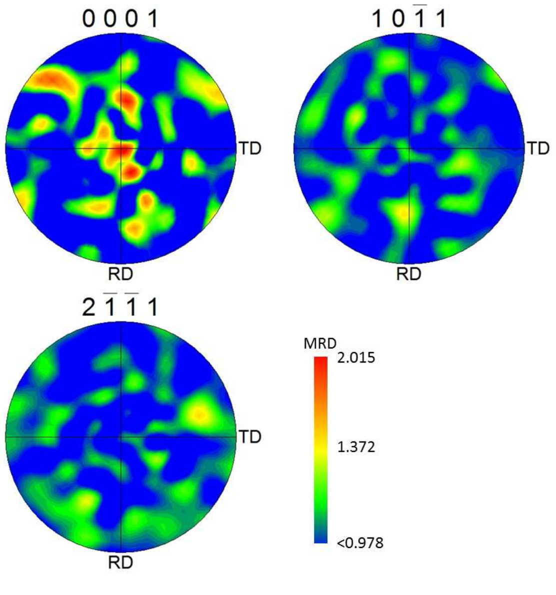

Figure 6.6: Polar maps of grain orientation from EBSD scans. Color map is in units of multiples of a uniform density (MRD) with a max = 2.015 and min = 0.978 (min cutoff used for display, the actual values can be smaller). TD is the transverse direction and RD the rolling direction.

We performed several SHPB experiments to characterize the dynamic behavior of the Be samples in strain-rate regimes between 2000 and 5000 s^{-1} and compare with models calibrated to previous data [227]. These experiments were performed at ambient conditions. The targets were made from the same batch of pressed S200F as the RT targets, and the SHPB tests were conducted at LLNL. The SHPB data usually end at low strains in the samples due to brittle failure. Figure 6.7 shows the stress-strain curve for an experiment with a strain-rate of 2000 s^{-1} (the data from a single experiment are shown for illustration purposes and the SHPB experimental data for all the experiments are available in MIDAS (Ref. [227])). The strength models based on previous SHPB results seem accurately to describe the stress-strain response at these relatively low strain-rates. It is not possible to discriminate among the different models in these regimes for these particular samples. The multiple parameter sets for the Preston-Tonks-Wallace (PTW) model all fit the SHPB data but they predict different behavior for the higher strain-rates observed in the RT experiments, see Figure 6.7(b). The RING model also fits the data well in this regime, though it predicts lower stress at higher strains than the data. The lack of differences in the models at these low strain-rates, and strains, and their significant divergence at high strain, strain rates, and pressures is the main motivation for performing these RT strength experiments. The RT experiments are designed to provide data in these regimes to help discriminate among the different available strength models.

6.3.2 Diagnostic techniques

Two diagnostic techniques were used to capture the experimental data. X-ray radiographs at the Eridan-3 facility at RFNC-VNIIEF imaged the target perturbation growth, see Figure 6.8. A 1 MeV, 0.15 μs pulse flash x-ray was used to record one image for each experiment, which was captured on a ADC-CR photochromatic screen [228]. Measurements of the free surface velocity of the targets were performed with a Velocity Interferometer System for Any Reflector (VISAR) during each experiment [229]. The VISAR spot size is 200 μm and the spot is centered on the back of the target to minimize the effects of potential bowing of the target as it is being driven (radiographs shown there is very little bowing until late in time for some shots, see Section 6.3.3). The pressure of the explosives on the

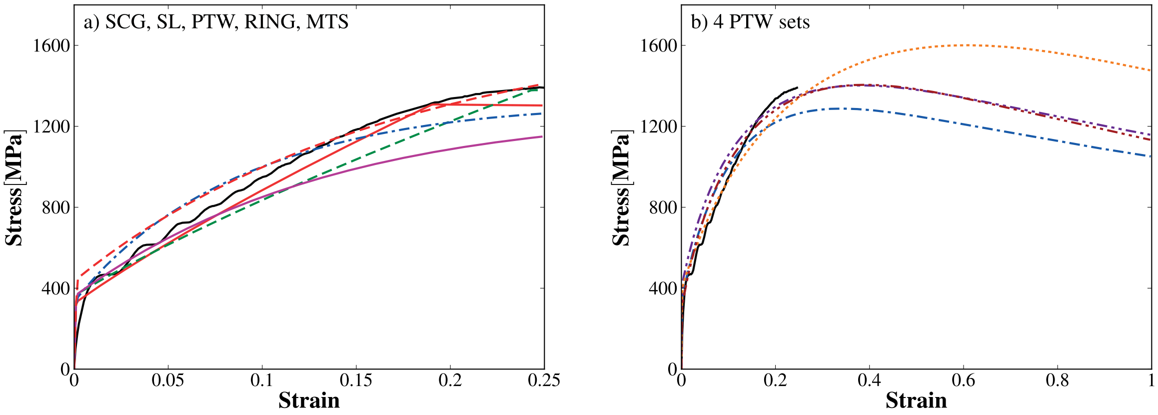

Figure 6.7: Stress as a function of strain in Be for a characteristic strain-rate of 2000 s^{-1}. Left (a): comparing to the SCG, SL, PTW, RING, and MTS models; right (b): comparing four different PTW parameter sets over a large range of strains. Solid black: SHPB experimental data at ambient temperature; solid red: SCG; dashed green: SL; dotted-dashed blue: PTW; dotted orange: PTW (Preston); dotted-dotted-dashed purple: PTW (Chen); dotted-dotted-dotted-dashed burgundy: PTW (Blumenthal); solid magenta: RING; dashed red: MTS.

loaded surface of the target determines the free surface velocity of the target, and hence the expected RT growth. Comparing the VISAR data with simulations indicates that the drive conditions in the simulations match that of the experiments so a proper interpretation of the growth data can be made (see Section 6.4).

6.3.3 Experimental results

We performed a total of six HE-driven Be RT experiments with x-ray diagnostics to measure the perturbation growth as a function of distance traveled. We use distance traveled since it can be measured directly in the experiment without having to account for fiducial timing in the HE drive. Time and distance are, of course, easily related through the velocimetry. The radiographs are shown in Figure 6.9. The clear white region in the center of the radiograph is the Be liner. The bright area on the bottom of the radiograph is the HE, and the bevels observed on the side are the Plexiglas brackets holding the liner. The apparent absence of any visible voids in the Be suggests that the targets have not spalled at image time, though there is the possibility that cracks formed at length scales below the camera detection limit. It is possible that the last radiograph shows signs of failure in the bubble, though this is not very clear. The perturbations exhibit non-linear growth at

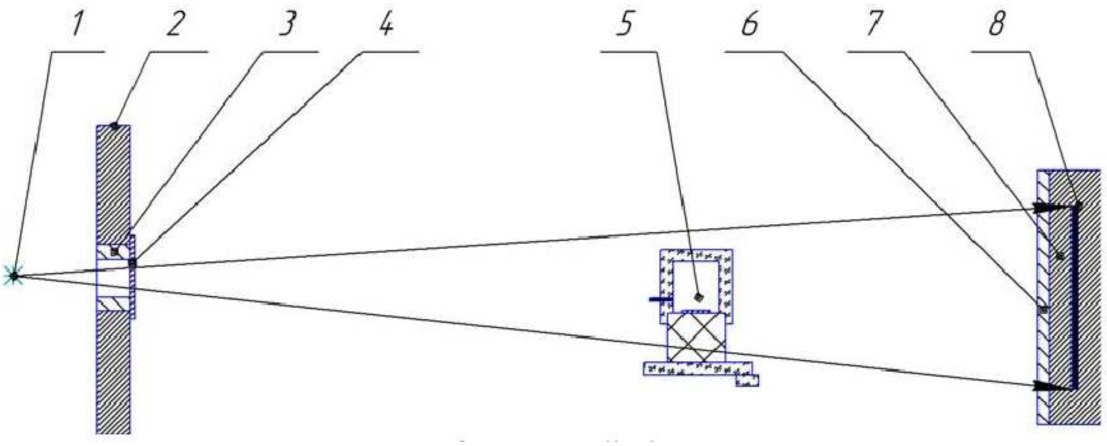

Figure 6.8: X-ray radiograph diagnostic setup. X-ray source (1); armored protection (2); collimator (3); protective screen (4); experimental assembly (5); protective setup (6); armored cassette (7); ADC-CR screen (8).

larger distances, see Figures 6.9(e) and 6.9(f). The evolution of the perturbation growth with increasing distance traveled was measured using the six radiographs, and the growth factors are shown in Figure 6.10.

Measurements of the free surface velocity during each of the experiments indicate consistent drive conditions, see Figure 6.11. Time $t = 0$ is the HE arrival time at the Be/HE interface. For a small part of the trace, there are some spurious fringes around 1 μs due to the large VISAR spot tracking different parts of the target with slightly different velocities. The velocimetry profile recovers at 1.2 μs and those fluctuations disappear.

6.4 Numerical simulations of the experiments

We model the experiments with Ares, an Arbitrary Lagrangian Eulerian hydrodynamics code [230]. The mesh resolution for all the simulations is 8 μm, at which point the simulation results are converged. We assumed planar symmetry and performed two-dimensional simulations of a half wavelength slice of the system, thereby neglecting the release at the edges of the system. The second layer of HE, which unloads against the target, is 90 mm in diameter while the target itself is 50 mm across. The gap between the two is only 2 mm (see Figure 6.2) so that even if the release in the unloading HE products was fast enough to decrease the planarity of the drive at a 45° angle, the target would still see a 1D planar

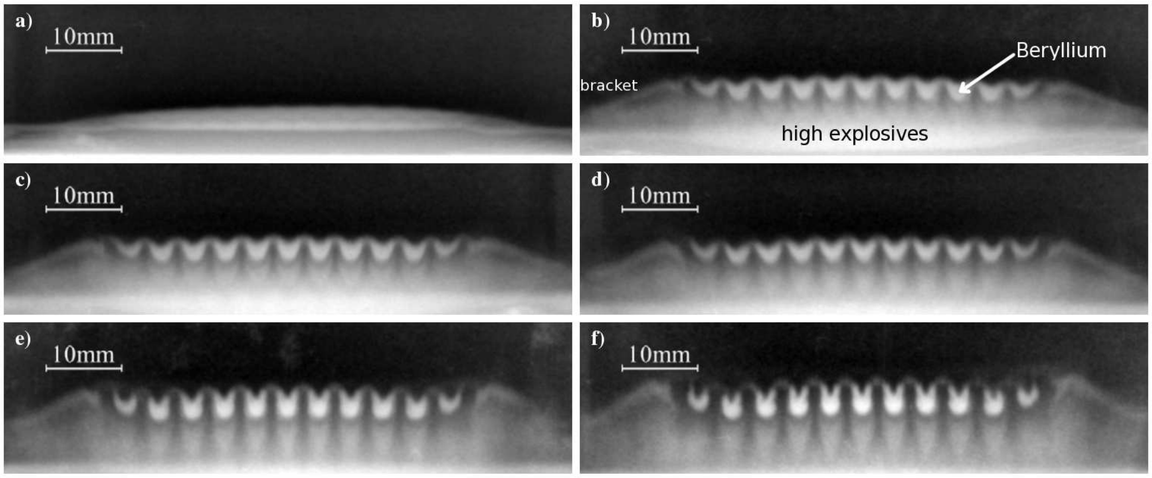

Figure 6.9: Radiographs of the six HE-driven Be RT experiments. The brighter area on the bottom of the radiograph is the HE. The clear white region in the center of the radiograph is the Be liner. (a) $A_0 = 0.38$mm, $h = 1.78$mm, $S = 1.4 \pm 0.2$mm, $A = 0.6 \pm 0.1$mm; (b) $A_0 = 0.48$mm, $h = 2$mm, $S = 6.3 \pm 0.3$mm, $A = 2.4 \pm 0.1$mm; (c) $A_0 = 0.48$mm, $h = 2$mm, $S = 7.1 \pm 0.3$mm, $A = 2.6 \pm 0.1$mm; (d) $A_0 = 0.38$mm, $h = 1.78$mm, $S = 8.9 \pm 0.3$mm, $A = 2.7 \pm 0.2$mm; (e) $A_0 = 0.48$mm, $h = 2$mm, $S = 11.7 \pm 0.3$mm, $A = 3.6 \pm 0.2$mm; (f) $A_0 = 0.48$mm, $h = 2$mm, $S = 14.6 \pm 0.2$mm, $A = 4.1 \pm 0.2$mm. A_0 is the initial peak-to-valley perturbation amplitude, h is the initial target thickness, S is the target displacement, and A is the measured peak-to-valley perturbation amplitude. The direction of motion is towards the top of the images.

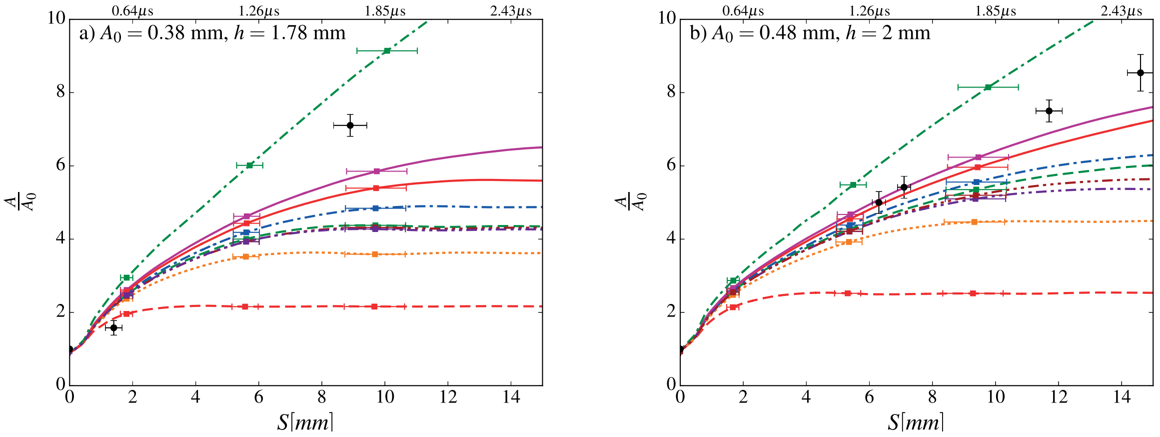

Figure 6.10: Growth factors as a function of displacement. Left (a): $A_0 = 0.38$mm and $h = 1.78$mm; right (b): $A_0 = 0.48$mm and $h = 2$mm. Black dots: experimental data; dotted-dashed green: no strength; solid red: SCG; dashed green: SL; dotted-dashed blue: PTW; dotted orange: PTW (Preston); dotted- dotted-dashed purple: PTW (Chen); dotted-dotted-dotted-dashed burgundy: PTW (Blumenthal); solid magenta: RING; dashed red: MTS. The error bars for the simulated growth factors are representative single point error bars capturing uncertainties in the simulated drive with respect to the scatter among the experimental drive measurements. These error bars were obtained by propagating the uncertainty in the simulated drives from Figure 6.11.

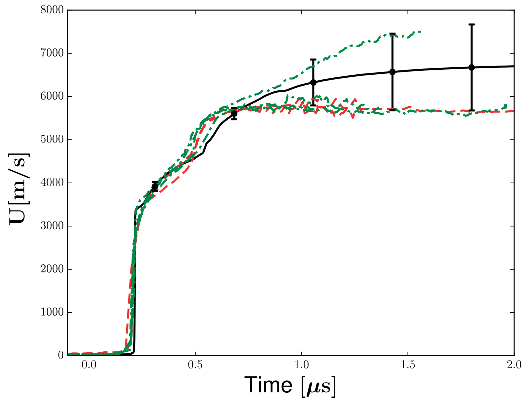

Figure 6.11: Free surface velocity, U, as a function of time. $t = 0$ is the HE arrival time at the Be/HE interface. The rise time of the first stress wave is greater than 15 ns and, therefore, is not a shock. Dashed red: $h = 1.78$ mm; dashed-dotted green: $h = 2$ mm; black: numerical simulation. The error bars for the simulated free surface velocity are representative single point error bars representing the scatter among the experimental drive measurements. The error in a single experimental measurement is typically much smaller (around 5%).

Table 6.1: JWL++ reactive flow equation of state parameters for the HE.

ρ_0 (g/cm^3)	A (Mb)	B (Mb)	R_1	R_2	ω	E$_0$ (Mb)	n	κ	G	b	β
1.89	7.8	3.9	0.1	1.2	0.3	0.159	7.4	7.8	3000	1	3.6

drive when the HE products arrived at the front surface. Assuming a sound speed in Be of 13 000 m s^{-1}, it takes the release wave from the edge of the Be about 2 μs to travel the radius of the target, affecting only the latest few data points, which were obtained after seeing limited growth at the earlier times taken first in the sequence. 2D simulations were performed in the target design to determine the shape of the bevel at the edge of the target, which was specifically designed to prevent bowing in the target that could interfere with the side-on view of the diagnostic. The results shown in Figure 6.9 demonstrate the planar behavior of the target even at long travel distances.

The simulated system consists of the iron impactor, the HE, the vacuum gap, and a half wavelength ripple on the Be target. The iron impactor initiates the HE detonation, with its impact velocity determining the peak pressure in the HE explosion. The HE was modeled with a JWL++ reactive flow equation of state [231] using the parameters in Table 6.1. All other materials used a tabulated equation of state from the LEOS data library based on a QEOS-like model [232]. We also compare the results using an analytic Gruneisen EOS. The drive, Figure 6.12(a), and the growth, Figure 6.12(b), are very similar regardless of the form of the equation of state. Though contributions to the results beyond plasticity might exist, we did not use a damage model for the Be as we assume that strength is the dominant effect in these experiments. Our analysis assumes that the observables are a direct result of plastic flow. We address this assumption at the end of this section.

We examined the behavior of several strength models, which typically have very different dependencies on strain, strain-rate, and shear modulus, as they relate to the Be flow strength. The Steinberg-Cochran-Guinan [233] (SCG) model is rate-independent but assumes “high” rates of order 10^5 s^{-1}. The flow strength goes as the strain to the nth power, where n is a work hardening parameter, and the shear modulus includes linear pressure and thermal terms. The Steinberg-Lund [234] (SL) model is based on the SCG model and adds an additional strain-rate dependence in the thermal activation regime. The strain-

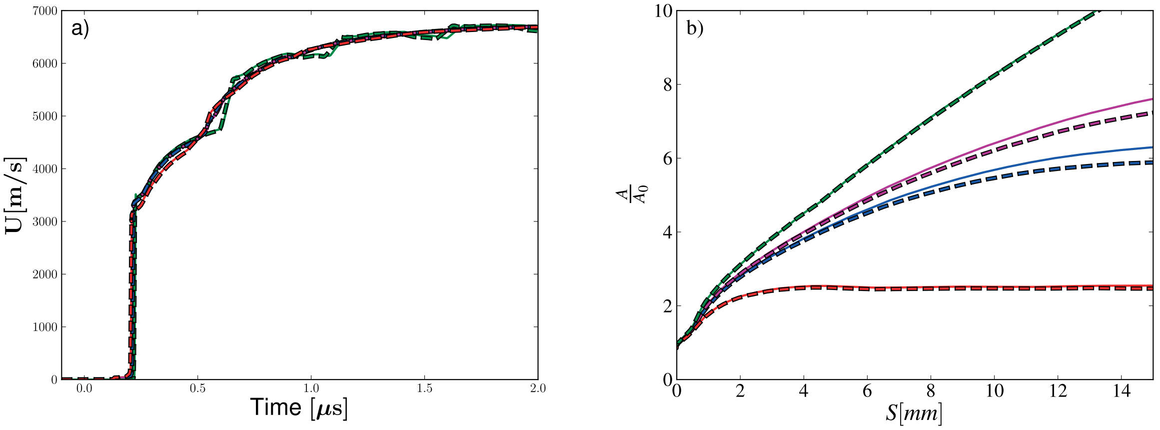

Figure 6.12: Simulation of a 2 mm thick target with $A_0 = 0.48$ mm. Left (a): free surface velocity as a function of time where $t = 0$ is the HE arrival time at the Be/HE interface; right (b): growth factors as a function of distance traveled. Solid: tabulated equation of state from the LEOS data library; black outlined dashed: analytic Gruneisen equation of state. Green: no strength; blue: PTW; magenta: RING; red: MTS.

rate depends on the inverse of the sum of an exponential of the thermal component of the stress with the inverse of the athermal component of the stress. The PTW (Ref. [1]) model describes material behavior in both the thermal activation and phonon drag regimes over many orders of magnitude of strain-rate. At low strain-rates ($< 10^4$ s^{-1}), two different expressions for the work hardened saturation stress and flow strength are used to describe the thermal regime and vary as the error function of the logarithm of the inverse of the strain rate. At high strain-rates, the phonon drag regime for dislocation motion is described using the theory of overdriven shocks where the saturation stress and yield stress are set equal and are related to a power of the strain-rate divided by the atomic vibration frequency. The stress in the transition region between the low and high strain-rate regimes is the maximum of the low and high strain-rate regime stresses. A single model can have different parameter sets to describe a given material. In this paper, we use four versions of the PTW model, each differing in their model parameters: the original values [1], and those proposed by Prime et al. [235] are shown for Be in Table 6.2. The relaxation model of beryllium strength [236, 237] (RING) model includes relaxation terms, a term to account for twinning and terms to account for recovery at elevated temperatures. Finally, the mechanical threshold stress [238] model, valid at strain-rates up to the phonon drag limit, includes thermal acti-

Table 6.2: Summary of the different PTW Be material parameters used in this paper (see Ref. [1] for the parameter definitions). The shear modulus is from Steinberg-Guinan, while the melt curve comes from the LEOS table.

	Original PTW	Chen's PTW (PTWC)	Preston's PTW (PTWP)	Blumenthal's PTW (PTWB)
θ	0.04	0.025	0.045	0.0394
p	1.4	2	2.5	2
s_0	0.007	0.0093	0.00845	0.0077
s_∞	0.0012	0.00135	0.00083	0.0006
κ	0.14	0.11	0.12	0.145
γ	1×10^{-5}	1×10^{-5}	7×10^{-5}	1×10^{-5}
y_0	0.0015	0.0009	0.00129	0.0018
y_∞	0.0005	0.0009	0.00051	0.0004
y_1	0.007	0.0093	0.00845	0.0077
y_2	0.25	0.16	0.16	0.4
β	0.25	0.16	0.16	0.25

vation effects. The stress is a linear combination of different stresses caused by dislocation barriers. These are scaled via factors representing the structure functions for the various dislocation barriers. The scaling factors are highly non-linear functions of temperature and strain-rate. These models have been calibrated to data from low pressures and low strain and strain-rate experiments. Predicting the RT growth in higher pressure and strain-rate regimes is therefore particularly challenging.

By tuning the velocity of the iron impactor detonating the second stage HE, Figure 6.2, we ensure that the simulations have the same drive conditions as the experiments. Comparisons between the velocimetry data of the Be targets measured by VISAR and a simulation using the PTW model are presented in Figure 6.11. Simulations with different strength models do not present significantly different predictions of the free surface velocity because the drive conditions are essentially independent of the strength models. The simulations are sufficient to allow for an interpretation of the growth data with an adequate acceleration profile. Small discrepancies between the experimental drives and simulated drives have little impact on our results. We performed sensitivity analysis of the drives by increasing and decreasing the simulated drives by one root mean square deviation (as measured between the simulated and experimental drives, illustrated with representative error bars in Figure 6.11). The impact of these changes on the growth factors is within the experimental error bars.

Simulations of the experiments indicate that the Be targets reached ~ 50 GPa and strain-rates of 10^6 s^{-1}, the phase-space where the model predictions of the perturbation growth differ. The simulations that best match the experimental data show a peak yield stress in Be of 2.2 GPa, which is comparable to the values of 1.8 GPa reported by Chhabildas et al. [202] and 16.5 reported by Brown et al. [212]. Though there is some agreement between these experiments, the comparison is not perfect because the strain rates and loading paths are different between an RT experiment and these shock-release and ramp-loading experiments. The rise time of the first stress wave is greater than 15 ns and, therefore, is not a shock. The simulations corroborate that this wave is a ramp and that the temperature is lower than that generated by a shock. According to the simulations, the temperature in the Be in these experiments is inferred to be approximately 700 K. In the SHPB experiments of Blumenthal [207], there is no evidence of Be failure even at strains as high as 1.0. Therefore, we have no evidence that the Be failure is occurring in the RT experiments, for which the peak strains do not exceed 1.0 (with the possible exception of very late in time). Simulations of the RT experiments indicate that the sample is under compressive strain during the entire process under which we take data. While a release wave propagates from the rear free surface of the target, the stress is continuously increased as the compressive ramp wave from the HE moves through the target. As a consequence, the Be target never experiences tension in the RT bubble. Additionally, the stress vs. strain curves from the SHPB experiments are smooth and do not show evidence of failure under compression (although microcracks develop at high strains (> 0.2), these will not affect the results unless the sample is under tension).We present pseudo-color plots of pressure and strain-rate in Figure 6.13. Initially, a compression wave induced by the iron impactor travels through the HE, causing detonation, see Figure 6.13(a). The HE then expands through the vacuum gap and loads against the Be target, see Figure 6.13(b). The ripples at the HE-Be interface grow as the target is accelerated by expanding HE gas, see Figures 6.13(d) and 6.13(e).

Figure 6.10 also presents a comparison between the predicted growth factors of the perturbations using different strength models and the experimental data points as a function of target displacement. The data suggest that the Be ripples grew close to classically and are

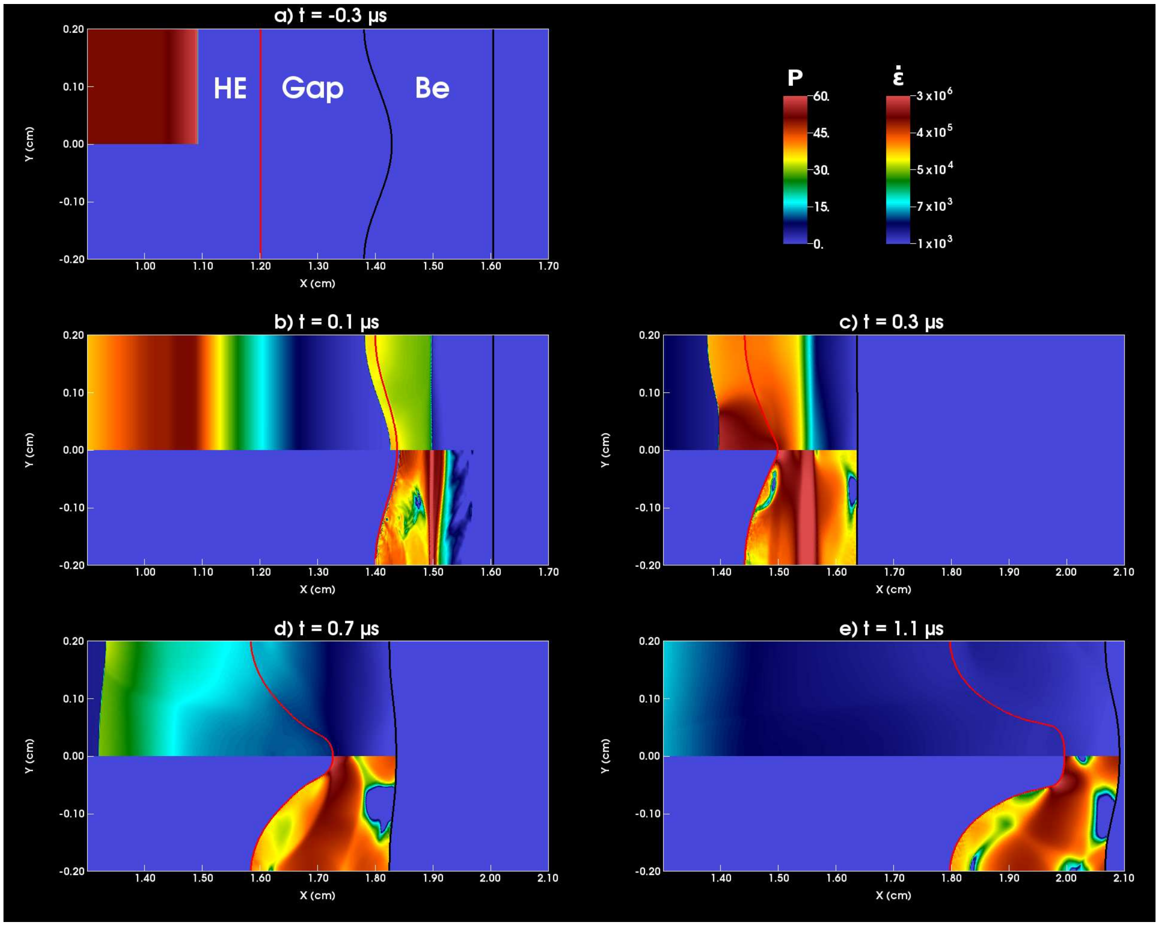

Figure 6.13: Pseudocolors of pressure (top half) and strain-rates (bottom half) in the HE and Be target. Red line: HE-Be interface; black line: Be back. $t = 0$ is the HE arrival time at the Be/HE interface. Pressure color map is in units of GPa with min=0 GPa and max=60 GPa. Strain-rate color map is in units of s^{-1} with min $= 10^3\mathrm{s}^{-1}$ and max $= 3 \times 10^6\mathrm{s}^{-1}$. (a) $t = -0.3\mu s$; (b) $t = 0.1\mu s$; (c) $t = 0.3\mu s$; (d) $t = 0.7\mu s$; (e) $t = 1.1\mu s$.

consistent with either low strength in the Be, or significant, but unobserved, damage. "Classically" usually refers to a constant acceleration at a non-viscous liquid/gas interface. In this context, we use it to describe growth in the presence of no strength or viscosity regardless of the dynamic loading profile. From the radiographs, we observe that the ripples have a significant mushroom shape, indicative of a classical RT growth in the non-linear regime. Consequently, most of the strength models under-predict the growth of the perturbations. The Mechanical Threshold Stress model predicts very little growth, which indicates that the work hardening is over-predicted for this region of the phase space. The MTS stress-strain curve, as shown in Figure 6.1, clearly illustrates this as it is steeper than the other stress-strain curves in this region of phase space. The RING model, as adopted in Ares, is the strength model with results closest to the experimental data. The experiments enable us to discriminate against certain models, such as MTS, which do not capture the data in this regime while the results indicate that the RING and SCG models are adequate in this regime. The small differences among the PTW models are not as significant as the differences between PTW and the other models in general. The data indicate that the models in general are inadequate for capturing the high strain, strain-rate, and pressure regime of the experiments. These models require better physics-based components to underwrite their validity. This is due in part to the fact that they are based on observations made in different parts of the phase space and they cannot be relied upon to predict material behavior away from their calibration points without accepting the inherent risk associated with extrapolation.

If the perturbation growth is due solely to plasticity, the RING model is the closest to the data but still misses the late-time behavior. However, an alternate theory is possible if damage occurs early in the experiment and manifests itself through the appearance of high growth. The data are insufficient to discriminate solely between plastic-driven growth and a combination of plasticity and damage. The recovery experiments (see Section 6.5) seem to indicate support for the idea of damage induced growth. Either way, the data indicate that existing strength models are insufficient in their current forms to capture properly the behavior of Be under extreme loading conditions.

6.5 Recovery experiments

Current plasticity models generally assume deformation mechanisms driven by dislocations. However, Be is known to incur substantial twinning and can experience brittle failure under room temperature conditions. For example, previous work [207] on hot isostatically pressed S200F indicates that at strains up to $\sim 20\%$ under uniaxial compression, the dominant deformation mechanism is basal slip. The contributions from twins peak at 10% strain but never become dominant. To understand the extent of twinning and failure that might be present in higher strain-rate regimes, such as our RT experiments, we also performed Be recovery experiments, where Be samples were loaded and then recovered for analysis. The goal of these experiments was to explore the effect of loading and shock strength on the Be microstructure and to determine Be dislocation dynamics. Unfortunately, it is not possible to recover the RT targets themselves since their thin nature causes them essentially to disintegrate at late times before they can be recovered. As such, thicker targets were used with different loading profiles from the RT experiments making an exact comparison of the deformation not possible; nonetheless, the path we chose is close enough to describe the behavior of Be under both uniaxial loading and at least similar drive conditions.

We performed two types of recovery experiments. In the first, a Be target disk of $\varnothing 60 \times 15$ mm (diameter × thickness) was sandwiched between two layers of aluminum ($\varnothing 120 \times 0.5$ mm for the front disk and $\varnothing 120 \times 5$ mm for the back disk) and placed near a charge of HE. The Be sample experienced quasi-isentropic loading resulting from the detonation of the HE. The compression wave steepened to a shock as it traveled in the Be. This experiment was designed to keep the pressure in the material constant, but to have a varying strain-rate (from 10^5 to 10^10 s^{-1}). In the second experiment, a Be sample of the same dimensions was also placed between two layers of aluminum, but this time an HE charge launched an aluminum impactor ($\varnothing 120 \times 2$ mm) resulting in a shock wave that decreased in strength as it traveled in the Be. In this case, the strain-rate was constant (approximately 10^5 s^{-1}), but the pressure varied from 15 to 10 GPa. Manganin-based pressure sensors (MPS) were used to measure the pressure in the sample. For both experiments, to minimize edge rarefactions, the Be target is surrounded by an aluminum (Al) sleeve. The impedance of

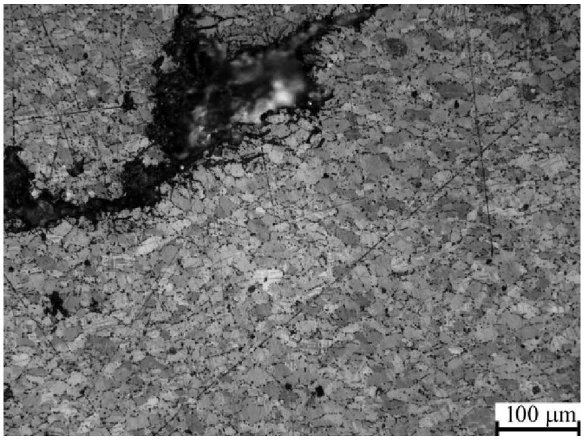

Figure 6.14: Microsection of Be sample loaded with a quasi-isentropic compression wave. The large black void on the upper left is a crack while the long straight lines are remnants of the cross-sectioning process. The grains are clearly visible with the small black dots around the grain boundaries showing concentrations of BeO.

the Be and Al is well matched due to the high Al sound speed (the intensity reflection coefficient is 0.03) and a simple one-dimensional hydrodynamic analysis shows little effect from interface rarefaction. Given the reputation of brittle failure in Be and uncertainty in the dominant deformation mechanism, a priori expectations from the experiments ranged from mild deformation to complete disintegration.

A microsection of the recovered Be sample for the first type of experiment is shown in Figure 6.14. The pressure sensors indicated a peak pressure of 25 GPa in the sample. The microsection reveals a fine-grained structure with an average grain size of $14 \pm 6.7 \mu$m. A crack is clearly visible. The observed twinning fraction was slightly less than 50%. A recovered sample from the second type of experiment illustrates the partial destruction of the Be sample under this type of loading, see Figure 6.15. In this case, the peak pressure in the sample was around 14 GPa. From these two types of recovery experiments, it is clear that the samples fractured but did not completely disintegrate.

Using the MPS data, we calibrated the simulations to obtain the same experimental conditions, see Figure 6.16. The different loading paths and target strains are clearly visible when comparing Figures 6.17 and 6.18. In the first experiment, the simulation indicates that the pressure inside the target reached 26 GPa and remained constant throughout the material for about 1 μs before decreasing smoothly. The strain inside the target reached

Figure 6.15: Picture of post-shot Be sample loaded with a thin metal impactor.

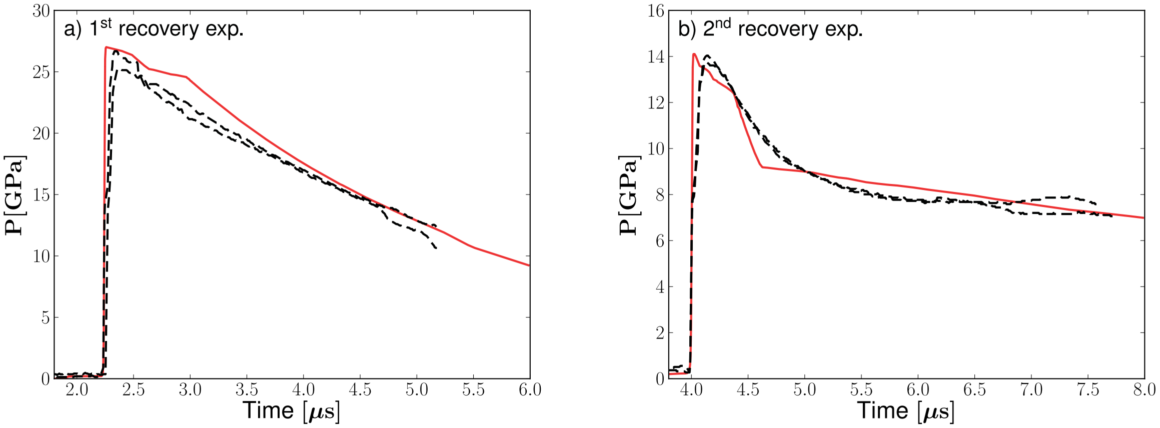

Figure 6.16: Pressure at the MPS locations as a function of time for the recovery experiments. $t = 0$ is the arrival time of the first pressure spike at the loaded surface of the Be. Left (a): for the first recovery experiment; right (b): for the second recovery experiment. Dashed black: experimental data from the MPS; solid red: simulation data.

0.1, remained constant, and then increased again. In the second experiment, the pressure at the leading edge of the Be target increased rapidly to approximately 15 GPa and decreased sharply thereafter to a near-constant value of 10 GPa. The amplitude of the shock wave decreased as it traveled in the Be. The strain varied from 0.15 to 0.11 depending on the depth in the Be target. The simulations also indicate different strain-rate behaviors in the two experiments, see Figure 6.19. In the first experiment, an initial spike in strain-rate is followed by a constant rate of $\sim 2 \times 10^4$ s^{-1}. In the second experiment, the strain-rate is around 10^5 s^{-1} for about 0.25 μs and then decreases rapidly to approximately 2×10^3 s^{-1}.

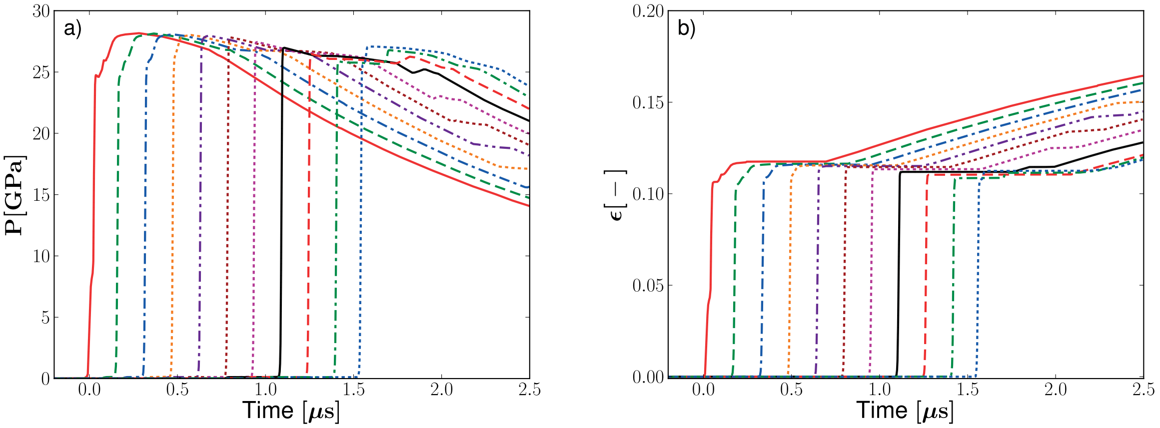

Figure 6.17: Pressure and strain for the first recovery experiment at various depths in the Be target. $t = 0$ is the arrival time of the first pressure spike at the loaded surface of the Be. Left (a): pressure as a function of time; right (b): strain as a function of time. Solid red: 0.015 cm; dashed green: 0.15 cm; dotted-dashed blue: 0.3 cm; dotted orange: 0.45 cm; dotted-dotted-dashed purple: 0.6 cm; solid black: 0.75 cm; dotted maroon: 0.9 cm; dotted magenta: 1.05 cm; dashed red: 1.2 cm; dotted-dashed green: 1.35 cm; dashed blue: 1.485 cm.

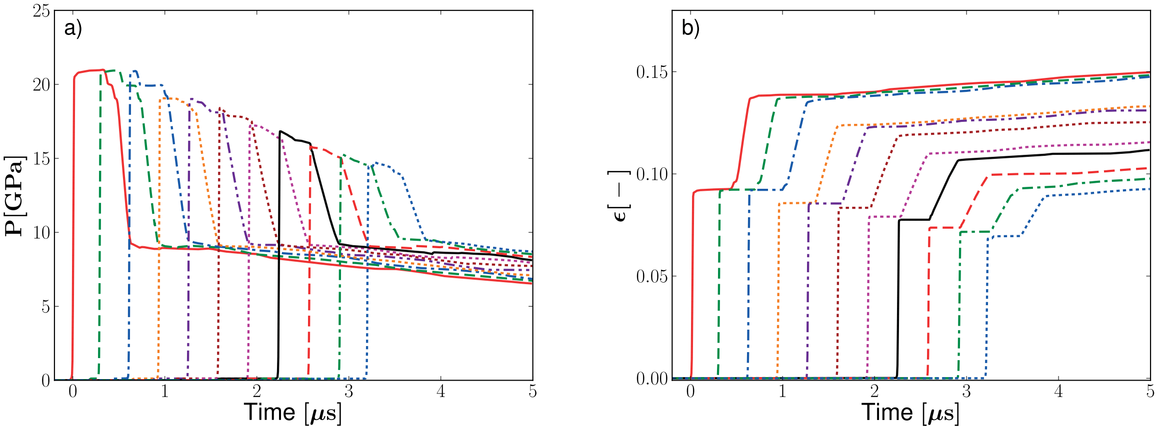

Figure 6.18: Pressure and strain for the second recovery experiment at various depths in the Be target. $t = 0$ is the arrival time of the first pressure spike at the loaded surface of the Be. Left (a): pressure as a function of time; right (b): strain as a function of time. Solid red: 0.015 cm; dashed green: 0.15 cm; dotted-dashed blue: 0.3 cm; dotted orange: 0.45 cm; dotted-dotted-dashed purple: 0.6 cm; solid black: 0.75 cm; dotted maroon: 0.9 cm; dotted magenta: 1.05 cm; dashed red: 1.2 cm; dotted-dashed green: 1.35 cm; dashed blue: 1.485 cm.

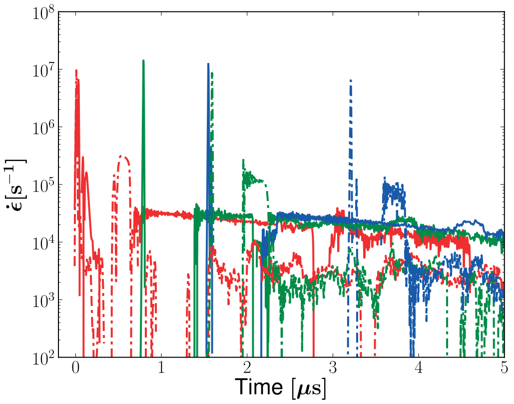

Figure 6.19: Strain-rate as a function of time for both recovery experiments at various depths in the Be target (red: leading edge; green: middle; blue: trailing edge). $t = 0$ is the arrival time of the first pressure spike at the loaded surface of the Be. Solid: first recovery experiment; dashed: second recovery experiment.

6.6 Discussion and conclusion

We performed six HE-driven Be RT experiments to discriminate among different strength models. These experiments were designed to reach a phase space where the models' growth predictions differed. Relative to the predicted behavior, the data suggest that the Be ripples growth was only slightly mitigated by strength, indicating weaker than anticipated strength. The RING model does reasonably well predicting the growth for the larger initial amplitude experiments. The other models under-predict the perturbation growth. The experimental results challenge the underlying assumptions of the existing strength models. Once the material enters a strain, strain-rate, and pressure phase space far from the calibration regimes of the current models, its predicted behavior breaks down. In part, the models rely on a limited range of data, but also limited physical assumptions, mostly having to do with how strain and strain rate carry the plastic flow. For example, the results raise questions about the ansatz formulations, such as what are the proper rate hardening relationships in the thermal activation and phone drag regimes; where do the regimes even cross; are strain and strain rate the proper independent variables or should they be explicitly replaced with dislocation density and velocity? To complicate the challenge of developing a complete constitutive model for Be, the recovery experiments showing a twinning fraction of slightly less than 50% suggest that twining should not be overlooked as an important physical mechanism in the material flow. Furthermore, while the RT experiments show no observable spall or cracks at length scales that could be imaged, the recovery experiments do. Granted, the loading profiles between the two experiments differ, and the recovery experiments by their nature are done late in time, long after release waves have traversed the samples. However, the recovery experiments do suggest failure mechanisms should be included in any advanced Be plasticity model. As such, experiments might be done that are specifically designed to catch material failure under loading to determine if the behavior observed in these experiments is more a result of failure mechanisms, such as shear localization, or if indeed the plastic flow is truly a result of weaker constitutive properties than those predicted by most models.

If similar experiments are proposed for future work, we recommend adjusting the existing models to match the data set presented here and then driving the targets through different regions of stress-strain-rate phase space by adjusting drive or initial perturbations, or by tamping the target to maintain the Be at pressure for longer periods of time. Varying the initial perturbation wavelength would lead to a dispersion curve that could increase our understanding of Be strength in these extreme regimes while higher temperature experiments could also be a means to distinguish the models in future experiments.

CHAPTER VII

Conclusions and future work

7.1 Summary and key findings

The objective of this work is (i) to develop a numerical and computational framework to perform studies of mixing phenomena in compressible multiphase flows, and (ii) to study mixing phenomena relevant to many scientific and engineering applications, including inertial confinement fusion, supernova explosions, fuel injection, plasma deposition, cancer treatments, and turbomachinery.

To accomplish the first objective,

- novel numerical techniques were presented to solve consistently compressible multiphase flows with shocks and interfaces [151, 131]. Spurious pressure oscillations generated at interfaces caused simulations using conventional methods to fail. A non-conservative approach for the material parameters, combined with a new limiting technique, reduced to unit roundoff these spurious pressure oscillations, Figures 2.1, 2.2, and 2.3. Additionally, new sensors were developed to detect flow discontinuities and apply limiting only at these discontinuities. This work enables the simulation of compressible multiphase flows using the Discontinuous Galerkin (DG) method, a state-of-the-art high-order numerical method. Using our methods and framework, scientific insight can be provided into many types of flows relevant to, among others, astrophysics, naval engineering, and biomedical engineering.
- A multi-Graphics Processing Units (GPU) parallel paradigm was implemented to resolve the flow features and the length scales of interest by combining the cuda frame-

work and the Message Passing Interface (MPI) to communicate between GPUs [239], Figure 2.4. The effectiveness and robustness of a new parallel computing framework that uses the latest hardware and software capabilities was demonstrated. The code exhibits good weak and strong scaling up to at least 32 GPUs, Figure 2.5. As the need for exascale computing increases, these types of heterogeneous computing which combine specialized hardware and software will be critical for the simulation of ever more complex flows.

- New enhancement procedures for the advection discretization of the DG method were proposed. Two new family of numerical schemes are stable and exhibit a theoretical $3P+1$ convergence rate. This work is particularly important because it fixes the order of accuracy mismatch between advection and diffusion DG discretization and enables the simulation of advection-diffusion problems without loss of accuracy.

Using this framework, we have also addressed our second objective by

- Studying the mixing dynamics of multi-layered Richtmyer-Meshkov (RM) instabilities and providing support to the idea that shocks and rarefactions can be used to control the instability growth [113], Figure 4.11. This concept of control is especially important in Inertial Confinement Fusion (ICF), where mixing from hydrodynamic instabilities is particularly detrimental. Control of mixing through complex accelerations may prove to be critical in other types of flows as well, *e.g.* in supersonic combustion.

- Modeling perturbation growth and vorticity dynamics of a blast-driven hydrodynamic instability. The circulation dynamics was related to the wave parameters, and shown to scale linearly with rarefaction length, Figure 5.14, and as a power law of rarefaction strength, Figure 5.15. Perturbation growth was shown to scale with the circulation, Figures 5.16 and 5.17. This approach to understanding wave interactions with interfaces can prove valuable to analyzing different types of waves driving hydrodynamic instabilities in many other contexts, including, for example, ultrasound induced lung hemorrhaging.

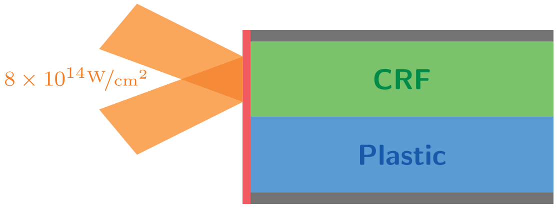

(a) Problem setup for the blast-driven KH experiment.

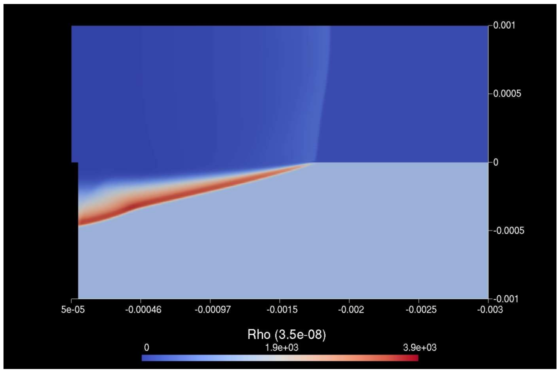

(b) Density at 35ns for our simulation.

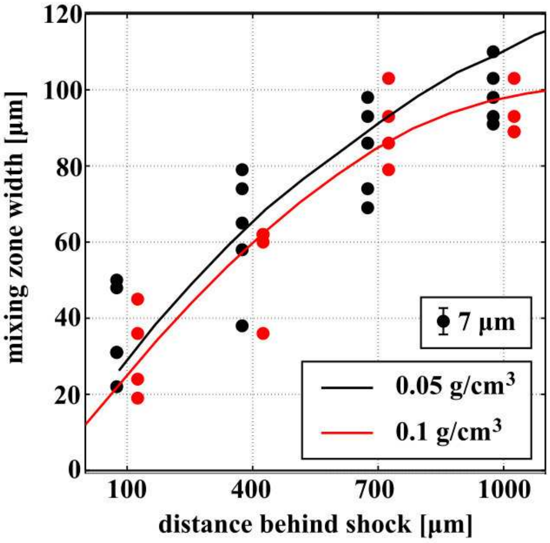

(c) Mixing zone width as a function of distance behind the shock. Symbols: experimental data. Solid lines: prediction using $h = C\int_0^\tau \Delta u_s \, \mathrm{d}t + h_0$, where Δu_s is the shear velocity in the mixing zone predicted from the simulation. Black: foam density of $0.05\mathrm{g/cm^3}$; Red: foam density of $0.05\mathrm{g/cm^3}$. From Di Stefano et al. [114]. © AIP Publishing LLC. Reproduced with permission.

Figure 7.1: Blast-driven KH instability experiments from Di Stefano et al. [114].

- Using the Rayleigh-Taylor (RT) instability to test material strength models of Beryllium in high-strain-rate ($10^6\mathrm{s}^{-1}$) and pressure (50GPa) regimes [240]. These experiments provided valuable data for the modeling of beryllium strength in regimes where the data is sparse. Beryllium in this phase-space exhibited weaker than anticipated strength, Figure 6.10. The experimental technique using the RT instability combines our knowledge of hydrodynamic instabilities with numerical simulations to infer properties of materials, in this case strength, and can be expanded to test many other materials in these regimes.

- Providing insights into the flow dynamics of the blast-driven Kelvin-Helmholtz (KH) instability, which were subsequently used to model experiments in [114], as summarized in Figure 7.1.

7.2 Suggestions for future work

Several active areas of research can be pursued on the basis of this work. In this section, we discuss potential extensions of the models to incorporate different physical effects, improvements to the numerical framework, further directions for the high performance computing paradigm, and studies of other fluid problems using our framework.

7.2.1 Extending the physical models

The evolution equations, Eq. (1.5), and models used throughout this thesis to represent multiphase flows, e.g the stiffened equation of state, Eq. (2.2), may be extended to explore a larger physical space and improve the fidelity of our simulations. Models for viscosity, surface tension, heat, mass transfer, and visco-elastic effects could be incorporated by adding the relevant modeling terms to the system of partial differential equations. In the context of plasma physics, where, for example, magnetic and electric fields highly influence the hydrodynamics, we could start by solving single-fluid plasma equations such as the ideal [241], Hall [242, 243], or resistive magneto-hydrodynamic equations. Further improvements in this direction may include solving "multifluid" plasma equations (e.g. the 5-moment [244, 245, 246] or 13-moment equations [247, 248]), where "multifluid" here means that the electrons and ions are evolved separately and coupled through source terms.

Turbulence arising from hydrodynamic instabilities or in multiphase flows is an active area of research today. Performing Large Eddy Simulations (LES) or Direct Numerical Simulations (DNS) of these types of flows would require the addition of subgrid scale models or viscous effects. This presents opportunities both for developing subgrid scale models for multiphase flows and for studying the effect of turbulence on mixing in multiphase flows.

Chemical reactions in many of the applications discussed in the introduction have a significant effect on the mixing dynamics. Incorporating these reacting flows into our framework is challenging due to the large number of possible chemical reactions and species but it would enable the fundamental study of these effects on mixing, with the objective of providing fundamental or even optimization insight into engineering applications such as internal combustion engines.

7.2.2 Improving the numerical methods

Three-dimensional flow solvers is the first priority to improve the fidelity of the simulation results and expand the code's capabilities. Additionally, while the mathematical models describing some of the physics presented in Section 7.2.1 have been well studied and established, their numerical implementation remains problematic and will have a significant impact on the numerical methods. Disparate time scales and length scales may constrain the spatial and time discretizations, making the simulations impractical on today's computers. Most significantly with respect to the work presented here, the hyperbolicity of the partial differential equations is no longer assured. Computing higher order derivatives efficiently becomes paramount. Recent efforts to extend the DG method to the Navier-Stokes equations with the Recovery Discontinuous Galerkin (RDG) method [139, 138, 137] have been successful in achieving very high order accuracy and could help resolve some of the effects of interest. Yet many open questions remain, including preserving accuracy in three-dimensions, at boundaries, and in unstructured grids. Finally, we mentioned in Chapter III several strategies and their shortcomings to increase the order of accuracy of the DG method for advection and match that obtained by the RDG method for diffusion. Chapter III presented some ideas that could be pursued to achieve a stable and strictly compact enhancement scheme for advection.

7.2.3 Directions for high performance computing

Supercomputing with GPUs is a very recent field and has seen many technological advances over the course of my dissertation work. Eight major versions of CUDA have been released since my start at the University of Michigan. The GPUs used for this work, the Tesla K20, has fifteen times the processing power and twice the bandwidth of the Tesla C1060, the GPU used for my Master's thesis. Our high performance computing paradigm, consisting of multiple GPUs each linked to a different Computing Processing Units (CPU) and communicating through these, is robust and easily adapted to a wide range of cluster configurations and GPUs. However, it does not take advantage of the recent developments in GPU to GPU communication, namely NVIDIA's GPUDirect and Unified

Memory capabilities. GPUDirect allows for memory transfers directly between GPUs and significantly reduces the communication overhead by eliminating many unnecessary memory copies from the host to the device and host to host. GPUDirect uses a similar syntax as MPI, and, as such, can be easily implemented provided the cluster supports this capability. Similarly, CUDA's Unified Memory model allows for easier memory management across GPUs and CPUs by blurring the line between GPU and CPU memories. Finally, the very recent OpenAcc programming standard abstracts the accelerator, which can be either a GPU or CPU, and attempts to simplify parallel programming and code optimizing with the help of the compiler.

Throughout this work, following Donald Knuth's advice [249], "premature optimization" was avoided and a robust implementation of the methods was prioritized. This choice implies that the code, through an in-depth profiling exercise, could most likely be optimized to further increase its efficiency.

Finally, as high performance computing clusters increase the number of nodes and computing devices, faults due to, for example, hardware failure, cosmic rays, and quantum tunneling, will increase as well and risk introducing errors in the computations. Making the numerical methods fault tolerant is rapidly becoming a priority. The DG method has the unique advantage that the solution is discretized in cells and represented inside each cell by a polynomial. This advantage can be exploited through intra- or inter-cell interpolation with limiting and recovery procedures to reconstruct missing data due to faults.

7.2.4 Investigating compressible multiphase flows

Our numerical framework can be used to study many interesting problems in high speed, compressible, multiphase flows with interfaces. Provided the necessary improvements in models, methods, and computing paradigms, the following problems could be investigated as a direct continuation of this work.

In the context of hydrodynamic instabilities, such as the blast-driven instability, the growth of multimode initial perturbations and the late time bubble merging can be easily investigated by changing the initial conditions. Studying the conditions under which the perturbation's growth is such that it interacts with the blast wave front (as observed for shocks by Rikanati et al. [182]) may also be of interest. The effect of reflected waves in the multilayered RM study, Chapter IV, can be further explored by simulating a single perturbed interface interacting with multiple waves (e.g. shocks, rarefactions, and blasts) coming from different sides of the interface. The timing between the waves and the types of waves is expected to have a significant impact on the growth. Various combinations of the waves and parameters could be used to quantify the increase or decrease of mixing. With the inclusion of thermal and radiation effects, the code may be used to investigate these effects on perturbation growth in regimes relevant to supernova collapse and ICF. Some preliminary studies of the multilayered KH instability were performed and presented at the APS 56^{th} Meeting of the Division of Plasma Physics. These studies could be further developed in two main directions. The first is to investigate the supersonic KH instability, such as was recently observed experimentally by Wan et al. [250]. The second is to analyze the perturbation growth and transition to turbulence of an evolving KH instability interacting with a shock, blast, or rarefaction wave.

Many interesting problems in multiphase flows can also be investigated. We have simulated supersonic liquid drops hitting walls and observed large negative tensions inside the drops, Figure 7.2. Analyzing this situation with a small air bubble inside the drop either by modeling it or with a very high resolution computation, may lead to interesting cavitation effects and wall damage mechanisms. Simulations of colliding drops and jets can offer insight into combustion engine flows. Additionally, for homogeneous bubbly flows, we developed a mixture model which modifies the stiffened equation of state to enforce the correct speed of sound in the mixture, Figure 7.3. Finally, studying the effect of air bubbles in a liquid flow on the turbulent statistics can lead to some interesting turbulence enhancing or reducing methods.

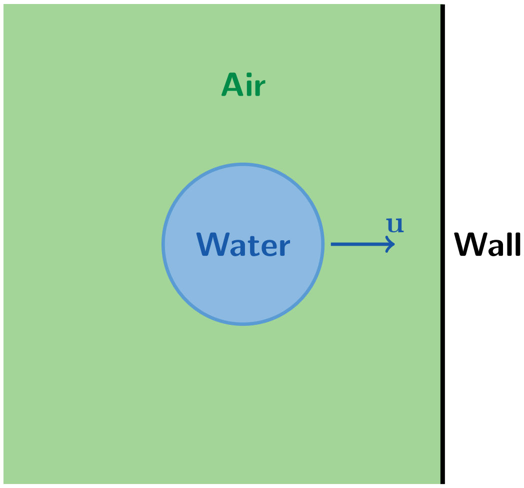

(a) Problem setup for a supersonic drop hitting a wall.

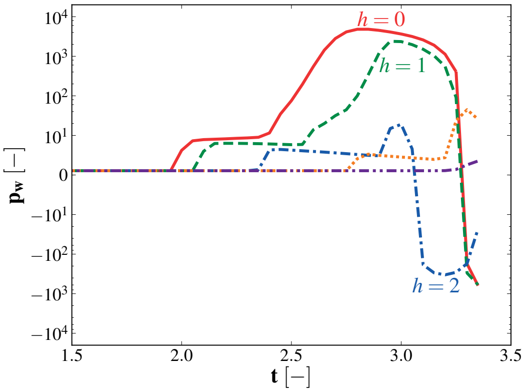

(b) Pressure at the wall at three different locations (Mach 2.5).

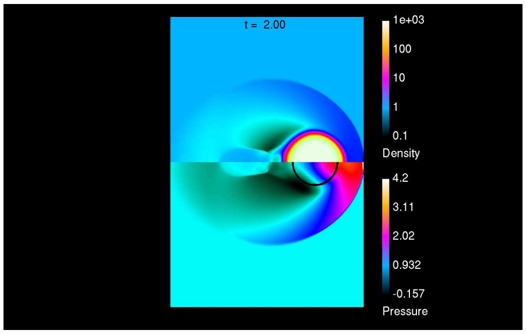

(c) $t = 2$

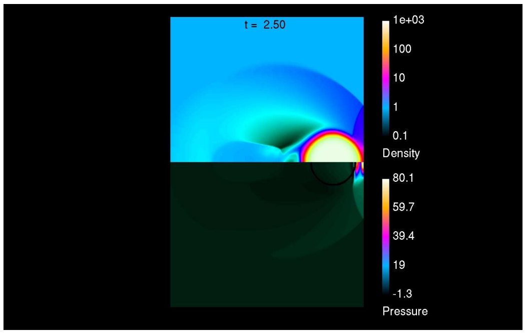

(d) $t = 2.5$

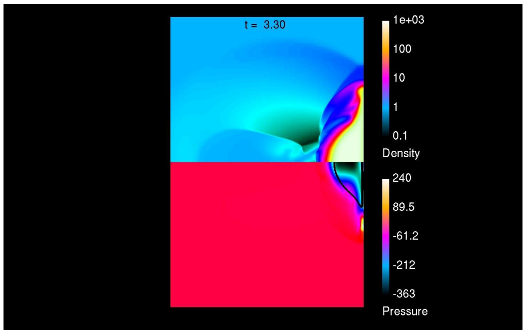

(e) $t = 3.3$

Figure 7.2: Setup and simulation results of non-dimensional density (top half of right column) and pressure (bottom half of right column) for a Mach 2.5 drop hitting a wall.

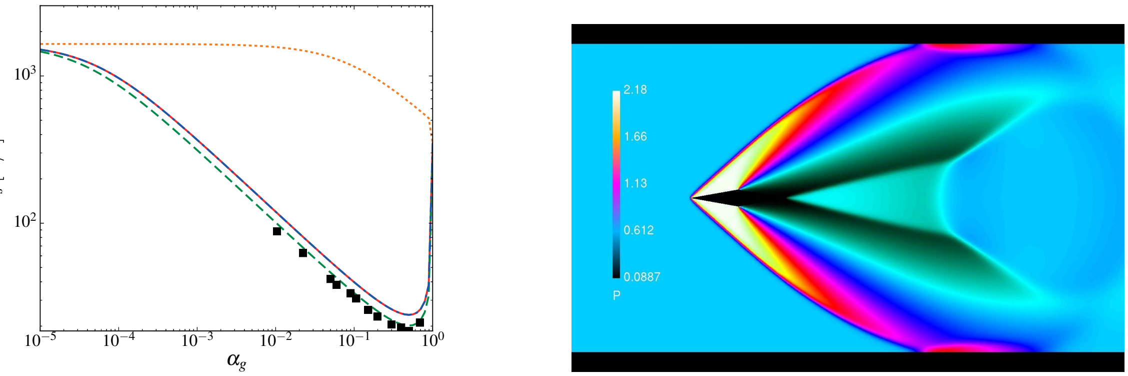

(a) Speed of sound as a function of gas volume fraction, α_g. Solid red: adiabatic theory [251]; dashed green: isothermal theory [251]; black squares: experiments by Brennen [251]; dotted orange: original stiffened equation of state; dash-dotted blue: proposed model.

(b) Pressure in the flow (Mach 3, angle of the wedge = 10°).

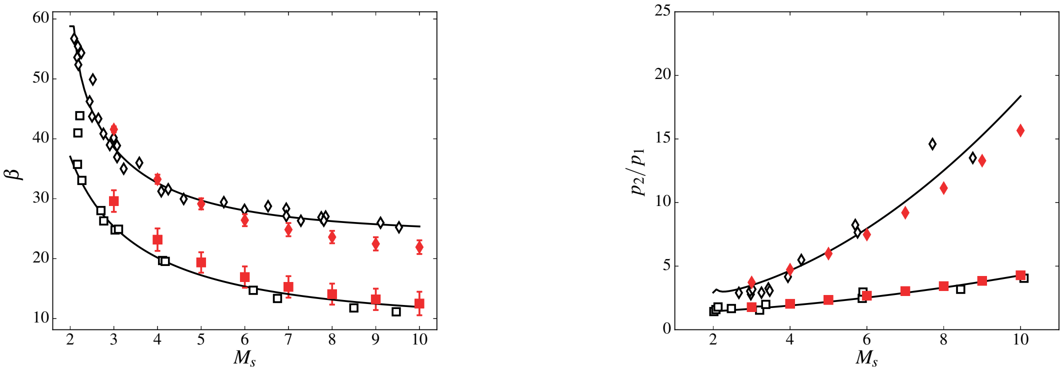

(c) Shock deflection angle as a function of inflow Mach number. Solid black: adiabatic theory; black symbols: experimental data [252]; red symbols: simulation data with proposed model; squares: 4° wedge; diamonds: 4° wedge.

(d) Shock pressure ratio as a function of inflow Mach number. Solid black: adiabatic theory; black symbols: experimental data [252]; red symbols: simulation data with proposed model; squares: 4° wedge; diamonds: 4° wedge.

Figure 7.3: Speed of sound in the bubbly mixture and simulation results of supersonic bubbly flow over a wedge.

APPENDICES

APPENDIX A

List of publications

Peer-reviewed journal publications

Henry de Frahan, M. T., Varadan, S. & Johnsen, E. 2015 A new limiting procedure for Discontinuous Galerkin methods applied to compressible multiphase flows with shocks and interfaces. *J. Comput. Phys.*, **280 (0)**, 489–509.

Henry de Frahan, M. T., Movahed, P. & Johnsen, E. 2015 Numerical simulations of a shock interacting with successive interfaces using the Discontinuous Galerkin method: the multilayered Richtmyer–Meshkov and Rayleigh–Taylor instabilities. *Shock Waves*, **25 (4)**, 329–345.

Henry de Frahan, M. T., Belof, J. L., Cavallo, R. M., Raevsky, V. A., Ignatova, O. N., Lebedev, A., Ancheta, D. S., El-dasher, B. S., Florando, J. N., Gallegos, G. F., Johnsen, E. & LeBlanc, M. M.. 2015 Experimental and numerical investigations of beryllium strength models using the Rayleigh-Taylor instability *J. Appl. Phys.*, **117 (22)**, 225901. **Cover of volume 117, number 22 of the Journal of Applied Physics (2015) and featured article**

Di Stefano, C. A., Malamud, G., Henry de Frahan, M. T., Kuranz, C. C., Shimony, A., Klein, S. R., Drake, R. P., Johnsen, E., Shvarts, D., Smalyuk, V. A. & D. Martinez. 2014 Observation and modeling of mixing-layer development in high-energy-density, blast-wave-driven shear flow, *Phys. Plasmas*, **21(5)**, 056306.

Henry de Frahan, M. T., Johnsen, E. 2016 Interaction of a blast wave with a perturbed interface, in preparation.

Henry de Frahan, M. T. & Johnsen, E. 2016 Improvement of the accuracy of Discontinuous Galerkin methods for advection-dominated problems, in preparation.

Henry de Frahan, M. T., Johnsen, E. 2016 Modeling high-void fraction bubbly flows with the stiffened equation of state, in preparation.

Conference proceedings

Henry de Frahan, M. T., Khieu, L. & Johnsen, E. 2015 High-order Discontinuous Galerkin Methods Applied to Multiphase Flows. 22d *AIAA Computational Fluid Dynamics Conference*, doi: 10.2514/6.2015-3045. **AIAA CFD Best Student Paper Award (3d place)**

Henry de Frahan, M. T., Movahed, P. & Johnsen, E.. 2015 Investigating the multilayered Richtmyer-Meshkov instability with high-order accurate numerical methods, 29th *International Symposium on Shock Waves 2.*

Henry de Frahan, M. T. & Johnsen, E, 2013 Discontinuous Galerkin method for multifluid Euler equations, 21st *AIAA Computational Fluid Dynamics Conference*, doi: 10.2514/6.2013-2595, 2013

APPENDIX B

Limiting properties and extensions

B.1 Proofs of the nonlinear properties of limiting

B.1.1 Addition

Let $U = A + B$, with two different limiting approaches $\widetilde{U} = \widetilde{A+B}$ and $\widetilde{\widetilde{U}} = \widetilde{A} + \widetilde{B}$. We denote three adjacent computational cells $L : x \in [-3,-1]$, $C : x \in [-1,1]$, and $R : x \in [1,3]$. Without loss of generality, we assume for simplicity $P = 1$ and Hierarchical Reconstruction (HR) limiting. In this case,

$$A(x) = A_0 + A_1 x, \quad \widetilde{A}(x) = A_0 + \widetilde{A}_1 x, \qquad B(x) = B_0 + B_1 x, \quad \widetilde{B}(x) = B_0 + \widetilde{B}_1 x. \tag{B.1}$$

where $\widetilde{A}_1 = \frac{1}{2}\text{minmod}\left(A_0^C - A_0^L, A_0^R - A_0^C\right)$ and $\widetilde{B}_1 = \frac{1}{2}\text{minmod}\left(B_0^C - B_0^L, B_0^R - B_0^C\right)$. We can write the limited slopes of U as

$$\begin{aligned} \widetilde{U}_1 &= \frac{1}{2}\text{minmod}\left(U_0^C - U_0^L, U_0^R - U_0^C\right) \\ &= \frac{1}{2}\text{minmod}\left((A_0^C - A_0^L) + (B_0^C - B_0^L), (A_0^R - A_0^C) - (A_0^R - A_0^C)\right), \end{aligned} \tag{B.2}$$

and, in the other case,

$$\widetilde{\widetilde{U}}_1 = \widetilde{A}_1 + \widetilde{B}_1 = \frac{1}{2}\left(\text{minmod}\left(A_0^C - A_0^L, A_0^R - A_0^C\right) + \text{minmod}\left(B_0^C - B_0^L, B_0^R - B_0^C\right)\right). \tag{B.3}$$

The non-linearity of the minmod procedure implies that $\widetilde{U}_1 \neq \widetilde{\widetilde{U}}_1$ and, therefore, $\widetilde{A+B} \neq \widetilde{A} + \widetilde{B}$.

B.1.2 Multiplication

Let $U = AB$ and $\widetilde{U} = \widetilde{A}\widetilde{B}$. Without loss of generality, we assume $P = 2$ and HR limiting. Through polynomial identification,

$$\widetilde{U}_0 = \widetilde{A}_0\widetilde{B}_0, \quad \widetilde{U}_1 = \widetilde{A}_1\widetilde{B}_0 + \widetilde{A}_0\widetilde{B}_1, \quad \widetilde{U}_2 = \widetilde{A}_2\widetilde{B}_0 + \widetilde{A}_1\widetilde{B}_1 + \widetilde{A}_0\widetilde{B}_2. \tag{B.4}$$

The cell averages of U and $\widetilde{U}$ are

$$\int U \,\mathrm{d}\Omega = U_0 + \frac{1}{6}U_2 = A_0B_0 + \frac{1}{6}\left(A_2B_0 + A_1B_1 + A_0B_2\right), \tag{B.5}$$

$$\int \widetilde{U} \,\mathrm{d}\Omega = \widetilde{U}_0 + \frac{1}{6}\widetilde{U}_2 = \widetilde{A}_0\widetilde{B}_0 + \frac{1}{6}\left(\widetilde{A}_2\widetilde{B}_0 + \widetilde{A}_1\widetilde{B}_1 + \widetilde{A}_0\widetilde{B}_2\right). \tag{B.6}$$

We can compute the difference in the cell averages of U and $\widetilde{U}$ to obtain

$$\int \widetilde{U} \,\mathrm{d}\Omega - \int U \,\mathrm{d}\Omega = A_0B_0 + \frac{1}{6}\left(\widetilde{A}_1\widetilde{B}_1 - A_1B_1\right) - \frac{1}{6^2}\left(\widetilde{A}_2\widetilde{B}_2 - A_2B_2\right) \neq 0. \tag{B.7}$$

Since this difference is non-zero in general, this implies that $\int \widetilde{A}\widetilde{B} \,\mathrm{d}\Omega \neq \int AB \,\mathrm{d}\Omega$.

APPENDIX C

Limiting properties and extensions

C.1 Proofs of the nonlinear properties of limiting

C.1.1 Addition

Let $U = A + B$, with two different limiting approaches $\widetilde{U} = \widetilde{A+B}$ and $\widetilde{\widetilde{U}} = \widetilde{A} + \widetilde{B}$. We denote three adjacent computational cells $L : x \in [-3, -1]$, $C : x \in [-1, 1]$, and $R : x \in [1, 3]$. Without loss of generality, we assume for simplicity $P = 1$ and HR limiting. In this case,

$$A(x) = A_0 + A_1 x, \quad \widetilde{A}(x) = A_0 + \widetilde{A}_1 x, \qquad B(x) = B_0 + B_1 x, \quad \widetilde{B}(x) = B_0 + \widetilde{B}_1 x. \tag{C.1}$$

where $\widetilde{A}_1 = \frac{1}{2}\text{minmod}\left(A_0^C - A_0^L, A_0^R - A_0^C\right)$ and $\widetilde{B}_1 = \frac{1}{2}\text{minmod}\left(B_0^C - B_0^L, B_0^R - B_0^C\right)$. We can write the limited slopes of U as

$$\begin{aligned}\widetilde{U}_1 &= \frac{1}{2}\text{minmod}\left(U_0^C - U_0^L, U_0^R - U_0^C\right) \\ &= \frac{1}{2}\text{minmod}\left((A_0^C - A_0^L) + (B_0^C - B_0^L), (A_0^R - A_0^C) - (A_0^R - A_0^C)\right),\end{aligned} \tag{C.2}$$

and, in the other case,

$$\widetilde{\widetilde{U}}_1 = \widetilde{A}_1 + \widetilde{B}_1 = \frac{1}{2}\left(\text{minmod}\left(A_0^C - A_0^L, A_0^R - A_0^C\right) + \text{minmod}\left(B_0^C - B_0^L, B_0^R - B_0^C\right)\right). \tag{C.3}$$

The non-linearity of the minmod procedure implies that $\widetilde{U}_1 \neq \widetilde{\widetilde{U}}_1$ and, therefore, $\widetilde{A+B} \neq \widetilde{A}+\widetilde{B}$.

C.1.2 Multiplication

Let $U = AB$ and $\widetilde{U} = \widetilde{A}\widetilde{B}$. Without loss of generality, we assume $P = 2$ and HR limiting. Through polynomial identification,

$$\widetilde{U}_0 = \widetilde{A}_0\widetilde{B}_0, \quad \widetilde{U}_1 = \widetilde{A}_1\widetilde{B}_0 + \widetilde{A}_0\widetilde{B}_1, \quad \widetilde{U}_2 = \widetilde{A}_2\widetilde{B}_0 + \widetilde{A}_1\widetilde{B}_1 + \widetilde{A}_0\widetilde{B}_2. \tag{C.4}$$

The cell averages of U and $\widetilde{U}$ are

$$\int U \,\mathrm{d}\Omega = U_0 + \frac{1}{6}U_2 = A_0B_0 + \frac{1}{6}\left(A_2B_0 + A_1B_1 + A_0B_2\right), \tag{C.5}$$

$$\int \widetilde{U} \,\mathrm{d}\Omega = \widetilde{U}_0 + \frac{1}{6}\widetilde{U}_2 = \widetilde{A}_0\widetilde{B}_0 + \frac{1}{6}\left(\widetilde{A}_2\widetilde{B}_0 + \widetilde{A}_1\widetilde{B}_1 + \widetilde{A}_0\widetilde{B}_2\right). \tag{C.6}$$

We can compute the difference in the cell averages of U and $\widetilde{U}$ to obtain

$$\int \widetilde{U} \,\mathrm{d}\Omega - \int U \,\mathrm{d}\Omega = A_0B_0 + \frac{1}{6}\left(\widetilde{A}_1\widetilde{B}_1 - A_1B_1\right) - \frac{1}{6^2}\left(\widetilde{A}_2\widetilde{B}_2 - A_2B_2\right) \neq 0. \tag{C.7}$$

Since this difference is non-zero in general, this implies that $\int \widetilde{A}\widetilde{B} \,\mathrm{d}\Omega \neq \int AB \,\mathrm{d}\Omega$.

C.2 Extension to other multiphase models

We illustrate the generality of our limiting approach by applying it to the five-equations model, also used to describe multiphase flows [89], written for a two-phase system as:

$$\frac{\partial \alpha_1}{\partial t} + u_j \frac{\partial \alpha_1}{\partial x_j} = 0, \tag{C.8a}$$

$$\frac{\partial(\rho_1\alpha_1)}{\partial t} + \frac{\partial}{\partial x_j}\left(\rho_1\alpha_1 u_j\right) = 0, \tag{C.8b}$$

$$\frac{\partial(\rho_2\alpha_2)}{\partial t} + \frac{\partial}{\partial x_j}\left(\rho_2\alpha_2 u_j\right) = 0, \tag{C.8c}$$

$$\frac{\partial(\rho u_i)}{\partial t} + \frac{\partial}{\partial x_j}\left(\rho u_i u_j + p\delta_{ij}\right) = 0, \tag{C.8d}$$

$$\frac{\partial E}{\partial t} + \frac{\partial}{\partial x_j}\left[u_j(E + p)\right] = 0, \tag{C.8e}$$

where ρ_i and α_i are the density and volume fraction of the i^{th} fluid, respectively, $\alpha_2 = 1 - \alpha_1$ and $\rho = \alpha_1\rho_1 + \alpha_2\rho_2$. The mixture internal energy is defined as $\rho e = \alpha_1\rho_1 e_1 + \alpha_2\rho_2 e_2$. Gryngarten and Menon [88] discuss a primitive reconstruction procedure but do not address possible conservation issues arising from limiting the primitive variables. For high-order accurate, non-oscillatory, and conservative limiting, we directly apply our limiting procedure detailed above. For a Mie-Grüneisen equation of state, we limit p and α_1 and reconstruct the internal energy as

$$\begin{aligned}\widetilde{\rho e}_n = {} & \frac{1}{\Gamma_1}\sum_{k=0}^{n}\binom{n}{k}\widetilde{p}_{n-k}\widetilde{(\alpha_1)}_k + \left(-\frac{p_{\text{ref},1}}{\Gamma_1} + \rho e_{\text{ref},1}\right)\widetilde{(\alpha_1)}_n \\ & + \frac{1}{\Gamma_2}\sum_{k=0}^{n}\binom{n}{k}\widetilde{p}_{n-k}\widetilde{(\alpha_2)}_k + \left(-\frac{p_{\text{ref},2}}{\Gamma_2} + \rho e_{\text{ref},2}\right)\widetilde{(\alpha_2)}_n, \quad \text{for } n = 1, \dots, P,\end{aligned} \tag{C.9}$$

where $\widetilde{\alpha_2} = 1 - \widetilde{\alpha_1}$. Our limiting procedure can readily be extended to other models, *e.g.*, Baer-Nunziato [83], in this way.

APPENDIX D

Circulation in two-dimensional inviscid flow

D.1 Compressible and advective terms in the circulation equation

In this appendix, we show that the advective and compressible terms in the evolution equation for circulation balance each other. This is important to show that the only contribution to circulation in a two-dimensional inviscid flow is baroclinic vorticity generation.

We start with the evolution equation for vorticity in a two-dimensional inviscid flow:

$$\frac{\partial \omega}{\partial t} = -(\mathbf{u} \cdot \nabla)\omega - \omega(\nabla \cdot \mathbf{u}) + \frac{1}{\rho^2}(\nabla \rho \times \nabla p)$$

where ω is the z-component of vorticity, $\mathbf{u}$ is the velocity vector, ρ is the density, and p is the pressure. Integrating this evolution equation in the half-domain around the interface yields the evolution equation for circulation

$$\begin{aligned}
\frac{\partial \Gamma}{\partial t} = \frac{\partial}{\partial t}\int_A \omega \,\mathrm{d}A &= \int_A \left(-(\mathbf{u} \cdot \nabla)\omega - \omega(\nabla \cdot \mathbf{u}) + \frac{1}{\rho^2}(\nabla \rho \times \nabla p)\right) \mathrm{d}A \\
&= \int_A \nabla \cdot (\mathbf{u}\omega) \,\mathrm{d}A + \int_A \frac{1}{\rho^2}(\nabla \rho \times \nabla p) \,\mathrm{d}A \\
&= \mathbf{u}\omega\big|_{\mathrm{d}A} + \int_A \frac{1}{\rho^2}(\nabla \rho \times \nabla p) \,\mathrm{d}A \\
&= \int_A \frac{1}{\rho^2}(\nabla \rho \times \nabla p) \,\mathrm{d}A
\end{aligned}$$

because $\mathbf{u}\omega|_{\mathrm{d}A}$ is zero on the boundary of the integration surface (ω is zero at the intergration boundaries). The evolution equation of circulation in our two-dimensional inviscid flow depends solely on the baroclinic vorticity generation term.

BIBLIOGRAPHY

BIBLIOGRAPHY

[1] D. L. Preston, D. L. Tonks, D. C. Wallace, Model of plastic deformation for extreme loading conditions, J. Appl. Phys. 93 (2003) 211.

[2] P. E. Dimotakis, Turbulent mixing, Annu. Rev. Fluid Mech. 37 (2005) 329–356.

[3] K.-H. Kim, G. Chahine, J.-P. Franc, A. Karimi (Eds.), Advanced Experimental and Numerical Techniques for Cavitation Erosion Prediction, volume 106 of *Fluid Mechanics and Its Applications*, Springer Netherlands, Dordrecht, 2014.

[4] J. C. Meng, T. Colonius, Numerical simulations of the early stages of high-speed droplet breakup, Shock Waves (2014) 399–414.

[5] P. Welch, P. Boyle, New turbines to Enable Efficient Geothermal Power Plants, Geotherm. Resour. Counc. Trans. 33 (2009) 8.

[6] T. Theofanous, Aerobreakup of Newtonian and Viscoelastic Liquids, Annu. Rev. Fluid Mech. 43 (2011) 661–690.

[7] K. K. Haller, Y. Ventikos, D. Poulikakos, P. Monkewitz, Computational study of high-speed liquid droplet impact, J. Appl. Phys. 92 (2002) 2821–2828.

[8] K. K. Haller, D. Poulikakos, Y. Ventikos, P. Monkewitz, Shock wave formation in droplet impact on a rigid surface: lateral liquid motion and multiple wave structure in the contact line region, J. Fluid Mech. 490 (2003) 1–14.

[9] L. P. Bayvel, Z. Orzechowski, Liquid Atomization, volume 94, Taylor and Francis, Washington, DC, 1993.

[10] J. Yang, T. Kubota, E. E. Zukoski, Applications of shock-induced mixing to supersonic combustion, AIAA J. 31 (1993) 854–862.

[11] E. Johnsen, Benchmark multifluid problems (2008) 1–11.

[12] E. Vlaisavljevich, A. Maxwell, M. Warnez, E. Johnsen, C. a. Cain, Z. Xu, Histotripsy-Induced Cavitation Cloud Mechanical Properties, IEEE Trans. Ultrason. Ferroelectr. Freq. Control 61 (2014) 341–352.

[13] K. M. Case, Taylor Instability of an Inverted Atmosphere, Phys. Fluids 3 (1960) 366.

[14] H. Michioka, Rayleigh-Taylor instability of a particle packed viscous fluid: Implications for a solidifying magma, Geophys. Res. Lett. 32 (2005) L03309.

[15] M. K. Davey, J. a. Whitehead, Rotating rayleigh-taylor instability as a model of sinking events in the ocean, Geophys. Astrophys. Fluid Dyn. 17 (1981) 237–253.

[16] M. Cuk, S. T. Stewart, Making the Moon from a Fast-Spinning Earth: A Giant Impact Followed by Resonant Despinning, Science (80-.). 338 (2012) 1047–1052.

[17] J. Lindl, Development of the indirect-drive approach to inertial confinement fusion and the target physics basis for ignition and gain, Phys. Plasmas 2 (1995) 3933.

[18] J. D. Lawson, Some Criteria for a Power Producing Thermonuclear Reactor, Proc. Phys. Soc. Sect. B 70 (1957) 6–10.

[19] O. L. Landen, R. Benedetti, D. Bleuel, T. R. Boehly, D. K. Bradley, J. a. Caggiano, D. a. Callahan, P. M. Celliers, C. J. Cerjan, D. Clark, G. W. Collins, E. L. Dewald, S. N. Dixit, T. Doeppner, D. Edgell, J. Eggert, D. Farley, J. a. Frenje, V. Glebov, S. M. Glenn, S. H. Glenzer, S. W. Haan, A. Hamza, B. a. Hammel, C. a. Haynam, J. H. Hammer, R. F. Heeter, H. W. Herrmann, D. G. Hicks, D. E. Hinkel, N. Izumi, M. Gatu Johnson, O. S. Jones, D. H. Kalantar, R. L. Kauffman, J. D. Kilkenny, J. L. Kline, J. P. Knauer, J. a. Koch, G. a. Kyrala, K. LaFortune, T. Ma, a. J. Mackinnon, a. J. Macphee, E. Mapoles, J. L. Milovich, J. D. Moody, N. B. Meezan, P. Michel, a. S. Moore, D. H. Munro, A. Nikroo, R. E. Olson, K. Opachich, A. Pak, T. Parham, P. Patel, H.-S. Park, R. P. Petrasso, J. Ralph, S. P. Regan, B. a. Remington, H. G. Rinderknecht, H. F. Robey, M. D. Rosen, J. S. Ross, J. D. Salmonson, T. C. Sangster, M. B. Schneider, V. Smalyuk, B. K. Spears, P. T. Springer, L. J. Suter, C. a. Thomas, R. P. J. Town, S. V. Weber, P. J. Wegner, D. C. Wilson, K. Widmann, C. Yeamans, A. Zylstra, M. J. Edwards, J. D. Lindl, L. J. Atherton, W. W. Hsing, B. J. MacGowan, B. M. Van Wonterghem, E. I. Moses, Progress in the indirect-drive National Ignition Campaign, Plasma Phys. Control. Fusion 54 (2012) 124026.

[20] R. P. Drake, High-Energy-Density Physics, Spring-Verlag, Berlin, 2006.

[21] S. Woosley, T. Janka, The physics of core-collapse supernovae, Nat. Phys. 1 (2005) 147–154.

[22] J. José, C. Iliadis, Nuclear astrophysics: the unfinished quest for the origin of the elements, Reports Prog. Phys. 74 (2011) 096901.

[23] W. D. Arnett, J. N. Bahcall, R. P. Kirshner, S. E. Woosley, Supernova 1987A, Annu. Rev. Astron. Astrophys. 27 (1989) 629–700.

[24] R. A. Chevalier, Supernova 1987A at five years of age, Nature 355 (1992) 691–696.

[25] R. A. Chevalier, Type II Supernovae SN 1987A and SN 1993J, Science (80-.). 276 (1997) 1374–1378.

[26] A. Goobar, B. Leibundgut, Supernova Cosmology: Legacy and Future, Annu. Rev. Nucl. Part. Sci. 61 (2011) 251–279.

[27] C. C. Kuranz, R. P. Drake, E. C. Harding, M. J. Grosskopf, H. F. Robey, B. a. Remington, M. J. Edwards, a. R. Miles, T. S. Perry, B. E. Blue, T. Plewa, N. C. Hearn, J. P. Knauer, D. Arnett, D. R. Leibrandt, Two-dimensional blast-wave-drive Rayleigh-Taylor instability: experiment and simulation, Astrophys. J. 696 (2009) 749–759.

[28] A. R. Miles, Nonlinear Rayleigh–Taylor instabilities in fast Z pinches, Phys. Plasmas 16 (2009) 032702.

[29] K. Kifonidis, T. Plewa, L. Scheck, H.-T. Janka, E. Müller, Non-spherical core collapse supernovae, Astron. Astrophys. 453 (2006) 661–678.

[30] R. D. Richtmyer, Taylor instability in shock acceleration of compressible fluids, Commun. Pure Appl. Math. 13 (1960) 297–319.

[31] E. E. Meshkov, Instability of the interface of two gases accelerated by a shock wave, Fluid Dyn. 4 (1969) 101–104.

[32] M. Brouillette, The Richtmyer Meshkov Instability, Annu. Rev. Fluid Mech. 34 (2002) 445–468.

[33] K. a. Meyer, Numerical Investigation of the Stability of a Shock-Accelerated Interface between Two Fluids, Phys. Fluids 15 (1972) 753.

[34] Q. Zhang, S.-I. Sohn, Nonlinear theory of unstable fluid mixing driven by shock wave, Phys. Fluids 9 (1997) 1106.

[35] O. Sadot, L. Erez, U. Alon, D. Oron, L. A. Levin, G. Erez, G. Ben-Dor, D. Shvarts, Study of Nonlinear Evolution of Single-Mode and Two-Bubble Interaction under Richtmyer-Meshkov Instability, Phys. Rev. Lett. 80 (1998) 1654–1657.

[36] R. Samtaney, N. J. Zabusky, Circulation deposition on shock-accelerated planar and curved density-stratified interfaces: models and scaling laws, J. Fluid Mech. 269 (1994) 45.

[37] J. W. Jacobs, J. M. Sheeley, Experimental study of incompressible Richtmyer–Meshkov instability, Phys. Fluids 8 (1996) 405.

[38] G. Taylor, The Instability of Liquid Surfaces when Accelerated in a Direction Perpendicular to their Planes. I, Proc. R. Soc. A Math. Phys. Eng. Sci. 201 (1950) 192–196.

[39] D. Oron, L. Arazi, D. Kartoon, A. Rikanati, U. Alon, D. Shvarts, Dimensionality dependence of the Rayleigh–Taylor and Richtmyer–Meshkov instability late-time scaling laws, Phys. Plasmas 8 (2001) 2883.

[40] R. E. Duff, F. H. Harlow, C. W. Hirt, Effects of Diffusion on Interface Instability between Gases, Phys. Fluids 5 (1962) 417.

[41] K. Read, Experimental investigation of turbulent mixing by Rayleigh-Taylor instability, Phys. D Nonlinear Phenom. 12 (1984) 45–58.

[42] S. B. Dalziel, P. F. Linden, D. L. Youngs, Self-similarity and internal structure of turbulence induced by Rayleigh–Taylor instability, J. Fluid Mech. 399 (1999) S002211209900614X.

[43] G. Dimonte, M. Schneider, Density ratio dependence of Rayleigh–Taylor mixing for sustained and impulsive acceleration histories, Phys. Fluids 12 (2000) 304.

[44] G. Dimonte, D. L. Youngs, A. Dimits, S. Weber, M. Marinak, S. Wunsch, C. Garasi, A. Robinson, M. J. Andrews, P. Ramaprabhu, a. C. Calder, B. Fryxell, J. Biello, L. Dursi, P. MacNeice, K. Olson, P. Ricker, R. Rosner, F. Timmes, H. Tufo, Y.-N.

Young, M. Zingale, A comparative study of the turbulent Rayleigh–Taylor instability using high-resolution three-dimensional numerical simulations: The Alpha-Group collaboration, Phys. Fluids 16 (2004) 1668.

[45] P. Ramaprabhu, G. Dimonte, Y.-N. Young, a. C. Calder, B. Fryxell, Limits of the potential flow approach to the single-mode Rayleigh-Taylor problem, Phys. Rev. E 74 (2006) 066308.

[46] P. Ramaprabhu, G. Dimonte, P. Woodward, C. Fryer, G. Rockefeller, K. Muthuraman, P.-H. Lin, J. Jayaraj, The late-time dynamics of the single-mode Rayleigh-Taylor instability, Phys. Fluids 24 (2012) 074107.

[47] A. W. Cook, P. E. Dimotakis, Transition stages of Rayleigh–Taylor instability between miscible fluids, J. Fluid Mech. 443 (2001) 69–99.

[48] D. Ryutov, R. P. Drake, J. Kane, E. Liang, B. a. Remington, W. M. Wood-Vasey, Similarity Criteria for the Laboratory Simulation of Supernova Hydrodynamics, Astrophys. J. 518 (1999) 821–832.

[49] D. Igra, K. Takayama, Experimental Investigation of Two Cylindrical Water Columns Subjected to Planar Shock Wave Loading, J. Fluids Eng. 125 (2003) 325.

[50] R. Samtaney, D. I. Pullin, On initial-value and self-similar solutions of the compressible Euler equations, Phys. Fluids 8 (1996) 2650–2655.

[51] K. J. Fidkowski, A High-Order Discontinuous Galerkin Multigrid Solver for Aerodynamic Applications, Ph.D. thesis, Massachusetts Institute of Technology, 2004.

[52] K. J. Fidkowski, A Simplex Cut-Cell Adaptive Method for High-Order Discretizations of the Compressible Navier-Stokes Equations, Ph.D. thesis, Massachusetts Institute of Technology, 2007.

[53] D. J. Mavriplis, An Assessment of Linear Versus Nonlinear Multigrid Methods for Unstructured Mesh Solvers, J. Comput. Phys. 175 (2002) 302–325.

[54] R. Abgrall, How to Prevent Pressure Oscillations in Multicomponent Flow Calculations: A Quasi Conservative Approach, J. Comput. Phys. 125 (1996) 150–160.

[55] S. Adjerid, K. D. Devine, J. E. Flaherty, L. Krivodonova, A posteriori error estimation for discontinuous Galerkin solutions of hyperbolic problems, Comput. Methods Appl. Mech. Eng. 191 (2002) 1097–1112.

[56] S. Adjerid, T. C. Massey, Superconvergence of discontinuous Galerkin solutions for a nonlinear scalar hyperbolic problem, Comput. Methods Appl. Mech. Eng. 195 (2006) 3331–3346.

[57] B. Cockburn, G. Lin, C.-W. Shu, TVB Runge-Kutta local projection discontinuous Galerkin finite element method for conservation laws III: One-dimensional systems, J. Comput. Phys. 84 (1989) 90–113.

[58] B. Cockburn, C.-W. Shu, TVB Runge-Kutta Local Projection Discontinuous Galerkin Finite Element Method for Conservation Laws II: General Framework, Math. Comput. 52 (1989) 411–435.

[59] B. Cockburn, S. Hou, C.-W. Shu, The Runge-Kutta local projection discontinuous Galerkin finite element method for conservation laws IV: The multidimensional case, Math. Comput. 54 (1990) 545–581.

[60] B. Cockburn, C.-W. Shu, The Local Discontinuous Galerkin Method for Time-Dependent Convection-Diffusion Systems, SIAM J. Numer. Anal. 35 (1997) 2440–2463.

[61] B. Cockburn, C.-W. Shu, The Runge-Kutta Discontinuous Galerkin Method for Conservation Laws V: Multidimensional Systems, J. Comput. Phys. 141 (1997) 199–224.

[62] R. Biswas, K. D. Devine, J. E. Flaherty, Parallel, adaptive finite element methods for conservation laws, Appl. Numer. Math. 14 (1994) 255–283.

[63] L. Krivodonova, Limiters for high-order discontinuous Galerkin methods, J. Comput. Phys. 226 (2007) 879–896.

[64] D. Kuzmin, A vertex-based hierarchical slope limiter for -adaptive discontinuous Galerkin methods, J. Comput. Appl. Math. 233 (2010) 3077–3085.

[65] Y. Liu, C.-W. Shu, E. Tadmor, M. Zhang, Central Discontinuous Galerkin Methods on Overlapping Cells with a Nonoscillatory Hierarchical Reconstruction, SIAM J. Numer. Anal. 45 (2007) 2442.

[66] Z. Xu, Y. Liu, C.-W. Shu, Hierarchical reconstruction for discontinuous Galerkin methods on unstructured grids with a WENO-type linear reconstruction and partial neighboring cells, J. Comput. Phys. 228 (2009) 2194–2212.

[67] R. Saurel, R. Abgrall, A simple method for compressible multifluid flows, SIAM J. Sci. Comput. 21 (1999) 1115–1145.

[68] R. Abgrall, S. Karni, Computations of compressible multifluids, J. Comput. Phys. 169 (2001) 594–623.

[69] E. Johnsen, T. Colonius, Implementation of WENO schemes in compressible multicomponent flow problems, J. Comput. Phys. 219 (2006) 715–732.

[70] T. Xiong, C.-W. Shu, M. Zhang, WENO Scheme with Subcell Resolution for Computing Nonconservative Euler Equations with Applications to One-Dimensional Compressible Two-Medium Flows, J. Sci. Comput. 53 (2012) 222–247.

[71] S. Kawai, H. Terashima, A high-resolution scheme for compressible multicomponent flows with shock waves, Int. J. Numer. Methods Fluids 66 (2011) 1207–1225.

[72] P. Movahed, E. Johnsen, A solution-adaptive method for efficient compressible multifluid simulations, with application to the Richtmyer–Meshkov instability, J. Comput. Phys. 239 (2013) 166–186.

[73] K.-M. Shyue, An Efficient Shock-Capturing Algorithm for Compressible Multicomponent Problems, J. Comput. Phys. 142 (1998) 208–242.

[74] K.-M. Shyue, A Fluid-Mixture Type Algorithm for Compressible Multicomponent Flow with van der Waals Equation of State, J. Comput. Phys. 156 (1999) 43–88.

[75] K.-M. Shyue, A Fluid-Mixture Type Algorithm for Compressible Multicomponent Flow with Mie–Grüneisen Equation of State, J. Comput. Phys. 171 (2001) 678–707.

[76] E. Johnsen, T. Colonius, Numerical simulations of non-spherical bubble collapse., J. Fluid Mech. 629 (2009) 231–262.

[77] G. Ward, D. Pullin, A hybrid, center-difference, limiter method for simulations of compressible multicomponent flows with Mie-Grüneisen equation of state, J. Comput. Phys. 229 (2010) 2999–3018.

[78] R. Saurel, R. Abgrall, A Multiphase Godunov Method for Compressible Multifluid and Multiphase Flows, J. Comput. Phys. 150 (1999) 425–467.

[79] R. Abgrall, R. Saurel, Discrete equations for physical and numerical compressible multiphase mixtures, J. Comput. Phys. 186 (2003) 361–396.

[80] A. Murrone, H. Guillard, A five equation reduced model for compressible two phase flow problems, J. Comput. Phys. 202 (2005) 664–698.

[81] R. K. Shukla, C. Pantano, J. B. Freund, An interface capturing method for the simulation of multi-phase compressible flows, J. Comput. Phys. 229 (2010) 7411–7439.

[82] S. Tokareva, E. Toro, HLLC-type Riemann solver for the Baer–Nunziato equations of compressible two-phase flow, J. Comput. Phys. 229 (2010) 3573–3604.

[83] E. Franquet, V. Perrier, Runge–Kutta discontinuous Galerkin method for the approximation of Baer and Nunziato type multiphase models, J. Comput. Phys. 231 (2012) 4096–4141.

[84] C. Michoski, J. Evans, P. Schmitz, A. Vasseur, A discontinuous Galerkin method for viscous compressible multifluids, J. Comput. Phys. 229 (2010) 2249–2266.

[85] B. Cockburn, C.-w. Shu, Runge – Kutta Discontinuous Galerkin Methods for Convection-Dominated Problems 16 (2001).

[86] E. Franquet, V. Perrier, Runge–Kutta discontinuous Galerkin method for interface flows with a maximum preserving limiter, Comput. Fluids 65 (2012) 2–7.

[87] C. Wang, C.-W. Shu, An interface treating technique for compressible multi-medium flow with Runge–Kutta discontinuous Galerkin method, J. Comput. Phys. 229 (2010) 8823–8843.

[88] L. D. Gryngarten, S. Menon, A generalized approach for sub- and super-critical flows using the Local Discontinuous Galerkin method, Comput. Methods Appl. Mech. Eng. 253 (2013) 169–185.

[89] G. Allaire, S. Clerc, S. Kokh, A Five-Equation Model for the Simulation of Interfaces between Compressible Fluids, J. Comput. Phys. 181 (2002) 577–616.

[90] R. Menikoff, B. J. Plohr, The Riemann problem for fluid flow of real materials, Rev. Mod. Phys. 61 (1989) 75–130.

[91] A. B. Wardlaw, H. U. Mair, Spherical Solutions of an Underwater Explosion Bubble, Shock Vib. 5 (1998) 89–102.

[92] G. Cochran, J. Chan, Shock initiation and detonation models in one and two dimensions, UCID 18024 (1979).

[93] P. G. LeFloch, Shock waves for nonlinear hyperbolic systems in nonconservative form, Inst. Math. its Appl., Minneapolis, Prepr. 593 (1989) 1989.

[94] G. Dal Maso, P. G. LeFloch, F. Murat, Definition and weak stability of nonconservative products, J. Math. Pures Appl. 74 (1995) 483–548.

[95] C. Parés, Numerical methods for nonconservative hyperbolic systems: A theoretical framework, SIAM J. Numer. Anal. 44 (2006) 300.

[96] M. J. Castro, P. G. LeFloch, M. L. Muñoz-Ruiz, C. Parés, Why many theories of shock waves are necessary: Convergence error in formally path-consistent schemes, J. Comput. Phys. 227 (2008) 8107–8129.

[97] A. Canestrelli, A. Siviglia, M. Dumbser, E. F. Toro, Well-balanced high-order centred schemes for non-conservative hyperbolic systems. Applications to shallow water equations with fixed and mobile bed, Adv. Water Resour. 32 (2009) 834–844.

[98] S. Rhebergen, O. Bokhove, J. van der Vegt, Discontinuous Galerkin finite element methods for hyperbolic nonconservative partial differential equations, J. Comput. Phys. 227 (2008) 1887–1922.

[99] W. Sollie, O. Bokhove, J. van der Vegt, Space–time discontinuous Galerkin finite element method for two-fluid flows, J. Comput. Phys. 230 (2011) 789–817.

[100] A. Harten, P. D. Lax, B. van Leer, On upstream differencing and Godunov-type schemes for hyperbolic conservation laws, SIAM Rev. 25 (1983) 35–61.

[101] P. D. Lax, Weak solutions of nonlinear hyperbolic equations and their numerical computation, Commun. Pure Appl. Math. 7 (1954) 159–193.

[102] V. Rusanov, The calculation of the interaction of non-stationary shock waves and obstacles, USSR Comput. Math. Math. Phys. 1 (1962) 304–320.

[103] E. F. Toro, M. Spruce, W. Speares, Restoration of the contact surface in the HLL-Riemann solver, Shock Waves 4 (1994) 25–34.

[104] M. Dumbser, E. F. Toro, A Simple Extension of the Osher Riemann Solver to Non-conservative Hyperbolic Systems, J. Sci. Comput. 48 (2010) 70–88.

[105] I. Toumi, A weak formulation of roe's approximate riemann solver, J. Comput. Phys. 102 (1992) 360–373.

[106] P. L. Roe, Approximate Riemann solvers, parameter vectors, and difference schemes, J. Comput. Phys. 43 (1981) 357–372.

[107] B. van Leer, Towards the ultimate conservative difference scheme. V. A second-order sequel to Godunov's method, J. Comput. Phys. 32 (1979) 101–136.

[108] X.-D. Liu, S. Osher, T. Chan, Weighted Essentially Non-oscillatory Schemes, J. Comput. Phys. 115 (1994) 200–212.

[109] E. Johnsen, J. Larsson, A. V. Bhagatwala, W. H. Cabot, P. Moin, B. J. Olson, P. S. Rawat, S. K. Shankar, B. Sjögreen, H. Yee, X. Zhong, S. K. Lele, Assessment of high-resolution methods for numerical simulations of compressible turbulence with shock waves, J. Comput. Phys. 229 (2010) 1213–1237.

[110] Y.-X. Ren, M. Liu, H. Zhang, A characteristic-wise hybrid compact-WENO scheme for solving hyperbolic conservation laws, J. Comput. Phys. 192 (2003) 365–386.

[111] M. Lombardini, Richtmyer-Meshkov instability in converging geometries, Ph.D. thesis, California Institute of Technology, 2008.

[112] C. Geuzaine, J.-F. Remacle, Gmsh: A 3-D finite element mesh generator with built-in pre- and post-processing facilities, Int. J. Numer. Methods Eng. 79 (2009) 1309–1331.

[113] M. T. Henry de Frahan, P. Movahed, E. Johnsen, Numerical simulations of a shock interacting with successive interfaces using the Discontinuous Galerkin method: the multilayered Richtmyer–Meshkov and Rayleigh–Taylor instabilities, Shock Waves 25 (2015) 329–345.

[114] C. A. Di Stefano, G. Malamud, M. T. Henry de Frahan, C. C. Kuranz, A. Shimony, S. R. Klein, R. P. Drake, E. Johnsen, D. Shvarts, V. a. Smalyuk, D. Martinez, Observation and modeling of mixing-layer development in high-energy-density, blast-wave-driven shear flowa), Phys. Plasmas 21 (2014) 056306.

[115] C.-W. Shu, S. Osher, Efficient implementation of essentially non-oscillatory shock-capturing schemes, II, J. Comput. Phys. 83 (1989) 32–78.

[116] T. Liu, B. Khoo, K. Yeo, Ghost fluid method for strong shock impacting on material interface, J. Comput. Phys. 190 (2003) 651–681.

[117] E. Johnsen, Analysis of Numerical Errors Generated by Slowly Moving Shock Waves, AIAA J. 51 (2013) 1269–1274.

[118] S. Jin, J.-G. Liu, The Effects of Numerical Viscosities, J. Comput. Phys. 126 (1996) 373–389.

[119] B. D. Collins, J. W. Jacobs, PLIF flow visualization and measurements of the Richtmyer–Meshkov instability of an air/SF6 interface, J. Fluid Mech. 464 (2002) 113–136.

[120] M. Latini, O. Schilling, W. S. Don, Effects of WENO flux reconstruction order and spatial resolution on reshocked two-dimensional Richtmyer–Meshkov instability, J. Comput. Phys. 221 (2007) 805–836.

[121] G. Ball, B. Howell, T. Leighton, M. Schofield, Shock-induced collapse of a cylindrical air cavity in water: a Free-Lagrange simulation, Shock Waves 10 (2000) 265–276.

[122] X. Y. Hu, B. C. Khoo, N. A. Adams, F. L. Huang, A conservative interface method for compressible flows, J. Comput. Phys. 219 (2006) 553–578.

[123] R. Nourgaliev, T. Theofanous, High-fidelity interface tracking in compressible flows: Unlimited anchored adaptive level set, J. Comput. Phys. 224 (2007) 836–866.

[124] S. P. Marsh, LASL Shock Hugoniot Data, Univ. California Press, Berkeley, CA, 1980.

[125] K. S. Holian, T-4 Handbook of Material Properties Data Bases, Technical Report, Los Alamos National Laboratory, Los Alamos, NM, 1984.

[126] J. P. Cocchi, R. Saurel, J. C. Loraud, Treatment of interface problems with Godunov-type schemes, Shock Waves 5 (1996) 347–357.

[127] B. Einfeldt, C. Munz, P. Roe, B. Sjögreen, On Godunov-type methods near low densities, J. Comput. Phys. 92 (1991) 273–295.

[128] J. J. Quirk, A contribution to the great Riemann solver debate, Int. J. Numer. Methods Fluids 18 (1994) 555–574.

[129] J. Meng, T. Colonius, Droplet Breakup in High-Speed Gas Flows, in: 8th Int. Conf. Multiph. Flow, 2011, ICMF, Jeju, Korea, 2013.

[130] D. Igra, K. Takayama, Investigation of aerodynamic breakup of a cylindrical water droplet, At. Sprays (2001).

[131] M. T. Henry de Frahan, S. Varadan, E. Johnsen, A new limiting procedure for discontinuous Galerkin methods applied to compressible multiphase flows with shocks and interfaces, J. Comput. Phys. 280 (2015) 489–509.

[132] D. N. Arnold, F. Brezzi, B. Cockburn, L. D. Marini, Unified Analysis of Discontinuous Galerkin Methods for Elliptic Problems, SIAM J. Numer. Anal. 39 (2002) 1749–1779.

[133] F. Brezzi, G. Manzini, D. Marini, P. Pietra, A. Russo, Discontinuous Galerkin approximations for elliptic problems, Numer. Methods Partial Differ. Equ. 16 (2000) 365–378.

[134] J. Douglas, T. Dupont, Interior penalty procedures for elliptic and parabolic Galerkin methods, Comput. methods Appl. Sci. (1976) 207–216.

[135] F. Bassi, S. Rebay, A High-Order Accurate Discontinuous Finite Element Method for the Numerical Solution of the Compressible Navier–Stokes Equations, J. Comput. Phys. 131 (1997) 267–279.

[136] J. Peraire, P.-O. Persson, The Compact Discontinuous Galerkin (CDG) Method for Elliptic Problems, SIAM J. Sci. Comput. 30 (2007) 25.

[137] M. Lo, B. van Leer, Recovery-Based Discontinuous Galerkin for Navier-Stokes Viscous Terms, AIAA Pap. (2011) AIAA–2011–3406.

[138] B. van Leer, M. Lo, Unification of Discontinuous Galerkin Methods for Advection and Diffusion 1 Introduction : history of RDG, New Horizons (2009) 1–12.

[139] B. van Leer, M. Lo, A Discontinuous Galerkin Method for Diffusion Based on Recovery, Fluid Dyn. (2007).

[140] L. H. Khieu, E. Johnsen, Analysis of Improved Advection Schemes for Discontinuous Galerkin Methods, in: 7th AIAA Theor. Fluid Mech. Conf., June, American Institute of Aeronautics and Astronautics, Reston, Virginia, 2014, pp. 1–14.

[141] V. N. Goncharov, P. McKenty, S. Skupsky, R. Betti, R. L. McCrory, C. Cherfils-Clérouin, Modeling hydrodynamic instabilities in inertial confinement fusion targets, Phys. Plasmas 7 (2000) 5118.

[142] M. Vetter, B. Sturtevant, Experiments on the Richtmyer-Meshkov instability of an air/SF6 interface, Shock Waves 4 (1995) 247–252.

[143] R. L. Holmes, G. Dimonte, B. Fryxell, M. L. Gittings, J. W. Grove, M. Schneider, D. H. Sharp, A. L. Velikovich, R. P. Weaver, Q. Zhang, Richtmyer–Meshkov instability growth: experiment, simulation and theory, J. Fluid Mech. 389 (1999) 55–79.

[144] B. Motl, J. Oakley, D. Ranjan, C. Weber, M. Anderson, R. Bonazza, Experimental validation of a Richtmyer–Meshkov scaling law over large density ratio and shock strength ranges, Phys. Fluids 21 (2009) 126102.

[145] D. J. Hill, C. Pantano, D. I. Pullin, Large-eddy simulation and multiscale modelling of a Richtmyer–Meshkov instability with reshock, J. Fluid Mech. 557 (2006) 29.

[146] O. Schilling, M. Latini, W. Don, Physics of reshock and mixing in single-mode Richtmyer–Meshkov instability, Phys. Rev. E 76 (2007) 26319.

[147] R. W. Houim, K. K. Kuo, A low-dissipation and time-accurate method for compressible multi-component flow with variable specific heat ratios, J. Comput. Phys. 230 (2011) 8527–8553.

[148] K. O. Mikaelian, Numerical simulations of Richtmyer–Meshkov instabilities in finite-thickness fluid layers, Phys. Fluids 8 (1996) 1269.

[149] B. J. Balakumar, G. C. Orlicz, C. D. Tomkins, K. P. Prestridge, Simultaneous particle-image velocimetry–planar laser-induced fluorescence measurements of Richtmyer–Meshkov instability growth in a gas curtain with and without reshock, Phys. Fluids 20 (2008) 124103.

[150] S. K. Shankar, S. K. Lele, Numerical investigation of turbulence in reshocked Richtmyer–Meshkov unstable curtain of dense gas, Shock Waves 24 (2013) 79–95.

[151] M. T. Henry de Frahan, E. Johnsen, Discontinuous Galerkin method for multifluid Euler equations, in: 21st AIAA Comput. Fluid Dyn. Conf., American Institute of Aeronautics and Astronautics, Reston, Virginia, 2013, pp. 1–12.

[152] W. Kutta, Beitrag zur näherungsweisen Integration totaler Differentialgleichungen, Zeitschrift für Angew. Math. und Phys. 46 (1901) 435–453.

[153] M. Hahn, D. Drikakis, D. L. Youngs, R. J. R. Williams, Richtmyer–Meshkov turbulent mixing arising from an inclined material interface with realistic surface perturbations and reshocked flow, Phys. Fluids 23 (2011) 046101.

[154] P. Movahed, E. Johnsen, Numerical simulations of the Richtmyer-Meshkov instability with reshock, in: 20th AIAA Comput. Fluid Dyn. Conf., June, American Institute of Aeronautics and Astronautics, Reston, Virigina, 2011, pp. 1–12.

[155] C. Weber, N. Haehn, J. Oakley, D. Rothamer, R. Bonazza, Turbulent mixing measurements in the Richtmyer-Meshkov instability, Phys. Fluids 24 (2012) 074105.

[156] G. Dimonte, Nonlinear evolution of the Rayleigh–Taylor and Richtmyer–Meshkov instabilities, Phys. Plasmas 6 (1999) 2009.

[157] B. Fryxell, D. Arnett, E. Mueller, Instabilities and clumping in SN 1987A. I - Early evolution in two dimensions, Astrophys. J. 367 (1991) 619.

[158] G. Taylor, The Formation of a Blast Wave by a Very Intense Explosion. I. Theoretical Discussion, Proc. R. Soc. A Math. Phys. Eng. Sci. 201 (1950) 159–174.

[159] L. I. Sedov, Propagation of strong shock waves, J. Appl. Math. Mech. 10 (1946) 241–250.

[160] R. Courant, K. Friedrichs, Supersonic Flow and Shock Waves, volume 21 of *Applied Mathematical Sciences*, Springer New York, New York, NY, 1976.

[161] X. Ribeyre, V. T. Tikhonchuk, S. Bouquet, Compressible Rayleigh–Taylor instabilities in supernova remnants, Phys. Fluids 16 (2004) 4661.

[162] P. J. McGregor, P. D. Nicholson, M. G. Allen, CASPIR Observations of the Collision of Comet Shoemaker–Levy 9 with Jupiter, Icarus 121 (1996) 361–388.

[163] L. Rayleigh, Aerial Plane Waves of Finite Amplitude, Proc. R. Soc. A Math. Phys. Eng. Sci. 84 (1910) 247–284.

[164] D. Sharp, An overview of Rayleigh-Taylor instability, Phys. D Nonlinear Phenom. 12 (1984) 3–18.

[165] W. H. Cabot, A. W. Cook, Reynolds number effects on Rayleigh–Taylor instability with possible implications for type Ia supernovae, Nat. Phys. 2 (2006) 562–568.

[166] S. Chandrasekhar, Hydrodynamic and Hydromagnetic Stability, Oxford University Press, London, 1961.

[167] E. Leinov, G. Malamud, Y. Elbaz, L. A. Levin, G. Ben-Dor, D. Shvarts, O. Sadot, Experimental and numerical investigation of the Richtmyer–Meshkov instability under re-shock conditions, J. Fluid Mech. 626 (2009) 449.

[168] R. V. Morgan, R. Aure, J. D. Stockero, J. a. Greenough, W. Cabot, O. a. Likhachev, J. W. Jacobs, On the late-time growth of the two-dimensional Richtmyer–Meshkov instability in shock tube experiments, J. Fluid Mech. 712 (2012) 354–383.

[169] R. V. Morgan, Experiments of the rarefaction wave driven Rayleigh-Taylor Instability, Ph.D. thesis, The University of Arizona, 2014.

[170] R. P. Drake, D. R. Leibrandt, E. C. Harding, C. C. Kuranz, M. a. Blackburn, H. F. Robey, B. a. Remington, M. J. Edwards, a. R. Miles, T. S. Perry, R. J. Wallace, H. Louis, J. P. Knauer, D. Arnett, Nonlinear mixing behavior of the three-dimensional Rayleigh–Taylor instability at a decelerating interface, Phys. Plasmas 11 (2004) 2829.

[171] C. C. Kuranz, R. P. Drake, M. J. Grosskopf, B. Fryxell, A. Budde, J. F. Hansen, a. R. Miles, T. Plewa, N. Hearn, J. Knauer, Spike morphology in blast-wave-driven instability experiments, Phys. Plasmas 17 (2010) 052709.

[172] A. R. Miles, M. J. Edwards, J. A. Greenough, Effect of initial conditions on two-dimensional Rayleigh–Taylor instability and transition to turbulence in planar blast-wave-driven systems, Phys. Plasmas 11 (2004) 5278.

[173] A. R. Miles, M. J. Edwards, B. Blue, J. F. Hansen, H. F. Robey, R. P. Drake, C. Kuranz, D. R. Leibrandt, The effect of a short-wavelength mode on the evolution of a long-wavelength perturbation driven by a strong blast wave, Phys. Plasmas 11 (2004) 5507.

[174] a. R. Miles, B. Blue, M. J. Edwards, J. a. Greenough, J. F. Hansen, H. F. Robey, R. P. Drake, C. Kuranz, D. R. Leibrandt, Transition to turbulence and effect of initial conditions on three-dimensional compressible mixing in planar blast-wave-driven systems, Phys. Plasmas 12 (2005) 056317.

[175] A. R. Miles, The blast-wave-driven instability as a vehicle for understanding supernova explosion structure, Astrophys. J. 696 (2009) 498–514.

[176] K. Mori, Two-fluid simulations of shock wave propagation and shock-bubble interaction in collisionless plasma, Phys. Plasmas 19 (2012) 032311.

[177] N. Zabusky, J. Ray, R. S. Samtaney, Vortex Models for Richtmyer – Meshkov Fast / Slow Environments : Scaling Laws for Interface Growth Rates, in: R. Young, J. Glimm, B. Boyton (Eds.), Proc. 5th Int. Work. Compressible Turbul. Mix., World Scientific, Singapore, 1996, pp. 89–97.

[178] N. J. Zabusky, Vortex paradigm for accelerated inhomogeneous flows: Visiometrics for the Rayleigh-Taylor and Richtmyer-Meshkov environments, Annu. Rev. Fluid Mech. 31 (1999) 495–536.

[179] a. Rikanati, U. Alon, D. Shvarts, Vortex model for the nonlinear evolution of the multimode Richtmyer-Meshkov instability at low Atwood numbers, Phys. Rev. E 58 (1998) 7410–7418.

[180] A. D. Kotelnikov, N. J. Zabusky, Vortex Dynamics of a Twice-accelerated Interface in an Incompressible Ideal Fluid, Astrophys. J. Suppl. Ser. 127 (2000) 389–394.

[181] G. Peng, N. J. Zabusky, S. Zhang, Vortex-accelerated secondary baroclinic vorticity deposition and late-intermediate time dynamics of a two-dimensional Richtmyer–Meshkov interface, Phys. Fluids 15 (2003) 3730.

[182] a. Rikanati, D. Oron, O. Sadot, D. Shvarts, High initial amplitude and high Mach number effects on the evolution of the single-mode Richtmyer-Meshkov instability, Phys. Rev. E 67 (2003) 026307.

[183] Y. Srebro, Y. Elbaz, O. Sadot, L. Arazi, D. Shvarts, A general buoyancy–drag model for the evolution of the Rayleigh–Taylor and Richtmyer–Meshkov instabilities, Laser Part. Beams 21 (2003) 347–353.

[184] a. R. Miles, Bubble merger model for the nonlinear Rayleigh–Taylor instability driven by a strong blast wave, Phys. Plasmas 11 (2004) 5140.

[185] V. N. Goncharov, Analytical model of nonlinear, single-mode, classical Rayleigh-Taylor instability at arbitrary Atwood numbers., Phys. Rev. Lett. 88 (2002) 134502.

[186] K. O. Mikaelian, Reshocks, rarefactions, and the generalized Layzer model for hydrodynamic instabilities, Phys. Fluids 21 (2009) 024103.

[187] R. P. Drake, Spike penetration in blast-wave-driven instabilities, Astrophys. J. 744 (2012) 184.

[188] R. Courant, K. Friedrichs, Interaction of shock and rarefaction waves in one-dimensional media, Technical Report, National Defense Research Committee, 1943.

[189] D. Shvarts, U. Alon, D. Ofer, R. L. McCrory, C. P. Verdon, Nonlinear evolution of multimode Rayleigh–Taylor instability in two and three dimensions, Phys. Plasmas 2 (1995) 2465.

[190] A. L. Velikovich, J. P. Dahlburg, A. J. Schmitt, J. H. Gardner, L. Phillips, F. L. Cochran, Y. K. Chong, G. Dimonte, N. Metzler, Richtmyer–Meshkov-like instabilities and early-time perturbation growth in laser targets and Z-pinch loads, Phys. Plasmas 7 (2000) 1662.

[191] B. Bishop, New experimental research exposes the strength of beryllium at extreme conditions, 2015.

[192] W. R. Blumenthal, S. P. Abeln, D. D. Cannon, G. T. Gray, R. W. Carpenter, Influence of strain rate and temperature on the mechanical behavior of beryllium, in: AIP Conf. Proc., volume 411, AIP, 1998, pp. 411–414.

[193] T. Sisneros, D. Brown, B. Clausen, D. Donati, S. Kabra, W. Blumenthal, S. Vogel, Influence of strain rate on mechanical properties and deformation texture of hot-pressed and rolled beryllium, Mater. Sci. Eng. A 527 (2010) 5181–5188.

[194] J. M. Marder, Beryllium in stress-critical environments, J. Mater. Energy Syst. 8 (1986) 17–26.

[195] F. Ayer, Materials for Space Optics, Generic Requirements, Technical Report, Rapid Optics Fabrication Technology, Defense Advanced Research Projects Administration, Daytona Beach, Florida, 1984.

[196] K. Bennett, R. Varma, R. Von Dreele, Texture development in S200-D, -E and P31664 beryllium blocks from neutron diffraction spectra, Scr. Mater. 40 (1999) 825–830.

[197] L. B. Norwood, How beryllium proved successful on the Space Shuttle Orbiter, J. Spacecr. Rockets 22 (1985) 560–566.

[198] S. P. Abeln, P. Kyed, Summary of Beryllium Specifications: Current and Historical, Technical Report, EG&G ROCKY FLATS, INC., Golden, Colorado, 1990.

[199] U. S. Lindholm, L. M. Yeakley, Effect of Strain Rate, Temperature and Multiaxial Stress on the Strength and Ductility of S-200E Beryllium and 6Al-4V Titanium, Technical Report, Southwest Research Institute, San Antonio, TX, 1972.

[200] D. R. Christman, N. H. Froula, Dynamic properties of high-purity beryllium, AIAA J. 8 (1970) 477–482.

[201] D. R. Christman, F. J. Feistmann, Dynamic Properties of S-200-E Beryllium, Technical Report, General Motors Technical Center, Warren, MI, 1972.

[202] L. C. Chhabildas, J. L. Wise, J. R. Asay, Reshock and release behavior of beryllium, in: AIP Conf. Proceeding Vol. 78, volume 422, pp. 422–426.

[203] U. S. Lindholm, L. M. Yeakley, D. L. Davidson, Biaxial Strength Tests on Beryllium and Titanium Alloys, Technical Report July, Southwest Research Institute, San Antonio, TX, 1974.

[204] L. E. Pope, J. N. Johnson, Shock-wave compression of single-crystal beryllium, J. Appl. Phys. 46 (1975) 720.

[205] S. Jönsson, J. Beuers, The dislocation structure in beryllium single crystals deformed by prismatic slip, Mater. Sci. Eng. 91 (1987) 111–123.

[206] J. Christian, S. Mahajan, Deformation twinning, Prog. Mater. Sci. 39 (1995) 1–157.

[207] W. R. Blumenthal, Evolution of Crystallographic Texture and Strength in Beryllium, in: AIP Conf. Proc., volume 706, AIP, 2004, pp. 525–528.

[208] D. W. Brown, B. Clausen, T. A. Sisneros, L. Balogh, I. J. Beyerlein, In Situ Neutron Diffraction Measurements During Annealing of Deformed Beryllium With Differing Initial Textures, Metall. Mater. Trans. A 44 (2013) 5665–5675.

[209] D. W. Brown, S. P. Abeln, W. R. Blumenthal, M. A. M. Bourke, M. C. Mataya, C. N. Tomé, Development of crystallographic texture during high rate deformation of rolled and hot-pressed beryllium, Metall. Mater. Trans. A 36 (2005) 929–939.

[210] D. W. Brown, S. R. Agnew, S. P. Abeln, W. Blumenthal, M. a.M. Bourke, M. Mataya, C. N. Tomé, S. C. Vogel, The Role of Texture, Temperature and Strain Rate in the Activity of Deformation Twinning, Mater. Sci. Forum 495-497 (2005) 1037–1042.

[211] D. Brown, J. Almer, B. Clausen, P. Mosbrucker, T. Sisneros, S. Vogel, Twinning and de-twinning in beryllium during strain path changes, Mater. Sci. Eng. A 559 (2013) 29–39.

[212] J. L. Brown, M. D. Knudson, C. S. Alexander, J. R. Asay, Shockless compression and release behavior of beryllium to 110 GPa, J. Appl. Phys. 116 (2014) 033502.

[213] V. Skokov, V. Arinin, D. Kryuchkov, V. Ogorodnikov, V. Raevsky, K. Panov, V. Peshkov, O. Tyupanova, Spall fracture of beryllium under shockwave loading, in: AIP Conf. Proc., volume 1073, pp. 1073–1076.

[214] C. Adams, W. W. Anderson, G. T. Gray, W. R. Blumenthal, C. T. Owens, F. J. Freibert, J. M. Montoya, P. J. Contreras, M. Elert, M. D. Furnish, W. G. Proud, W. T. Butler, Spall and damage behavior of S200F Beryllium, in: AIP Conf. Proc., volume 509, pp. 509–512.

[215] C. D. Adams, W. W. Anderson, W. R. Blumenthal, G. T. Gray, Elastic precursor decay in S-200F beryllium, J. Phys. Conf. Ser. 500 (2014) 112001.

[216] Y. Mescheryakov, A. Divakov, N. Zhigacheva, Shock-induced structural transitions and dynamic strength of solids, Int. J. Solids Struct. 41 (2004) 2349–2362.

[217] Y. I. Mescheryakov, A. K. Divakov, Y. A. Petrov, C. F. Cline, On the dynamic plasticity and strength of polycrystalline beryllium, Int. J. Impact Eng. 30 (2004) 17–29.

[218] C. Cady, C. Adams, L. Hull, G. Gray, M. Prime, F. Addessio, T. Wynn, P. Papin, E. Brown, Characterization of shocked beryllium, EPJ Web Conf. 26 (2012) 01009.

[219] E. N. Brown, C. M. Cady, G. T. Gray, L. M. Hull, J. H. Cooley, C. a. Bronkhorst, F. L. Addessio, Characterization of shocked beryllium, J. Phys. Conf. Ser. 500 (2014) 112013.

[220] M. L. Wilkins, M. W. Guinan, Impact of cylinders on a rigid boundary, J. Appl. Phys. 44 (1973) 1200.

[221] J. W. Miles, General Atomic Division of General Dynaumics Report No. GAMD-7335, (unpublished) (1966).

[222] J. F. Barnes, P. J. Blewett, R. G. McQueen, K. a. Meyer, D. Venable, Taylor instability in solids, J. Appl. Phys. 45 (1974) 727.

[223] J. H. Cooley, R. T. Olson, D. Oro, Modeling and analysis of high-explosive driven perturbed plate experiments at Los Alamos, J. Phys. Conf. Ser. 500 (2014) 152003.

[224] V. A. Raevsky, Influence of dynamic material properties on perturbation growth in solids, Technical Report, All-Russian Research Institute of Experimental Physics VNIIEF, Sarov, 2009.

[225] H.-S. Park, K. T. Lorenz, R. M. Cavallo, S. M. Pollaine, S. T. Prisbrey, R. E. Rudd, R. C. Becker, J. V. Bernier, B. a. Remington, Viscous Rayleigh-Taylor instability experiments at high pressure and strain rate., Phys. Rev. Lett. 104 (2010) 135504.

[226] H.-S. Park, N. Barton, J. L. Belof, K. J. M. Blobaum, R. M. Cavallo, a. J. Comley, B. Maddox, M. J. May, S. M. Pollaine, S. T. Prisbrey, B. Remington, R. E. Rudd, D. W. Swift, R. J. Wallace, M. J. Wilson, A. Nikroo, E. Giraldez, Experimental results of tantalum material strength at high pressure and high strain rate, AIP Conf. Proc. 1371 (2012) 1371–1374.

[227] M. Tang, P. D. Norquist, J. Barton, N.R., Durrenberger, J. K., Florando, A. Attia, MIDAS: A Comprehensive Resource of Material Properties, Technical Report, Lawrence Livermore National Laboratory, 2010.

[228] V. a. Arinin, B. I. Tkachenko, Achieving the ultimate quality of image registration in radiography, Pattern Recognit. Image Anal. 19 (2009) 63–68.

[229] C. F. McMillan, D. R. Goosman, N. L. Parker, L. L. Steinmetz, H. H. Chau, T. Huen, R. K. Whipkey, S. J. Perry, Velocimetry of fast surfaces using Fabry–Perot interferometry, Rev. Sci. Instrum. 59 (1988) 1.

[230] G. Bazan, No Title, in: B. A. Remington (Ed.), Proc. from 2nd Int. Work. Lab. Astrophys. with Intense Lasers, Lawrence Livermore National Laboratory, Livermore, CA, 1998.

[231] P. C. Souers, S. Anderson, J. Mercer, E. McGuire, P. Vitello, JWL++: A Simple Reactive Flow Code Package for Detonation, Propellants, Explos. Pyrotech. 25 (2000) 54–58.

[232] R. M. More, K. H. Warren, D. a. Young, G. B. Zimmerman, A new quotidian equation of state (QEOS) for hot dense matter, Phys. Fluids 31 (1988) 3059.

[233] D. J. Steinberg, S. G. Cochran, M. W. Guinan, A constitutive model for metals applicable at high-strain rate, J. Appl. Phys. 51 (1980) 1498.

[234] D. J. Steinberg, C. M. Lund, A constitutive model for strain rates from 10-4 to 106 s-1, J. Appl. Phys. 65 (1989) 1528.

[235] M. B. Prime, S.-R. Chen, C. Adams, Advanced plasticity models applied to recent shock data on beryllium, in: AIP Conf. Proc., volume 1035, pp. 1035–1038.

[236] V. A. Raevsky, O. Aprelkov, O. Ignatova, V. Igonin, A. Lebedev, S. Nadezhin, M. Zocher, D. Preston, A. Coul, Development of wide-range constitutive equations for calculations of high-rate deformation of metals, EPJ Web Conf. 10 (2011) 00022.

[237] B. L. Glushak, O. Ignatova, N. S. S. Nadezhin, V. A. Raevsky, Relaxation model of shear strength of five metals, VANT Ser. Math. Model. Phys. Process. (2012) 25–36.

[238] P. Follansbee, U. Kocks, A constitutive description of the deformation of copper based on the use of the mechanical threshold stress as an internal state variable, Acta Metall. 36 (1988) 81–93.

[239] M. Henry de Frahan, E. Johnsen, High-order Discontinuous Galerkin Methods Applied to Multiphase Flows, in: 22nd AIAA Comput. Fluid Dyn. Conf., June, American Institute of Aeronautics and Astronautics, Reston, Virginia, 2015, pp. 1–14.

[240] M. T. Henry de Frahan, J. L. Belof, R. M. Cavallo, V. a. Raevsky, O. N. Ignatova, A. Lebedev, D. S. Ancheta, B. S. El-dasher, J. N. Florando, G. F. Gallegos, E. Johnsen, M. M. LeBlanc, Experimental and numerical investigations of beryllium strength models using the Rayleigh-Taylor instability, J. Appl. Phys. 117 (2015) 225901.

[241] K. G. Powell, P. L. Roe, T. J. Linde, T. I. Gombosi, D. L. De Zeeuw, A Solution-Adaptive Upwind Scheme for Ideal Magnetohydrodynamics, J. Comput. Phys. 154 (1999) 284–309.

[242] M. J. Lighthill, Studies on Magneto-Hydrodynamic Waves and other Anisotropic Wave Motions, Philos. Trans. R. Soc. A Math. Phys. Eng. Sci. 252 (1960) 397–430.

[243] E. a. Witalis, Hall Magnetohydrodynamics and Its Applications to Laboratory and Cosmic Plasma, IEEE Trans. Plasma Sci. 14 (1986) 842–848.

[244] J. Freidberg, Ideal magnetohydrodynamic theory of magnetic fusion systems, Rev. Mod. Phys. (1982).

[245] U. Shumlak, J. Loverich, Approximate Riemann solver for the two-fluid plasma model, J. Comput. Phys. 187 (2003) 620–638.

[246] A. Hakim, J. Loverich, U. Shumlak, A high resolution wave propagation scheme for ideal Two-Fluid plasma equations, J. Comput. Phys. 219 (2006) 418–442.

[247] A. H. Hakim, Extended MHD Modelling with the Ten-Moment Equations, J. Fusion Energy 27 (2007) 36–43.

[248] S. Gilliam, A 13-Moment Two-Fluid Plasma Physics Model Based on a Pearson Type-IV Distribution Function, Ph.D. thesis, University of Washington, 2011.

[249] D. E. Knuth, Structured Programming with go to Statements, ACM Comput. Surv. 6 (1974) 261–301.

[250] W. C. Wan, G. Malamud, A. Shimony, C. A. Di Stefano, M. R. Trantham, S. R. Klein, D. Shvarts, C. C. Kuranz, R. P. Drake, Observation of Single-Mode, Kelvin-Helmholtz Instability in a Supersonic Flow, Phys. Rev. Lett. 115 (2015) 145001.

[251] C. E. Brennen, Cavitation and Bubble Dynamics, Oxford University Press, New York, 1995.

[252] R. B. Eddington, Investigation of supersonic phenomena in a two- phase liquid-gas tunnel, AIAA J. 8 (1970) 65–74.